

Novel Systems for Position and Force Control of Slender and Compliant Robots for In-Situ Machining

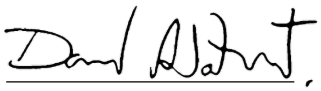
Submitted to the University of Nottingham for the degree of **Doctor of Philosophy, May 2020.**

David Alatorre Troncoso
MEng, Mechanical Engineering & Mechatronics

Supervised by Prof. Dragos Axinte
Dr. Amir Rabani
Dr. David Branson III
Dr. Xin Dong

Department of Mechanical, Materials and Manufacturing Engineering
University of Nottingham

I hereby declare that this dissertation is all my own work, except as indicated in the text:

Signature 

Date 13 / July / 2020

I hereby declare that I have all necessary rights and consents to publicly distribute this dissertation via the University of Nottingham's e-dissertation archive.

Public access to this thesis is restricted until: 29/05/2025

Abstract

This thesis presents a number of advances in the area of manufacturing engineering, specifically in the topic of robotics and automation, and more specifically still in the subject of feedback and control; applied to the special example of slender and compliant machining instruments for in-situ repair of gas turbines and industrial assets. A thorough literature search of in-situ repair robots, such as continuum and conventional robotic arms with material removal or non-destructive testing end effectors, is compiled and presented with particular attention to the applicability of past architectures, technologies, control methods and sensors to "industrial minimally invasive surgery" carried out via a borescope port. A novel robot for localised grinding of aeroengine compressor blades (boreblending) is described and analysed as a case study in-situ repair robot - an example lacking advanced position and force feedback methods and therefore limited in its capabilities and scalability. The slender probe (less than $10mm$ diameter and more than $100mm$ in length) includes a number of short continuum segments as well as rotary and prismatic stages. Following an open loop control scheme with tendon stretch compensation, the maximum position error at full deflection is 8.5% of the continuum length. Areas for improvement in position feedback, force feedback and control strategies are identified.

A novel method to obtain position feedback and hence improve position accuracy, is described in the form of a shape sensor. Tubular ionic liquid stretch sensors are used as hyper-elastic strain gauges and applied as skin sensors to continuum-style robots such as those used for in-situ repair; the sensors are characterised and employed as feedback for closed-loop position control of a complex continuum arm. Closed loop trials on a complex continuum manipulator yield errors equivalent to 2.3% of continuum length, demonstrating a substantial improvement over open-loop methods.

A novel method to obtain force feedback in the form of airborne sound features from a grinding end effector is then described. Calibration and signal processing of two microphone voltage lines returns a value of contact force between instrument and workpiece based on sound features such as dominant frequency and sound intensity; this force feedback is employed for closed-loop force control of a conventional robotic arm during machining. Results from the test rigs and robot arm show that such a sound-based control approach can achieve consistent cutting forces with an accuracy of

$0.08N$. The robot arm is shown to be capable of grinding features of consistent depth (to within $0.05mm$) on beams with unknown topology.

Finally, a simultaneous position-force controller is devised to make use of tubular ionic liquid stretch sensors position feedback and audible sound features force feedback to accurately machine an aeroengine compressor blade using a slender continuum arm. The parallel controller separates the task space into reactive and non-reactive directions based on the orientation of the end effector and imposes a force hierarchy and position completion threshold. The results show 80% improvement in machining time over manual methods and 33% improvement over open loop control methods.

Acknowledgements

With special thanks:

To my mother and father, in whose footsteps I should hope to follow; for affording me a life full of love and opportunities.

To my girlfriend, turned fiancée, turned wife, Elle; for her unconditional love and support through this chapter of my life.

To my principal supervisor Prof. Dragos Axinte; for his relentless commitment to my success, in work and in life.

To Dr. Amir Rabani, Dr. David Branson III and Dr. Xin Dong; for their wisdom and support.

To Rolls-Royce plc for their funding of this PhD, and Dr. James Kell for his enduring engagement and assistance.

To the Aeospace Technology Institute for their funding of the remote boreblending project under SAMULET II.

And to the technical staff at the Faculty of Engineering; for their vast contribution of time and skill.

Contents

Abstract i

Acknowledgements iii

List of Publications ix

List of Figures x

List of Tables xxii

Nomenclature xxiv

1 Introduction 1

1.1 Background 1

1.2 Problem definition 3

1.3 Objectives of this study 6

1.4 Structure of the thesis 7

1.5 Contributions 8

1.5.1 New concepts for specialist in-situ machining robotics 8

1.5.2 New concepts for position control of continuum robots 9

1.5.3 New concepts for force control of continuum robots 10

1.5.4 Publication summary 10

2 Literature Review 13

2.1 Introduction 13

2.2 Review of continuum robots 14

2.2.1 Continuum robots for industrial applications 14
2.2.2 Continuum robots for medical applications 18
2.3 Challenges in position control methods of continuum robots 22
2.3.1 Continuum robot kinematics modelling 22
2.3.2 Extrinsic position measurement methods 26
2.3.3 Intrinsic position measurement methods 28
2.4 Review of robot force control methods for in-situ machining 35
2.4.1 Force sensing in conventional jointed robots 35
2.4.2 Force sensing in continuum flexible robots 39
2.4.3 Process force control using remote sensors 43
2.5 Review of simultaneous position and force controllers 46
2.5.1 Simultaneous position and force control of conventional robots . . . 46
2.5.2 Simultaneous position and force control of continuum robots 50
2.6 Research gaps for potential future investigation 53

3 Case study of a slender robot for in-situ machining to identify challenges in position and force control 56

3.1 Background 57
3.2 Degree of freedom study for in-situ boreblending 59
3.3 In-situ boreblending robot hardware 62
3.3.1 Mechanical system architecture 62
3.3.2 Compliant joint buckling study 66
3.3.3 Tensile characterisation of driving tendons 68
3.4 Robot kinematics 72
3.4.1 Forward Kinematics 72
3.4.2 Inverse Kinematics 75
3.5 In-situ boreblending robot software 78
3.5.1 Remote Control System Architecture 78
3.5.2 Proposed System Workflow 84
3.6 Robotic boreblending demonstration 86

3.6.1 Laboratory demonstration of machining capabilities 86
3.6.2 In situ demonstration on Trent XWB aeroengine 88
3.7 Conclusions of case study and areas of improvement in position and force control 90

4 New methods of position control for slender and compliant in-situ machining robots 93
4.1 Background 95
4.2 Resistive proprioception concept and sensor characterisation 97
4.2.1 Tubular resistive sensor concept 97
4.2.2 Continuum robot proprioception 100
4.3 Sensor and manipulator construction methodology 101
4.3.1 Tubular stretch sensor material compatibility 101
4.3.2 Manufacture and assembly of tubular ionic liquid stretch sensors (TILSS) 106
4.3.3 Construction and characterisation of 1-axis continuum manipulator 112
4.3.4 Construction of 4-axis continuum manipulator 117
4.4 Closed loop control of slender and compliant robots 121
4.4.1 Closed loop controller design 121
4.4.2 Control of continuum segments 124
4.5 Conclusions and future work 130

5 New methods of force control for slender and compliant robots for in-situ machining 132
5.1 Background 133
5.2 Characterisation of sound features for force control 135
5.2.1 Description of audible sound emissions during grinding 135
5.2.2 Acquisition of calibration data 138
5.2.3 Acoustic sensor calibration 141
5.3 Closed loop force control using sound features 147

5.3.1 Controller calibration methodology 148
5.3.2 Closed loop controller design 149
5.3.3 Experimental validation of the controller 152
5.4 Conclusions and future work 160

6 Simultaneous position and force control of a slender and compliant in-situ machining robot 162

6.1 Background 162
6.2 In-situ machining simultaneous control scheme 164
6.2.1 Simultaneous position and force control methodology 164
6.2.2 Control method implementation 168
6.3 Machining demonstration using simultaneous position and force control . . 173
6.4 Conclusions and further improvements 178

7 Thesis conclusions and further work 180

7.1 Discussion of challenges and project objectives 180
7.2 Academic findings and engineering validations 184
7.2.1 Novel combined architecture slender and compliant robot for remote controlled in-situ boreblending 184
7.2.2 Novel methodology for position feedback using tubular ionic liquid stretch sensors 186
7.2.3 Novel methodology for force feedback using airborne sound machining force sensor 187
7.2.4 Novel simultaneous position and force control scheme for slender and compliant machining robots 188
7.3 Future work 189
7.3.1 Enhancing position control of slender and compliant robots for in-situ machining 189
7.3.2 Enhancing force control of compliant robots for in-situ machining . 189

7.3.3 Enhancing simultaneous position and force control of slender and compliant robots for in-situ machining 190
7.3.4 The future of specialised slender and compliant robotic systems for in-situ machining 191
7.4 Closing remarks 192

References **193**

Appendices **214**

A Equipment index **214**

List of Publications

Academic papers

1. D. Alatorre, A. Rabani, D. Axinte and D.T. Branson III. Closed loop force control of in-situ machining robots using audible sound features. *Mechanical Systems and Signal Processing*, 136:106-517, 2019

2. D. Alatorre, B. Nasser, A. Rabani, A. Nagy-Sochacki, X. Dong, D. Axinte, J. Kell. Robotic boreblending: the future of in-situ gas turbine repair. *2018 IEEE/RSJ International Conference on Intelligent Robots and Systems (IROS)*, Vols 1-10, pp. 1401-1406, 2018

3. D. Alatorre, B. Nasser, A. Rabani, A. Nagy-Sochacki, X. Dong, D. Axinte, J. Kell. Teleoperated in-situ repair of an aeroengine. *IEEE Robotics & Automation Magazine*, Vol 26, pp. 10-20, 2019

4. M.F. Wang, D. Palmer, X. Dong, D. Alatorre, D. Axinte, A. Norton. Design and development of a slender dual-structure continuum robot for in-situ aeroengine repair. *2018 IEEE/RSJ International Conference on Intelligent Robots and Systems (IROS)*, Vols 1-10, pp. 5648-5653, 2018

5. H.Habibi, P. Land, M.J. Ball, D. Alatorre, D.T. Branson III. Optimal integration of pneumatic artificial muscles with vacuum-jammed surfaces to characterise a novel reconfigurable moulding system. *Journal of Manufacturing Processes*, Vol 32, pp. 241-253, 2018

Patents

1. Closed-loop position control of continuum robots: describes the use of flexible strain sensors placed some distance from the axis of bend of a continuum robot for closed-loop position control. Suggests possible options of sensors such as tubular ionic liquid stretch sensors. Priority 9 March 2017, published as *EP3372353A1; GB2560354A; SG10201801266WA; US2018257235A1*

2. Apparatus and methods for enabling determination of a shape of at least a portion of a continuum robot: Describes the application of a sleeve containing stretch sensors for closed-loop position control of a previously open-loop continuum robot. Suggests possible manufacture methods for such a sensor assembly, such as 3-D printing using elastomers. Priority 9 March 2017, published as *EP3372352A1; GB2560355A; SG10201801270UA; US2018264643A1*

List of Figures

2.1 Continuum robot for in-situ inspection and repair of nuclear installations developed by Rob Buckingham and Andrew Graham [14] and consisting of a number of $40mm$ diameter discs with 20 flexible degrees of freedom. . . . 15

2.2 Detail of the principle of operation of a twin compliant backbone continuum robot segment with alternating bend direction for dual direction bend [8] . 15

2.3 Continuum robot for in-situ repair of gas turbine IPC stages showing simulated kinematics (a), experimental validation (b) and close-up of end effector (c) [16]. Robot employs twin compliant backbones and vertebral discs of incrementing size to achieve 24 degrees of freedom. 16

2.4 Elephant trunk manipulator developed by Hannan and Walker using universal joints in series together with tension springs to provide a restoring force [17]. 17

2.5 Detail of universal joints in Hannan and Walker's elephant trunk robot [17] showing the lack of a central passage to deliver services to an end effector. 17

2.6 Construction of Simaan's laryngeal surgery robot using concentric nitinol tubes [7]. Concentric tubes allow for pushing and pulling action at intermediate locations along the continuum length. 19

2.7 Nitinol notched tubes continuum robot by [28] flexed to its mechanical limits. The notched tubes architecture provides flexibility while maximising available central passage space. 20

2.8 Nitinol concentric tubes continuum robot by [32]. Relative rotation and translation of pre-bent needles allows for steering of the needle tip, which may in turn deliver an end effector through a small access. 20

2.9 Gait sequence for percussively actuated non-continuum snake robot [21]. Selective rigidisation of two concentric "snakes" allows the tip to follow complex trajectories. 21

2.10 Flexed continuum segment with constant radius of curvature in flexible segment of length a. Tendons are assumed to follow straight lines between holes in adjacent vertebrae. 23

2.11 Demonstration of the revolute joint discretisation model by Jeon et al. [35] showing the model without (a) and with the effect of gravity (b). 24

2.12 Comparison of two approaches for modelling continuum segments. Elastica and discretised arcs iterative approach [36]. While both arrive at accurate shape estimations, the iterative beam bending approach is more versatile when it comes to the exact shape of the bends. 25

2.13 Configuration of magnetic sensors for shape tracking by Song et al. [9]. Magnetic sensors require an emitter unit to calculate their relative position and are susceptible to interference from even small metallic objects. 26

2.14 Shape tracking using computer vision by Mahl et al. [10]. Optical motion tracking requires externally-mounted cameras with line-of-sight to trackers on the continuum robot, making them suitable only for laboratory environments and tasks in controlled spaces. 27

2.15 Pneumatic bellows continuum actuator with four PVDF sensors by Shapiro et al [44]. While such sensors may be used to measure curvature directly, they must be mounted close to the neutral axis of the robot, reducing the available space for services. 28

2.16 SMA bending module integrated with SMA sensor (a), and detail of the FBG bending sensor (b) [57]. Like PVDF sensors, fibre sensors with Bragg gratings must be located near the central axis of the continuum robot. . . . 30

2.17 Two segment pneumatic actuator equipped with 16 eutectic Gallium Indium resistive strain sensors [77]. Various orientations and a number of redundant sensors allow for monitoring of parameters such as contact with objects and internal pressure. 31

2.18 Capacitive strain sensor principle of operation: stretching the elastic element reduces the size of the gap between conductive layers and increases the conductive layer surface area [86]. 33

2.19 Hall effect magnetic sensor attached to flexible substrate to measure curvature [91]. Hall effect sensors can detect small changes in magnetic fields but require bulky integrated circuits and magnets. 34

2.20 A prototype rotary series-elastic actuator presented by [104]. The torsion accumulated in a spring can be used to control joint torque. 37

2.21 A wrist force sensor mounted on a robot arm, presented by [111]. Six-axis load cells can be used to obtain detailed measurements of reaction forces at the end effector but are difficult to miniaturise. 38

2.22 A wrist-style force sensor of cylindrical construction using three optoelectronic sensors and three mirrors, as presented by [119]. 39

2.23 Cable tension sensors enable continuum robots to measure force and detect hard objects embedded in a silicone matrix from Xu and Simaan [11]. . . . 41

2.24 Location and magnitude of contact is detected using knowledge of cable tension and position of the arm [123]. The method relies heavily on external measurement methods (electromagnetic trackers). 42

2.25 RMS signal level in specific wave bands for two different types of concrete (E30 and A30) as obtained by airborne sound signal detection in [138]. . . 45

2.26 Two parallel and independent control loops, where Y_{sp} is the set point for the variable, Y is the output, G_c is the controller transfer function and G_p is the process transfer function [141]. 47

2.27 Block diagram for multi-loop control with controller interactions [141]. The coupled controllers can result in positive feedback and pose challenges for control. 47

2.28 Block diagram for multiloop control specific to position and force feedback from a manipulator. The interaction between two loops is expected and inevitable. 48

2.29 Block diagram for Chiaverini's parallel force/position controller. C is the Controller, M is the Manipulator, E is the Environment, f is force and p is position [145]. 50

2.30 Motion/force control strategy for continuum robots from Bajo and Simaan [124], ω_m and ω_f are projection matrices, $J_{x\psi}$ is the Jacobian matrix, K_ψ is the configuration-space stiffness matrix, ψ is the configuration space vector, K_a is the joint-space stiffness matrix. 51

2.31 Stiffness control manual experiment by Mahvash and Dupont using position-only feedback [146]. The method relies on position feedback from actuators and from an electromagnetic tracking sensors mounted on the end effector. 52

3.1 Conventional boreblending tool for gas turbines (Richard Wolf blending scope [154]) consists of a long and slender insertion tube with a belt-driven machining end effector. An endoscope window allows the operator to see the grinding or polishing tools as they contact compressor and turbine blades. 59

3.2 Cross section of gas turbine borescope port showing degrees of freedom of manual probe (simplified as a cylindrical rod) and rotor blade positions. On some aeroengine compression stages, multiple layers of casing material make access more restricted. 60

3.3 Simplified system with compressor rotor blade fixed relative to machine tool. Z_0 marks the axis of the borescope port and Φ indicates the necessary angular offset for perpendicular machining. 61

3.4 Mechanical architecture of boreblending robot including installation overview, electromechanical systems and detail of flexible actuated tip. . . 63

3.5 Detail of measurement probe, flexible articulation and end effector. The stereo camera is used for measurement of the affected target, but cannot be used to oversee the machining operation due to its position on the insertion tube. 64

3.6 Hardware schematic for boreblending robot, including details of the communication methods used throughout. 65

3.7 Illustration (A) and design process (B) for determining the key parameters of the flexible actuated segments to prevent joints from buckling under compression. 67

3.8 Spot weld (a) and collet (b) used to fix tendons to the robot end effector and linear actuator respectively. 68

3.9 Fixtures for tensile tests of twisted cables (a) and black and white pattern for video gauge calibration and measurement (b). 69

3.10 Tensile test results for representative tendons. Plots show ten destructive trials of two types of twisted stainless steel cables. Results show consistent ultimate tensile strength for like tendons and only one collet slip (trial 7). . 70

3.11 Denavit-Hartenberg convention diagram for remote boreblending robot. Continuum degrees of freedom are modelled as two revolving joints either side of a link with variable length. 73

3.12 Inverse kinematics calculation flowchart using iterative Jacobian pseudo-inverse method. 76

3.13 Kinematics validation experiment setup (top) and position results (bottom) using optical motion capture system. Error bars visible in expanded view show typical standard deviation. 78

3.14 Skilled technician remotely operating boreblending robot from high-level control computer. 80

3.15 User interface for boreblending robot, including A) point cloud map of affected area, B) video stream from on-board stereo camera, C) machining path generation console and D) real-time simulator. 81

3.16 System software architecture diagram showing two separate, network-connected computers for high-level control and low-level control. . 83

3.17 Proposed remote control workflow for routine robotic boreblending operation from establishing network connection to completing a machining operation. 85

3.18 Experimental setup (top) and results (bottom) of repeatability study on compressor test rig. Top figure shows the boreblending robot attached to a Trent XWB aeroengine compressor mock-up with the insertion tube inserted such that the end effector is line with the compressor blades (yellow). Bottom left plot shows completed cut on a metal blade, bottom right shows experimental point cloud data of blade (obtained using a 3D scanner) compared to expected tool path (red). 87

3.19 Root mean square error for each of the eleven compressor blade machining operations, shown in red. Each result was obtained from the point cloud data obtained using a 3D scanner. 88

3.20 Remote boreblending demonstration carried out on a training aeroengine: A) setup and establishing of internet connection, B) ground support attaching robot to aeroengine, C) robot machining compressor blade and D) finished stress relief cut (in-engine images captured with separate camera, not built-in measurement camera). 89

4.1 Concept for dual-backbone continuum robot proprioception with resistive stretch sensor. Curvature is calculated by measuring the resistance of a stretch sensor capable of large deflections and positioned some distance from the bending plane in question. 98

4.2 Schematic of the construction of a single continuum segment equipped with stretch sensors (S_1 and S_2) for bi-directional feedback and tendons (T_1, T_2 and T_3) for motion. 100

4.3 Construction of tubular ionic liquid stretch sensor electrode assemblies consisting of gold electrode (1), sensor wire (2), electrical joint (3), PVC sleeving (4), silicone tubing (5), ionic liquid (6) and heat shrink tubing (7). 106

4.4 Setup for motion of a linear actuator and characterisation of a tubular ionic liquid stretch sensor. Reflective markers are used for tracking by the Vicon motion capture system. 109

4.5 Plot of sensor 1 resistance over time during cyclical loading and unloading, showing the 10 to 12 minute warm-up time necessary for stable operation. 110

4.6 Raw stretch and resistance data from Sensor 2 during characterisation test. 110

4.7 Plot of normalised resistance of three tubular ionic liquid stretch sensors with varying dissolved air content at strains from $\epsilon \approx 0.15$ to $\epsilon \approx 0.48$. Black lines show model using second order polynomial regression of ξ. . . . 111

4.8 Single-segment, single-bend-direction, tendon-driven continuum robot with ionic liquid resistive stretch sensor for position feedback. Robot consists of vertebral discs (1) with tendon holes (2), sensor holes (3) and backbone holes (4). Vertebrae are linked together using super-elastic Nitinol rods (5). A central passage (6) can be used to deliver services to the robot end. Twisted stainless steel tendons (7) are attached to tension load cells (8) and driven by pulleys (9) on the shafts of stepper motors (10). Tubular ionic liquid stretch sensors (11) are used as proprioceptive feedback and are connected to a data acquisition device (12). 113

4.9 Single-segment continuum robot driving electronics including motor driver (1), micro-controllers (2) and voltage regulator (3). 114

4.10 Single-segment continuum control schematic showing mechanical interfaces and electrical connections. 114

4.11 Raw bend angle and resistance data from one-segment continuum arm sensor characterisation tests. 115

4.12 Plot of normalised resistance of single continuum segment ionic liquid stretch sensor for characterisation. Sub figures show the continuum segment at left and right limits of bend for the characterisation experiment (but not at mechanical bend limits). Resistance data shows hysteresis caused by the viscoelasticity of the sensor material. 116

4.13 Two-segment, 4-axis, tendon-driven continuum robot with tubular ionic liquid stretch sensor proprioception. Details show distal segment (furthest from the base and actuators) tendons (I), proximal segment (closest to the base and actuators) tendons (II), distal segment sensors (III), proximal segment sensors (IV), flexible backbone (V), retroreflective tracking markers (VI), motor drivers (VII), linear actuators ($VIII$) and continuum robot base component (IX). 117

4.14 Plot of normalised resistance versus strain of two segment (proximal and distal), two bend direction (X and Y) continuum robot tubular ionic liquid stretch sensors for characterisation. Subtle differences in the sensors behaviour arising from the manufacture and assembly process can be seen as differences in sensor constants and electrical resistance. Hysteresis is present due to the viscoelasticity of the sensor material. . . . 119

4.15 Closed loop control architecture for a single input, single output system. Desired position is compared to measured position (negative feedback) and error is used to influence the commands sent to the robot actuators. 122

4.16 Closed loop response to square wave setpoint input for linear actuator with ionic liquid resistive stretch sensor feedback. Constant slope regions show saturation of actuator velocity. Overshoot during contraction is caused by the elastic force of the sensor assisting the actuator. Undershoot during extension is caused by the elastic force of the sensor opposing the actuator. 124

4.17 Closed loop response (black) to step and sinusoidal input (yellow) for single segment, single direction, serpentine continuum robot with tubular ionic liquid stretch sensor feedback. Grey lines mark standard deviation for 40 acquisitions. 125

4.18 Experimental setup and results of point-to-point closed loop position control trials using ionic liquid stretch sensors as proprioceptive feedback, with three target position inputs for two-segment, dual bend direction continuum manipulator. Plots show distal vertebra position error for each of 50 cycles through three positions P1, P2 and P3 (with 100 points in vertical position P1 due to movement order). 126

4.19 Results of closed loop position control using ionic liquid stretch sensors as proprioceptive feedback, with circular trajectory input for two-segment, dual bend direction continuum manipulator. Plot shows relative density of distal vertebra x-y position data points (for each mm^2 in the plot area) for 40 consecutive revolutions. End effector speed was commanded at $5.24mm/s$ or 1 revolution per minute. 127

4.20 Comparison of open loop (dotted line) and closed loop control (solid line) accuracy for a two-segment, dual bend direction continuum manipulator following a $100mm$ diameter circular trajectory (red line). End effector speed was commanded at $5.24mm/s$ or 1 revolution per minute. 129

5.1 An example continuum manipulator equipped with a machining end effector for in-situ repair of high-value equipment (developed by [16]). Robot is deflected by contact during grinding operation on an aluminium sample. Red outline indicates the estimated position of the continuum robot without obstruction from the aluminium beam. 133

5.2 An example of in-situ repair of high-value equipment using robots with limited sensing capabilities to access difficult-to-reach components. 134

5.3 Representation of a small grinding tool driven by a miniature air-driven spindle and the forces, velocities and displacements of the tool relative to workpiece surface. 137

5.4 Theoretical dependence radial force v. spindle speed for an air turbine tool of radius r with engagement coefficient μ. 138

5.5 Test rig for monitoring audible sound signals during grinding at different radial force intervals. Variable offset mass was used to control the radial force. Two microphones were used to capture the sound and pressure gradient in the direction of propagation from the tool. A 3-axis load cell captured the calibration force data. 139

5.6 Tap test frequency response of cantilever beams and corresponding modes of vibration as simulated in Creo Simulate software. Vertical axis shows the ratio of workpiece acceleration to hammer force input (inertance or accelerance). 140

5.7 Power spectral density plot at audible frequency S for a typical sample with electroplated diamond grinding tool. 142

5.8 Measured radial force F_R vs. spindle speed S (dominant audible frequency). Dotted lines show engagement coefficient μ during sliding friction ($\mu = 0.25$) and after the tool's abrasive grains engage the workpiece ($\mu = 0.90$). . 143

5.9 Sound intensity level I vs. measured radial force F_R. Sound intensity increases with force, variance between tests is high. 144

5.10 Sound intensity level vs. measured radial force for discrete frequencies. Correlation is weaker at low forces. 145

5.11 Sound signal RMS voltage vs. measured radial force for discrete frequencies. 146

5.12 Proposed closed loop control of radial grinding force with single actuator using audible sound features as feedback. $W_D(I)$, $K_P(I)$ and $W_B(I)$ determine the effect of intensity on deadband width, proportional gain and bandpass filter width respectively. 148

5.13 Test setup for controller validation. Microphones are separated from the source of the sound by a number of obstruction and reflection surfaces during some tests. 153

5.14 Material removal rate experiment sample for EPD tool at constant radial force force of $1.32N$ taken with Keyence VHX-100 digital microscope at 175X magnification. 154

5.15 Closed loop radial force controller performance for 72 cutting trials, each lasting 60 seconds. Top sub-plot shows unobstructed closed loop (UCL) trials, bottom sub-plot shows obstructed closed loop (OCL) trials. Markers indicate mean force error for a given trial. Bars indicate standard deviation. 154

5.16 Material removal rates at known radial forces and using airborne sound features for closed loop radial force control. Tool was found to stall at forces greater than $1.0N$. 155

5.17 Tool wear experiment results show radial force tracking works effectively until control is lost at excessive wear levels. Inset figures show worn abrasive grains in area of contact. 156

5.18 Demonstration setup for closed loop force control using sound features. 5-axis robot arm was used to control the feed speed u_f along a cantilever beam and a linear actuator was used to control the tool radial force F_R. . . 157

5.19 Demonstration results: A straight (a), concave (b) and convex (c) target workpiece geometry machined using a 5-DoF robot to feed the spindle and tool back and forth 50 times, and using audible sound features for closed loop force control. Red area shows removed material. Standard deviation of depth calculated from 10 samples taken at 1mm intervals. 158

5.20 Radial force during first two passes of convex protrusion cut (going back and forth once, hence the mirror image). 159

6.1 Simultaneous position and force control methodology schematic for airborne sound machining force sensor and tubular ionic liquid stretch sensor equipped continuum robot. 165

6.2 Hardware schematic and initial setup for simultaneous position and force control implementation. 169
6.3 Simultaneous position and force control setup schematic (side view). An adjustable fixture holds the sample at an angle close to the machining end effector of the continuum manipulator. Two microphones measure sound and pressure gradient in the direction of propagation from the tool. 170
6.4 Measured radial force F_R vs. spindle speed S (dominant audible frequency) for miniature air spindle calibration. Dotted lines show engagement coefficient μ during sliding friction and after abrasive grain engagement. 171
6.5 Simultaneous position and force control implementation results, with duration for each trial (hours:minutes:seconds). Red line shows desired trajectory. Samples 1-5 are 304 stainless steel; samples 6-8 are thin wood (mixing sticks). 172
6.6 Simultaneous position and force control demonstration on damaged 304 stainless steel component with unknown topology. Frames show progress at various times (hours:minutes:seconds). 175
6.7 Radial force F_R and approximate position for select points during controller demonstration on damaged component with unknown topology. Force data is based on airborne sound machining force sensor output. 176
6.8 Experimental setup for simultaneous position and force control of a continuum manipulator. End effector is a high-speed air-driven grinding tool, workpiece is an aeroengine high-pressure compressor blade secured using an adjustable fixture. Further trials aligned blade edge with manipulator x axis. 176
6.9 Simultaneous position and force control demonstration on lightly dented high pressure compressor blade from Rolls-Royce *Trent XWB* turbofan engine. Frames show before (a) and after (c) images of the compressor blade as well as setup during edge calibration. 177

List of Tables

3.1 Summary of tensile test results for 0.45 and 0.39mm diameter twisted cables 71

3.2 Hybrid robot Denavit-Hartenberg convention parameters. 74

4.1 Long-duration static corrosion tests for $Sn99-1Cu$, $Au83-17Zn$ and silicone rubber in 1-M-3O C ($C_{12}H_{23}ClN_2$) and 1-B-3M T ($C_9H_{15}F_3N_2O_3S$).104

4.2 Long-duration galvanic corrosion tests for $Sn99-1Cu$, $Au83-17Zn$ and silicone rubber in 1-M-3O C ($C_{12}H_{23}ClN_2$) and 1-B-3M T ($C_9H_{15}F_3N_2O_3S$) at $12V$. 105

4.3 Characterisation table for tubular stretch sensors. 109

4.4 Characterisation table for tubular stretch sensors mounted on single-segment continuum robot. 117

4.5 Sensor constants for dual-segment, multi directional continuum manipulator.120

4.6 Corrected Denavit-Hartenberg convention parameters for dual-backbone, two-segment continuum robot. 128

5.1 Description of calibration experiment trials. 141

5.2 Control constants used in closed loop controller tests. 151

5.3 Standard deviation values for obstructed and unobstructed closed loop control tests. 155

Nomenclature

The following notation is used throughout this work.

Symbol	Description	Units
x, y, z	Cartesian directions	
X_n, Y_n, Z_n	Cartesian reference frame	
A_n, B_n, C_n	Rotation in roll (X_n), pitch (Y_n) and yaw (Z_n)	
D	Diameter	m
r	Radius	m
$\mathcal{E}$	Error	
s	Sine	
c	Cosine	
a	Continuum arc or robot segment length	m
d	Straight line distance between arc ends	m
θ	Continuum segment bend angle	rad
b	Distance from bending plane	m
l	Tendon movement distance	m
$\mathcal{P}$	Electrical resistivity	$\Omega \cdot m$
L	Stretch sensor length	m
$\mathcal{A}$	Stretch sensor cross-sectional area	m^2
R	Electrical resistance	Ω
λ	Standoff distance	m
Φ	Tool angle of attack	rad
$\mathcal{L}$	Total flexible or continuum length	m
F_{cr}	Critical buckling load	N
E	Elastic modulus	Pa
$\mathcal{I}$	Second moment of area	m^4

Symbol	Description	Units
$\mathcal{K}$	Effective length factor	
$\mathfrak{L}$	Prismatic stage displacement	m
$\mathfrak{q}$	System degree of freedom	
$\mathfrak{w}$	Pseudo-inverse configuration vector	
J	Jacobian matrix	
$\mathfrak{p}_i$, $\mathfrak{a}_i$	Configuration transformations	
ξ	Deformation ratio	
ϵ	Strain	
α, β, γ	Stretch sensor characterisation constants	
K	Control gain	
ϕ	Sensor offset from principal bending plane	rad
ψ	Tendon offset from principal bending plane	rad
$\mathfrak{b}$	Discrete backbone length	m
$\mathfrak{v}$	Discrete vertebra length	m
F_R, F_T	Radial and tangential forces	N
S	Spindle speed	Hz
v_f	Machining feed speed	$m \cdot s^{-1}$
h	Machining depth of cut	m
μ	Engagement coefficient	
τ	Spindle torque	$N \cdot m$
I	Sound intensity	$W \cdot m^{-2}$
P	Instantaneous air pressure	Pa
ρ	Air density	$kg \cdot m^{-3}$
V	Electric potential difference	V
k	Interpolation smoothness factor	
σ	Saturation limit	
ζ	Reaction force orientation vector	

The following acronyms and abbreviations are used throughout this work.

Short	**Standing for**
1-B-3M T	1-Butyl-3-methylimidazolium trifluoromethanesulfonate
1-M-3O C	1-Methyl-3-octylimidazolium chloride
AC	Alternating current
ADC	Analogue-to-digital converter
AE	Acoustic emission
ASMFS	Airborne sound machining force sensor
AWG	American wire gauge
BEMF	Back electro-motive force
CMM	Coordinate-measuring machine
DC	Direct current
DH	Denavit-Hartenberg
DNS	Domain name system
DoF	Degree of freedom
e.g.	Exempli gratia - for example
EDM	Electrical discharge machining
EGaIn	Eutectic Gallium-Indium
EIS	Electrical impedance spectroscopy
EM	Electromagnetic
et al.	Et alia - and others
FBG	Fibre Bragg gratings
FEA	Finite element analysis
FOD	Foreign object damage
FPGA	Field programmable gate array

Short	Standing for
HAZ	Heat-affected zone
HPC	High-pressure compressor
i.e.	Id est - that is
IFR	International Federation of Robotics
IL	Ionic liquid
IPC	Intermediate-pressure compressor
LED	Light-emitting diode
LLC	Low-level controller
MIS	Minimally-invasive surgery
NiTi	Nitinol Nickel-Titanium alloy
PC	Personal computer
PCD	Pitch circle diameter
PID	Proportional, integral, derivative (or combination of)
PSD	Power spectral density
PVC	Polyvinyl chloride
PVDF	Polyvinylidene fluoride
PWM	Pulse width modulation
RMS	Root mean square
RPM	Revolutions per minute
RTP	Real-time transport protocol
RUDP	Reliable user datagram protocol
SEA	Series-elastic actuator
SIP	Session initiation protocol
SMA	Shape memory alloy
TILSS	Tubular ionic liquid stretch sensor
UDP	User datagram protocol
USB	Universal serial bus
UTL	Ultimate tensile load

Chapter 1

Introduction

1.1 Background

From stone-tip spears to metal axes to horse-drawn ploughs, humans have always sought to create tools that make life easier and improve living conditions. The availability of iron and the spread of steam power in the late eighteenth century helped bring about the industrial revolution which in turn resulted in unprecedented population growth and quality of life [1]. Innovations in manufacturing, materials and the advent of electrical power started a technological revolution [2] that accelerated innovation and the spread of ideas. The twentieth century saw the invention of the semiconductor transistor – the fundamental building block of all modern electronic devices – as well as the start of the computer age and the birth of the field of robotics. The twenty-first century has seen great leaps in the field of robotics and greatly advanced the variety and function of tools at mankind's disposal.

According to the International Federation of Robotics (IFR), the field of service robotics is experiencing an unprecedented annual growth of 32% per year on average based on statistics up to 2018, and this value is expected to increase to 39% as the data comes in for the period 2019 to 2020. This would mean a value of around 27 billion U.S. dollars for the industry as a whole [3]. According to IFR's Martin Hägele, "The growing interest in service robotics is partly due to the variety and number of new start-ups which currently account for 29% of all robot companies".

Service robots assist humans with dangerous, inaccessible and sometimes repetitive or dull tasks [4]. In industries such as aerospace and energy, such tasks could include inspection, cleaning, non-destructive testing and material removal operations on high-value industrial installations. It is often desirable to carry out these tasks in-situ due to the costs associated with disassembly and transport of industrial equipment as well as the impact of downtime on related systems. The desire to keep installations assembled results in challenging tortuous access routes to target components, which in turn leads to maintenance robots that are designed to be long and slender [5].

Conventional robotic manipulators consist of a number of actuated joints arranged in series. These are usually revolving joints (articulations that turn around a pivot), prismatic joints (components that change in length such as pistons) or combinations of the two. Conventional joints have the advantage of being easy to operate accurately using rotary or linear encoders, load and torque sensors and closed loop controllers. However, in situations where space is restricted, large actuators and joint assemblies pose a critical design obstacle.

Unlike conventional robots with revolving and prismatic joints, continuum robots have a compliant backbone capable of flexing under the influence of an actuation force. While their construction and actuation method can vary from one instance to another, continuum robots by definition assume curved shapes when flexed. Robots made up of a number of continuum segments in series, referred to as *serpentine*, *tentacle* and *elephant trunk* robots, have the advantage of being able to traverse cavernous environments and be inserted through a relatively small access. Depending on the number of of individually flexible segments, continuum arms may also be hyper-redundant, meaning that a single end effector position may be achieved by a large number of different actuator configurations.

In general, continuum robots are made up of an actuation pack and a number of continuum segments. Continuum segments can have a flexible backbone and rigid cable guides (called serpentine robots for the parallels to a spine and its vertebra) or they can be made entirely of flexible materials that change volume by hydraulic or pneumatic

action (called tentacle or elephant trunk robots due to their soft nature). The actuation pack contains the actuators, speed controllers, pressure regulators, and other hardware necessary to move the continuum segments, and any other electronic, mechanical, pneumatic or hydraulic equipment necessary to operate the end effector.

Continuum robots have limitations that arise from requirements imposed by applications that demand remote dexterity in tight spaces. The growing need for more slender serpentine robots for minimally invasive surgery [6, 7] and inspection and repair of industrial components [5] means that the space must be used efficiently by the actuation tendons and any mechanical or electrical connection to the end effector. The constrained space in the slender continuum sections means that a lot of the sensing for feedback is carried out in the actuation pack away from the end-effector [8]. This means that the accuracy of the end effector position and force control currently depends on an accurate model of the system that incorporates not only the deformation of the backbone, but also the elongation of the tendons and the friction between cables and vertebra. Hence, accurate automatic position and force control of continuum robots is challenging and computationally expensive.

The ability to reach remote areas within industrial equipment through narrow ports of access and address repair tasks such as material removal in affected components is a key driver of in-situ robotics technology development. The requirement for accurate position and force control methods becomes even more important in slender and compliant robots equipped with machining end effectors such as grinding burrs or cutting tools, as the reaction forces directly influence the speed and quality of machining tasks.

This work explores new approaches to the problems of position and force control of slender and compliant robots for in-situ machining.

1.2 Problem definition

The goal of this work is to identify novel solutions for sensing, modelling, actuating and controlling slender and compliant robots to enhance the accuracy of positioning and the repeatability of operations when applying forces to the environment. However, it

is essential that any findings of this thesis be applicable to service continuum robots for in-situ repair, meaning that approaches that cannot practically be used outside of a laboratory must be considered only as partial fulfilment of the criteria.

In this context, a **slender** manipulator is defined as having a length to width ratio (or length to diameter ratio) greater than 10, and a **compliant** manipulator is defined as having sufficiently low stiffness to cause significant deflections (greater than 5%) in its own structure by movements of its own actuators and interactions with its environment.

The following list describes the individual challenges addressed in this work:

1. **Design and implementation of a teleoperated in-situ machining robot:** Aeroengine compressor and turbine blades are sometimes damaged by foreign object debris, leading to sharp kinks and stress-concentrating features that could result in cracks and component failures. The repair of blades in-situ, a procedure referred to as boreblending, is presently carried out using manual tools to abrasively remove the damaged material and leave a smooth profile, but recent interest from industrial partners has led to the development of a slender and compliant robotic probe. This work presents the progress towards a remote-controllable boreblending robot without distal position and force feedback.

2. **Position control of slender and compliant in-situ machining robots:** The majority of tendon and fluid-driven continuum robots rely on open loop control where, based on knowledge of a model of the system, the actuators are commanded to move to a position that is expected to result in the desired end effector position. Despite the fact that actuators may be controlled accurately and with closed loop controllers, it is risky to assume that the continuum robot will behave exactly as predicted by a model. While continuum robot shape sensing has been achieved and described in existing literature (such as using electromagnetic position and attitude sensors, cameras, and motion capture systems) [9, 10] and has been used for direct closed loop control, no solutions have been identified that achieve intrinsic (i.e built-in and without peripheral sensors) closed loop capabilities with a high degree of repeatability.

3. **Force control of slender and compliant in-situ machining robots:** Current methods of closed loop force control for in-situ instruments are generally reliant on direct feedback from sensors such as load cells and strain gauges. For example, in [11], load cells mounted on cables in the actuation pack are used to measure forces acting on the end effector. Other cable-driven manipulators such as those used for minimally invasive surgery have also been fitted with similar sensors for force measurement and control [12, 13]. However, these methods rely on accurate knowledge of the instantaneous configuration and geometry of the instrument which, like the position control problem, relies on an accurate model of the system. Moreover, methods that employ tendon tension sensors mounted near the actuators must make assumptions about the hysteresis, friction losses and tendon elasticity along the continuum arm, making them variable in performance. While it is possible to mount accurate force sensors on the end effector itself, this presents other problems when striving for miniaturisation of continuum robots for in-situ repair, as well as resulting in a loss of available space within the robot central passage.

4. **Simultaneous position-force control of slender and compliant in-situ machining robots:** Position and force influence each other, as driving an effector into an obstacle results in an increase of reaction forces. A controller that combines both forms of feedback must be capable of assigning hierarchy or authority to the different control loops. Parallel or hybrid position/force control allow a manipulator to interact with the environment with precise motion and applying precise forces, which is essential for machining manipulators - particularly manipulators that are slender and compliant. While simultaneous controllers have been described in great depth in the literature, the specific combination of novel sensors and continuum robots addressed in this work has not been attempted.

The resolution of these problems would help to achieve fine control and automation of machining operations in confined environments using continuum robots of slender construction.

1.3 Objectives of this study

The recent demonstration of a novel instrument for remote-controlled on-wing repair (described in detail in Chapter 3) has served to highlight that further development of the position and force control capabilities of such robots will multiply the possibilities of applications for the technology, and may even allow for previously impossible repair tasks to be addressed by highly sophisticated slender and compliant robot arms. Hence, the objectives of this work are to:

- Present an in-depth case study of an in-situ machining instrument optimised to its full potential with the available sensors, and identify the shortcomings of existing open-loop control methods and opportunities for improvement in position and force control.

- Develop a method for closed-loop shape and position control of slender and compliant robots which results in demonstrable improvement over open-loop model-based approaches both in terms of precision and repeatability, and to demonstrate the capabilities of the closed-loop shape and position control method on a representative continuum robot;

- Develop a method for closed-loop reaction force control of an active process end effector that is applicable to slender and compliant robots and results in demonstrable improvement over open-loop methods both in terms of precision and repeatability, and to demonstrate the capabilities of the above closed-loop reaction force control method using an appropriate end effector representative of industrial needs and an adequate actuation method;

- Identify appropriate hybrid position-force control strategies and apply them to the above method for closed-loop shape and position control of slender and compliant robots in conjunction with the above closed-loop reaction force control method.

1.4 Structure of the thesis

Chapter 2 provides a review of existing literature on in-situ repair instruments, continuum robots, position control methods for revolute-jointed robots, position control methods for slender and compliant robots, force control methods for revolute-jointed robots, and force control methods for slender and compliant robots. This chapter cites a wide range of publications that address the key elements necessary to develop control methods applicable to slender and compliant robots, including continuum robot designs, kinematic modelling approaches, sensor designs, and control strategies. The strengths and weaknesses of the previous literature are discussed in the context of the objectives of this study.

Chapter 3 presents a case study for in-situ repair in the form of a remotely controllable boreblending robot. This chapter gives details on the design, kinematics and control of an instrument that is equipped only with actuation pack sensors for position and force. A detailed description of the modes of operation is presented and a description of the validation and demonstration tests is given. This chapter is intended to shed light on the areas of required improvement for position and force control, particularly in ways that are applicable to highly constrained, miniaturised, slender and compliant robots for in-situ machining.

Chapter 4 presents advances in position control for slender and compliant in-situ machining robots and introduces the concept solution of tubular ionic liquid stretch sensors. This chapter outlines the decision process that led to the development of a highly elastic polymer strain sensor based on ionic liquids. A detailed description of the design process, calibration and testing methodology for the stretch sensors is presented. The design process for experiments and test equipment used for various stages of control demonstration is documented in this section. Finally, the proposed closed-loop position control method is demonstrated on a multi-section continuum manipulator equipped with tubular ionic liquid resistive stretch sensors and the results are compared with open-loop position control of the same arm.

Chapter 5 presents advances in force control for slender and compliant in-situ

machining robots and introduces the solution of using audible machining sounds from the end effector process to inform a controller on the contact force of the tool. This chapter outlines the decision process that led to the development of a force controller that uses airborne sound signals from the machining tool to infer forces rather than directly measuring contact forces. The chapter presents the design of testing apparatus for identification of useful sound features during grinding with high speed turbine tools. The sound signals at various cutting forces are analysed and used to calibrate a remotely mounted microphone sensor and signal processing control unit. The design of a novel control method is described and validated using a robotic arm to machine beams with unknown surface topology.

Chapter 6 introduces a parallel controller for simultaneous position and force control using the sensors developed in Chapters 3 and 4. Different control strategies for multiple input and multiple output systems are discussed and the selection of a nested architecture with constrained outer force loop and unconstrained inner position loop is justified. The implementation of a force threshold for completion is presented and a test rig is developed for the simultaneous testing of force and position control using a slender and compliant machining robot. The results are presented and discussed in contrast to open loop methods.

Chapter 7 presents the conclusions of this research work, emphasising the contributions of this thesis and future work required in this field.

1.5 Contributions

1.5.1 New concepts for specialist in-situ machining robotics

1. Remote boreblending robot: novel design (led by Dr Adam Nagy-Sochacki and assisted by Dr Amir Rabani, Prof. Dragos Axinte and the present author) of a 5 degrees-of-freedom robot capable of machining aeroengine compressor blades through an access hole with diameter 8.5mm. The working envelope and degrees of freedom are based on an analysis of manual boreblending tools. Motion control

and peripheral hardware was developed and assembled by the present author. Boreblending robot was assembled and commissioned by the present author.

2. Compliant joint buckling study: details of the continuum portion of the robot were based on an analysis of the buckling behaviour of Nitinol rods under axial compression. The iterative approach optimises the range and stability of the robot's flexible joints.

3. Data packets and self sufficiency for latency-invariant remote control: A high-latency internet-based remote control protocol and strategy (led by Dr Bilal Nasser and assisted by the present author) uses measurements taken by local inspection instruments and transferred to a remote machine to define a set of commands for the Low-Level Controller to carry out. The LLC is self-sufficient enough to detect faults and alert the operator regardless of internet latency. Open loop motion control and tension force monitoring software were developed and implemented by the present author.

1.5.2 New concepts for position control of continuum robots

1. Tubular ionic liquid stretch sensors principle: Mathematical modelling and characterisation of resistive sensors for feedback control of actuated systems. Using stretch sensors to quantify the deflection of the backbone can help reduce the computational load of position control by giving the user information about the true shape of the robot section. Stretch sensors placed on the outside of a serpentine robotic actuator provide feedback about the curvature achieved by the segment in question.

2. Tubular ionic liquid stretch sensor engineering: Study of sensor and conductor material compatibility and manufacturing methodology of a cylindrical construction, chosen to make sensors compatible with the existing architecture of serpentine continuum robots (as the sensors can be fed through unused cable guides).

3. Demonstration continuum robots: Two continuum robots were constructed for the demonstration of tubular ionic liquid stretch sensors. A first robot consisting of a single planar continuum stage was used to validate control models. A second robot consisting of two dual axis continuum segments was used to demonstrate four sensors simultaneously on a complex manipulator.

1.5.3 New concepts for force control of continuum robots

1. Audible sound features for force control of in-situ machining robots: while sound features have been used extensively in machining for condition monitoring, this application of signal processing is new to the field of robotics. The use of sound signals as an input to a closed loop robot velocity control has not been attempted before. The sensor was demonstrated to have sufficient accuracy to perform machining operations on aerospace super-alloy blades.

2. Airborne sound features calibration rig: The calibration device consists of a pivoting mount for an air-driven grinding tool and allows measurement of machining forces and airborne sound at known force intervals or with an actuator stage.

3. Controller design for extracting grinding force from airborne sound features: The controller uses intensity of sound to mitigate the effects of resonance with workpiece natural frequencies while controlling the spindle velocity of the tool based on the dominant audible frequency. The performance of the controller is validated using a representative test rig and demonstrated using a robotic arm to machine thin Ni-Cr-Co alloy cantilever beams with a miniature air-driven grinding tool. Results from the test rig show that such a sound-based control approach can achieve consistent cutting forces.

1.5.4 Publication summary

1. D. Alatorre, A. Rabani, D. Axinte and D.T. Branson III. Closed loop force control of in-situ machining robots using audible sound features. *Mechanical Systems and*

Signal Processing, 136:106-517, 2019

Abstract: Detecting, measuring and controlling the forces between cutting tools and machined components is essential in circumstances where direct position control (e.g. depth of cut, feed speed, etc.) is inaccurate and/or impossible. This paper explores the use of airborne sound signals that result from the machining process to control the cutting force in closed loop for generating accurate machined features when performing in-situ robotic repair of complex installations. The sound signals during indentation at various cutting forces are analysed and used to calibrate a remotely mounted microphone sensor and signal processing control system. The power spectral density of the audible sound is used to estimate tool cutting force and the sound intensity used in turn to estimate the resulting process energy. The described controller uses intensity of sound to mitigate the effects of resonance with workpiece natural frequencies while controlling the spindle velocity of the tool based on the dominant audible frequency. The performance of the controller is validated using a representative test rig and demonstrated using a robotic arm to machine thin Ni-Cr-Co alloy cantilever beams with a miniature air-driven grinding tool. Results from the test rig show that such a sound-based control approach can achieve consistent cutting forces with an accuracy of 0.08 N. The robot arm is shown to be capable of grinding features of consistent depth (to within 0.05 mm) on beams with surface defects of undefined shape using only the sound of the process for closed loop force control.

2. D. Alatorre, B. Nasser, A. Rabani, A. Nagy-Sochacki, X. Dong, D. Axinte, J. Kell. Robotic boreblending: the future of in-situ gas turbine repair. *2018 IEEE/RSJ International Conference on Intelligent Robots and Systems (IROS)*, Vols 1-10, pp. 1401-1406, 2018

Abstract: Automation of inspection and repair tasks on complex installations is gaining attention from industries with high-value assets such as aerospace, nuclear and marine. This paper reports on a five degrees of freedom robotic system capable of performing accurate and repeatable repair procedures through a narrow inspection port, which minimizes the cost and downtime associated with unscheduled maintenance. Careful study of the target working volume and repair process informed the design of a robotic probe capable of replicating the operation. Kinematic analysis of the robot's flexible, prismatic and rotary joints was used to define accurate machining paths in 3D space, and the results were verified using an optical motion capture system (accuracy of 0.25 mm). After comprehensive verifications of the constitutive elements, the robotic system was successfully demonstrated for repair of a high-pressure compressor aerofoil in a gas turbine. The results not only proves the ability of the system to address such difficult repair scenarios but also highlights a domain of opportunities in developing specialist robotics for repair of high-value assets, which is a subject to growing global demand.

3. D. Alatorre, B. Nasser, A. Rabani, A. Nagy-Sochacki, X. Dong, D. Axinte, J. Kell. Teleoperated in-situ repair of an aeroengine. *IEEE Robotics & Automation Magazine*, Vol 26, pp. 10-20, 2019

Abstract: This work outlines the design and remote-control strategy for a novel robotic system to carry out repairs on aeroengine compressors in situ via the Internet. A high-level control computer serves as an interface with the skilled operator. A low-level controller (LLC) receives instruction packets from the high-level controller (HLC) via the Internet and uses them to determine the necessary movements to carry out a machining operation. The robot, comprising a combination of rotary, prismatic, and flexible (continuum) joints, was designed to replicate the degrees of freedom (DoF) of handheld tools. Sensors and encoders on the robot enabled the LLC to independently detect faults and stop all motion despite the high latency of Internet communications.

4. M.F. Wang, D. Palmer, X. Dong, D. Alatorre, D. Axinte, A. Norton. Design and development of a slender dual-structure continuum robot for in-situ aeroengine repair. *2018 IEEE/RSJ International Conference on Intelligent Robots and Systems (IROS)*, Vols 1-10, pp. 5648-5653, 2018

Abstract: In-situ aeroengine maintenance works (e.g. inspection, repair) are highly beneficial as it can significantly reduce currently accepted maintenance cycle which is extensive and costly due to the need to remove engines from the wing of an aircraft. However, feeding in/out via inspection ports and performing a multi-axis movement of an end-effector in a very constrained environment such as aeroengine combustion chamber is a fairly challenging task. This paper presents the design and development of a highly slender (i.e., low diameter-to-length ratio) dual-structure continuum robot with 16 degrees of freedom (DoFs) to provide the feeding motion needed to navigate into confined environments and then perform a required configuration shape for further repair operation. This continuum robot is a compact system and presents a set of innovative mechatronic solutions such as: (i) two-stage tendon-driven structure with bevelled disk design to perform required configuration shape and to provide selective stiffness for the ability of taking high payloads; (ii) various compliant joints to enable different flexibility requirement in each stage; (iii) three commanding cables for each 2-DoF section to minimise the number of actuators with a precise actuation. To be able to achieve the desired configuration shape, a kinematic model has been established and the configuration-cable kinematics has been implemented. Finally, the continuum robot has been built and tested for performing the predefined configuration shape.

5. H.Habibi, P. Land, M.J. Ball, D. Alatorre, D.T. Branson III. Optimal integration of pneumatic artificial muscles with vacuum-jammed surfaces to characterise a novel reconfigurable moulding system. *Journal of Manufacturing Processes*, Vol 32, pp. 241-253, 2018

Abstract: Producing mould tooling systems is a considerable proportion of manufacturing cost and time, especially for low volume productions. Producing a reconfigurable mould to shape surfaces into complex geometries with multiple curvatures would obviate the need to design and fabricate individual moulds for different products. Current reconfigurable mould tooling systems are mainly variations on a 'bed of pins' design through differing patterns of actuated pins. These systems are heavy, mechanically complex and expensive to manufacture. Soft pneumatic actuators such as Mckibben muscles, also known as pneumatic artificial muscles (PAMs) are recognised for their high strength to weight ratio, ease of manufacture and low cost. In this work, PAMs are used to influence a soft elastomeric surface, allowing the formation of spatial curved profiles. This thin, hollow surface is packed with a granular medium that exhibits jamming under the negative pressure of a vacuum. This allows the flexible surface to transform to a rigid surface of greatly increased stiffness with a specific geometry for moulding purposes. This paper presents the design, experimental development and experimental performance of two sample prototypes to actualizes the idea of such adaptable moulding tools. The prototypes contain different actuator arrangements to form jamming surfaces into diverse, simple-to-complex 3D profiles. In addition, the kinematic performance for one of the prototypes is shown by a numerical model. Future work on this system will tailor it for production of fibre carbon composites.

Chapter 2

Literature Review

2.1 Introduction

In today's climate of accelerating advances in technology, robotics is making a substantial impact on the field of in-situ maintenance for industries such as aerospace, oil, gas, nuclear power, marine power and other sectors. While each application in a specific sector may require a unique robotic system, there are parallels in constraints that often result in similarly constructed robots. One such parallel is the requirement to access the working space through small openings or inlets: in aerospace the access to gas turbine components is often through small inspection ports; in oil and gas the access to pressure vessels is often through small valves or pipes; in nuclear power plants the access to reactor components is often through highly shielded ports and airlocks. Robots designed for these tasks therefore share a requirement for long and slender construction.

Commercially available devices are currently intended for use in large installations and are therefore limited by their relatively large diameter and high stiffness. Few solutions exist for in-situ repair tasks in restricted spaces like gas turbines, where the allowable access space is in the order of millimetres in diameter. The field of minimally invasive surgery (MIS), however, shares these requirements of small access and dexterity (indeed, minimally invasive surgery may be called a type of in-situ repair). Continuum robots have been a focus of MIS research for decades, and this construction shows great promise in the area of industrial asset maintenance.

There are, however, crucial challenges when employing continuum robots for physical interventions. Position and force control accuracy can define the suitability of this architecture for applications such as machining of difficult-to-access components. In this chapter, a number of publications on the topics of in-situ maintenance robots and specifically continuum robots is analysed to identify the challenges of developing reliable robots for in-situ repair. Further, existing methods of position control and force control are evaluated and discussed in the context of continuum robots for in-situ repair. Finally, existing methods of simultaneous, parallel or hybrid position and force control of robotic manipulators are presented and discussed in the context of slender and compliant machining robots.

2.2 Review of continuum robots

Continuum robots have several advantages which make them well suited for challenging environments. A long and slender shape allows them to access areas through small openings; redundancy in actuation allows them to assume complex shapes and navigate through tortuous passages; flexible joints and their inherent ability to absorb shock make them safe to use near humans and delicate components. These advantages make continuum robots particularly useful in the fields of industrial inspection and repair as well as minimally invasive surgery.

2.2.1 Continuum robots for industrial applications

Serpentine robots have been investigated by various researchers for industrial applications [8, 14, 15] to exploit their dexterity and slender shape. In the paper titled *Nuclear snake-arm robots*, Buckingham and Graham describe the use of two serpentine robots that were commissioned to address inspection and welding repairs in an otherwise inaccessible area of a nuclear power plant. One robot carries cameras for stereoscopic view of the area. This robot consists of a succession of 40mm diameter discs controlled in groups or segments, allowing a total of 20 DoF along its 800mm length. The second robot carries various

components that are used to aid a cutting and welding procedure. This robot consists of a succession of 60mm diameter discs along a 600mm length, with 8 DoF. Wile the cutting and welding operations were carried out from inside the pipe using other instruments, the continuum robots have enough dexterity and stiffness to hold replacement pipe sections in place. Figure 2.1 shows the small inspection snake arm in-situ gaining access through the bottom of the installation.

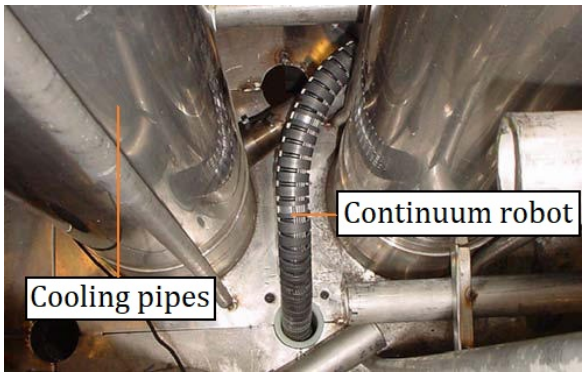


Figure 2.1: Continuum robot for in-situ inspection and repair of nuclear installations developed by Rob Buckingham and Andrew Graham [14] and consisting of a number of $40mm$ diameter discs with 20 flexible degrees of freedom.

Despite its dexterity, even the smaller 40mm diameter snake arm is too big for aerospace applications, where target environments have cavities smaller than 20mm and access ports have diameters smaller than 10mm.

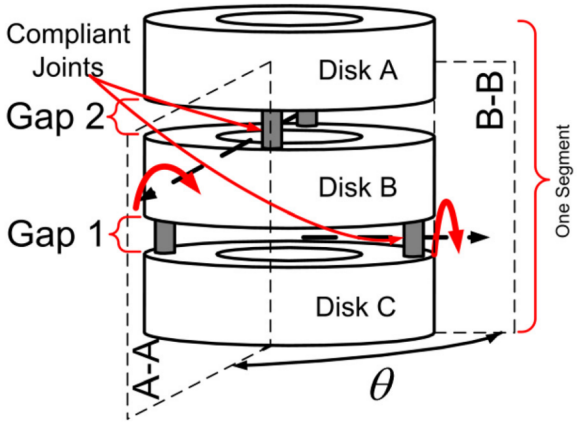


Figure 2.2: Detail of the principle of operation of a twin compliant backbone continuum robot segment with alternating bend direction for dual direction bend [8]

Dong et al. developed a continuum robotic system for inspection and repair of gas turbines with a variable diameter ranging from 40mm at its base to 13mm at its tip [16].

Their robot consists of 12 independently actuated segments giving it a total of 24 DoF along 1270mm. Each segment consists of a number of vertebrae connected by twin nitinol backbones (i.e. two flexible elements at opposite sides of the disc), giving it moderate torsional rigidity and space for a central passage of 7.5mm. The direction of bend of the dual backbone alternates with every disc to achieve two DoF in segments consisting of at least two vertebrae and two sets of flexible backbones (Figure 2.2). This instrument was designed to address a repair on the the second rotor stage of the intermediate pressure compressor (IPC) of a gas turbine. It enters the engine through the gap between fan blades instead of through inspection ports due to its large base vertebral disc diameter as seen in Figure 2.3. Long hyper-redundant manipulators such as this have low stiffness and high control friction. The design presented in this work does not include any form of position feedback from the tip, and relies on encoder information from the spools that drive each pair of cables. However, sophisticated control schemes could be used to improve such robots for in-situ repair applications.

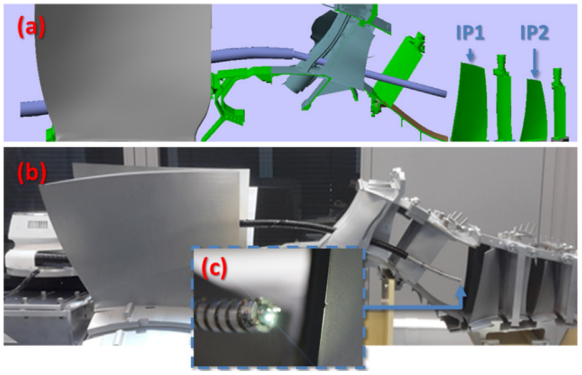


Figure 2.3: Continuum robot for in-situ repair of gas turbine IPC stages showing simulated kinematics (a), experimental validation (b) and close-up of end effector (c) [16]. Robot employs twin compliant backbones and vertebral discs of incrementing size to achieve 24 degrees of freedom.

In their paper titled *Kinematics and the implementation of an elephant's trunk manipulator and other continuum style robots*, Hannan and Walker describe an eight DoF continuum robot made up of spring-loaded universal joints in series [17] as shown in Figure 2.4. Some of the applications described in this and other publications by Walker et al. [18–20] include grasping irregular large objects, exploring pipes and holes, recovering loose objects and inspecting inaccessible areas. Universal joints have the

benefit of being capable of transferring torque, making continuum robots constructed in this way torsionally stiff. Figure 2.5 shows detail of the series universal joints with spring elements. Continuum robots that employ conventional universal joints often have the major disadvantage of lacking an internal channel that may be used as an umbilical passage to deliver services to the distal end. The ability to deliver complex devices such as cameras, grippers, tools, fluid pressure and energy to the area of interest is essential for most in-situ repair applications, particularly in the aerospace field. Another disadvantage of universal joints is scalability, as the complexity of manufacturing and assembling smaller joint elements limits them to continuum robots bigger than around 10mm diameter.

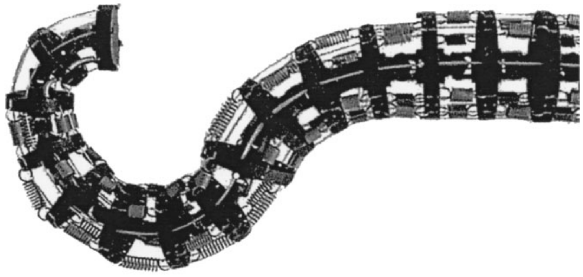


Figure 2.4: Elephant trunk manipulator developed by Hannan and Walker using universal joints in series together with tension springs to provide a restoring force [17].

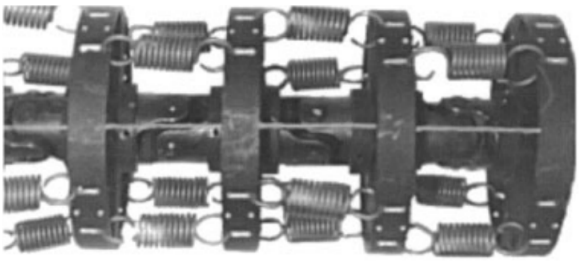


Figure 2.5: Detail of universal joints in Hannan and Walker's elephant trunk robot [17] showing the lack of a central passage to deliver services to an end effector.

The dexterity, flexibility and slenderness of continuum robots make them well suited for work in hazardous or inaccessible spaces. The versatility offered by an uninterrupted internal passage makes such deployment instruments particularly useful in industries such as aerospace and energy, where a variety of measurement, inspection, cleaning, non-destructive testing and other end effectors are deployed. Despite growing interest in the application of continuum robotics technology to address specialised tasks in industrial

assets, challenges in control (accuracy and repeatability) prevent these example systems from being used outside of a laboratory.

2.2.2 Continuum robots for medical applications

Continuum robotics research is particularly prominent in the field of minimally invasive surgery [7, 12, 13, 21, 22], as the diameter of the instrument or instruments used for a procedure affects incision size and patient recovery time [23]. Medical continuum robots come in a variety of types, lengths and operating principles.

In their paper titled *A dexterous system for laryngeal surgery*, Simaan et al. describe a serpentine continuum robot that consists of 2 independently actuated segments [7]. The actuation method uses concentric Nitinol tubes as secondary backbones and to drive end discs by pushing and pulling about a central primary backbone, as shown in Figure 2.6. The use of thin tubes and super-elastic Nitinol ensures that flexibility is maintained, while the use of concentric and hollow components allows for further services such as electric cables, mechanical tendons, optical fibres, suction channels, pharmaceuticals and other fluids to be deployed to the end effector; in this case nitinol wires for a parallel stage wrist and gripper. The concentric tubes construction enables this design to be scaled down to diameters of less than $5mm$, making it an attractive option for in-situ repair of gas turbine components through borescope inspection ports. A disadvantage of this design is that the backbone tube diameter limits the size of the services that can be delivered to the end effector. Large internal diameter tubes cannot be used as a backbone due to their buckling load being higher than their bending load, i.e. they pinch at one point rather than bending uniformly.

Inherently flexible or soft robots provide an alternative to serpentine robots with vertebral discs. Robots made entirely from soft materials like those described in [24–27] have multiple advantages including shock absorption and safety around humans. Despite this, soft robots do suffer from a lack of repeatability, accuracy, torsional rigidity and payload-carrying capacity [20]. Some groups have researched robots made entirely from non-soft flexible materials like nitinol [28] that overcome some of these shortfalls while

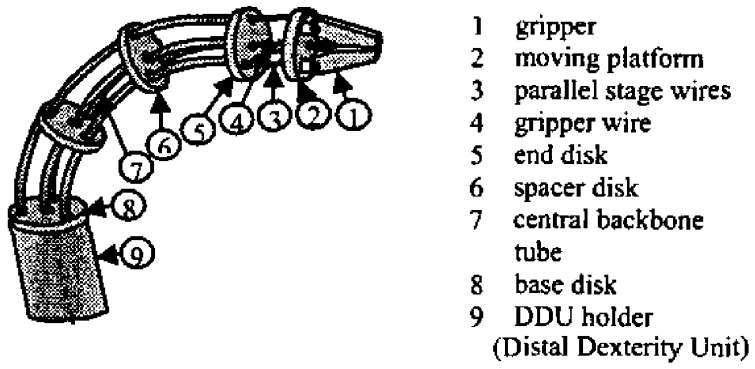


Figure 2.6: Construction of Simaan's laryngeal surgery robot using concentric nitinol tubes [7]. Concentric tubes allow for pushing and pulling action at intermediate locations along the continuum length.

maintaining the advantages of soft continuum arms. In their paper titled *Design and kinematic characterisation of a surgical manipulator with a focus on treating osteolysis*, Murphy et al. [28] describe a 1 DoF continuum robot consisting of notched nitinol tubes (due to the high elastic limit) with cable passages. Murphy's robot is manufactured by first cutting axial notches on thin nitinol tubes for tendon channels. A larger nitinol tube is press-fitted onto the smaller tube with a slight interference fit. Electrical discharge machining (EDM) wires are then fed through the notches on the first tube and used to expand the cable channels. Finally, radial notches are carved into both tubes to weaken the structure strategically to bend in the desired direction (Figure 2.7). This simple design gives the robot improved torsional rigidity and stiffness but limits motion to one DoF per section and hence limits its application to environments which only require movement in a circular envelope - in this case the treatment of osteolysis on on hip implants. A robot constructed in this way but notched in a way to allow it to bend in two directions could find more applications for in-situ repair of industrial assets.

A different continuum robot architecture for medical applications is the concentric needles continuum robot [29–34]. Two or more elastic (typically nitinol) tubes with pre-existing curvatures are nested and actuated relative to each other. The arrangement usually includes an outermost needle that is left straight or only minimally curved. The stiffness of the outermost needle overpowers the internal needles making its curvature (or lack thereof) dominate. Extending an internal needle past the end of a larger layer allows

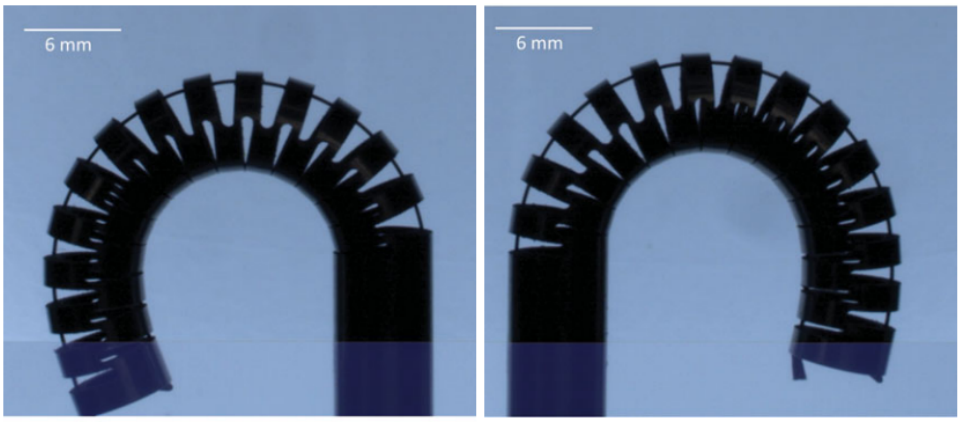


Figure 2.7: Nitinol notched tubes continuum robot by [28] flexed to its mechanical limits. The notched tubes architecture provides flexibility while maximising available central passage space.

it to start deforming to assume its natural pre-bent shape. Rotating the needle allows for orientation of the direction of bend. Further layers can then be extended and allowed to bend in different directions. An example of an extended concentric needles robot is shown in Figure 2.8. This construction allows for the delivery of pharmaceuticals or small instruments to the tip through access holes as small as 2mm via the smallest needle, but the reach, dexterity and payload-carrying ability are limited by the length and number of needles used.

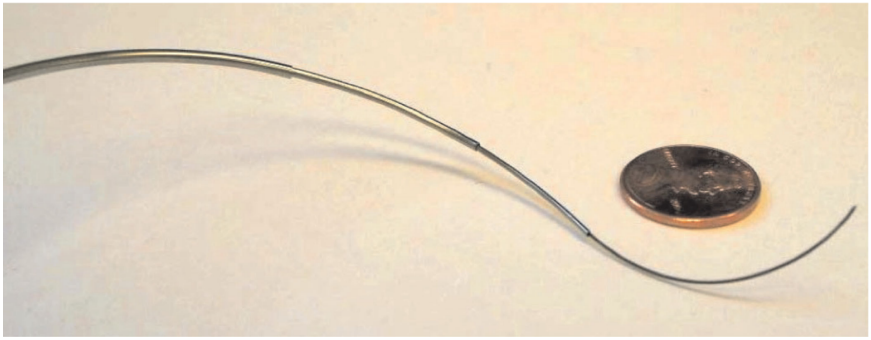


Figure 2.8: Nitinol concentric tubes continuum robot by [32]. Relative rotation and translation of pre-bent needles allows for steering of the needle tip, which may in turn deliver an end effector through a small access.

In their conference paper titled *Highly articulated robotic probe for minimally invasive surgery*, Degani et al. [21] describe a snake-like robot that is not a continuum robot. Instead, this robot uses selectively rigidisable concentric snakes and a steerable outer snake to percussively advance into an environment following a shape that does not change over

time. Any joints behind the head cannot be changed from the position defined when the head moved past that point in the environment. Figure 2.9 shows a typical gait sequence for this type of snake robot. While this construction has various limitations, it shows an alternative construction and navigation method for long and slender instruments with high levels of articulation.

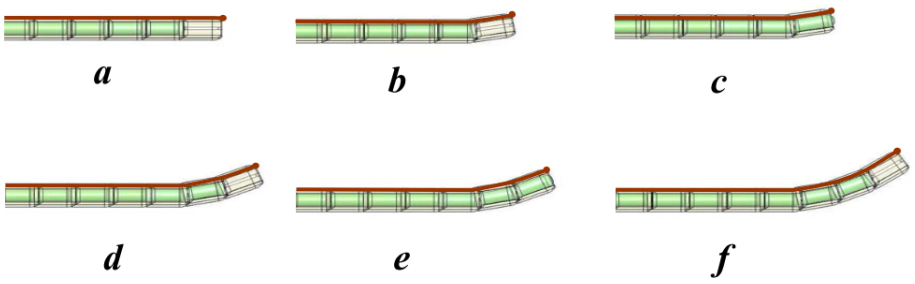


Figure 2.9: Gait sequence for percussively actuated non-continuum snake robot [21]. Selective rigidisation of two concentric "snakes" allows the tip to follow complex trajectories.

Flexibility, small diameter and the ability to deliver pharmaceuticals, tools, cameras and instruments through narrow incisions makes continuum robots an obvious choice for minimally invasive surgery. Decades of research and development has resulted in a variety of architectures, control methods and applications for continuum robots in the medical field. Despite this, most surgical instruments have and will likely continue to have a human in the control loop.

Inherently flexible robots present clear opportunities for applications in diverse fields, from medicine to aerospace technology and manufacturing engineering. The advantages of hyper-redundant robots come at a cost, however, as their unconventional joints and slender shape makes them significantly more challenging to control than revolute-jointed machines. Improvements to position and force control of such instruments, particularly for the industrial application of in-situ repair of gas turbines, is the focus of this work.

2.3 Challenges in position control methods of continuum robots

Position control of continuum robots to the level of accuracy required for in-situ repair of aerospace assets presents a number of technological challenges, especially when the robotic systems in question operate in challenging environments and have strict size limitations. The use of accurate kinematic models and unobtrusive sensing methods is essential. This review of literature aims to explore the current state of the art of continuum robot navigation.

2.3.1 Continuum robot kinematics modelling

The under-actuation of individual flexible segments presents a critical challenge when modelling the kinematics of continuum robots, as assumptions have to be made about the nature of the shape of the bend and distribution of forces. In a paper titled *Kinematics and the Implementation of an Elephant Trunk Manipulator and Other Continuum Style Robots* [17], Hannan and Walker describe the kinematic model of an elephant trunk continuum robot manipulator. The approach assumes constant curvature throughout the actuated elements, i.e. circular bends along the segments. The Dennavit-Hartenberg parameters assume two revolute joints either side of the circular arc and are used to find the position and velocity transformation matrices. These matrices are directly transferable to other continuum robots if the same assumptions are deemed acceptable. The kinematics are verified experimentally and put to the test with line-following and collision avoidance tasks. The kinematic model used is simple and fast to calculate, making it scalable (in terms of computational efficiency) for a higher number of continuum segments. This method assumes that the straight line d between two points of an arc of length a at angle θ is given by:

$$d = \sqrt{\frac{2a^2\left(1 - \cos\left(\theta\right)\right)}{\theta^2}} \tag{2.1}$$

with the special case of $d = a$ when $\theta = 0$. At this bend angle, a continuum robot (Figure 2.10) with effective tendon offset b (distance between the backbone plane and the tendon, calculated from the cable Pitch Circle Diameter (PCD) and the angular position of the cable guide) requires the pulling cable to be drawn by

$$l_{in} = a - \sqrt{\left(\frac{2a^2}{\theta^2} - \frac{4ab}{\theta} + b^2\right)(1 - \cos(\theta))} \tag{2.2}$$

and the slack cable to be released by

$$l_{out} = a - \sqrt{\left(\frac{2a^2}{\theta^2} + \frac{4ab}{\theta} + b^2\right)(1 - \cos(\theta))} \tag{2.3}$$

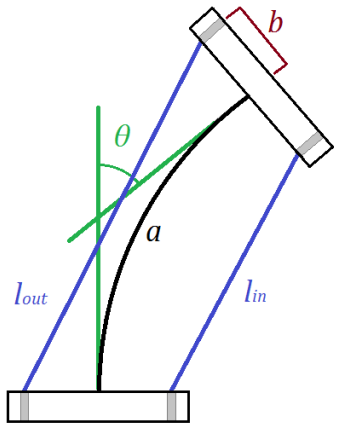


Figure 2.10: Flexed continuum segment with constant radius of curvature in flexible segment of length a. Tendons are assumed to follow straight lines between holes in adjacent vertebrae.

This approach does not take into account the material non-linearities of flexible elements such as Nitinol wires which are present in most robots' backbones developed for in-situ repair. The method also ignores the presence of external forces such as gravity and the effect of friction and stretch on the tendons, which are likely to play an important role in manipulators with higher payload capacity.

Efforts have been made to model the configuration of continuum and flexible robots in a robust way, such as that by Jeon et al. [35] where the authors discuss the application of a method to model the configuration of an elastic wire. The wire is discretised into

a number of rigid links with double revolute joints, allowing for gravity and differences in stiffness along the beam to be considered, as shown in Figure 2.11. Minimising the stored potential energy in imaginary torsion springs in the joints optimises the process. The model was validated experimentally using two magnetic tracking sensors. The paper focuses on very long wires with linear bending behaviour, but hyper-elastic NiTi wires have non-linear flexural rigidity when bent past a certain bend angle. Improvement could incorporate an elastic behaviour that changes as a function of bend angle and not just along the length of the arm.

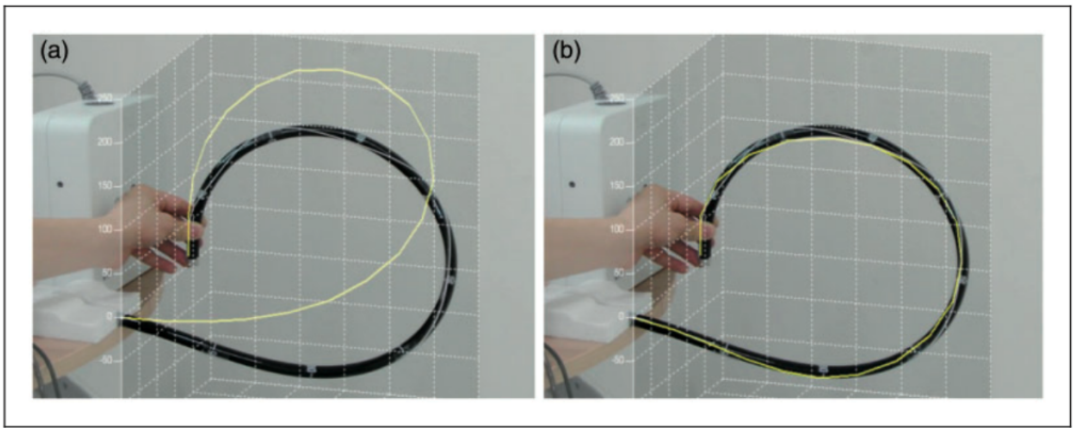


Figure 2.11: Demonstration of the revolute joint discretisation model by Jeon et al. [35] showing the model without (a) and with the effect of gravity (b).

Hasanzadeh and Janabi-Sharifi [36] describe a new method to model the statics of a continuum robot by discretising the length of the continuum segment into a number of elastic arcs of varying rigidity. The statics of the system are calculated using Euler-Bernoulli beam equations iteratively and compared to standard models such as the Elastica theory model that assumes a single section bending like a beam. A comparison of the models can be seen in Figure 2.12. The results are validated experimentally using a coordinate-measuring machine (CMM) and are found to be effective in calculating the position based on the cable tension force and externally applied loads. Like Jeon et al., this method allows for varying stiffness along the length but uses linear material behaviours. However, beam equations can easily be modified to include the nonlinearities if it is deemed necessary. This paper only describes the

method applied to one bending direction in planar space, making it quite limited in scope. The experimental setup used also relies on manual inspection which can be a significant source of error.

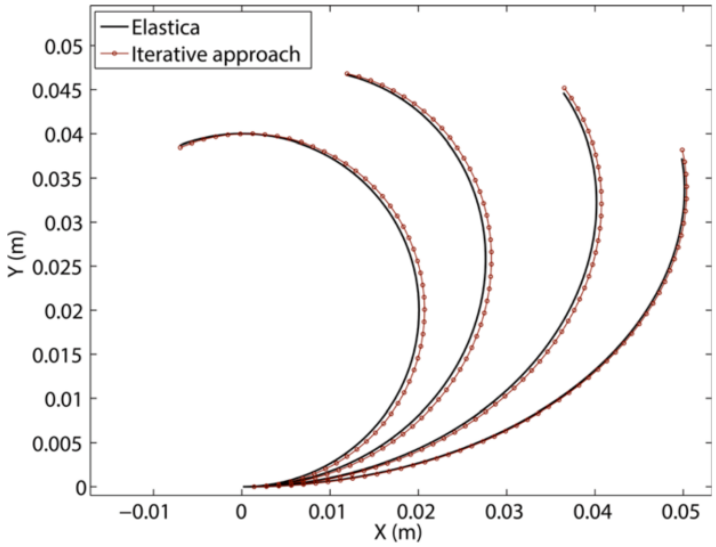


Figure 2.12: Comparison of two approaches for modelling continuum segments. Elastica and discretised arcs iterative approach [36]. While both arrive at accurate shape estimations, the iterative beam bending approach is more versatile when it comes to the exact shape of the bends.

In their paper *Dynamic Model of a Multibending Soft Robot Arm Driven by Cables*, Renda et al. describe a method for characterising the shape of the soft material using Cosserat rod theory based on the tension of the cables [25]. Their method incorporates the effect of gravity and external loads, and the axial and radial forces created by the cables are quantified to predict the deformation of the soft robot material around the tendons. The method used in this paper to calculate the forces exerted by the tendons can be used to quantify the friction along the length of a rigid disc-segmented continuum arm.

Kinematic models are essential for calculating the actuator-space configuration required for a given end effector position and orientation. Models that can accurately represent the deflection of flexible segments and take into consideration external forces acting on the robot make it possible to calculate positions accurately and control robots in open loop. Any model-based open-loop control method is limited by the susceptibility to unknown contacts with the environment and non-linearities in cable friction and

elongation. The only way to overcome these obstacles is by using some sort of feedback for closed-loop control.

2.3.2 Extrinsic position measurement methods

Measuring the position and shape of continuum robots presents a number of challenges on its own, as it is impractical to track every individual point along the curve. It is important to be able to describe the robot's shape to validate kinematic models and eventually control continuum robots in closed loop. Extrinsic methods use equipment mounted externally to the robot to measure its shape, position, orientation or a combination of these attributes. Multiple researchers [9, 37–39] have used electromagnetic trackers to measure the shape of continuum robots. Electromagnetic tracking systems consist of an emitter base unit that transmits electromagnetic waves with known properties and one or more sensors that measure the local field to calculate their position and attitude relative to the emitter.

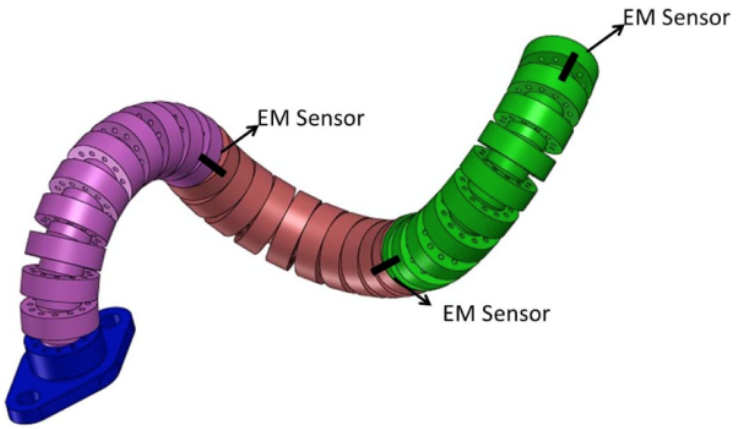


Figure 2.13: Configuration of magnetic sensors for shape tracking by Song et al. [9]. Magnetic sensors require an emitter unit to calculate their relative position and are susceptible to interference from even small metallic objects.

Song et al. [9] describe a continuum arm with three sensors placed at the joints between segments and at the tip of the arm (Figure 2.13). The position and orientation are used to create a smooth Bezier curve of best fit to predict the position of the snake arm. The real position of the points between the sensors is validated experimentally using computer

vision and compared by simulation to a physical model, with accuracy within 3.2 mm. The position of the middle sections (control points) of the Bezier curve are not used in this paper, instead the orientation of the intermediate points is used to deduce a position that meets the physical constraints of the robot. Electromagnetic trackers have a key disadvantage in industrial fields, as interference from metal objects makes measurements unreliable. Using electromagnetic sensors inside a completely metallic object such as a gas turbine is impossible with current technology.

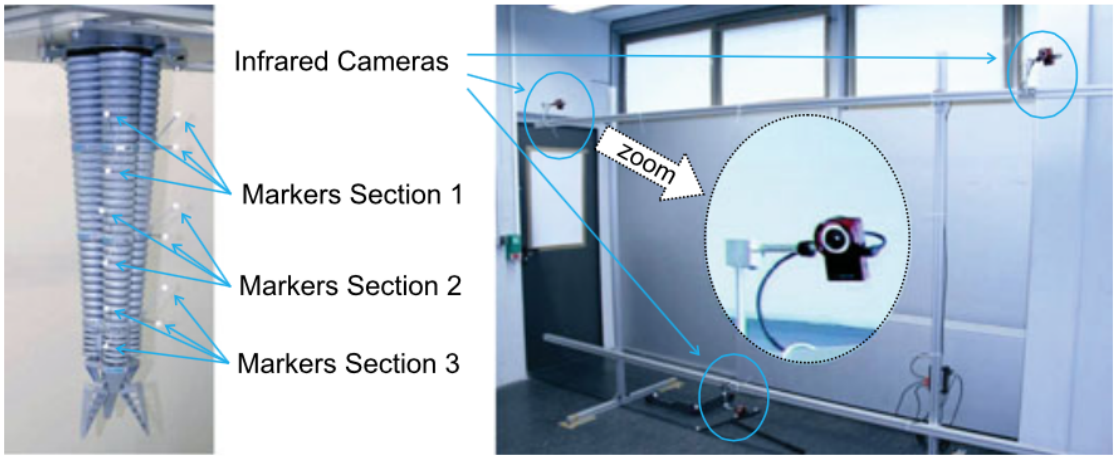


Figure 2.14: Shape tracking using computer vision by Mahl et al. [10]. Optical motion tracking requires externally-mounted cameras with line-of-sight to trackers on the continuum robot, making them suitable only for laboratory environments and tasks in controlled spaces.

Computer vision can also be used for 3-dimensional tracking [10, 40] and applied to continuum robots, as demonstrated by Mahl et al. [10] using the Festo Bionic Handling Assistant. Reflective markers were positioned at the ends of the segments to track the configuration of the arm (Figure 2.14). This method is useful for validation of kinematic models, but is not applicable in confined spaces where it is impossible to insert cameras.

A review of the state of the art shows that externally mounted sensors, cameras and vision systems can be used for closed loop position control of continuum robots. However, magnetic tracking sensors are inadequate in metal environments and large, static camera arrays are impractical or impossible for in-situ repair applications. Hence, intrinsic methods for position measurement must be explored for tracking the position of continuum robot segments and for closed loop control.

2.3.3 Intrinsic position measurement methods

Intrinsic methods use equipment mounted internally to the robot to measure its shape, position, orientation or a combination of these attributes. A large number of continuum robots in literature rely on encoders positioned at the proximal actuation end to infer the end effector position by means of a kinematic model [10, 23, 35, 41–43]. This reliance on inverse kinematics and lack of distally mounted sensors results in relatively large inaccuracies and vulnerability to external forces and disturbances. Built-in distal strain or shape sensors come with a penalty in available space for services, but they can dramatically improve performance by allowing for closed loop position control.

In their paper *Shape Tracking of Planar Hyper-Flexible Beams via Embedded PVDF Deflection Sensors*, Shapiro et al. [44] discuss the use of piezoelectric sensors to measure the deflection of flexible segments of structure in continuum robots. The deflection information is compared to data obtained visually and matches to within 3%. The entire continuum surface does not need to be covered to achieve this result; only 4 short sensors were used at strategic locations along the length of the arm (as shown in Figure 2.15). Despite the success, the sensors used in this work effectively measure backbone flexural strain, meaning that the flexible elements and sensors must be placed near the centre of the continuum robot, which limits their application to robots where the central passage can be utilised for sensing. In addition to this, architectures such as serpentine robots often alternate the direction of bend of adjacent vertebra (such as [45]), which leaves only the interval between two vertebrae to use for 1D sensing.

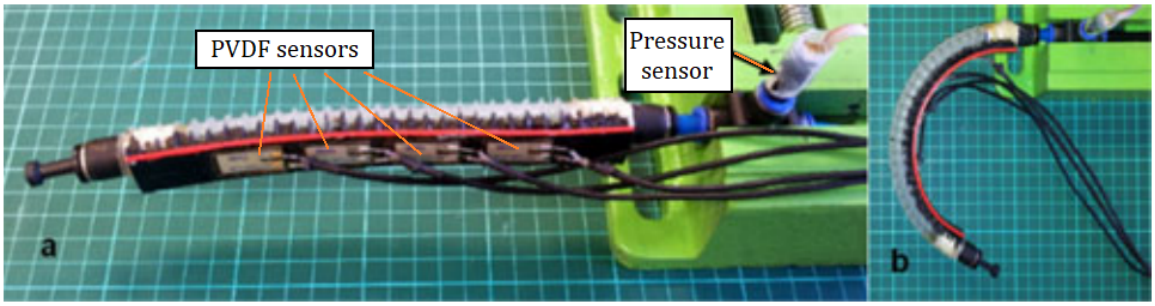


Figure 2.15: Pneumatic bellows continuum actuator with four PVDF sensors by Shapiro et al [44]. While such sensors may be used to measure curvature directly, they must be mounted close to the neutral axis of the robot, reducing the available space for services.

Optical fibres with Bragg gratings (FBG) can be used to measure the shape of complex curved components. FBGs are strain sensors that work by measuring changes in the frequency of reflected light caused by the distortion under strain of etched gratings on the fibre [46]. Gratings can be positioned in specific sections of fibre to measure local strains or they can be distributed along the entire length of fibre to measure strain distribution throughout. FBGs are currently used to measure surface strain, for example by embedding them in fibre composites [47–50] and some elastomers [51]. In their paper titled *Instrumentation of integrally stiffened composite panel with fiber Bragg grating sensors for vibration measurements*, Oman et al. describe a method for acquiring the shape and the modes of vibration of a carbon fibre panel using FBGs with discrete gratings in strategic locations [52].

Recently, FBGs have been used for curvature measurement in continuum robots [53]. Using a single grated fibre near an inextensible bending plane gives one DoF of curvature measurement [54–56]. In their paper titled *Large-deflection FBG bending sensor for SMA bending modules for steerable surgical robots*, Sheng et al. [57] investigate the use of opposed fibres with FBG sensors for bend measurement of a one segment, one DoF flexible backbone, serpentine continuum robot with shape memory alloy (SMA) actuation (Figure 2.16). Their results show that, despite a level of hysteresis and sensitivity to temperature, FBG sensors can measure the large strains associated with continuum arms.

Single fibres can also be used in such a way as to provide 2-dimensional measurement. Feng et al. [58] demonstrate that using orthogonal angled gratings within the same fibre can be used to measure bend in orthogonal directions. Wang et al. [59] demonstrate that a single fibre can be rotated inside a curved vessel to obtain curvature and direction of bend. While such methods increase the complexity of the fibre and measurement system, they present an opportunity to reduce the diameter penalty within the umbilical passage, allowing more space for services to be delivered to an end effector.

Multi-core FBGs can be used to measure strain in 2 directions of bend [53, 60–62]. Shape reconstruction of flexible bodies such as demonstrated by [53] can be adapted and

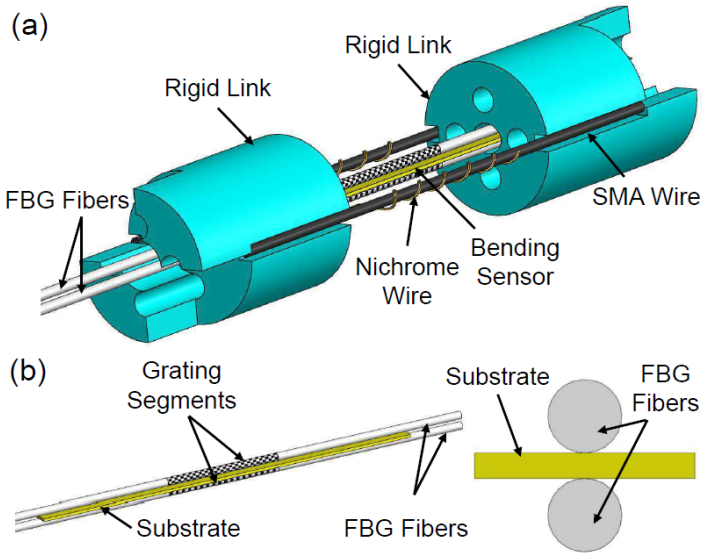


Figure 2.16: SMA bending module integrated with SMA sensor (a), and detail of the FBG bending sensor (b) [57]. Like PVDF sensors, fibre sensors with Bragg gratings must be located near the central axis of the continuum robot.

used for closed loop control of active flexible structures such as continuum robots. Using redundant fibres also allows for temperature compensation and elongation measurement [63].

Despite their undeniable advantages, fibre Bragg sensors and the required interrogators and software are prohibitively expensive and therefore not suitable for production devices at the present time.

A number of authors have researched the use of resistive and capacitive sensors for large deflection strain sensing and shape reconstruction in continuum robots [64, 65]. Resistive sensors are frequently constructed out of elastic materials that are made conductive by the inclusion or by layers of low-dimensional carbons (carbon nanotubes [66–68], graphene [69, 70] and carbon black [71, 72]) metal nanowires [73–75] and nanoparticles [76]. Sensors are also often composed of electrically insulating and elastic vessels, membranes or media coupled with electrically conductive fluids (such as eutectic Gallium Indium alloy - EGaIn - [77, 78] and ionic liquids [79–81]), gels [82] or elastomer films [83]. When stretched, the conductive layer with resistivity $\mathcal{P}$ changes length L and cross-sectional area $\mathcal{A}$, resulting in a change in resistance given by $R = \mathcal{P}L/\mathcal{A}$.

In their paper titled *Multi-task sensorization of soft actuators using prior knowledge*, Wall and Brock [77] describe a pneumatic actuator containing 16 eutectic Gallium Indium (EGaIn) resistive strain sensors in a multi-layer construction (Figure 2.17). The sensors consist of elastomer microchannels moulded into sheets of silicone and filled with the liquid metal.

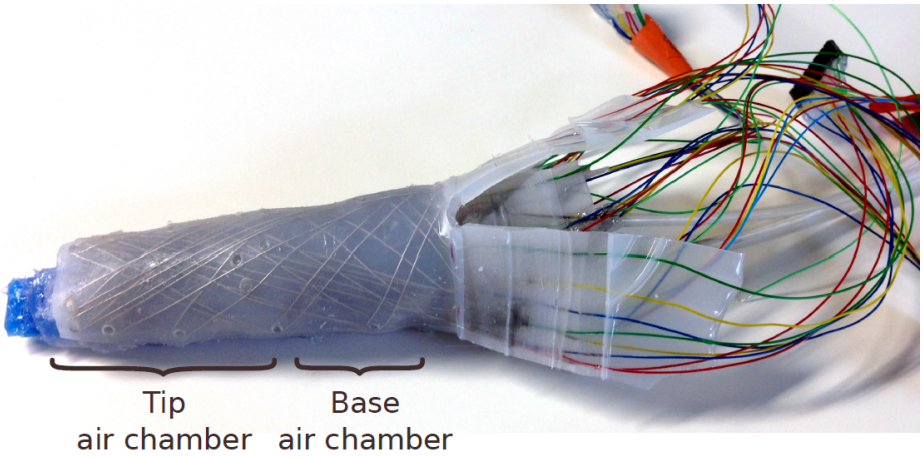


Figure 2.17: Two segment pneumatic actuator equipped with 16 eutectic Gallium Indium resistive strain sensors [77]. Various orientations and a number of redundant sensors allow for monitoring of parameters such as contact with objects and internal pressure.

Resistive stretch sensors have been used in physical therapy and wearable technology research due to their inherent bio-compatibility. In their communication titled *Volume-Invariant Ionic Liquid Microbands as Highly Durable Wearable Biomedical Sensors* [80], Wang et al. describe the manufacture of a stretchable sensor with rectangular cross section capable of detecting strains from 0.1% to 100% at frequencies up to 7 Hz with high signal-to-noise ratio. Crucially, the hysteresis time was observed to be as low as 0.027 seconds, suggesting such a sensor could be used at even higher frequencies. In their tests, they used printed moulds to manufacture silicone sensors containing a layer of ionic liquid only 0.5mm thick. The stretch sensor was applied to participants skin in different locations on the body to detect movements and gestures to a high degree of repeatability. Similarly, Noda et al. describe a sensor containing stretchable elastomer sections encapsulating conductive liquids [84]. The impedance of the stretch sensor was observed to vary linearly with strains up to 30%, with an alternating current (AC) voltage of 1V (peak to peak) at 250 kHz going through the conductive liquid. The depth of the conductor channel used

in this work is also 0.5mm.

In their paper titled *Soft and stretchable sensor using biocompatible electrodes and liquid for medical applications*, Russo et al. Describe an elastomer sensor with a channel containing dissolved sodium chloride for biocompatibility [85]. The design includes a novel stretchable electrode made by coating the elastomer substrate in a thin sputtering of gold ($100\mu m$ thick), also chosen for biocompatibility. Test results show repeatable behaviour in agreement with theoretical predictions based on predicted sensor deformation. However, the questionable long-term stability of saline solutions and the likely challenges of miniaturising the gold sputtering process makes this type of sensor less well suited for repair applications, particularly as there is no need for biocompatibility.

Resistive macro-strain sensors offer a cost-effective solution to closed-loop position control by allowing for direct curvature measurement of continuum sections or curved bodies. The variety of possible shapes and sizes also allows for continuum robots to be retro-fitted with sensors and closed-loop controllers. However, any sensor that relies on the resistivity of conductive materials is likely to be highly susceptible to temperature changes and will require temperature compensation to operate correctly in a mature implementation.

Capacitive stretch sensors are similar in construction and operation to resistive sensors, but make use of two conductors running parallel to each other and separated by an elastic membrane. Conductive layers may employ elements such as metal nanowires and carbon nanotubes suspended in a stretchable matrix, or they may be composed of inherently conductive flexible materials such as carbon-black infused rubber, or they may use conductive fluids contained in a flexible vessel. Sensors are commonly constructed with rectangular cross-sections to allow for larger capacitive surfaces. When a sensor is stretched, the surface area of the conductive layers increases and the distance between the layers decreases, resulting in a larger capacitance at higher strains. In their paper titled *Super-stretchable, transparent carbon nanotube-based capacitive strain sensors for human motion detection*, Cai et al. [86] report on the realisation of soft

sensors capable of measuring strains up to 300% using a silicone sensor with carbon nanotubes conductive layers (Figure 2.18).

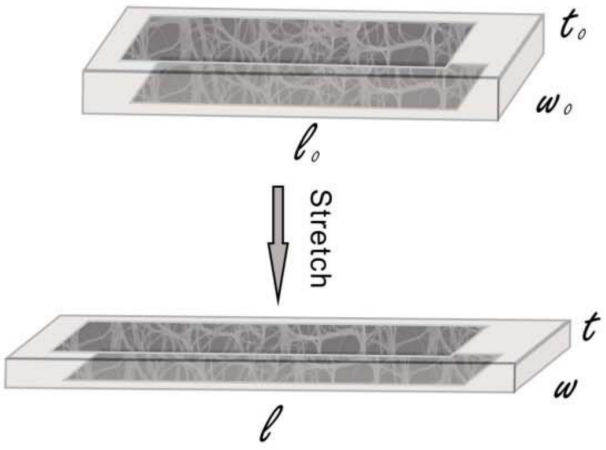


Figure 2.18: Capacitive strain sensor principle of operation: stretching the elastic element reduces the size of the gap between conductive layers and increases the conductive layer surface area [86].

While capacitive sensors have an excellent signal-to-noise ratio and good durability, the complex AC instrumentation required to interrogate the sensors and their rectangular cross-section make them less well suited for in-situ repair continuum robots. Capacitive sensors require a precise source of alternating current and an instrument such as an electrical impedence spectroscopy system (EIS) [87] or a capacitive Wheatstone bridge with digital potentiometer [88]. This increases the cost and complexity of the system compared to equivalent resistive sensors. While resistive sensors may be constructed in a way to allow them to follow disused cylindrical tendon conduits, the dual surfaces of capacitive sensors mean that they require specialised channels to be built into a continuum joint.

A group of researchers investigated the use of Hall effect magnetic sensors mounted on flexible structures to measure strain on highly elastic continuum robots [89–92]. A magnetic sensor is attached to the flexible substrate and a permanent magnet is attached to the same flexible material some distance up the arm in the direction of stretch or bend (as seen in Figure 2.19), hence the distance and attitude of the magnet as measured by the Hall effect integrated circuit gives an indication of the curvature and shape of the continuum segment. The RMS error of the signal between the actual and

reference curvature was found to be $0.0239cm^{-1}$, which is comparable to the more accurate embodiments of capacitive and resistive stretch sensors.

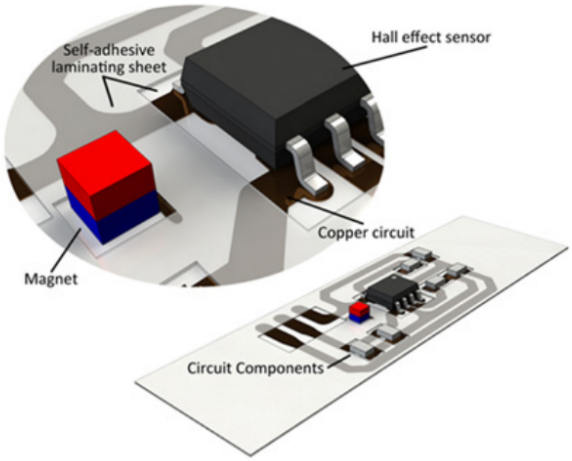


Figure 2.19: Hall effect magnetic sensor attached to flexible substrate to measure curvature [91]. Hall effect sensors can detect small changes in magnetic fields but require bulky integrated circuits and magnets.

Another example of an elastic stretch sensor is the optoelectronic sensor such as that described in [93–95] and [96]. An elastic transparent waveguide mounted in the exterior of a prosthetic hand in one case and a walking octopod in the other changes transmissivity according to deformation. An infrared light-emitting diode (LED) at one end of the lightguide acts as a light source, while a phototransistor detects light intensity at the other. As the sensor stretches, the intensity of light transmitted drops in a repeatable way. Other methods for position measurement on continuum robots that use optoelectronic sensors, such as the one described in [97], use cables as mechanical links between the moving end of the robot segment and a number of reflective surfaces which can be used to calculate tip position. Optoelectronic sensors such as these have not been used in multi-degree-of-freedom continuum robots, probably because of the need to mount emitters and detectors along the robot or the need to route optical fibres through a central passage.

Despite the large variety of strain sensors described in the literature, none have successfully been demonstrated on a multiple DoF continuum robot. Although Bragg-grated glass fibre sensors show great promise in this field, their high cost and complexity makes them an unlikely option for repair in hazardous environments. Of the

surface strain sensors researched, resistive sensors show the most promise for adaptation to continuum robot shapes, due to their variable cross-section and ease of design.

Using sensors such as resistive surface stretch sensors for shape feedback can dramatically improve the position controllability of continuum robots, providing for the first time closed loop control of the backbone curvature with built-in sensors. This will be the focus of the work presented in this thesis towards the advancement of position control of slender and compliant in-situ machining robots.

2.4 Review of robot force control methods for in-situ machining

Controlling the interaction of a machining or abrasive tool with the workpiece is essential to guarantee that the continuum robot can perform high quality machining operations. When the tool is in contact with the workpiece, its motion is constrained by the shape of the environment and appropriate reactions by the robot are required to accommodate the interaction. The review of literature aims to explore the current state of the art in force measurement in conventional jointed robots and continuum robots, and particularly robots with intrinsic cable tension sensors or extrinsic, remotely mounted sensors.

Control schemes used to convert the measured torques and forces into usable control commands fall broadly into stiffness control and impedance control. Stiffness control treats the joint as a spring (whether or not a phisical spring is present) and the system is tuned to achieve a desired static behaviour. Impedance control treats the joint as a mass-spring-damper system and the robot is tuned to achieve a desired dynamic behaviour [98].

2.4.1 Force sensing in conventional jointed robots

Conventional joints allow for forces acting on an end effector to be measured directly: Torques acting on individual rotary joints can be measured directly using dedicated torque sensors, such as those described in [99], or indirectly using actuation parameters such as current [100] or back electromotive force (BEMF) from joint motors such as in [101].

Modifying conventional joints by adding elastic elements in series (series elastic actuators) also allows for force measurement based on a well-defined model of the robot's joints [102–105]. Other methods such as using load cells on prismatic joints or indeed directly on the end effector [98] lend themselves well to conventional jointed robots and are widely used for force control.

Torque sensors are often used for control of rotary articulations, both in position [106] and in reaction force [99]. Measuring joint torque directly is a simple way to provide force feedback and allow for closed loop control of the reaction between parts of the robot and its environment.

Motor current and BEMF methods of force calculation and control are widely used due to the ability to retrofit such a control scheme on a manipulator that does not have intrinsic (and often expensive) force or torque sensors. In their paper titled *External torque estimation for an industrial robot arm using joint torsion and motor current measurements*, Gold et al. [107] demonstrate the use of motor current for estimating internal joint torques in contrast to (and in conjunction with) an approach that relies on subtle deformations of the robot structure. Other authors have used this approach to achieve force control in the context of robotic assembly and human-safe robots [100, 108–110]. Using current and motor state to estimate torques and reaction forces with the environment stops being suitable when gearboxes, belts, tendons or other drive transmission elements separate the motor from the load-bearing joint. Friction forces and environmental effects on transmission efficiency make current measurements unreliable for complex robots such as slender and compliant manipulators.

Series-elastic actuators have received considerable attention lately for their versatility and safety, in areas such as rehabilitation robotics and automated assembly [104]. In SEAs, a flexible element is intentionally introduced in the transmission between motor and joint (Figure 2.20). The stiffness and dynamics of the elastic element being known, it is possible to model the joint as a mass-spring-damper and control the torque of the rotary or prismatic joint with high accuracy. Furthermore, the stiffness and dynamics of the elastic element being tuned correctly, it is possible to make the joint behave as a fully

back-drivable actuator regardless of details of the rest of the transmission.

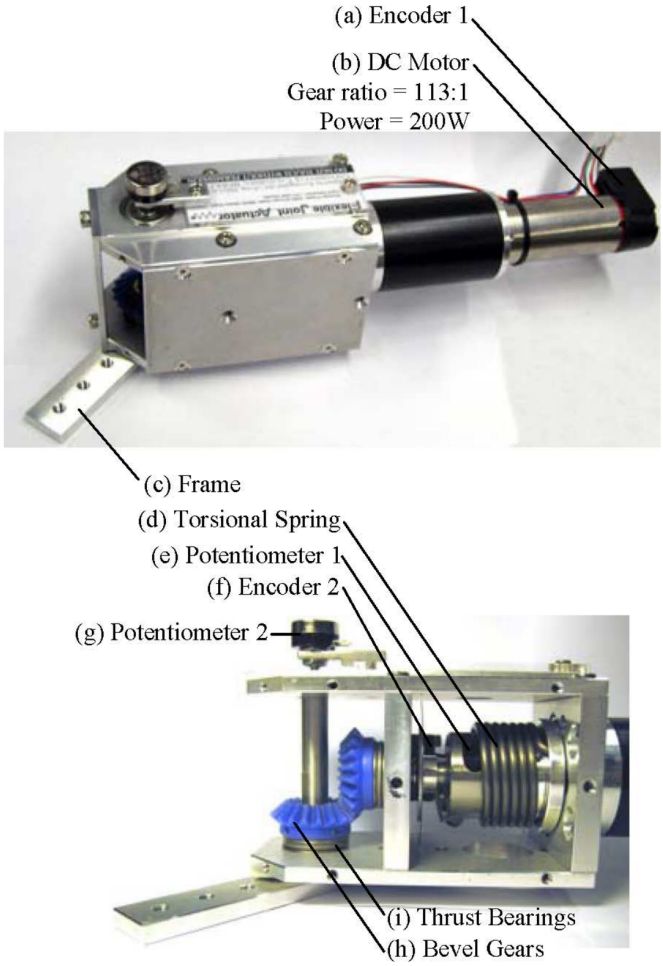


Figure 2.20: A prototype rotary series-elastic actuator presented by [104]. The torsion accumulated in a spring can be used to control joint torque.

Wrist force sensors (such as the example shown in Figure 2.21) are also widely used to measure interactions between the robot end effector and environment [111–113]. Despite the obvious advantage of measuring forces directly hence negating the need to calculate wrenches, wrist sensors are difficult to miniaturise and can only detect reactions downstream of the wrist, making them unsuitable for robots operating in unpredictable environments where the body might contact surfaces at points other than the wrist, or for robots that operate in conjunction or close proximity to humans.

Tactile and skin sensors for robotic manipulators have been described by multiple researchers [114–117] and applied to various types of robots. In their paper titled *Design and characterisation of a three-axis Hall effect-based soft skin sensor*, Tomo et al. [118]

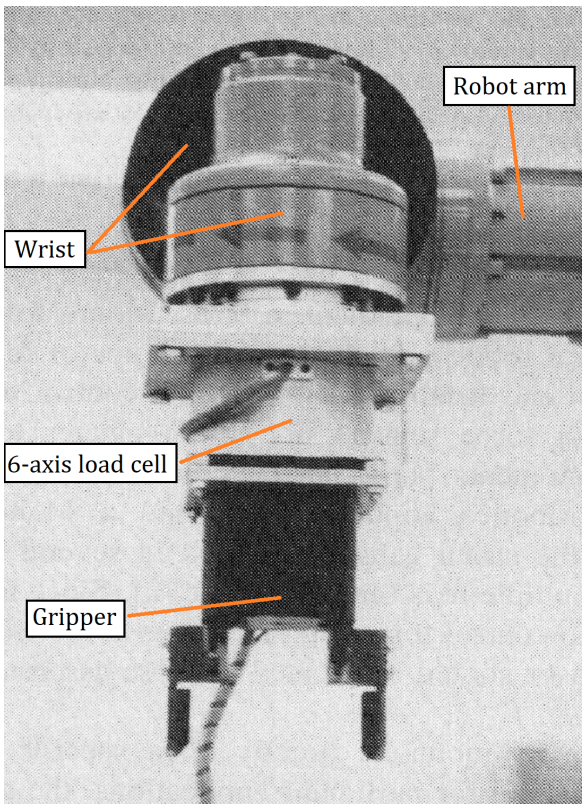


Figure 2.21: A wrist force sensor mounted on a robot arm, presented by [111]. Six-axis load cells can be used to obtain detailed measurements of reaction forces at the end effector but are difficult to miniaturise.

describe a construction that places a small magnet in close proximity to a Hall effect sensor and suspended in an elastomer. Forces acting on the membrane at or near the magnet can be measured with the sensor integrated circuit. While the specific construction of tactile sensors described in the literature is not applicable to machining robots, the approach could be modified to measure forces acting on a robot wrist or joint by introducing a flexible layer and strategically placed magnets and sensors.

The solutions to robotic force control described so far have their application in relatively large robots with conventional rotary or prismatic joints. Load cells, torque sensors and elastic joint elements present a sizeable challenge of miniaturisation to make them suitable for slender in-situ machining instruments. The following section explores force control strategies specific to continuum robots with low stiffness.

2.4.2 Force sensing in continuum flexible robots

Force control of continuum robots is a growing area of research, as the versatility and inherent safety to humans of flexible and slender robots makes them popular for tasks such as minimally invasive surgery, search and rescue and in-situ repair of industrial assets.

In a paper titled *Multi-axis force/torque sensor based on simply-supported beam and optoelectronics*, Noh et al. present a versatile wrist-style sensor that is compatible with continuum robots [119]. A cylindrical chassis with selectively weakened structure is designed to flex under the influence of axial forces and radial moments, moving a distal end relative to a proximal end and affecting the returned signal from three optoelectronic sensors (consisting of co-planar LED and photo transistor pairs and a parallel mirror) mounted inside the cylinder as seen in Figure 2.22. In their work the authors describe the construction of a multi-segment continuum robot equipped with one such force/torque sensor at the end of every segment, endowing the manipulator with comprehensive proprioception (referring to the ability to sense a body's own position and movement). Despite the clear advantages of a low-cost continuum wrist-style force sensor, the ability to miniaturise this particular design in a practical way below a diameter of $10mm$ is called into question.

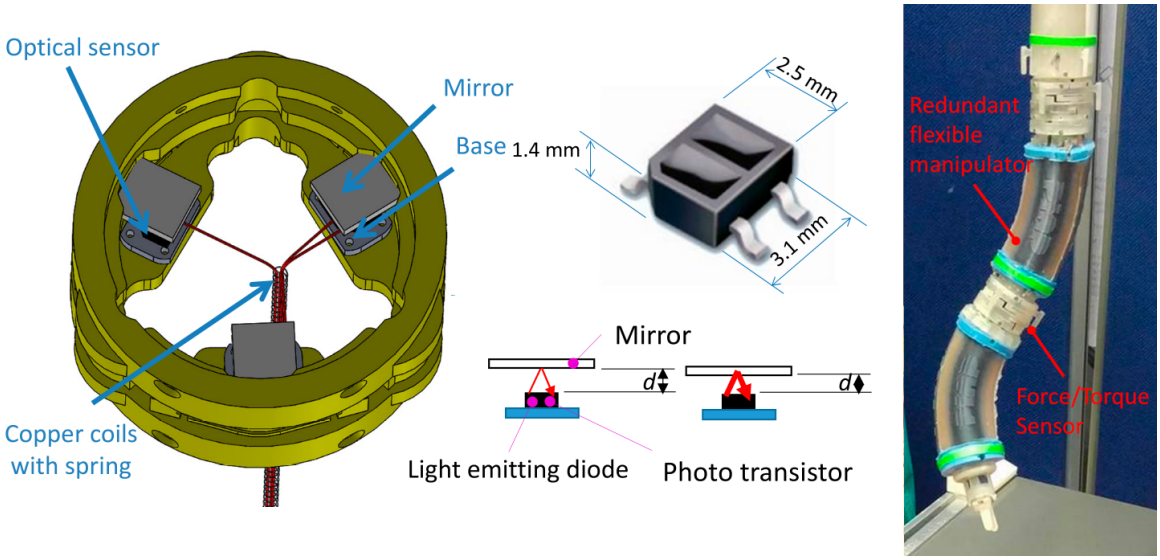


Figure 2.22: A wrist-style force sensor of cylindrical construction using three optoelectronic sensors and three mirrors, as presented by [119].

A related approach is presented in [120, 121], where the optoelectronics are not

mounted on the wrist sensor and are instead located outside the continuum section altogether. A light is emitted by a source, transmitted through the continuum robot using an optical fibre and reflected back into the fibre by a mirror mounted on the mobile part of a flexible wrist component. Flex of the wrist caused by external forces changes the relative angle of the mirror and the fibre, modulating the intensity of reflected light which can be measured by a photodiode. The approach was miniaturised to fit within a 4mm maximum diameter catheter, however it required contextual knowledge from additional sensors (such as X-ray and magnetic resonance imaging) to differentiate between axial and radial forces. While it may be possible to use a plurality of fibres in strategic arrangements to measure axial forces and radial moments acting on the wrist, this increases the number of required fibres and mirrors further impinging on the available central passage space.

Xu and Simaan [11] have explored the ability of continuum robots to be used for force sensing by means of monitoring the tension in the actuation cables. The method they use is to decompose the Jacobian - a matrix that maps the partial derivatives that describe the effects of each degree of freedom on each point of interest or end effector - to obtain the expected tensions from the actuation pack and hence be able to calculate the external forces. Screw theory is used to create a mapping between the configuration space and the twist space (forces and moments). The process is validated experimentally by using a continuum arm fitted with tension sensors and an optical motion capture system to track its shape to detect hard objects buried under a layer of silicone (Figure 2.23). They were able to measure force to within 0.83 grams. For this paper, the radius of curvature of the NiTi backbone is assumed to be constant, which it is unlikely to be. For multi-segment robots where the displacement of each wire is minimal this assumption might hold, but for machines with greater displacement this will not be enough. This method uses optical motion capture to deduce the twist space. This approach is unsuitable for in-situ repair operations as it is impossible to have cameras pointing at the continuum arm during machining in a confined space.

In their paper *Compliant Motion Control for Multisegment Continuum Robots with*

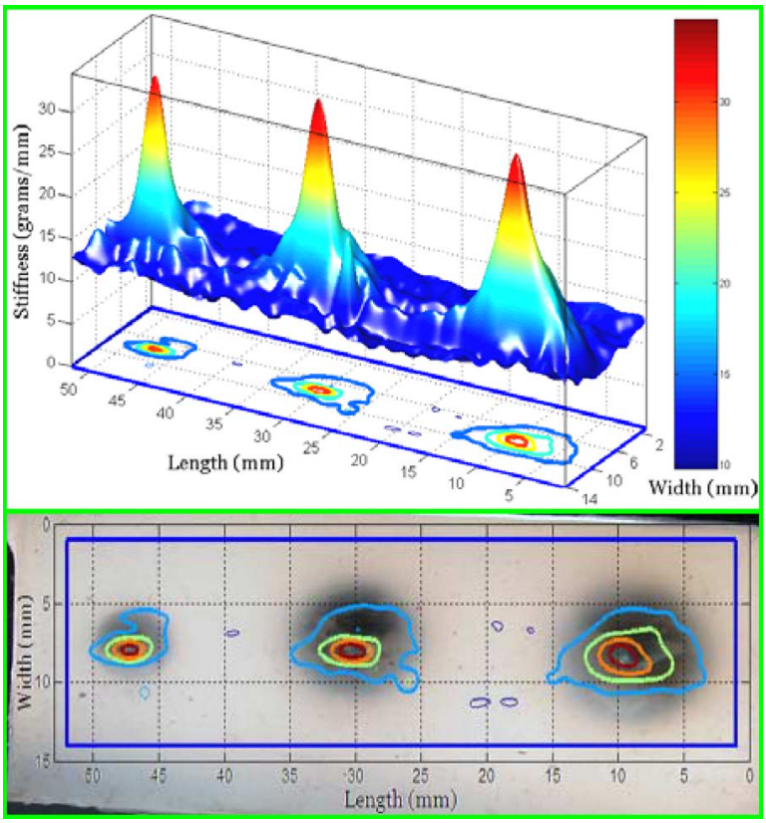


Figure 2.23: Cable tension sensors enable continuum robots to measure force and detect hard objects embedded in a silicone matrix from Xu and Simaan [11].

Actuation Force Sensing [122], Goldman et al. propose a method to control a compliant continuum robot subjected to unknown contacts with the environment. The measured cable tensions are compared to the forces that are expected from a model of the unperturbed generalised system. The paper describes a method to turn cable tensions into a matrix of unexpected forces (i.e forces that cannot be attributed to the unperturbed model) that can be used to compute a response. The correction is calculated using a support vector machine, which uses machine learning to generate an output. This is a compact method that can be used during live motion. The objective of this paper is to minimise the forces acting on the continuum arm and it is tested by inserting the robot into a cavernous passage. The robot reacts to the cavernous environment and moves accordingly.

The experimental setup uses force gauges to measure the cable tension and EM tracking sensors in conjunction with video gauges to track the position of the robot. The method for obtaining the matrix of unexpected forces can be applied to control the

amount of cutting force transferred to the cutting tool.

Bajo and Simaan [123] described the use of screw theory to detect collisions on any segment of a continuum arm as well as to detect complete constriction of the arm. The algorithm compares instantaneous screw axes created using a model of the unperturbed system and created from the sensory data of the segment position using EM tracking. Deviation in the motion of the screw axes can be translated into strength and location of contact; hence the algorithm can detect collisions in any number of segments. This was validated by touching against different joints and holding the arm to constrict it (Figure 2.24). In the context of in-situ repair applications, contact detection is only useful if it can be done without the use of electromagnetic tracking or other extrinsic position feedback methods. If an instantaneous screw axis could be obtained from tension sensor data instead of EM tracker data then this approach could be employed for force control during machining.

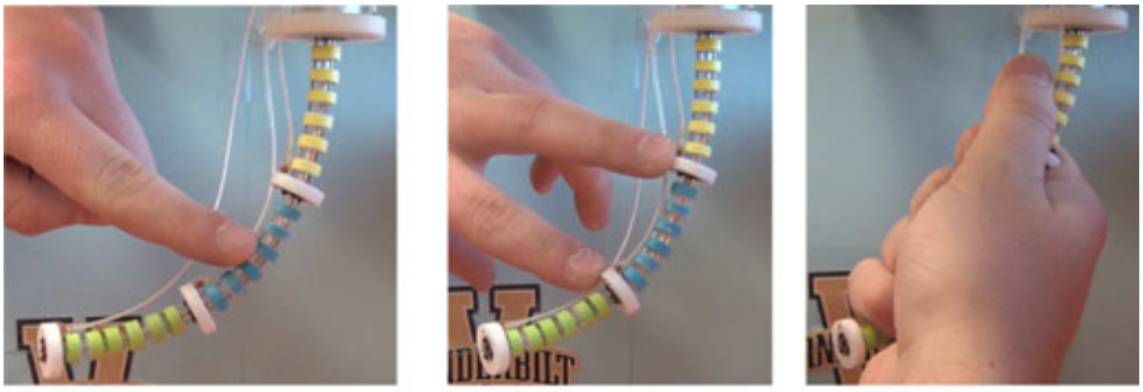


Figure 2.24: Location and magnitude of contact is detected using knowledge of cable tension and position of the arm [123]. The method relies heavily on external measurement methods (electromagnetic trackers).

In [124], Bajo and Simaan describe the modelling and control of a family of continuum robots with intrinsic force sensing capabilities for force control. They make the assumption that the segments bend in circular arcs and that the only point of contact between the robot and the environment is at the operational point. This paper shows the ability to use intrinsic force sensing with tendon tension to accurately control the contact force at the interaction point with the environment, which will allow machining to be carried out safely and efficiently. The method is validated using a two segment continuum arm to

touch a surface with known defects and equipped with a force sensor. Their continuum robot was able to regulate the contact to within 1.5 grams of force for high angles of incidence, but the method is less effective when the contact occurs at shallow angles.

A review of literature concerning physical reaction sensing in continuum robots has shown that it is possible to use cable tension information to deduce the forces acting on a continuum segment. However, these methods rely on a thorough model of the system kinematics and an accurate knowledge of the position of the actuator (often done with cameras and other extrinsic position feedback methods in previous work). Hence, work in this area will focus on developing methods to directly measure contact forces for slender and compliant in-situ machining robots to make measurement and control more robust and reliable.

2.4.3 Process force control using remote sensors

Current methods of closed loop control using force signals for in-situ instruments are generally reliant on direct feedback from sensors (e.g. load cells, strain gauges). These methods rely on accurate knowledge of the instantaneous configuration and geometry of the instrument, which is a difficult task considering the possible deflection of slender robots. In addition to the limitations of force sensing via tendons on long robots, the approach cannot be used on a sensorless robot without modifying it by adding load cells or other such hardware.

In the case of robots equipped with machining end effectors, an alternative method could be to use Acoustic Emission (AE) to monitor machining parameters due to its high signal-to-noise ratio. In [125], AE is used to monitor surface quality during machining of nickel-based superalloys. In [126], AE is used to detect dullness of grinding wheels. Other authors have also demonstrated the use of AE to monitor different machining parameters [127–132]. Similarly, vibration signals measured with an accelerometer and amplified with a vibrometer were used to monitor parameters during grinding in [133]. However, despite its numerous advantages, the AE sensor or accelerometer needs to be mounted directly on the surface where the waves are to be

captured, which is impossible when remote workspaces are accessed for performing in-situ material removal interventions.

Audible sound features have also been used to monitor or predict various parameters of machining processes and machine tools performance. In [127], airborne sound is used to identify appropriate abrasive densities during honing. Rubio et al. [134] used frequency signatures of audible sound to identify cutting parameters during milling, such as rotation speed and depth of cut. Other authors have used sound signal-processing methods — RMS of pressure, intensity and frequency spectrum of the signals — to monitor or predict different quality parameters (e.g. surface roughness, chatter) during band sawing [135, 136]. However, no attempt is made to control the machining parameters in closed loop using the airborne sound features.

In their paper titled *Acoustic sensing for soft pneumatic actuators*, Zöller et al. [137] present a method for determining the location and strength of contacts on a pneumatic actuator by positioning a microphone within the air chamber. The amplitude spectrum of a sound signal from the microphone from various events is used to train a machine learning algorithm (support vector machine) to recognise and classify the sounds. Labels include discrete positions such as "tip", "middle", "base" and discrete force levels of "light", "middle" and "strong". While this use of airborne sound shows promise in the area of contact detection for manipulators and grasping robots, it is unlikely to provide sufficient signal strength for closed loop control of contact forces, particularly as it relies on identification of percussive force events.

Robben et al. [138] described a method for determining tool settings and predicting the material composition of concrete (i.e. rocks, inclusions and cement content) during disc cut-off grinding with diamond wheels using airborne sound features, and were able to create a map of the hardness and compositions of the concrete slabs (Figure 2.25. Khan et al. [139] use sound features (such as RMS of microphone voltage and cumulative amplitudes of dominant frequencies) to determine wear damage in mechanical components with multiple contact points under load. These reports show extensive efforts on the use of features of sound signals for process monitoring but, it seems, no examples of employing

sound signals to control the material removal processes in closed loop have been reported.

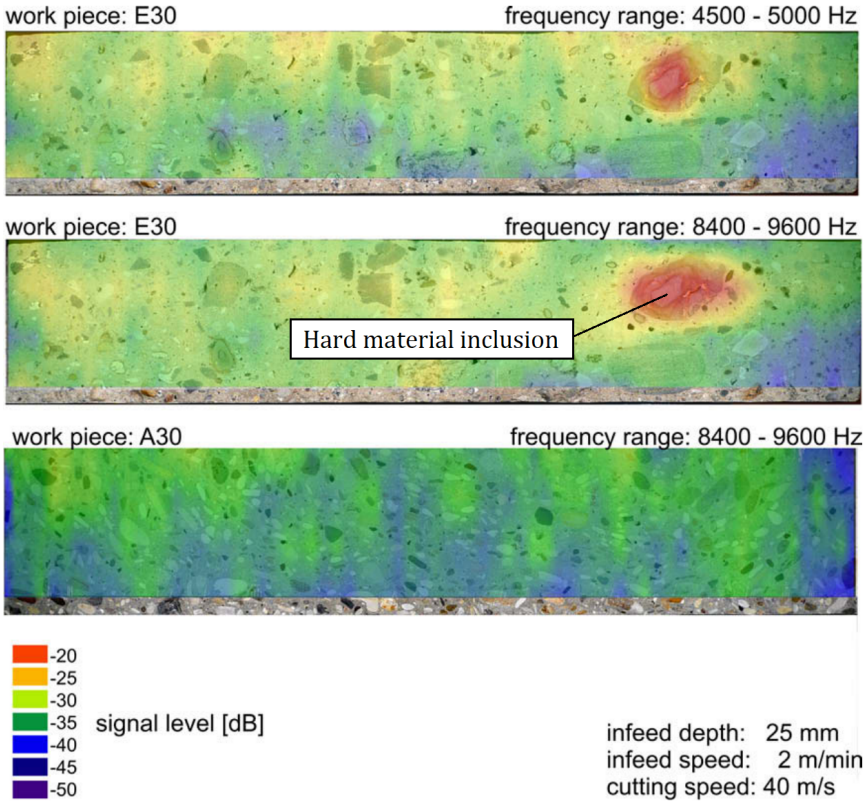


Figure 2.25: RMS signal level in specific wave bands for two different types of concrete (E30 and A30) as obtained by airborne sound signal detection in [138].

While airborne sound signals are more susceptible to distortion and noise, the sensors can be placed some distance away from the machining operation making them more suitable for an in-situ repair application. This work seeks to identify a method for closed loop force control that is applicable to sensorless robots and useful for repair of difficult-to-access industrial assets.

In this context, a robotic tool equipped with a method for online process monitoring using sound signals derived from the machining operation can be highly efficient for closed loop control of different operations (e.g. grinding, milling) in inaccessible and especially in blind workspaces. With such facilities in place, automated in-situ repair applications could be performed with precision and reliability.

Real manipulation and machining tasks involve interactions between the robot and its environment. There is a substantial volume of research into the details of force control in robotics and, while many of the approaches for continuum robots may have applications

in the area of in-situ repair, it is likely that remote force sensors will prove most useful if incorporated together with a reliable position control scheme.

2.5 Review of simultaneous position and force controllers

Controlling position and force simultaneously is essential for robots that contact and affect their immediate environment; this is true for most practical manipulatory tasks but becomes particularly evident when the environment is variable and unknown. Position control alone risks damage to the robot or its surroundings by collision or over-exertion if a nearby object constrains its motion. Force control alone leaves the robot without a reference to its surroundings and hence unable to achieve particularly useful tasks. Precise interactions with nearby objects requires a combination of two conflicting control strategies which often leads to hierarchical algorithms, i.e., dominance of the force control action. The challenge presented in this work is one where the shape and surface quality of the machining output are determined by tool trajectory and contact force respectively, requiring some form of multiple-input-multiple-output control.

2.5.1 Simultaneous position and force control of conventional robots

As mentioned above, most practical applications of force control in manipulators include some form of simultaneous position control. Multiple simultaneous control strategies have been explored for robot arms and other conventional jointed manipulators.

In multiloop control, each manipulated variable depends only on a single controlled variable. In the context of manipulator robot control, this means that position and force would be controlled independently with their own feedback loop. This simplistic approach is common in industry, as it makes troubleshooting and tuning easier. However, problems may arise if the outcome of one loop has an effect on the others, as this can result in more difficult tuning and even in the closed loop system becoming unstable [140].

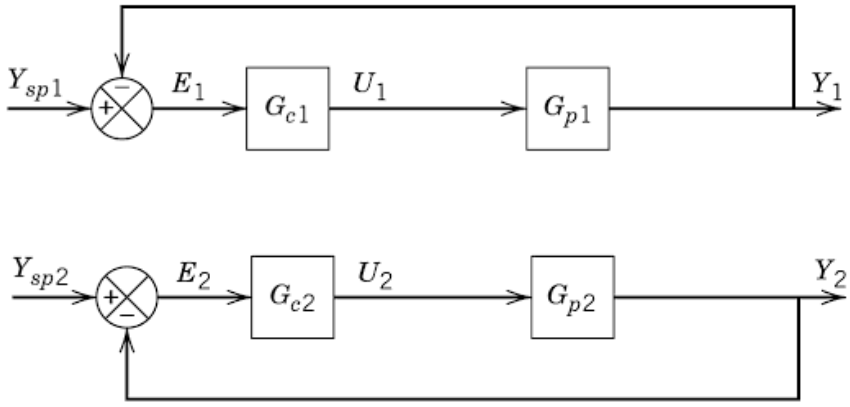


Figure 2.26: Two parallel and independent control loops, where Y_{sp} is the set point for the variable, Y is the output, G_c is the controller transfer function and G_p is the process transfer function [141].

The idealised scenario in Figure 2.26 shows two loops controlling two aspects Y_1 and Y_2 of the same system completely independently. However, in reality there are always process interactions that induce relations between the control loops. In the case of most robots (and particularly compliant robots), movement of actuators changes the state of both variables, which introduces strong interactions between motion and force control. This is shown in a simplified form in Figure 2.27.

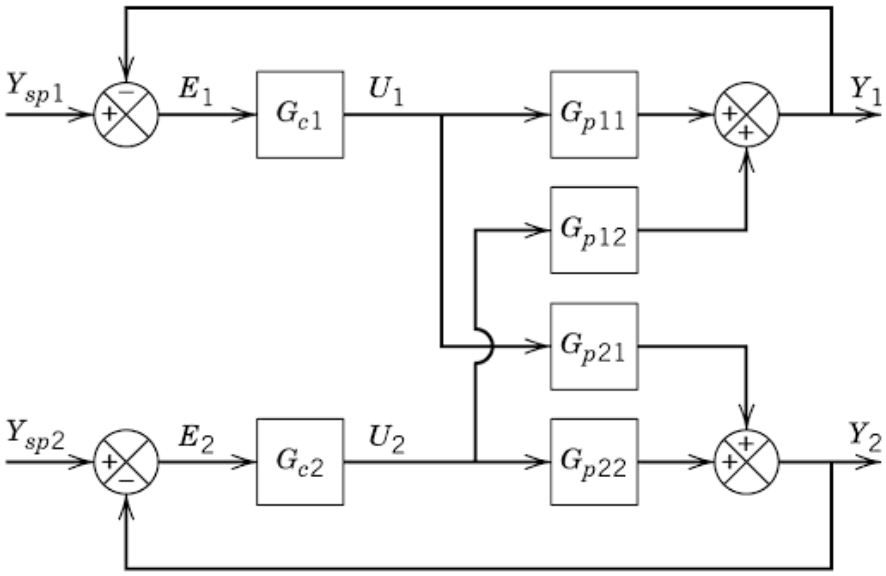


Figure 2.27: Block diagram for multi-loop control with controller interactions [141]. The coupled controllers can result in positive feedback and pose challenges for control.

Applying some realistic transfer functions to the case where the two loops are position and force, the resulting control structure can be rearranged to resemble two nested loops due to the causality of force feedback (Figure 2.28). In practice, an inner position loop and an outer force loop that modifies the position setpoint appear as a consequence of the physics of manipulators. This direct force control by nested loops has been extensively investigated in literature [142] with large variability in, among other things, loop hierarchy, impedance versus stiffness force control and position versus velocity motion control.

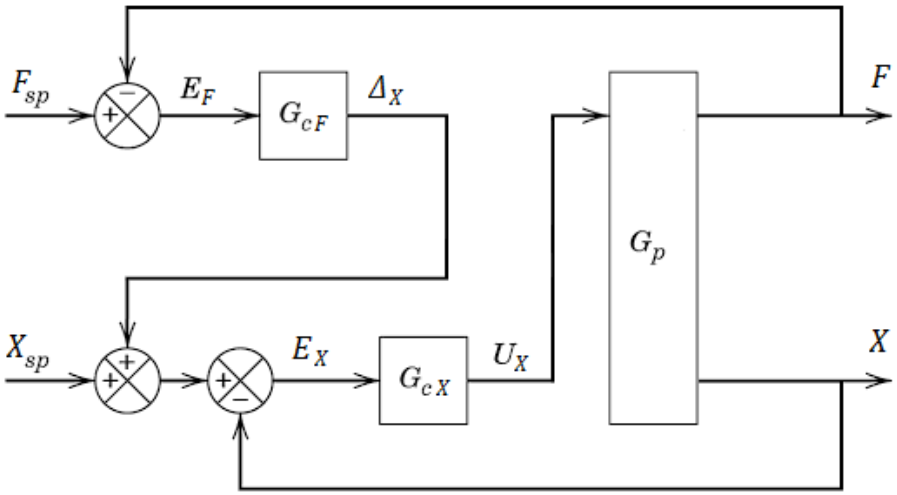


Figure 2.28: Block diagram for multiloop control specific to position and force feedback from a manipulator. The interaction between two loops is expected and inevitable.

Another approach to simultaneous control is to separate the task into elements that require position control and tasks that require force control. This is described by Khatib in the paper titled *A unified approach for motion and force control of robot manipulators - the operational space formulation* [143], where evaluation of the current parameters returns a task specification that assigns the required weights and directions to the different control variables. An accurate model of the environment is used to give the system a sort of situation awareness that allows it to transition from, for example, positioning a screwdriver to tightening the screw; from placing a gripper over an object to gripping said object; from positioning a component to press-fitting said component. In all of these examples, the context of the task instructs the force controller to act only in the relevant degrees of freedom and can therefore be separated from position constraints altogether. By

removing conflicting control loops and the necessary hierarchy, the force control becomes more predictable and fine-adjustable.

The clear disadvantage of hybrid position-force control as described by Khatib and others [140, 144] is that a detailed model of the environment is necessary to return a task specification. If an unknown object were to come into contact with the manipulator in an unexpected place or from an unexpected direction, the manipulator would continue to operate in position control. This is unacceptable in any scenario where the environment may change and objects may move unintentionally, as is often the case for in-situ repair (if everything was as expected a repair should not be needed). Another disadvantage is that changing between control schemes results in discontinuities unless every interaction is as predicted and every motion carried out with high precision. The consequence of this is an overall inability to respond to errors in these critical transitional moments.

In their paper titled *The parallel approach to force/position control of robotic manipulators*, Chiaverini and Sciavicco [145] present a simultaneous position and force controller (Figure 2.29). In their words, "a position feedback loop acts in parallel to a force feedback loop. Dominance of the force control action ensures force regulation along the constrained task-space directions, while the position control action can be designed to achieve either regulation or tracking of the end-effector position along the unconstrained task-space directions" [98]. The subtle difference from the nested control loops approach is therefore mostly in the nature of the hierarchy definitions and in the increased versatility of each of the control loops.

When it comes to assigning a hierarchy, this is usually achieved by selecting strategically weighted controllers. In the case of Chiaverini's parallel controller (and indeed often in nested-loop simultaneous controllers), these are a *proportional + integral* (PI) controller for force and a *proportional + derivative* controller for position. The inclusion of an integral term makes the force controller dominate, as it is guaranteed to overpower the position loop in a conflict of inputs.

While the theory of simultaneous position and force control has been well studied for robots with conventional joints and robots equipped with wrist sensors and other direct

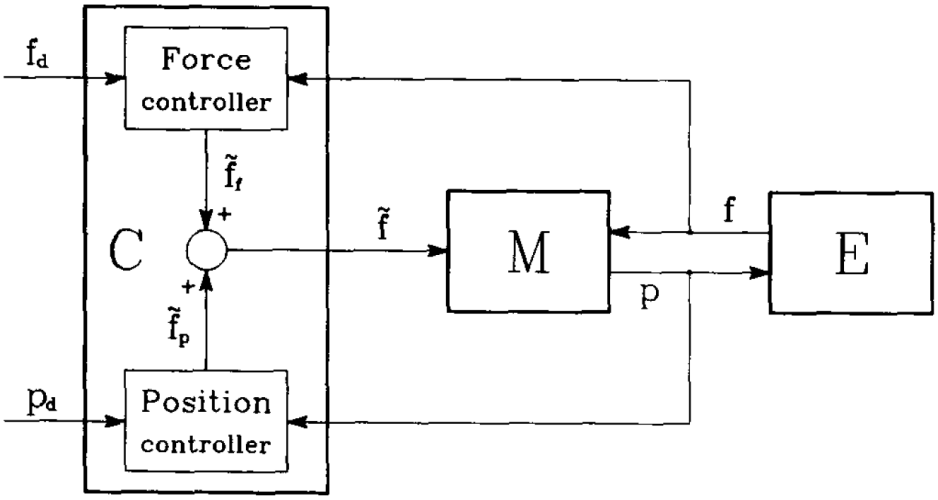


Figure 2.29: Block diagram for Chiaverini's parallel force/position controller. C is the Controller, M is the Manipulator, E is the Environment, f is force and p is position [145].

feedback sources, the relatively new field of continuum and soft robotics presents a number of unique control challenges.

2.5.2 Simultaneous position and force control of continuum robots

In their paper titled *Hybrid motion/force control of multi-backbone continuum robots*, Bajo and Simaan [124] demonstrate an example control architecture for multiple input multiple output systems. In this paper, the challenge is not accessibility but rather the need to adhere to strict sterilisation guidelines in the field of minimally invasive surgery robots, making it impossible to use force sensors at the end effector. The authors describe an approach that uses knowledge of the tension on the tendons to predict the external forces acting on the continuum robot. While their method relies on assumptions of the kinetostatic model of the bend of the robot (a model where forces are at static equilibrium), they were able to show experimentally that the cable tension can be used to measure and control contact forces at the operational point. Figure 2.30 illustrates the strategy employed by Bajo and Simaan for merging force and motion control.

It can be seen that Bajo and Simaan's simultaneous controller is fundamentally similar to Chiaverini's parallel controller (Figure 2.29), but with the added layers of complexity

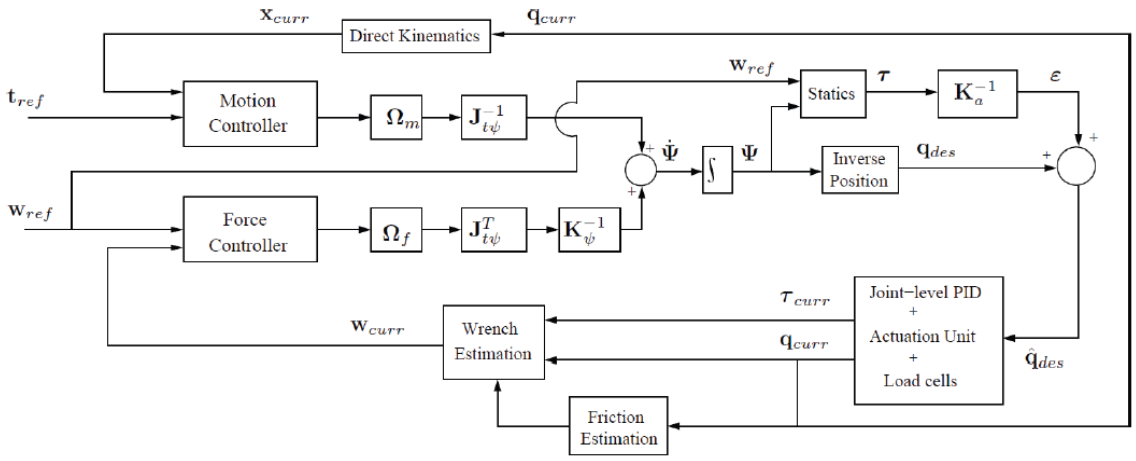


Figure 2.30: Motion/force control strategy for continuum robots from Bajo and Simaan [124], ω_m and ω_f are projection matrices, $J_{x\psi}$ is the Jacobian matrix, K_ψ is the configuration-space stiffness matrix, ψ is the configuration space vector, K_a is the joint-space stiffness matrix.

introduced by tendon friction losses, complex statics and kinematics. In Figure 2.30, t_{ref} is the desired twist and w_{ref} is the desired wrench, where the wrench describes a system of forces reduced to a point with an axis and a pitch, and the twist describes the translation and rotation of the object that is affected by said wrench. Hence in simplified terms, t is the desired end effector configuration and w is the desired force interaction between the end effector and its surroundings. As above, a PI force control scheme is used to assign a hierarchy.

In Bajo and Simaan's control strategy a motion controller and a force controller work independently and contribute different amounts to the output. The motion controller compares the reference twist vector to an estimate of the real position of the end effector, a vector based on the kinematic model of the system and the actuator positions. The force controller compares the reference wrench to an estimate of the real wrench based, again, on kinematic and static models of the system which are a function of the assumed position of the robot and the information from the tendon tension sensors. Hence, this method relies on a thorough and accurate model of the system and extrinsic position sensors; without force feedback from the end effector, is vulnerable to compounded errors and unexpected non-linearities.

The success of this method in the context described in Bajo and Simaan's paper

[124] can be attributed to the relative simplicity and safety of the one-degree-of-freedom continuum robot used. However, due to the reliance on exact models, the scalability of this approach without closed feedback loops to continuum robots with more degrees of freedom can be called into question.

In the paper titled *Stiffness control of surgical continuum manipulators*, Mahvash and Dupont [146] explore stiffness and force control for continuum robots not equipped with force sensing by using a detailed model of the kinematic and static forces of the instrument. An extrinsic electromagnetic position sensor (3D guidance Trak STAR electromagnetic tracker from Ascension Tech. Corp.) is used to provide feedback real-time feedback and serves as the basis of the force controller for a concentric needles continuum robot (Figure 2.31). The simultaneous control method used is a nested loop control approach, where the position setpoint is modified along the constrained direction to a point that is expected to achieve the desired force based on the modelled statics and dynamics, but there is no force feedback for true stiffness control.

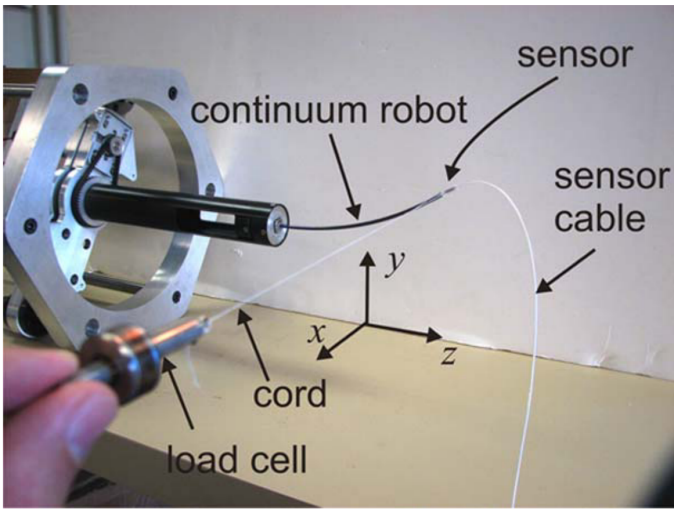


Figure 2.31: Stiffness control manual experiment by Mahvash and Dupont using position-only feedback [146]. The method relies on position feedback from actuators and from an electromagnetic tracking sensors mounted on the end effector.

Recently, other approaches such as model-less controllers [147] have been explored for simultaneous position/force control of a one-segment serpentine continuum robot equipped with tendon load cells, where the controller learns the robot's Jacobian in real-time allowing it to adapt to new constraints in the environment. Like Mahvash's

stiffness control however, this method relies heavily on accurate knowledge of the robot tip position (using trackers and a camera).

It can be seen that, despite recent advances towards practical simultaneous force and position control of continuum robots, the solutions are limited by their need for accurate position and force feedback sources which are incompatible with in-situ repair of industrial assets with challenging access. Hence, a versatile and easy to tune scheme such as nested loops or parallel position/force control applied to a continuum robot with novel shape sensors and remote force sensors may prove to be a suitable solution for an in-situ machining robot.

2.6 Research gaps for potential future investigation

The last half century has seen a large volume of research and innovation in the area of robot control, which has resulted in unprecedented capabilities for automation and remote operation of complex machines. However, specialist disciplines of robotics such as miniaturised industrial serpentine in-situ repair instruments still present mostly unexplored domains. As previously discussed, this work explores new approaches to the problems of position and force control of serpentine robots for in-situ repair. In light of the existing literature presented above, the following opportunities for contribution have been identified:

1. Scalable sensors for shape feedback

   Of the wide variety of position feedback methods discussed in past research, fibre Bragg grated sensors are clearly best suited for continuum robot control and for control of slender instruments of any length. Their versatility is unparalleled and they present a new area of research for closed loop position control of continuum or soft robots. However, the high cost and delicate nature of grated fibres and interrogators makes them unlikely options for instruments that are to be widely deployed in industry (and unlikely options given the funding available in this doctorate research). Another area of unexplored territory is the application of

resistive stretch sensors - such as those used for detection of human motion and soft tentacles - to closed loop shape control of miniature serpentine continuum robots or other slender and compliant instruments. While other curvature and shape sensing options such as capacitive, optoelectronic and magnetic may also present opportunities for further investigation, resistive sensors have the most potential for miniaturisation and are therefore the logical direction of this research. The following specific gaps in knowledge remain:

- Construction and characterisation of cylindrical resistive shape sensors for their application in vertebral discs with existing circular actuation holes,
- Application of resistive strain sensors as skin curvature measurement devices for rigid-construction serpentine robots,
- Design and validation of closed loop control schemes for multi-section, high-degree-of-freedom slender and compliant robots equipped with resistive shape sensors and capable of three-dimensional end effector positioning.

2. Remote sensors for force feedback

   Existing methods of force control for slender robots rely largely on detailed models, accurate knowledge of the robot configuration and often tendon load cells susceptible to friction and non-linearitites. This is because the low stiffness of slender and compliant robots renders accurate control from the proximal or actuation side impossible. However, the possibility of using remote signals such as airborne sound to serve as feedback for a machining force controller is an encouraging area of research. While previous work has used airborne sound to monitor machining processes, there has not been to the author's knowledge an application of a feedback control loop using such signals. The following specific gaps in knowledge remain:

   - Characterisation of remote signals from in-situ machining instruments at various cutting forces,

- Design of a closed loop force control strategy that utilises the characteristics of the specific remote signals as feedback,
- Application of a closed loop force control scheme using remote signals on a robot equipped with in-situ machining tools.

3. Simultaneous position-force controller for in-situ repair

   The topic of simultaneous position/force control is already well understood, but the specialised application of a slender and compliant machining robot presents challenges that have not been addressed in past literature, such as the need to achieve accurate machined shapes. The novelty therefore lies in the application of specialised sensors for a specific application:

   - A highly elastic resistive shape sensor for closed loop curvature and shape control of a high-degree-of-freedom continuum robot, and
   - A remote machining force sensor based on signal processing of remote signal features from an in-situ machining end effector.

Each of these factors presents an opportunity for research, all within the context of in-situ repair using slender, compliant, in-situ machining robotic instruments.

Chapter 3

Case study of a slender robot for in-situ machining to identify challenges in position and force control

Repair tasks in complex installations such as gas turbines often require expert technicians with very specific sets of skills travelling around the world to address these maintenance needs. One such repair task is the in-situ removal of stress concentrating defects on gas turbine compressor blades that could be caused by foreign object damage. This repair is currently carried out using slender grinding and polishing tools that are manually inserted into the compressor though inspection ports to remove material and smooth the damaged blade edge profile. While it is possible to make a robot with the necessary degrees of freedom to replicate the movements of the technician, it is essential that such a robot be controlled by a person with the required skill and experience. The ability to carry out these operations remotely would significantly reduce downtime, but worldwide remote control comes with a number of challenges. To address this gap in capabilities, this chapter presents a novel system architecture for remotely repairing high-value industrial assets such as aeroengine compressor blades.

In-situ maintenance technicians currently employ a complex customised set of tooling for successive tasks, from visualisation and measurement to surface preparation and material removal. The variety of interventions that need to be performed often results in a significant volume of customized tooling. These operations are currently performed manually, and therefore lack repeatability and precision. Hence, it follows that a robotic solution for such inspection and repair tasks would be a breakthrough for high-value asset industries with worldwide operations (e.g. aerospace and energy). A robotic approach would offer the possibility for some level of automation of these interventions, eliminating the human errors during manipulation of tools. Adding to this the ability to control such an instrument remotely under the supervision of a trained expert would dramatically reduce the time taken to address complex tasks, from several days to a few hours.

The case study presented in this chapter is the culmination of a collective effort between five parties including the present author. The remote boreblending robot was part of a SAMULET II project funded by the Aerospace Technology Institute (ATI) titled Remote Inspection and Engine Repair (ReInER). The University of Nottingham deliverables were managed by Dr Amir Rabani and Prof. Dragos Axinte. Dr Adam Nagy-Sochacki led the mechanical design aspects, Dr Bilal Nasser led the software design aspects and the present author led the electronics and hardware aspects of the project. However, all areas of the project were influenced and contributed to by all parties. Further details about the specific contributions by the author of this thesis can be found in Section 1.5.1.

3.1 Background

The use of robots to automate high-skill tasks in inaccessible or inhospitable environments and reduce downtime is growing year on year. In [16], Dong et al. demonstrate the use of a long hyper-redundant continuum robot to address in-situ inspection and repair tasks on the intermediate pressure compression stages of an aeroengine. In [148] and [149], the authors demonstrate the use of a track-based robot to address in-situ a number of processes on hydropower equipment, from post-weld heat treatment to grinding. Robotic

instruments are also being deployed for applications such as minimally invasive surgery [13, 21, 23], where precision, repeatability and smoothness are essential for success.

Tele-operation of in-situ robotic systems has been explored extensively in the field of minimally invasive surgery. Robots with high precision and flexible articulation [13,21,23] are used to operate on patients through a single point of access, reducing the recovery time and allowing for potential remote operation by an expert surgeon anywhere in the world. A well-known, currently in-use system in robotic surgery named DaVinci [150] consists of multiple surgical arms with cutting, grasping and observation end effectors. This device relies on a direct wired connection with the operator-level control system to ensure near-synchronous movement between the surgeon's hand and the robot arm.

The application considered here is the realization of a stress relief feature on a gas turbine compressor blade via a successive set of tasks: navigation into the compressor via a borescope inspection port, positioning of sensors in the required position for measurement of defects, analysis of measurement data, and machining passes to remove the required material as a stress relief feature on a dented blade (a procedure known as boreblending). Currently, in-situ boreblending is carried out using manual tools and instruments: a flexible or rigid boroscope such as the ones described in [151] is used to identify the affected area; borescopes with structured light phase measurement [152] or stereo vision point cloud [153] capabilities are used to measure the dimensions of the defect; a slender, belt-driven grinding tool with an articulated tip (Figure 3.1) is used to machine a smooth scallop over the defect. Multiple measurements are taken throughout the procedure to ensure that the stress relief reaches the shape required by the aerospace safety standards, meaning that this procedure can take as much as 3 hours to complete.

This section presents a novel robotic system which combines continuum type joints [45] with rotary and prismatic stages to replicate the movement of a manual tool, navigate inside a gas turbine and deliver measurement instruments and a grinding end effector to a damaged compressor blade.

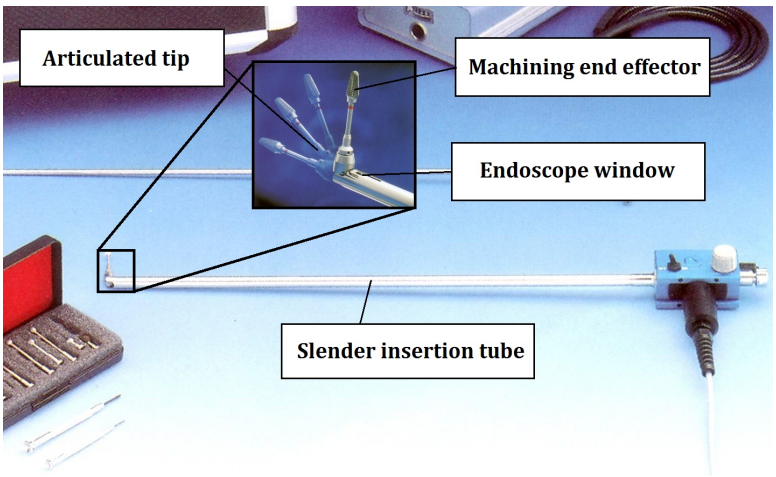


Figure 3.1: Conventional boreblending tool for gas turbines (Richard Wolf blending scope [154]) consists of a long and slender insertion tube with a belt-driven machining end effector. An endoscope window allows the operator to see the grinding or polishing tools as they contact compressor and turbine blades.

3.2 Degree of freedom study for in-situ boreblending

To assess the degree of freedom (DoF) required to perform an automated blending operation, the motion of current manual tools was studied and a computer model of an agreed set of stages within a gas turbine compressor was evaluated as an example environment. The stage of compression, i.e. the location and function of the specific ring of compressor blades within the engine, was chosen as a worst case scenario with reduced space for manoeuvring.

Manipulation of existing manual blending tools from outside the casing provides 6 degrees of freedom (Figure 3.2). That being said, some of these allowable motions (X_0, Y_0, A_0, B_0) are substantially restricted due to collisions with the environment, as discussed later. The articulation of the tip represents an additional DoF. The pivot joint at the end of the scope is set to 90° after insertion but, due to the nature of the tool drive shaft, cannot be articulated during operation. The length of the tool and the shape of the cutter are also variable and are therefore relevant to the required DoF for completing abrasion of defects on the compressor blades.

In addition to the movements of the tool there is one degree of freedom associated with the environment, and this is the rotation of the rotor. This DoF can be controlled using a turning tool (seen in Figure 3.4), a powerful stepper motor that is connected to

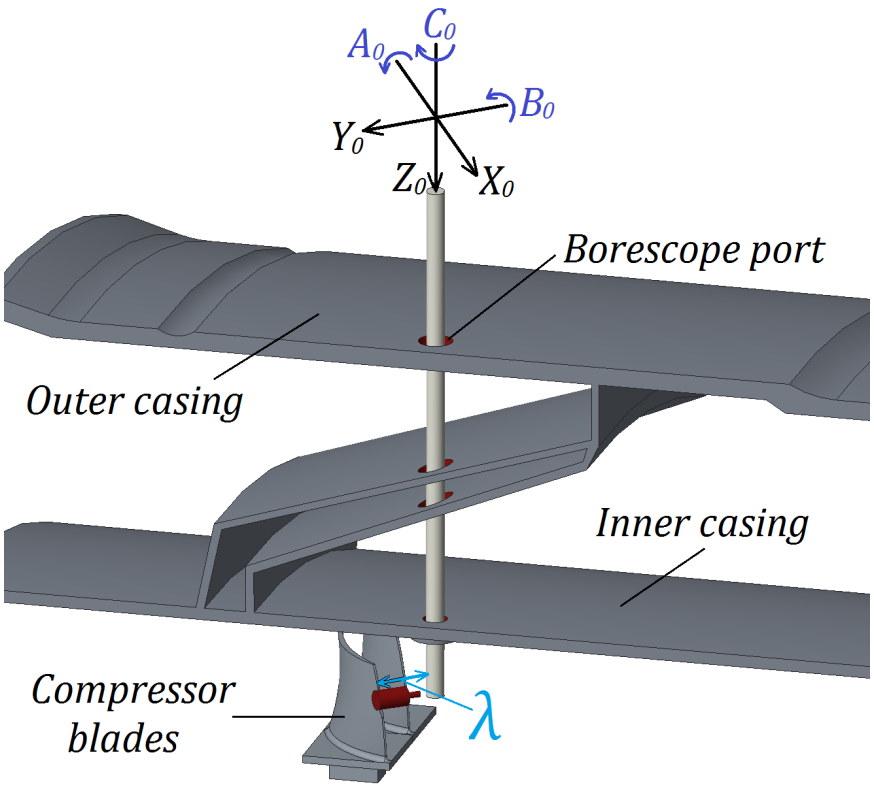


Figure 3.2: Cross section of gas turbine borescope port showing degrees of freedom of manual probe (simplified as a cylindrical rod) and rotor blade positions. On some aeroengine compression stages, multiple layers of casing material make access more restricted.

the turbine gearbox. Because of the location of the turning tool, the backlash and friction of this DoF make it difficult to control the rotor with accuracy and repeatability. It is therefore assumed that once the rotor has been moved to an appropriate position it will not be moved again during operation.

Considering a simplified system (i.e. a blade oriented and fixtured as in a machine tool) an approximation of a perpendicular blend can be achieved with only two degrees of freedom. Setting a plane approximately sectioning the target site ($X_0 - Z_0$ plane) allows movement of a tool in X_0 and Z_0 to produce a cut (Figure 3.3). The movement in X_0 could also be approximated by rotation in C_0, at the expense of squareness of the cut. However, due to the curvature of compressor blades and the varying angle of attack of the tool (Φ in Figure 3.3), some independent articulation in C_0 is desirable to maintain perpendicularity in this axis. Finally, to maintain perpendicularity to the aerofoil curvature running vertically, some deliberate motion in A_0 is also desirable. Hence,

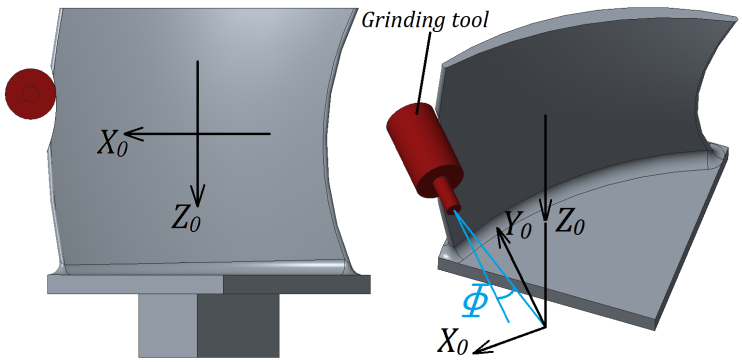


Figure 3.3: Simplified system with compressor rotor blade fixed relative to machine tool. Z_0 marks the axis of the borescope port and Φ indicates the necessary angular offset for perpendicular machining.

the required DoFs for full perpendicularity are X_0, Z_0, A_0 and C_0.

Access into the compressor is through a series of narrow concentric holes, usually smaller than $10mm$, in the inner and outer engine casings as seen in Figure 3.2, the first and last of which limit the motion of the tool. Current hand-held boreblending tools, for example, have a maximum linear movement in X_0 or Y_0 of 1.2 mm and a maximum rotation in A_0 and B_0 of 2.22°. This shows that, even in a scenario where the robotic boreblending tool is as slender as existing tools, translation and rotation in these DoFs are of limited usefulness. Hence, the required degrees of freedom must come from translation in Z_0, rotation in C_0 and strategic articulation near the tip. A single DoF of articulation in A_0 could achieve blends of the required shape but sacrifice perpendicularity of the cut to the blade plane. Two or more orthogonal articulation DoFs at the tip could theoretically achieve the same shape and perpendicularity as a manual tool including accounting for Φ. A multiple articulation approach has the added benefit of being able to use the entire diameter of access space, not requiring gaps for pitch, roll and lateral translation.

The distance between the axis of the borescope holes and the edges of the adjacent compressor blades λ depends on the position of the rotor, the angles of the nearby stator blade surfaces and the dimensions of the blades themselves. For the stage under consideration this is between 21.5 mm and 26.7 mm when the rotor edges are positioned half-way between stator blades (Figure 3.2). This defines the space available for articulation of the tip and end effector.

Based on this analysis of the required degree of freedom and dimensions, the robotic system was developed and is presented in the section that follows.

3.3 In-situ boreblending robot hardware

3.3.1 Mechanical system architecture

The design solution that was chosen (overseen by Dr Adam Nagy-Sochacki with assistance from the present author in the areas of tendon re-direction and attachment among others) consists of a hybrid robotic system that makes use of linear and rotary actuators for motion in Z_0 and C_0, as well as three tendon-driven flexible joints that articulate the tip within the gas turbine in A_0 and to some extent in B_0 and C_0 (Figure 3.4).

The robot presented in Fig. 3.4 is composed of a cylindrical outer frame that houses actuators, sensors and a $8.5mm$ diameter insertion tube and grinding end effector with five degrees of freedom. The outer frame (2) is rigidly attached to the gas turbine casing for the repair intervention. An FHA-8C-50 rotary servo motor (1) (Harmonic Drive, encoder resolution of $6,553,600$ points per revolution) mounted to the outer frame turns an inner frame (blue in Figure 3.4) about the axis C_0 of the borescope port. The inner frame (3) consists of three linear rails and a L-220.50SG linear actuator (Physik Instrumente, $0.022\mu m$ design resolution, $0.1\mu m$ minimum increment) that slides the insertion tube and relevant actuators (yellow in Figure 3.4) along the inspection port axis Z_0. Six L-220.20SG linear actuators (Physik Instrumente, $0.022\mu m$ design resolution, $0.1\mu m$ minimum increment) (4) are used to drive stainless steel tendons that bend a flexible actuated tip (two tendons for each of θ_2, θ_3 and θ_4 in Fig. 3.11) and tilt the end effector; six LCM201 load cells (5) (Omega Engineering, $\pm 100N$) monitor cable tensions. A summary of all equipment used in this chapter can be found in Appendix A.

The 8.5 mm diameter insertion tube (7) houses six tendons (6), an air conduit and a Mentor Visual iQ Video Borescope stereo camera (Waygate Technologies) (8) with a $440,000$ pixels sensor capable of taking 3D measurements of the affected area. The camera is rigidly attached to the insertion tube. Hence, the orientation is determined by

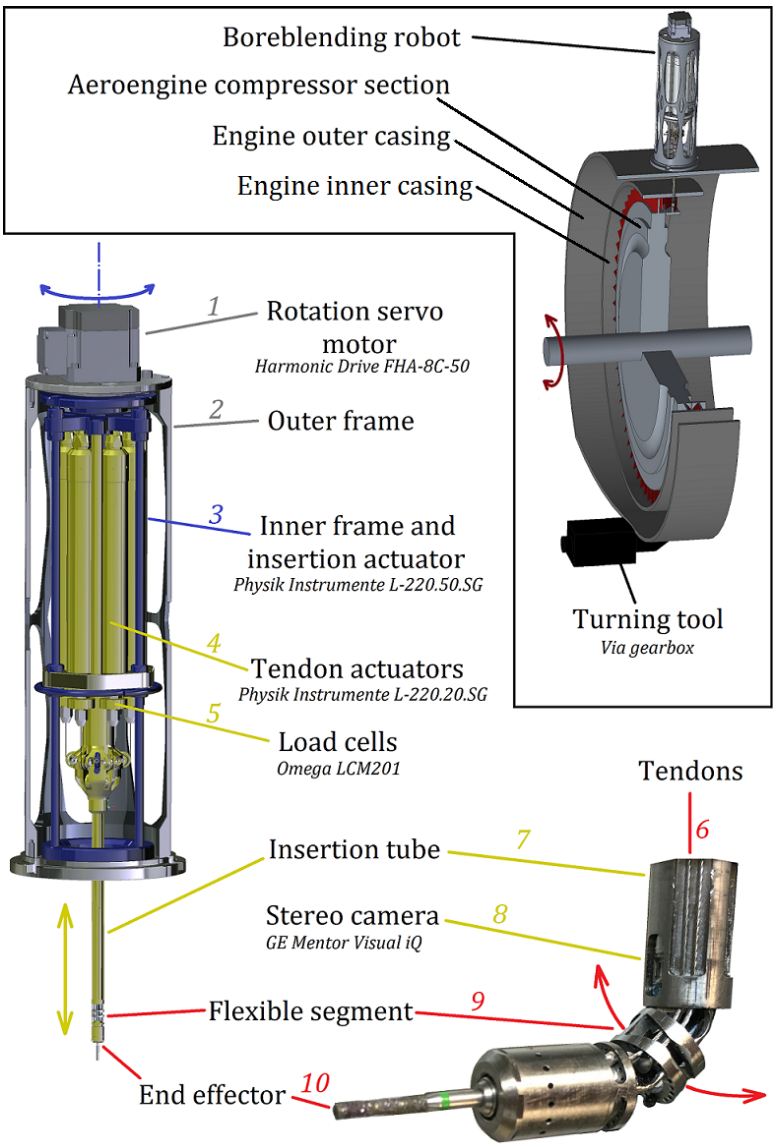


Figure 3.4: Mechanical architecture of boreblending robot including installation overview, electromechanical systems and detail of flexible actuated tip.

the rotation stage and any images or measurements are in the reference frame of the robot. While it is possible for part of the outer enclosure of the air turbine to enter the field of view of the camera, this only occurs at high bend angles and is therefore not practical to be used as a means of visual servoing or position control. In addition to this, the high computational burden of feature recognition would add complication to the low-level control of the device. A camera mounted on the end effector itself would be better suited for such methods, but would invariably require sacrifices in diameter and mobility.

The flexible segments (shown in Figure 3.5) make use of hyper-elastic NiTi backbones that constrain the bend in particular directions, with the added advantage of providing a

central umbilical passage for driving of the rotary tool. Due to the high forces required to achieve a 90 degree bend, the articulation in A_0 was split into two independently controllable flexible joints, each capable of bend angles of 50°. A smaller orthogonal flexible joint was placed between the other two, allowing for 22.5° of bend (in C_0 and/or B_0 depending on inclination) in each direction to achieve perpendicularity at the edge of the blade.

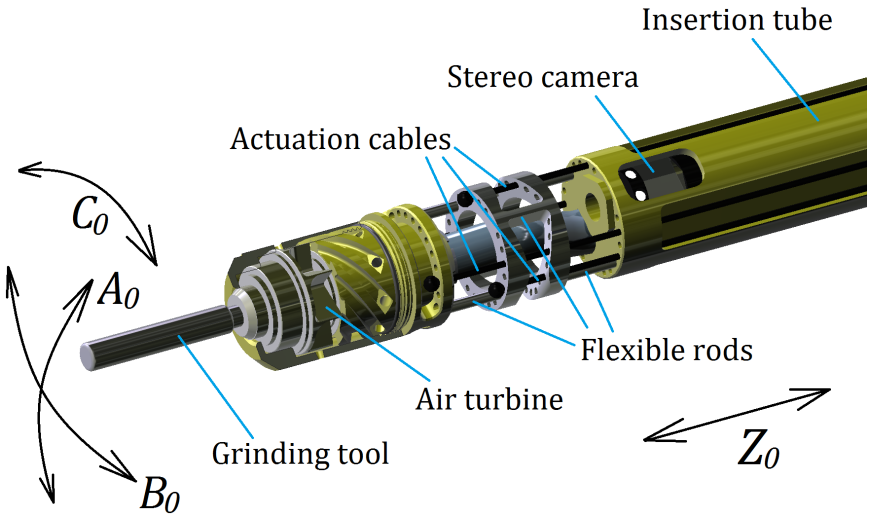


Figure 3.5: Detail of measurement probe, flexible articulation and end effector. The stereo camera is used for measurement of the affected target, but cannot be used to oversee the machining operation due to its position on the insertion tube.

The end effector (10) consists of a miniature air-driven spindle that has been incorporated into the last stage of the flexible segment. This miniature spindle can hold friction grip tools of 1.6 mm shaft diameter (such as a 1.8mm diameter cylindrical electroplated diamond grinding burr, 118 μm grit) and achieve speeds of over 250,000 RPM.

The high speed and low torque nature of miniature air-driven spindles means that the contact forces between the end effector and the target blade never exceed 1.5 N (stall observed at forces around 1.3 N). The low reaction force during grinding means that it is appropriate to use tendon-driven flexible structures, as the tension in the tendons is more than enough to achieve sufficient stiffness and stability.

The robot is controlled using a EMP373 (ACME Portable) ruggedised PC that interfaces with the following modules (Figure 3.6):

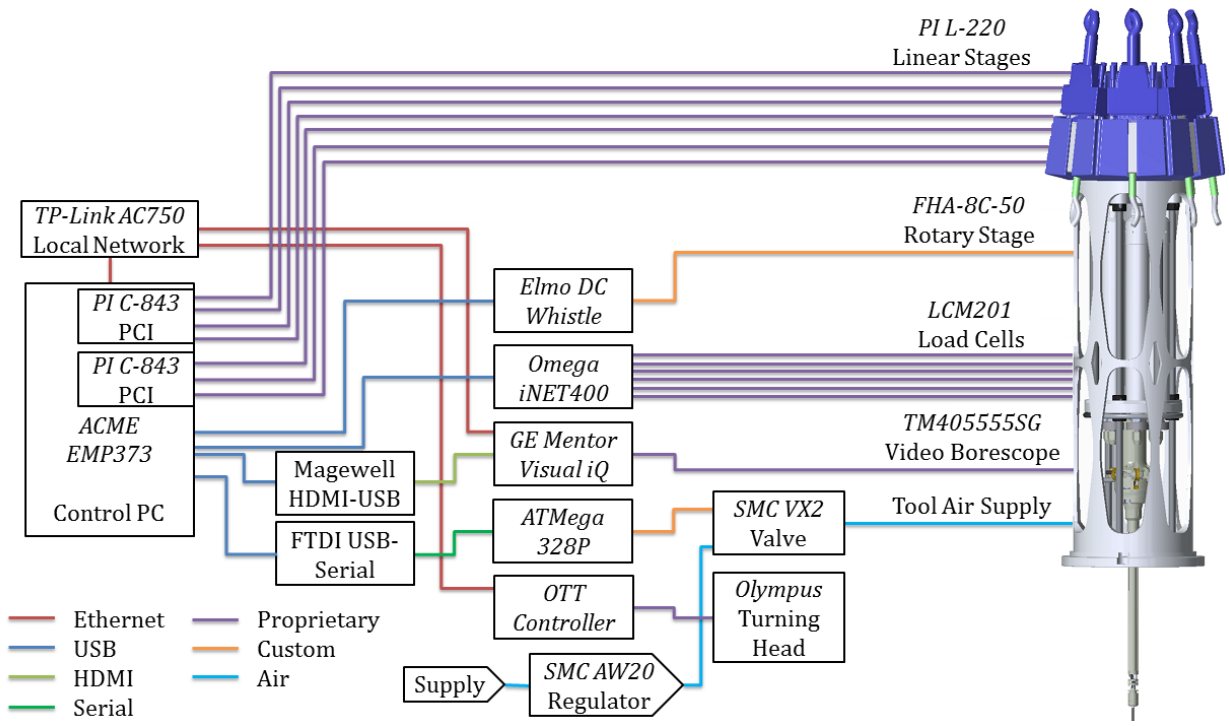


Figure 3.6: Hardware schematic for boreblending robot, including details of the communication methods used throughout.

- A turning tool controller (Olympus) that provides positioning of the compressor blade under repair

- Two C-843 (P.I.) precision linear actuator controllers that drive robot's seven linear actuators

- A Gold DC Whistle (ELMO Motion Control) servo drive controller that drives the robot's C_0 rotation stage

- A microprocessor (Arduino Pro Mini 328) that controls a pneumatic valve that drives the robot's air spindle tool

- A M V-iQ stereo vision measurement system (GE) that uses optical metrology to produce a point cloud of the area of interest

- An iNET-400 data acquisition system (Omega Engineering) that monitors the cable tensions for the flexible joints

3.3.2 Compliant joint buckling study

The flexible segments of the robot were designed to achieve the necessary number of degrees of freedom and to reach the required positions in the compressor. Two main factors, flexibility and buckling, were considered. Flexibility is the maximum bending capability of the flexible segments, which affects the working volume of the end effector. Buckling is the unwanted collapse of the backbone elements, and is one of the major considerations when designing flexible structures [16,155]. In the design, the total flexible joint length (i.e. the sum of the length of each individual joint) is required to be large enough to allow a sufficient bending angle, but the length of each individual joint must not exceed the buckling threshold since the critical buckling load is inversely proportional to the length of the flexible structure. The critical buckling load is the maximum force that can be applied along the axial direction of the flexible structure before it reaches the stability boundary of its shape.

Three key parameters can be changed to adjust the flexibility and buckling: the backbone diameter D_a, the total length $\mathcal{L}$ of the flexible segment and the number of discrete flexible backbone elements n, each of length a. The following design process was developed to determine D_a, $\mathcal{L}$ and n:

First, a maximum bending angle of 100° in the direction of articulation *iii* was defined based on the compressor geometry to cover the whole possible repair area. Super-elastic Nitinol rods were selected for the backbone (based on previous experience with the material [16]), and different diameters ($0.8mm$, $1.0mm$ and $1.2mm$) were considered for the design with a target to keep the strain below 8% (to prevent plastic deformation). To avoid buckling, the flexible joint is divided into multiple shorter segments (Fig. 3.7A). Given that the total tension of the cables is expected to be around $180N$ (based on initial worst-case-scenario calculations), each flexible joint was analysed to be able to withstand no less than $200N$ in the axial direction before buckling. Finally, the length of all the flexible segments are required to be less than $15mm$, due to the geometry constraints of the working environment in the engine.

The critical buckling load F_{cr} can be calculated using the Euler buckling theory:

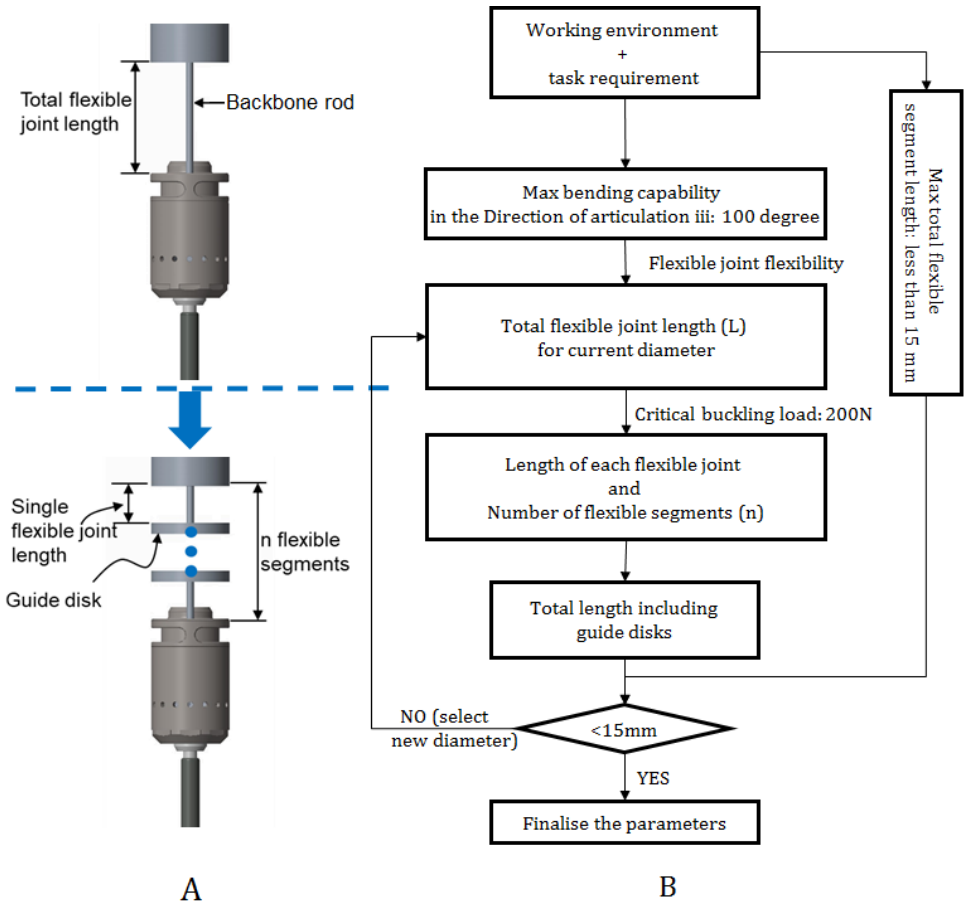


Figure 3.7: Illustration (A) and design process (B) for determining the key parameters of the flexible actuated segments to prevent joints from buckling under compression.

$$F_{cr} = \frac{\pi^2 E\mathcal{I}}{(\mathcal{K}a_f)^2} \tag{3.1}$$

where E is the Young's modulus of the material ($41GPa$ for Nitinol), I is the second moment of area, a_f is the flexible rod length and K is an effective length factor which depends on the conditions of end support of the rod (in continuum segments it is assumed to be $\mathcal{K} = 2$ as a worst-case scenario).

Hence, two flexible segments were employed in the direction of articulation A_0 (each with flexible joint length $4mm$ and joint diameter $0.8mm$) and one segment in the orthogonal direction (flexible joint length $1.2mm$ and joint diameter $0.8mm$) as shown in Fig.3.4. Each of the flex degrees of freedom is actuated by two opposed tendons, which are loaded with as much as 180 N when fully flexed.

3.3.3 Tensile characterisation of driving tendons

The boreblending instrument is controlled using linear actuators with integrated force sensors attached to the robot tendons. The tendons used are $0.45mm$ stainless steel 7 core twisted wire rope with a quoted tensile strength of $55lbs$ ($244N$). A spot weld on the distal end of the cable (Figure 3.8a) acts as an anchor for the cables to be fed through holes in the discs. The cables are then attached to the force sensors using a custom made conical collet (Figure 3.8b). The distance between the spot welds and the collets is 180mm.

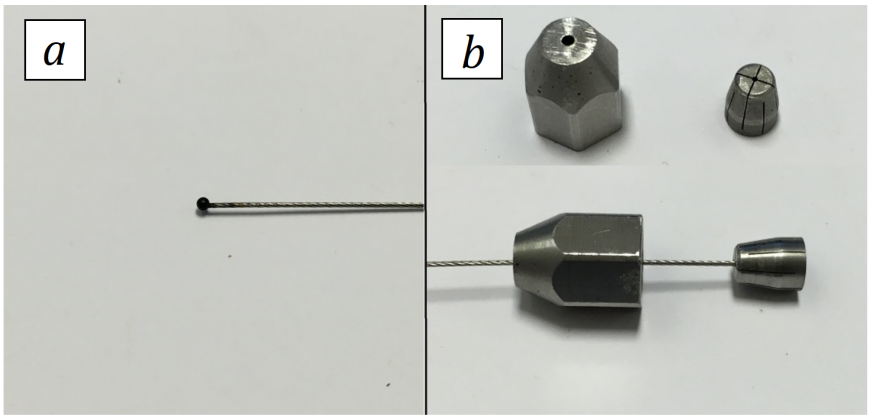


Figure 3.8: Spot weld (a) and collet (b) used to fix tendons to the robot end effector and linear actuator respectively.

To control the position of the end effector with accuracy and precision, it is important to be able to quantify the elongation of the cables. This becomes especially important for distal segments where the cables are longer, as a small elongation of $1mm$ could translate to an error of over 20° in the position of the end effector. The twisted construction of the cables makes it difficult to model accurately the stretch of the cables under load, making experimental tests desirable. It is also important to have an accurate measure of real ultimate tensile load (UTL), especially because the spot welds at the distal end are likely to have a heat-affected-zone (HAZ) which may compromise their strength. Under high loads, it is also possible for the cable to slip out of the collet, compromising the end effector. By measuring the UTL of a number of cables it is possible to give the robot a safe working envelope to prevent tendons from snapping or collets from slipping.

Tests were set up to determine whether:

- The cables are linearly elastic and have consistent elasticity.
- If the cable is loaded axially, there will be a measurable elongation due to the twisted structure.
- If there is a HAZ near the spot weld, there will be a drop in UTL from the manufacturers' specifications.
- If the collet has inadequate grip, the cable will slip before breaking.

A rig was designed to hold the cable with a 0.6mm hole on one fixture (weld side) and a collet on the other (Figure 3.9a) $180mm$ apart. The cable was mounted to a vertical tensile testing machine with a video gauge (IMETRUM) for measuring elongation. The video gauge uses a high resolution camera to track a black and white pattern painted on the aluminium plates as shown in Figure 3.9b. Using a video gauge ensures that any slip between the fixture and the test machine is not recorded as cable strain in the results. However, slip occurring between the collet and the fixture or between the collet and the cable is recorded as elongation, as this is representative of the real system.

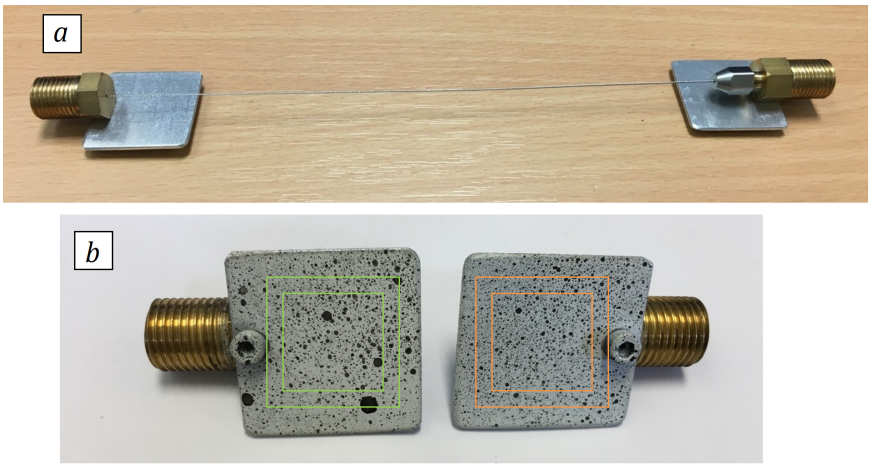


Figure 3.9: Fixtures for tensile tests of twisted cables (a) and black and white pattern for video gauge calibration and measurement (b).

Two cable diameters and constructions were tested. The first is the cable used in the current prototype, the second is a candidate tendon for a future design:

1. 0.45mm 7-core Stainless steel, 244 N UTL

2. 0.39mm 3-core Stainless steel, 178 N UTL

Five samples of each diameter were tested, for a total of 10 observations.

Cable tension (from instrument load cells) and cable elongation (from the video gauge) were recorded at increments of 0.1 seconds during the trials.

The cable was tensioned at a rate of 1mm/min. The collet was tightened using a torque wrench to 1.5 Nm on all samples. The threaded brass fixtures were screwed into the test machine to the same depth, but without tightening so as to make it possible to orient the target plates towards the camera. The spot welds were produced by a single technician using the same tool settings as the ones mounted on the boreblending robot.

Figure 3.10 show the stress-elongation curve of the 10 trials. With the exception of trial 7, every cable tested failed at the weld, confirming the presence of a heat affected zone (HAZ). The mode of failure of the cables is brittle, as can be seen by the sudden transition between the elastic region and the fracture, with minimal plateau. The step failures observed in trials 1 and 3 were attributed to asynchronous fracture of the wires in the 7-core cable, where 2 of the wires broke at different points and hence presumably at different times.

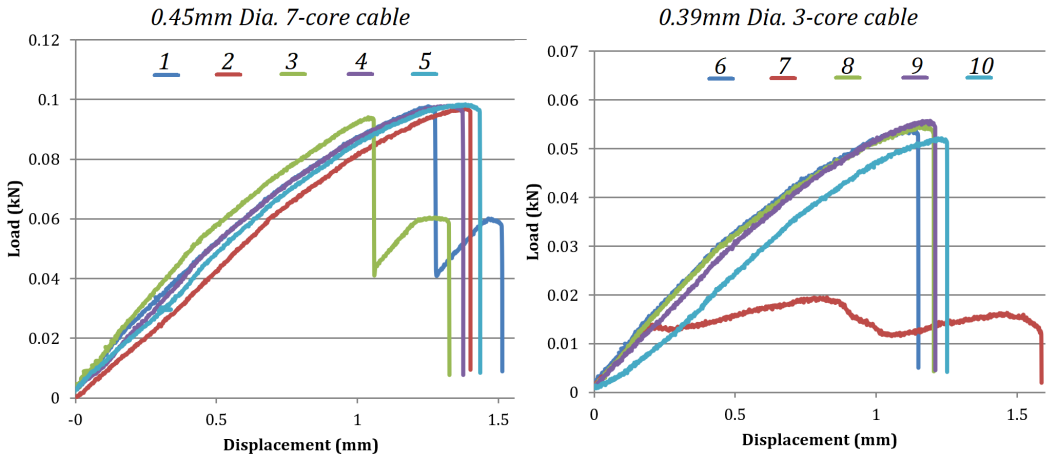


Figure 3.10: Tensile test results for representative tendons. Plots show ten destructive trials of two types of twisted stainless steel cables. Results show consistent ultimate tensile strength for like tendons and only one collet slip (trial 7).

During trial 7 the cable slipped from the collet. While it is difficult to verify the exact cause, it is likely to be a result of human error when inserting the cable into the mouth of the collet. Inserting it at a slight angle or with a slight twist could have led to the

strands untwisting and the cable becoming loose. Whatever the cause, the resulting drop in failure load shows a vulnerability of the collet system that will inform future designs and assembly strategies.

The elasticity of the samples in N/mm can be obtained by calculating the slope of the linear region of the plot of each sample. In the case of trials 1 to 5 the elastic region was observed to be from the start of the test to the point where it crossed 0.08kN. In trials 6 to 10 the limit is 0.045kN (in trial 7 the linear region ends before the slip at 0.013kN).

Table 3.1 shows a summary of the UTL and elasticity of the samples studied (where applicable).

Table 3.1: Summary of tensile test results for 0.45 and 0.39mm diameter twisted cables

Trial	**Cable Spec.**	**Ultimate tensile load (N)**	**Elasticity (N/mm)**
1	0.45 x 7	97.77	88.29
2	0.45 x 7	97.04	81.55
3	0.45 x 7	94.13	97.12
4	0.45 x 7	97.92	88.29
5	0.45 x 7	98.44	84.90
Mean	0.45 x 7	97.06	88.03
Std. Dev.		1.53	5.19
1	0.39 x 3	54.04	55.36
2	0.39 x 3	N/A	66.66
3	0.39 x 3	54.74	55.37
4	0.39 x 3	55.75	54.74
5	0.39 x 3	52.13	50.16
Mean	0.45 x 7	54.16	56.46
Std. Dev.		1.32	5.46

The ultimate tensile load of the 9 trials that failed at the weld varied only slightly between samples of the same diameter, with standard deviations of under 2N for both diameters. This suggests that the welds had a uniform effect on all the samples and the manufacturing method has high repeatability.

All the samples that fractured failed due to a HAZ that changes the metallic structure

resulting in embrittlement. On average, the $0.45mm$ diameter cables had a 60.2% drop in UTL from the quoted value due to the heat effect of the welds. The $0.39mm$ diameter cables had a 69.6% drop in maximum tensile strength.

Table 3.1 shows only a small variance in the elasticity of similar cables. This allows for more accurate navigation control of the robot end effector by predicting the stretch caused by the tension on the cables. In light of this, a tension compensation algorithm was added to the robot's controller taking into account the static forces exerted by the compliant joints and the reaction forces of the opposing driving tendons. The load cells on the tendon linear stages were not used to control the tension in closed loop or to calculate the elongation compensation, as the feed-forward loop resulted in instability without suitable simultaneous motion/force control schemes. Instead, the load cells were used to monitor tension to prevent the cables from being overloaded and breaking.

3.4 Robot kinematics

The kinematics is divided into forward and inverse kinematics: the former adapts the Denavit-Hartenberg (D-H) convention mechanism to find the angular and displacement values, and the latter uses the pseudo-inverse Jacobian functions method to find the optimal solutions for the rigid and flexible (non-linear) joints values to reach the end-effector target with sufficient accuracy.

3.4.1 Forward Kinematics

It is assumed that the backbone bends into a circular arc when loaded. Finite element analysis (FEA) of the non-linear hyper-elastic backbone rods suggests that in reality the backbone assumes a tighter bend closer to the ends than in the middle but, due to the dimensions of the components, the assumption only results in an error of 0.16° or 56 μm at the end effector which is within the acceptable tolerance of the cut shape. Like in [17], each backbone is described as two revolving joints in the D-H matrix, linked by a rod of varying length. It can be shown that the straight-line distance d between the two ends of

an arc of length a (a curved backbone) at flex angle θ is given by:

$$d = \sqrt{\frac{2a^2\left(1-\cos\left(\theta\right)\right)}{\theta^2}} \tag{3.2}$$

with the special case of $d = a$ when $\theta = 0$. The two revolving joints either side of each flexible rod share the angle θ as shown in Figure 3.11. The D-H parameters of the robot are listed in Table 3.2.

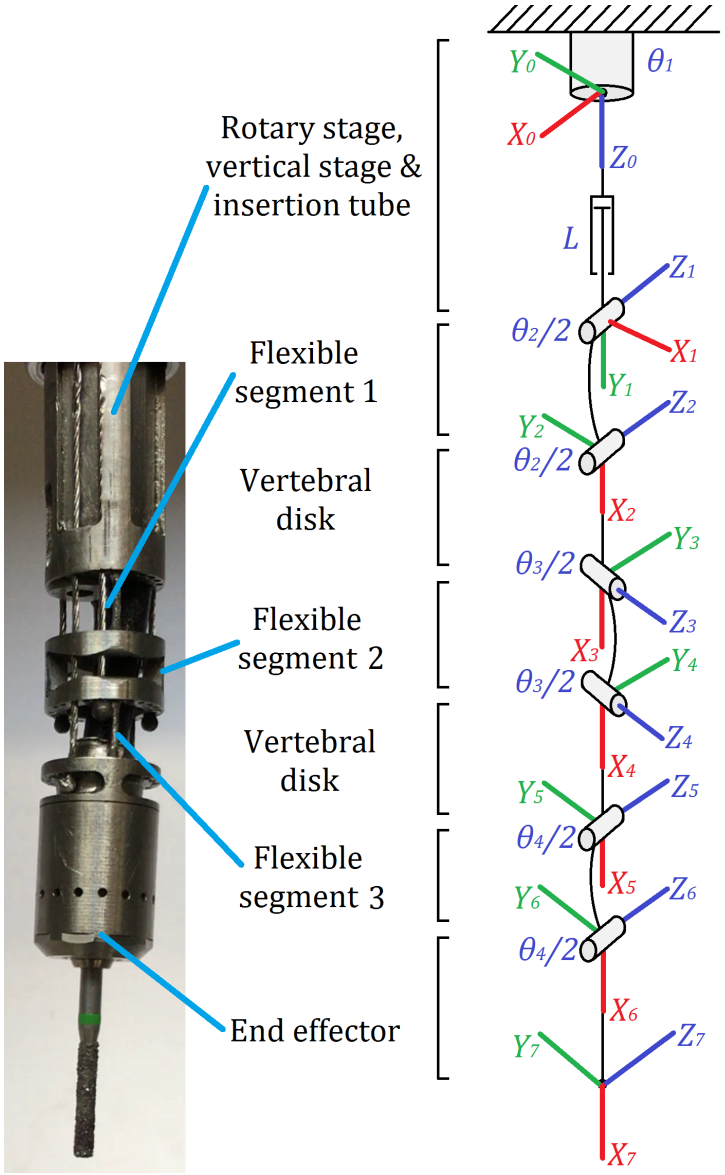


Figure 3.11: Denavit-Hartenberg convention diagram for remote boreblending robot. Continuum degrees of freedom are modelled as two revolving joints either side of a link with variable length.

where $a_1 \ldots a_7$ are the lengths of the respective sections and $\mathfrak{L}$ is the travel of the

Table 3.2: Hybrid robot Denavit-Hartenberg convention parameters.

Joint	$\boldsymbol{\theta}$	$\boldsymbol{\alpha}$ (°)	$\boldsymbol{d}$	$\boldsymbol{r}$
1	θ_1	90	$a_1 + \mathfrak{L}$	0
2	$\frac{\theta_2}{2}$	0	0	$\sqrt{\frac{2a_2^2(1-\cos(\theta_2))}{\theta_2^2}}$
3	$\frac{\theta_2}{2}$	90	0	a_3
4	$\frac{\theta_3}{2}$	0	0	$\sqrt{\frac{2a_4^2(1-\cos(\theta_3))}{\theta_3^2}}$
5	$\frac{\theta_3}{2}$	-90	0	a_5
6	$\frac{\theta_4}{2}$	0	0	$\sqrt{\frac{2a_6^2(1-\cos(\theta_4))}{\theta_4^2}}$
7	$\frac{\theta_4}{2}$	0	0	a_7

insertion linear actuator along Z_0. The robot's forward transformation matrix T can be calculated using

$$T = {}^0T_1 \times {}^1T_2 \times {}^2T_3 \times {}^3T_4 \times {}^4T_5 \times {}^5T_6 \times {}^6T_7 \tag{3.3}$$

where, using $c\theta$ and $s\theta$ to signify $\cos(\theta)$ and $\sin(\theta)$,

$${}^0T_1 = \begin{bmatrix} c\theta_1 & 0 & s\theta_1 & 0 \\ s\theta_1 & 0 & -c\theta_1 & 0 \\ 0 & 1 & 0 & a1 + \mathfrak{L} \\ 0 & 0 & 0 & 1 \end{bmatrix} \tag{3.4}$$

$${}^1T_2 = \begin{bmatrix} c\frac{\theta_2}{2} & -s\frac{\theta_2}{2} & 0 & c\frac{\theta_2}{2}\sqrt{\frac{2a_2^2(1-c\theta_2)}{\theta_2^2}} \\ s\frac{\theta_2}{2} & c\frac{\theta_2}{2} & 0 & s\frac{\theta_2}{2}\sqrt{\frac{2a_2^2(1-c\theta_2)}{\theta_2^2}} \\ 0 & 0 & 1 & 0 \\ 0 & 0 & 0 & 1 \end{bmatrix} \tag{3.5}$$

$$\vdots$$

$${}^6T_7 = \begin{bmatrix} c\frac{\theta_4}{2} & -s\frac{\theta_4}{2} & 0 & c\frac{\theta_4}{2}a_7 \\ s\frac{\theta_4}{2} & c\frac{\theta_4}{2} & 0 & s\frac{\theta_4}{2}a_7 \\ 0 & 0 & 1 & 0 \\ 0 & 0 & 0 & 1 \end{bmatrix} \tag{3.6}$$

The cable displacement calculations assume a straight line between guide hole centres in the bent configuration.

3.4.2 Inverse Kinematics

The inverse kinematics uses the Jacobian pseudo-inverse method [156] to find the optimal solution for each joint in multiple iterations. The presence of three consecutive continuum joints makes it impossible to arrive at an analytical inverse kinematics solution, as redundant solutions are guaranteed for a large portion of the working volume. While it may be possible to use a simplified analytical solution to reduce the computational load of the calculation, it was found that the relatively small Jacobian for the present construction (7×3) was fast enough to process as to make the gains negligible. However, for efficiency, an initial guess is made based on the general direction of the desired position. An average of 25 iterations is expected to arrive at an appropriate solution with error $\mathcal{E} < 0.1\mu m$ (smaller than the effective resolution of the actuators), and therefore a limit is set at 100 attempts before the desired position is deemed out of reach.

It is assumed that the intermediate flexible joint angle (for perpendicularity) is defined based on the geometry at the start of the process and remains constant for a given machining operation. The iterative procedure (illustrated in Figure 3.12) is as follows:

1. The initial iteration counter is defined as $j = 0$

2. The robot's degrees of freedom are annotated as $\mathfrak{q} = [\mathfrak{q}_1, \mathfrak{q}_2, \ldots, \mathfrak{q}_n]^\top$, where n is the total number of DoF

3. To avoid local minima there are four initial guesses defined as $\mathfrak{q}^{(0)} \rightarrow \{{}_1\mathfrak{q}^{(0)}, {}_2\mathfrak{q}^{(0)}, {}_3\mathfrak{q}^{(0)}, {}_4\mathfrak{q}^{(0)}\}$. These initial guesses were defined based on the

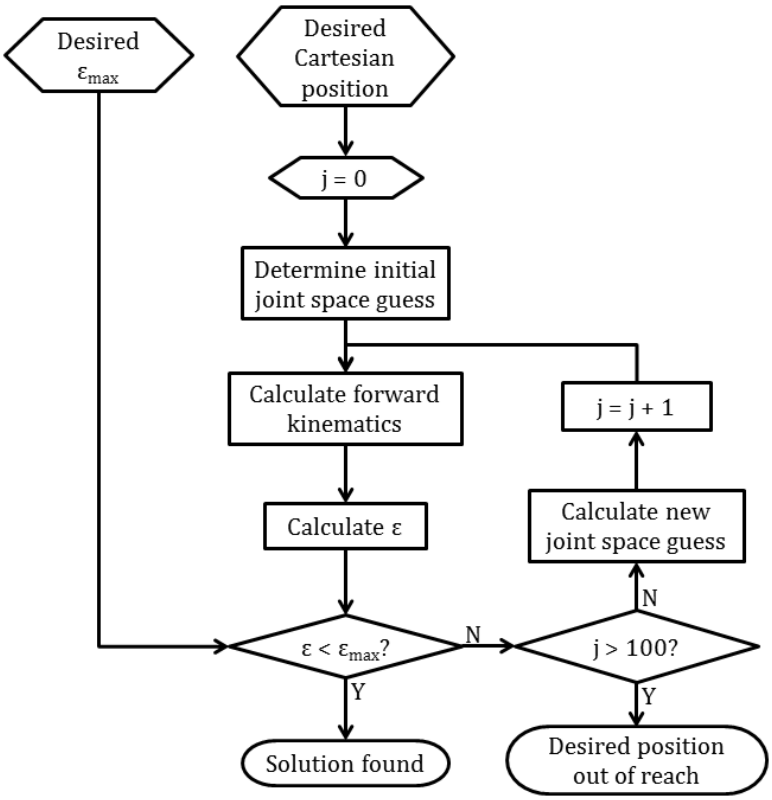


Figure 3.12: Inverse kinematics calculation flowchart using iterative Jacobian pseudo-inverse method.

geometry and reach of the robot:

$$\begin{cases} \theta_2 = 45, & \theta_4 = 45 & \text{if } y \geq 20 \\ \theta_2 = 22.5, & \theta_4 = 22.5 & \text{if } 0 \leq y < 20 \\ \theta_2 = -22.5, & \theta_4 = -22.5 & \text{if } -20 < y < 0 \\ \theta_2 = -45, & \theta_4 = -45 & \text{if } y \leq -20 \end{cases} \tag{3.7}$$

4. To calculate $\mathfrak{q}^{(j+1)}$, the remainder can be found using:

$$\delta\mathfrak{w}\left(\mathfrak{q}^{(j)}\right) = J\left(\mathfrak{q}^{(j)}\right)\delta\mathfrak{q}^{(j)} = \mathfrak{w}\left(\mathfrak{q}^{(0)}\right) - \mathfrak{w}\left(\mathfrak{q}^{(j)}\right) \tag{3.8}$$

and $\mathfrak{w}$, the configuration vector, can be defined as:

$$\mathfrak{w}\left(\mathfrak{q}^{(j)}\right) = \left[\frac{\mathfrak{p}_i}{\mathfrak{a}_i * e^{\frac{\mathfrak{q}_n}{\pi}}}\right] \tag{3.9}$$

where $\mathfrak{p}_i = [T(1,4), T(2,4), T(3,4)]^\top$ (from 3.3) and $\mathfrak{a}_i = [T(1,3), T(2,2), T(3,2)]^\top$ [156]

5. The initial 4x6 Jacobian matrix used to calculate the joint values can be derived by differentiating $\mathfrak{w}\left(\mathfrak{q}^{(j)}\right)$, hence:

$$J\left(\mathfrak{q}^{(j)}\right) = \frac{\delta \mathfrak{w}\left(\mathfrak{q}^{(j)}\right)}{\delta \mathfrak{q}^{(j)}} \tag{3.10}$$

Solving $J\left(\mathfrak{q}^{(j)}\right)$ is a matter of using the pseudo-inverse method to calculate $J^{+}\left(\mathfrak{q}^{(j)}\right)$

6. $\mathfrak{q}^{(j+1)}$ is then calculated using:

$$\mathfrak{q}^{(j+1)} = \mathfrak{q}^{(j)} + J^{+}\left(\mathfrak{q}^{(j)}\right) \delta \mathfrak{w}\left(\mathfrak{q}^{(j)}\right) \tag{3.11}$$

7. The last step to find a suitable solution is to set a tolerance value ϵ close to zero and to check whether the new joint coordinate values are within ϵ of the target:

$$\begin{cases} \text{Solution is found} & \text{if } \mathfrak{q}^{(j+1)} - \mathfrak{q}^{(j)} < \mathcal{E} \\ j = j+1, \text{ repeat from 4)} & \text{otherwise} \end{cases} \tag{3.12}$$

The kinematic model was validated using an optical motion capture system (Vicon Motion Systems Ltd) to track the 3D motion of the robot's end effector. The system consists of four high-resolution Vantage 16 cameras and five retro-reflective passive markers positioned on a surface attached to the end effector of the robot (Figure 3.13).

The robot was commanded to follow a pre-defined arc with the end effector on the $Y_0 - Z_0$ plane such that, at any point, the unique solution has the distal and proximal flexible segments bent equally. Discrete measurements were taken at 5 degree intervals. The results (Figure 3.13) show high correlation between the expected angular motion of the robot's individual joints and the actual movement with an average standard deviation of 0.94° or 0.26 mm at the tip of the air spindle housing. The maximum error occurs at full deflection and has a magnitude of $0.82mm$ to $0.85mm$, equivalent to 8.5% of the

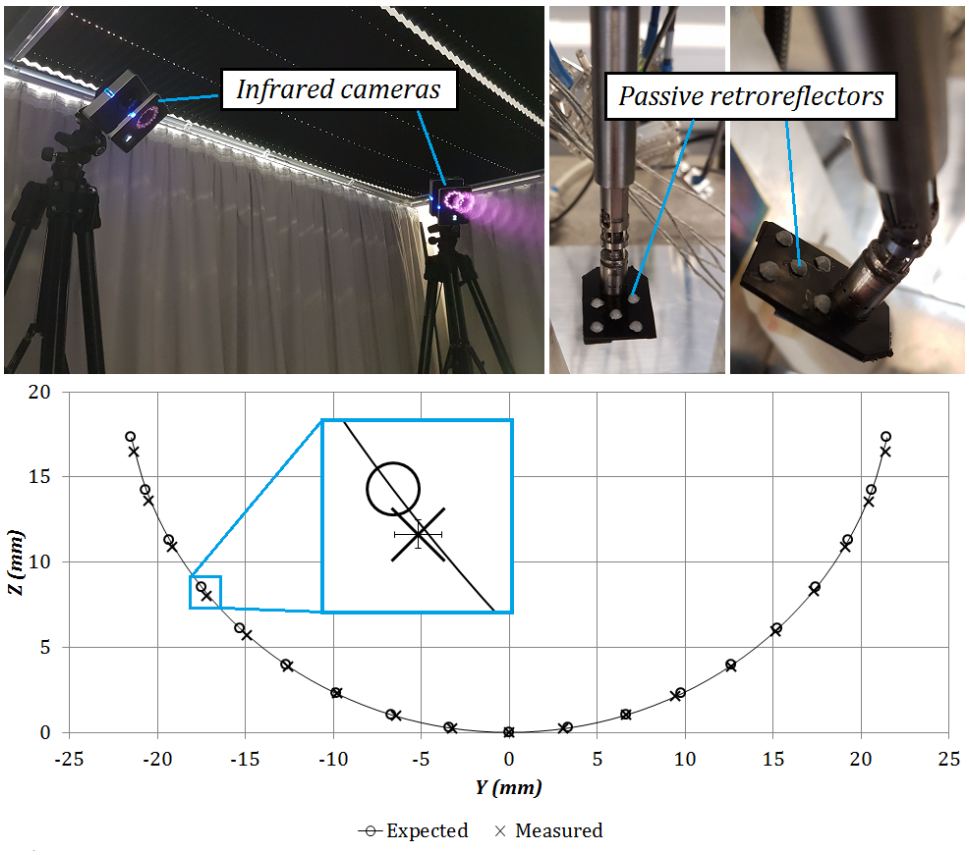


Figure 3.13: Kinematics validation experiment setup (top) and position results (bottom) using optical motion capture system. Error bars visible in expanded view show typical standard deviation.

continuum length. It is assumed that the errors in position were caused by insufficient or asymmetric pre-tension on the tendons, as well as small errors in compensating for the elasticity of the cables under load as discussed in previous sections. Despite these errors, the results confirm the validity of the kinematic model.

3.5 In-situ boreblending robot software

3.5.1 Remote Control System Architecture

The proposed overall system architecture (overseen by Dr Bilal Nasser with assistance from the present author in the areas of motion control and pneumatic system operation) consists of a high-level controller (HLC) with a versatile user interface, a secure network communication protocol, and a self-sufficient and fail-safe low-level controller (LLC) for commanding the robot's mechatronics.

The network communication is managed using a dedicated protocol developed in this work, named compact-RUDP (reliable user datagram protocol). This combines data and live video transfer across the global network and ensures that data transfer is reliable, secure and with priority given to the data control packets. It uses the real-time transport protocol (RTP) to establish the data communication on the web and the session initiation (SIP)/ user datagram protocol (UDP) for registering and identifying the transmitter and receiver transport. An application called OnSight Connect (developed by Librestream [157]) is used to manage the data communication and video/picture streaming at both ends.

Depending on the distance and internet service quality, round trip delays in network communications are often greater than $50ms$ [158] and can, in extreme cases, exceed $350ms$ [159]. While delays of $50ms$ may seem appropriately small when compared to human reaction times, the cumulative nature of the latency means that during a chain of commands, the effective round trip delay between operator action and feedback may exceed the practical limits of remote control. For example, the mean round trip time for two computers running OnSight Connect, one connected to a fibre optic broadband provider (UK-based) and the other connected to the 3G mobile network (UK-based), was measured to be $74ms$ (standard deviation of $9ms$), but after the necessary sequences of automated interactions (e.g. handshakes, DNS look-ups), the effective time between operator action and feedback was measured to be $968ms$ (standard deviation of $57ms$). Thus it is reasonable to expect that this would increase significantly across greater distances on a global scale. Hence, "direct" remote control where the operator commands the position of the various degrees of freedom of the robot and closes the control loop is not a viable option with the current setup.

Thus the proposed solution is to use a HLC to define a machining path using operator inputs, and to send a list of end effector position commands to a LLC for execution, with the ability to request interruptions and further measurements. The LLC interprets the task-space position commands and calculates the required actuator positions using the inverse kinematics of the robotic system. Awareness of the status of the robot, the state

of the sensors and the network connection allows the LLC to autonomously send the HLC error notifications, status updates and, in the case of loss of signal, retreat the robot into a safe position and await further instructions. By separating the path generation tasks from the low-level control signals, the latency can be arbitrarily high without impairing the performance of the robot.



Figure 3.14: Skilled technician remotely operating boreblending robot from high-level control computer.

The proposed HLC is a Seahawk 100 ruggedised computer (ACME Portable) (Fig. 3.14) in a remote location from the site of the repair and connected to the internet. The purpose of the HLC is to serve as a high-level user interface for the expert operator. Hence, all the information that would be available to the operator if they were carrying out the repair in person must be represented in this interface. A number of windows across a few monitors are used to display information relating to the in-situ repair performed by the robot according to the stage in the work flow. For the boreblending application (Fig. 3.15), these include:

- Live video stream from external cameras mounted at the site of the repair. This stream allows the operator to oversee installation of the robotic instrument on the engine inspection port and see the repair environment.

- Live video stream from robot's on-board cameras (B). Once the robot is installed, this stream is used to oversee the tip navigation and aid in positioning the rotor correctly to acquire measurements of the affected area.

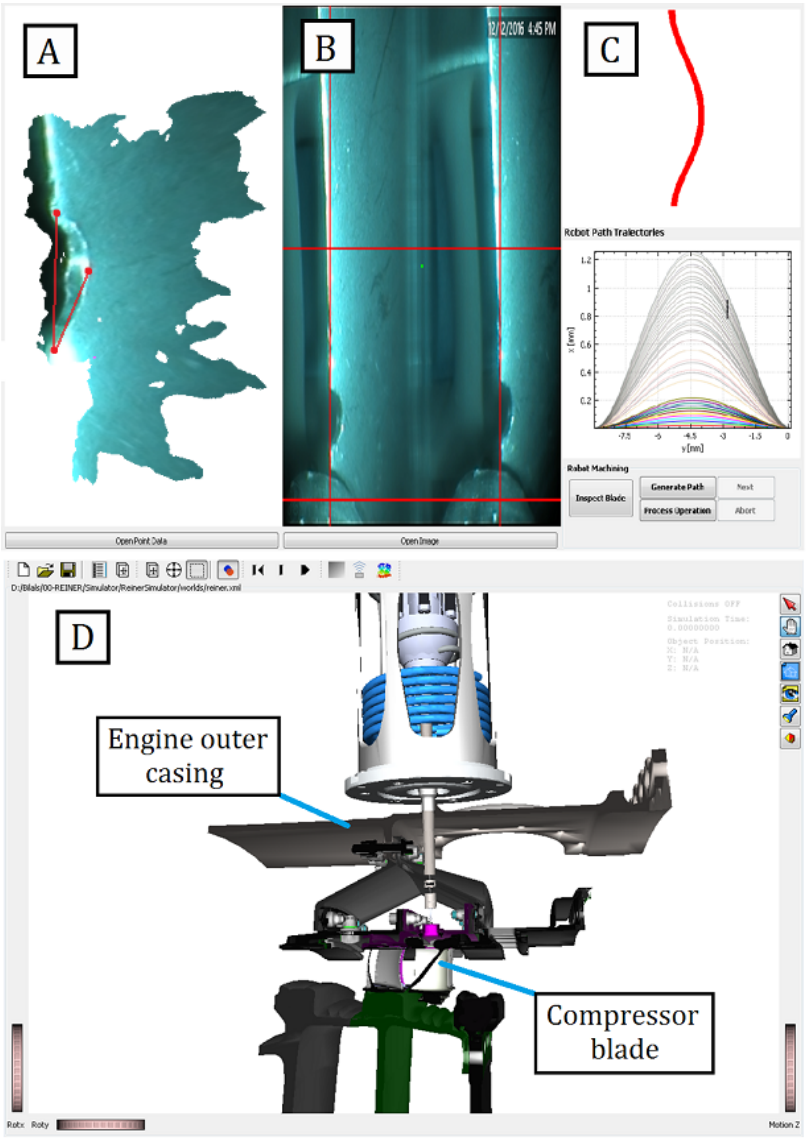


Figure 3.15: User interface for boreblending robot, including A) point cloud map of affected area, B) video stream from on-board stereo camera, C) machining path generation console and D) real-time simulator.

- Console for commanding the robot to move to inspection, measurement and repair positions. A similar interface can be used to remotely control the engine turning tool and move the rotor until the target blade is in the desired position.

- 3D point cloud display of the affected area (A). This console allows the operator to view and re-orient the object, select key measurements and obtain information about the size and shape of the defect. This display is also used to select the points marking the bounds of the defect used to generate the machining path – in the Fig. 3.15 example, the two points where the defect meets the blade edge and the

deepest part of the defect (red dots on A).

- Console for machining path generation (C). This allows the operator to define the geometry (e.g. aspect ratio, size and shape) of the stress relief feature depending on the level of damage on the blade.

- Console for inquiring on the status of the robot's subsystems, network connection and actuators. This allows the operator to verify that all motors and sensors are working correctly before starting the repair task.

- Live simulation of the robot and the repair site environment (D). A rendered 3D model of the environment and the robot's live position gives the operator an internal view that would otherwise be impossible, allowing them to safely navigate the robot.

- Display of the current machining operation. This console shows the progress and current status of the machining task and allows the operator to interrupt the blend and take new measurements to verify the robot is performing adequately and the rotor blade has not moved away from the grinding tool.

- Live sound from repair site. The operator can communicate with on-site ground crew and hear the grinding tool as it removes material, allowing them to sense changes in machining parameters, tool wear and stalling. Microphones can be mounted on the actuation pack and worn by the technical staff.

The software running on the HLC (Fig. 3.16) interprets the operator instructions and converts them into data packets containing information about the size, shape and position of the tool path, as well as machining parameters such as depth of cut and surface finish requirements. The data packets are then sent to the LLC to process the operation.

The proposed LLC is a portable computer with internet access located at the site of the repair and connected to the boreblending robot and other hardware required for the repair operation. The LLC has a minimalistic user interface with a console for inquiring about the status of the robot's subsystems, network connection and actuators similar to the one on the HLC. The LLC interfaces with the following hardware modules:

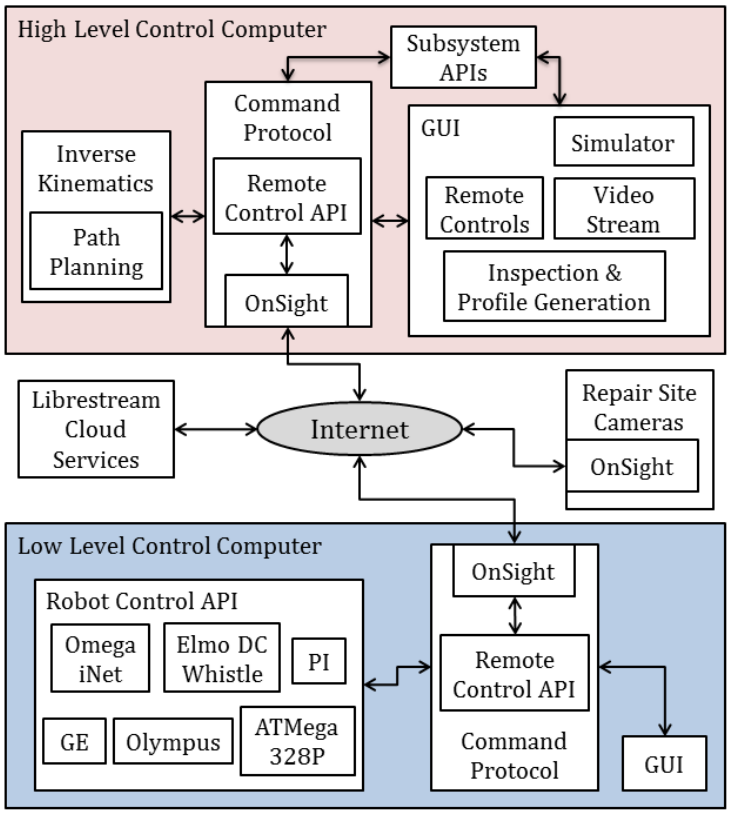


Figure 3.16: System software architecture diagram showing two separate, network-connected computers for high-level control and low-level control.

- A turning tool controller (Olympus) that provides positioning of the compressor rotor
- Two C-843 (P.I.) precision linear actuator controllers that drive the robot's tendon stages and insertion actuator
- A Gold DC Whistle (ELMO Motion Control) servo drive controller that drives the robot's rotation stage
- A M V-iQ stereo vision measurement system (Waygate Technologies) that uses optical metrology to produce a point cloud of the area of interest
- An iNET-400 data acquisition system (Omega Engineering) that monitors the cable tensions for the flexible joints
- A micro controller (Arduino Pro Mini 328) that operates a pneumatic valve to supply the air-spindle-driven grinding tool

- An external camera for visualisation of the repair environment

The software running on the LLC (Fig. 3.16) receives the size, shape, position and depth of cut parameters from the HLC and calculates the necessary actuator positions using the Jacobian pseudo-inverse method [156] for inverse kinematics. The trajectory is offset by the tool diameter (similar to the calculation of g-code) and discretised to a list of positions with increments of length $10\mu m$. The inverse kinematics calculations return a joint-space configuration that can be converted into tendon actuator displacement using a modified version of (3.2). The LLC can navigate the robot to the correct inspection, measurement and machining positions using stored safe-approach trajectories based on the environment geometry.

The LLC is intended to be self-diagnosing and self-protecting. Information from the load cells on tendon stages is used to detect unplanned collisions with the environment (abnormally large loads) or tendon failures (abnormally low loads) and report these back to the operator via the HLC computer. Should a collision occur, the LLC commands the actuators to retreat to the previous safe position and informs the operator. Should an unexpected tendon failure occur, the LLC commands the other tendons and stages to return to a known safe position (assuming the damaged stage is at angle $0°$) to prevent a chain reaction failure. Communication failure with sensors, valves or actuators is informed to the HLC and addressed on a case by case basis. Finally in the event of a network failure, the LLC saves the last position and action in memory and retreats to a position that is safe to allow withdrawal of the robot from the engine; if connection is restored the operator can choose to continue the blend.

3.5.2 Proposed System Workflow

The remote boreblending process (Fig. 3.17) starts by initializing the communication between the HLC and LLC using the Onsight Connect application. Using voice communication and site cameras, the operator instructs technical staff on site to mount the robot to the appropriate inspection port and attach the engine turning tool to the gearbox. It should be noted that features such as the spacing and angle of bolts that

attach the robot to the engine (the bolts used to plug the borescope access port during flight) are unique for specific ports. Concentric locating features on the robot ensure alignment with the port. It is therefore impossible to accidentally attach the instrument to the incorrect port or in the wrong direction.

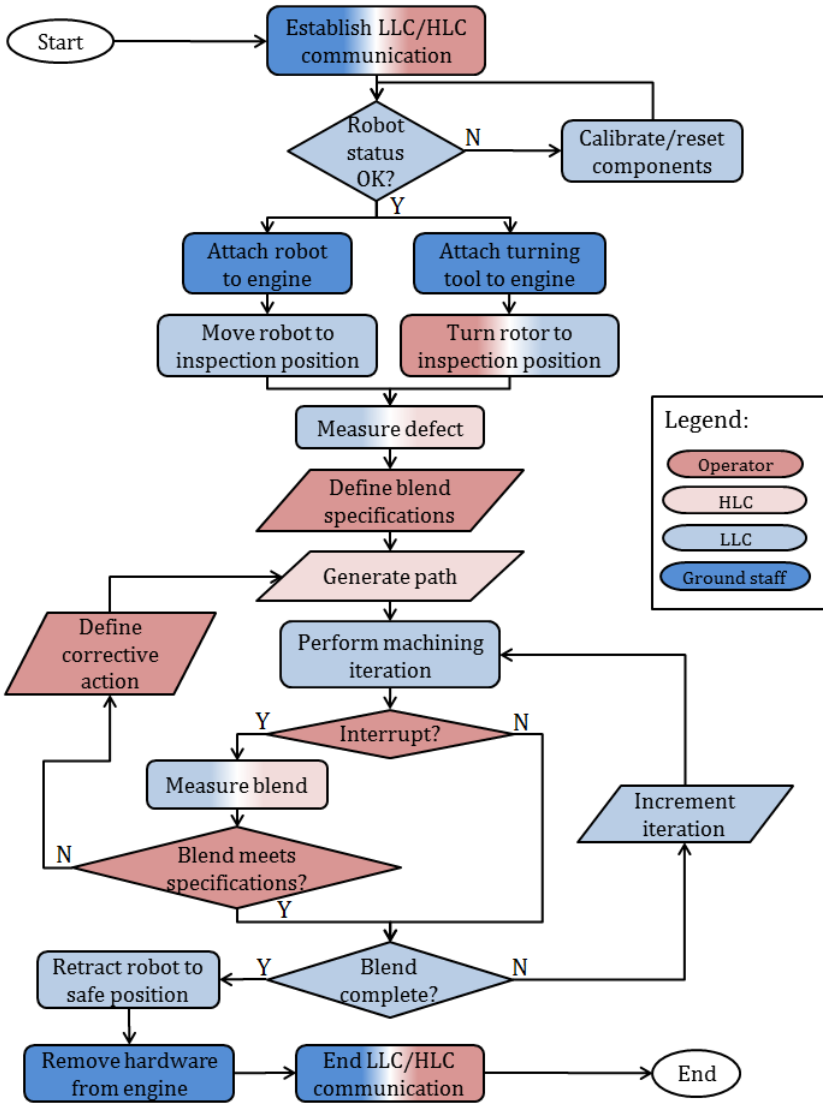


Figure 3.17: Proposed remote control workflow for routine robotic boreblending operation from establishing network connection to completing a machining operation.

Once the robot is attached, the operator can instruct it to move to an inspection position (with the on-board camera within the gas stream) and use the turning tool console to move the engine shaft until the defective blade is in the correct position in the field of view. The stereo vision measurement system is then commanded to take a measurement of the defect and generate a point cloud, which is used by the operator to

define the shape, size and position of the cut.

The robot is then sent the machining data and instructions over the internet to start removing material in small increments. The operator oversees the process in real time (with some latency) using the simulator screen on the HLC to reproduce the movement of the robot, and listens to the grinding tool with the audio stream. Any problems with the robot's tendons or hardware connections are independently handled and reported to the HLC. After some initial time, the operator can pause the operation and instruct the robot to take another measurement, ensuring no tool problems or unexpected misalignment have occurred. Misalignment can be a result of environmental factors such as wind and temperature changes moving the rotors and blades, or it could be caused to a smaller extent by the contact and vibration of the grinding tool. Misalignment can be identified by overlaying consecutive images from the on-board cameras. If a problem is identified, the operator can make corrections to the desired path based on the new point cloud and send new instructions to the LLC. If, based on experience, the operator identifies issues with surface quality or tool wear, the depth of cut can be modified for each pass to cut more or less aggressively.

Once the blending operation is complete, the robot automatically moves to the inspection position to measure the repair for approval. If satisfied, the operator orders the robot to retract from the compressor and communicates with ground staff to remove it from the engine.

3.6 Robotic boreblending demonstration

The robotic boreblending system was demonstrated first using a representative test rig in a lab environment and then on an appropriate gas turbine compressor.

3.6.1 Laboratory demonstration of machining capabilities

To study the repeatability of the system, eleven compressor blades were intentionally damaged on the leading edge with similar defects (1.5 mm wide, 800μm deep) on a mock-

up compressor stage (Figure 3.18). The robot was inserted into the borescope port and the defects were scanned using the embedded stereo measurement camera to identify the target area from the point cloud. Key elements of each point cloud were selected in the HLC user interface to generate a machining path with a pre-defined aspect ratio and shape. The start point of the machining path was defined based on the height of the measurement camera above the tool bending plane. To prevent the air turbine tool from stalling upon contacting the blade, the machining operation was broken up into thirty passes with a maximum depth of cut of $30.7\mu m$.

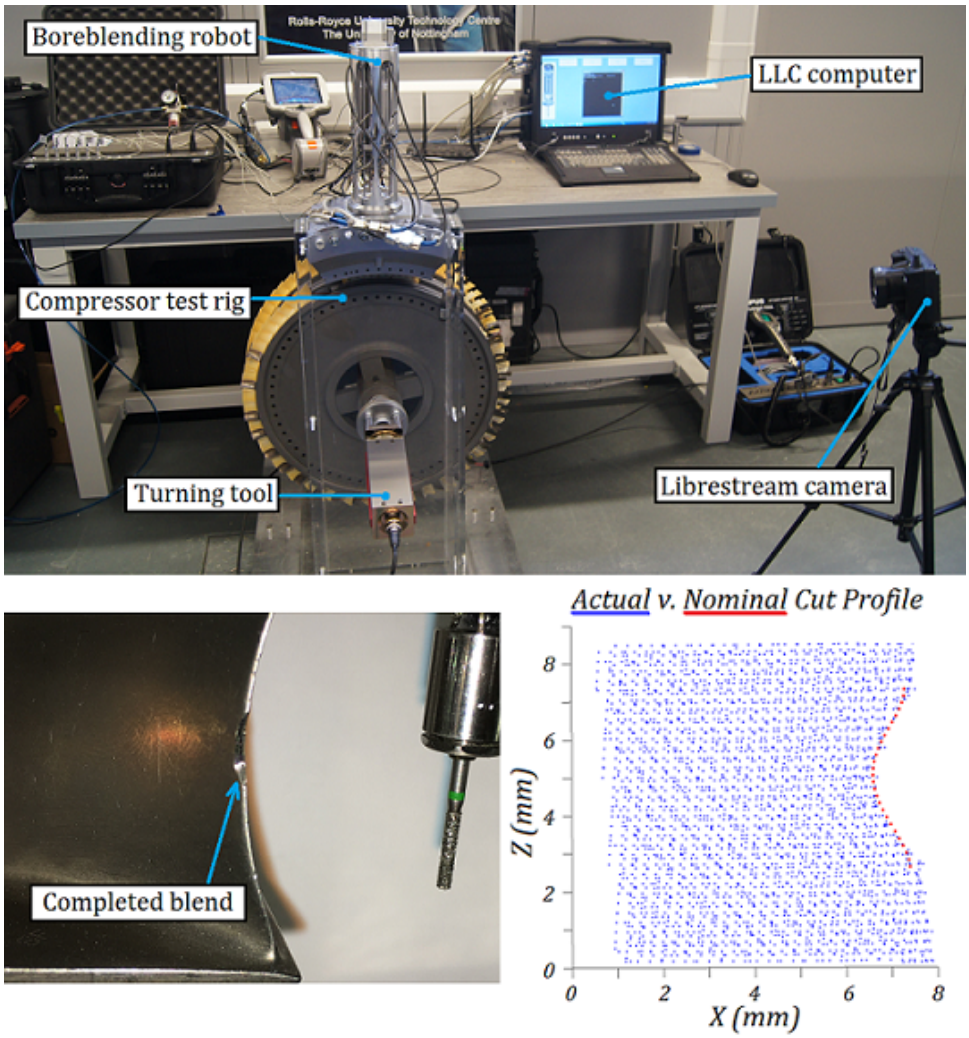


Figure 3.18: Experimental setup (top) and results (bottom) of repeatability study on compressor test rig. Top figure shows the boreblending robot attached to a Trent XWB aeroengine compressor mock-up with the insertion tube inserted such that the end effector is line with the compressor blades (yellow). Bottom left plot shows completed cut on a metal blade, bottom right shows experimental point cloud data of blade (obtained using a 3D scanner) compared to expected tool path (red).

Once the blends were completed, each blade was scanned using a structured light 3D scanner (Artec Spider) with a quoted accuracy of 0.05 mm. The scans were conducted by attaching the blade to an elevated fixture and moving the Artec device free-hand around it to build a fine tessellation output. The point clouds were compared to nominal simulated machining curves using the iterative closest point registration method. The results show strong correlation between the point clouds and the nominal curves, with a median RMSE of $64\mu m$ and a standard deviation between blades of 32 μm (Figure 3.19). Consistent dimensions were observed along all eleven blades, confirming the repeatability of measurement, manual point selection and machining. The average cut duration was 45 minutes, demonstrating a substantial improvement over the manual method (2 to 3 hours). This duration corresponds to a material removal rate of approximately $0.075 mm^3/min$.

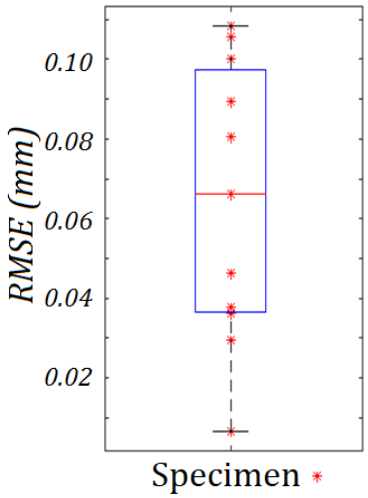


Figure 3.19: Root mean square error for each of the eleven compressor blade machining operations, shown in red. Each result was obtained from the point cloud data obtained using a 3D scanner.

3.6.2 In situ demonstration on Trent XWB aeroengine

The system's capabilities were demonstrated on a production aeroengine (Fig. 3.20) with a previously identified defect. The HLC was connected to the internet using a WiFi router, while the LLC was connected using a 3G mobile network device (A). This configuration of internet devices was chosen as a realistic scenario with high likelihood of inconsistent network delay and command latency.

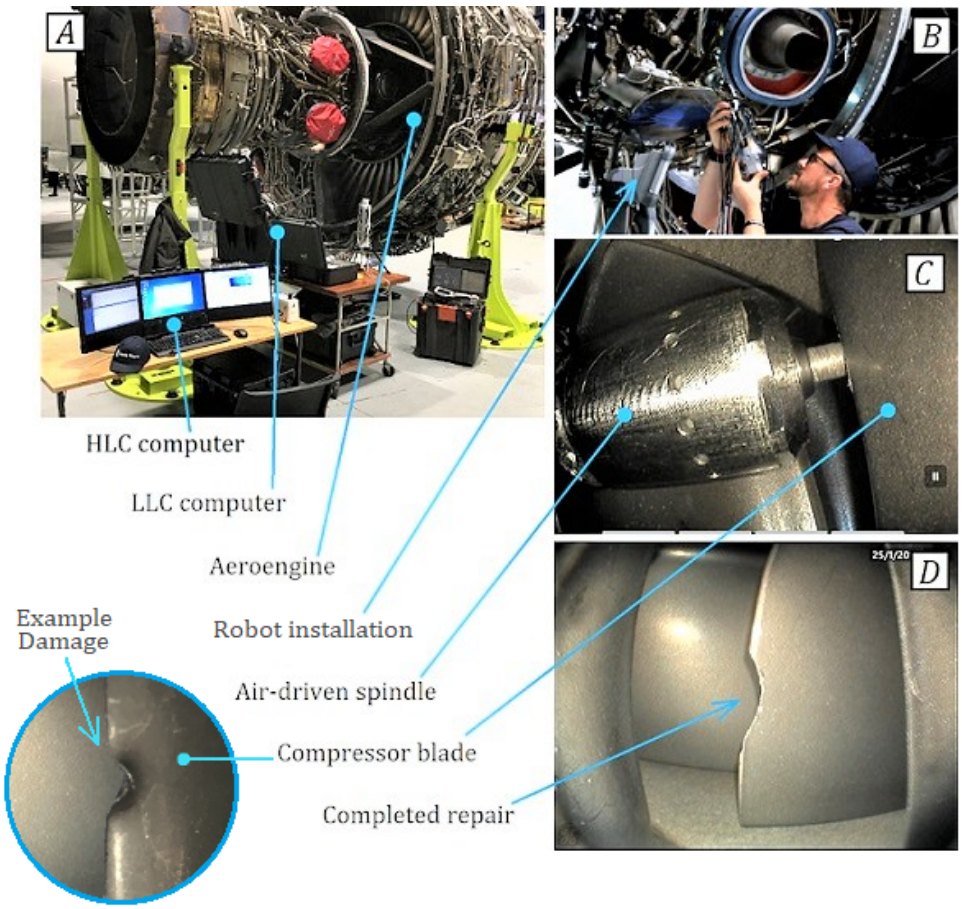


Figure 3.20: Remote boreblending demonstration carried out on a training aeroengine: A) setup and establishing of internet connection, B) ground support attaching robot to aeroengine, C) robot machining compressor blade and D) finished stress relief cut (in-engine images captured with separate camera, not built-in measurement camera).

The robot was inserted through a borescope port (B) and manoeuvred for inspection; measurements of the defect were made using the built-in probe (an example capture is shown in Figure 3.15) and the point cloud was analysed to fit the correct scallop curve. The robot successfully machined the blade (C) over 54 minutes (more passes were used than during the lab tests as the defect was larger), demonstrating that despite the likely variability between the rotor position in a lab setting and a real scenario, the point cloud selection methodology accurately aligns the curve with the blade edge. The robot was then retracted to the borescope port to be removed from the engine. After inspection (using a separate borescope with a high-resolution monocular camera from Waygate Technologies) by a trained professional, the shape, size and finish of the scallop (D) were deemed adequate for aerospace standards (the accuracy of the cut shape was comparable to that

observed during the lab trials), demonstrating the practical application of remote robotic boreblending.

While the example scenario chosen for demonstration is fairly specific, the approach is scalable to other in-situ repair tasks usually carried out manually, through narrow passages and by highly specialised technicians, and could be adapted to suit the maintenance needs of industrial assets such as turbines and compressors or key parts of hazardous hardware such as nuclear reactors.

3.7 Conclusions of case study and areas of improvement in position and force control

The degree of freedom of current manual boreblending tools was analysed and the results were used to inform the design of a 5 degree of freedom robotic probe fitted with 3D measurement instrumentation and an air-driven grinding tool for machining. The robot moves using a combination of rotary, prismatic and continuum joints for a novel hybrid architecture well suited for work in confined spaces.

The forward and inverse kinematics of this hybrid design were derived using the Denavit-Hartenberg convention and the Jacobian pseudo-inverse method and tested experimentally to be capable of navigating its flexible joints with 0.26 mm accuracy (standard deviation of position) and a maximum position error at full deflection of $0.85mm$.

A high level control computer displays the necessary information to a skilled operator and sends commands to a self-sufficient low level control computer connected to the robot. An operator can use the HLC to view video streams from the repair site, to identify the defect that needs to be repaired on a point cloud, to oversee the repair operation with a rendered simulation of the environment and verify the status of various subsystems. The LLC receives position and machining commands and independently carries out the repair. The LLC uses sensors to identify unexpected problems and retreat to a safe location before alerting the operator, making the system impervious to latency. The

network communication uses a custom protocol named compact-RUDP that combines reliable data and media transfer.

The system was put to the test by machining a number of stress relief scallops on compressor blades with a shape RMS error of 0.064 mm, and was demonstrated by removing a defect on a gas turbine compressor blade. The target defect was manually selected from point cloud data on the HLC and the shape, size and position of the blend was streamed to the LLC for machining. The demonstration showed the ability of the remote control system to produce consistent results despite human influence when defining the cut. The demonstration showed the ability of the system to reduce the time taken for the operation and improve the repeatability.

The following opportunities for future improvement were identified:

1. Despite efforts to achieve consistent tendon pre-tension and compensate for cable elongation, position control of the continuum segments is not optimal as it lacks a source of position feedback. The open-loop approach that was implemented in this case study made the assumptions that: *1)* the loading and unloading of the tendons follows a linear force trajectory, *2)* the slender instrument upstream of the continuum segments has high stiffness and does not deform under load and *3)* friction losses through the tendon holes are negligible. These assumptions can be circumvented altogether by introducing a form of position feedback such as a resistive stretch sensor in each of the continuum degrees of freedom.

2. The instrument lacks a source of end-effector physical reaction feedback for machining. The open-loop approach that was implemented in this case study assigned a fixed depth of cut and tool feed speed without a way to react to unexpected forces. In a case where the defect protrudes more than the controller is expecting, the grinding end effector would certainly stall and the operation would fail. A method for using tendon load cells or remote sensors to measure grinding force directly would allow for the interaction between tool and compressor blade to be better understood and yield superior performance.

3. The cautious approach to machining path planning resulted in unnecessarily long machining times. Regardless of the fact that the machine time was an improvement over manual methods, it is certain that, by optimising the cutting trajectory and cutting force, the cutting time could be reduced significantly more, adding more value to a remote boreblending instrument. This can be achieved by using a simultaneous position/force controller to achieve the desired shape while optimising the cutting force to maximise material removal rate.

The following sections will aim to address these improvements to in-situ repair robot control technology.

Chapter 4

New methods of position control for slender and compliant in-situ machining robots

Proprioception, or the ability to sense a body's position and movement, is a valuable trait in complex robotic systems. Unlike conventional robots with revolving and prismatic joints, continuum robots have a compliant structure (or backbone) capable of flexing under the influence of an actuation force (such as fluid pressure or tendon tension) [20]. While their construction and actuation method can vary from one instance to another, continuum robots by definition assume curved shapes when flexed. Slender continuum robots (with length to diameter ratios greater than ≈ 10) have the advantage of being able to traverse complex environments and be inserted through a relatively small access points. These features make them well suited for extreme applications including inspection and maintenance of industrial assets such as gas turbines [16] and nuclear reactors [14], minimally invasive surgery [7], search and rescue and marine inspection. The ability to deliver services (e.g. cameras, sensors, machining tools and others) to an end effector through a hollow central passage further adds to the potential use cases for slender and compliant manipulators [8].

Intrinsic proprioception, or built-in position sensory feedback, has been described in

prior work on continuum and soft robots, although not in a way compatible with in-situ repair of complex machinery. Ionic liquid stretch sensors have been identified as a possible method for closed loop position control of continuum robots due to their portability and ability to measure large strains while still allowing use of a hollow central passage. Existing literature on ionic liquid sensors shows that they have been used for displacement sensing in human body parts and robot revolute joints, but have not been applied for position control of continuum robots.

This chapter presents a novel tubular resistive stretch sensor with ionic liquid conductors to enable closed loop position control continuum robots. The following sections describe a methodology for sensor characterisation and calibration drawing from a model of their behaviour under strain, allowing the application of four stretch sensors as proprioceptive feedback for motion control of a four-axis slender continuum manipulator. Experiments described herein demonstrate a substantial ($\approx$ 65%) improvement in position control accuracy and repeatability over open-loop methods, and show a promising step towards low-cost, scalable position feedback for slender continuum robots.

The restricted space in continuum sections with diameters below $15mm$ means that a lot of the sensing for position feedback (such as by means of position encoders and flow regulators) is often residing outside continuum sections and carried out in an actuation pack where more space is available [23, 35, 41, 42]. This means that the accuracy of the end effector navigation depends on a model of the mechanical system that incorporates not only the backbone deformation, but also the elongation of tendons, distortion of soft bodies, compressibility of fluids, tendon friction, external disturbances and many other variables. Low cost or low-accuracy manipulators (such as 3D printed continuum robots, pneumatic soft robots and others) are particularly susceptible to such sources of position error. One way to eliminate the compounded effect of these uncertainties is to have closed loop position control through a single source of proprioceptive feedback per degree of freedom; this can be achieved by direct measurement of the shape of the backbone.

The objective of this work is to demonstrate the application of a novel, minimalistic

sensor for intrinsic closed loop control of continuum robots. A method for constructing, characterising, calibrating and operating ionic liquid stretch sensors is described, the sensors are applied to a closed loop system and the performance of the system is compared to open loop methods.

4.1 Background

Position control of continuum joints is more challenging than for regular prismatic joints due to the fact that bending the backbone changes the shape of the entire arm. Measuring the position and shape of continuum robots presents a substantial challenge as it is impractical to attempt to track the infinite number of points along its curvature. Instead, most methods aim to measure the position and/or attitude of the endpoints of independently drivable continuum segments or the curvature of points within a segment. As discussed in detail in Chapter 2, extrinsic and intrinsic sensors can be used to measure the shape, curvature and position of slender and compliant robots. Extrinsic methods (such as electromagnetic trackers [37, 38] and optical motion capture systems [10, 40] are not well suited for closed loop position control in applications outside strictly controlled environments, as they require previously installed equipment. Intrinsic methods (such as Hall effect sensors [90–92], optoelectronic sensors [95, 96], optical fibre sensors [97], piezoelectric sensors [44] and fibre Bragg grating (FBG) sensors [53, 55, 56, 61, 63] require difficult to miniaturise electronics and often impinge on the available central passage space.

Another intrinsic curvature measurement approach is to use resistive sensors for large deflection strain sensing [65, 160]. Resistive sensors are frequently constructed out of elastic materials that are made conductive by the inclusion or by layers conductive materials [77–82, 84, 85]. When stretched, the conductive layer changes length and cross-sectional area, resulting in a change in resistance.

Using stretch sensors to quantify the deflection of the backbone can help reduce the computational load of position control by giving the system information about the true shape of the robot section. Stretch sensors placed on the outside of a serpentine robotic

actuator provide feedback about the curvature achieved by the segment in question. For a sensor mounted on a continuum segment at a distance b from the bending plane, the stretch δL of the sensor at a given bend angle θ can be described as the difference between the length of the circular arc described by the sensor and the length of the segment when straight. For an angle in radians this reduces to:

$$\delta L = b\theta \tag{4.1}$$

Soft continuum robots such as those made up of elastomer bladders that extend or retract using fluid pressure [161,162] can also change length by compressing or extending multiple bladders in a single segment at the same time. Stretch sensors can be used to quantify the length of each bladder to accurately predict the end effector position.

Ionic liquids can be described as compounds composed entirely of combinations of anions and cations that are liquid at temperatures less than $100°C$ [163]. Ionic liquids exhibit conductive properties that make them attractive for numerous applications in electrochemistry such as electrodeposition, energy storage, catalysis and synthesis of other compounds. Their conductivity can also be exploited to construct electronic circuits with transparent and fully compliant conductors, which has led to the development of flexible stretch sensors.

In addition to measuring flex, stretch sensors may be applied to continuum robots to measure and counteract undesirable twist movements. Torsion of the continuum robot along the principal axis is an inevitable side effect of long thin structures arising from asymmetric cable tensions and torques acting on the end effector. The effect becomes more noticeable for longer continuum robots and there is no existing intrinsic way to measure the magnitude of this twist. Mounting stretch sensors in counter-rotating helices up the circumference of the continuum arm provides a method of directly measuring the torsion of the structure.

This work introduces a novel low cost tubular-construction resistive stretch sensor with ionic liquid conductor as curvature feedback for closed loop control of slender continuum robots with hollow central passages. A scalable construction methodology is

described, a theoretical model based on the sensor's mechanical properties is developed and used to establish a control strategy for continuum robots and a calibration procedure is outlined. Continuum robot proprioception is demonstrated on a 3D printed (low cost) four-axis tendon-driven serpentine manipulator equipped with tubular ionic liquid stretch sensors (TILSS) and controlled in closed loop with shape feedback.

4.2 Resistive proprioception concept and sensor characterisation

The proposed method for continuum robot proprioception places tubular resistive sensors some distance away from the robot's neutral axis and bending plane (Figure 4.1), resulting in a strain measurement linked to backbone curvature. The robot construction used in this paper is a dual-flexible-backbone, rigid vertebrae, tendon-driven serpentine continuum robot with alternating bend directions similar to that described in [8], but the methodology can be applied to any continuum robot or soft actuator.

4.2.1 Tubular resistive sensor concept

Tubular ionic liquid stretch sensors consist of an elastomeric membrane filled with a viscous room-temperature-liquid salt. However, for the purpose of modelling their behaviour, it is assumed that sensors behave as single-material cylinders which are electrically conductive, linearly elastic and anisotropic at large strains.

The material deformation ratio ξ of a sensor stretched along z axis and contracting along x and y axes is given by

$$\xi = -\frac{d\epsilon_x}{d\epsilon_z} \tag{4.2}$$

and is analogous to Poisson's ratio in isotropic materials. It follows that for small strains the diametric compression along x or y can be described as

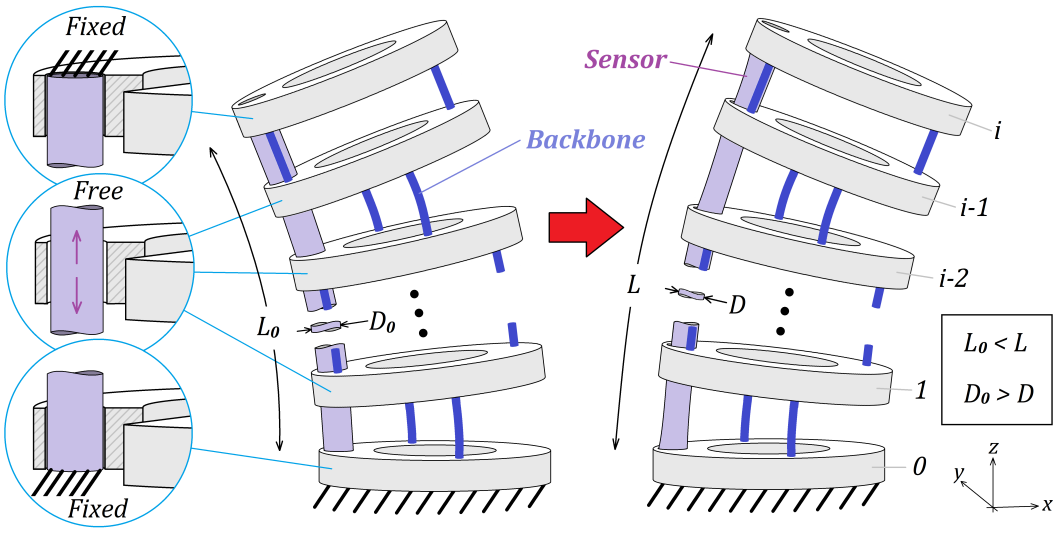


Figure 4.1: Concept for dual-backbone continuum robot proprioception with resistive stretch sensor. Curvature is calculated by measuring the resistance of a stretch sensor capable of large deflections and positioned some distance from the bending plane in question.

$$\frac{dx}{x} = \frac{dy}{y} = -\xi \frac{dz}{z} \tag{4.3}$$

which can be integrated to give the stretched conditions.

$$\int_{D_0}^{D} \frac{dx}{x} = -\xi \int_{L_0}^{L} \frac{dz}{z} \tag{4.4}$$

$$\ln\left(\frac{D_0 - \Delta D}{D_0}\right) = -\xi \ln\left(\frac{L_0 + \Delta L}{L_0}\right) \tag{4.5}$$

$$\left(1 - \frac{\Delta D}{D_0}\right) = \left(1 + \frac{\Delta L}{L_0}\right)^{-\xi} \tag{4.6}$$

given that $L = L_0 + \Delta L$ and $D = D_0 - \Delta D$.

The electrical resistance R of the stretched cylinder is given by

$$R = R_0 + \Delta R = \rho \frac{L}{\pi \left(\frac{D}{2}\right)^2} \tag{4.7}$$

$$R_0 + \Delta R = \rho \frac{L_0 + \Delta L}{\pi \left(\frac{D_0 - \Delta D}{2}\right)^2} \tag{4.8}$$

$$R_0 + \Delta R = \left(\rho \frac{L_0}{\pi \left(\frac{D_0}{2}\right)^2}\right) \left(\frac{1 + \frac{\Delta L}{L_0}}{\left(1 - \frac{\Delta D}{D_0}\right)^2}\right) \tag{4.9}$$

Substituting Equation 4.6 into Equation 4.9 gives the resistance in terms of the elongation and the instantaneous deformation ratio:

$$R_0 + \Delta R = R_0 \left(1 + \frac{\Delta L}{L_0}\right)^{2\xi+1} \tag{4.10}$$

Hence, normalised resistance R_{norm} can be given in terms of strain ϵ_L as

$$R_{norm} = (1 + \epsilon_L)^{2\xi+1} - 1 \tag{4.11}$$

where $R_{norm} = \frac{\Delta R}{R_0}$ and $\epsilon_L = \frac{\Delta L}{L_0}$.

The deformation ratio of the sensors is anisotropic due to the viscous ionic liquid in the conductive cavity. Dissolved air bubbles (observed to occur in the ionic liquids under investigation) change volume with sensor elongation due to the negative pressure that results from the elastic extension of the membrane. Assuming isothermal expansion, the diameter of dissolved bubbles D_B is proportional to the change in length of the sensor ΔL.

It has also been shown [164] that in viscoelastic materials with dissolved particles, shear modulus G increases with emulsion size. If the sensor as a whole behaves as a homogeneous viscoelastic material, it follows that the growing dissolved bubbles also influence the deformation ratio in the same way as the Poisson's ratio of any homogeneous material:

$$G = \frac{E}{2\,(1 + \xi)} \propto D_B \propto \Delta L \tag{4.12}$$

where E is the Young's modulus of the material.

Given that changes in both dissolved air volume and shear modulus have linear effects on the deformation ratio, each sensor ξ can be described in terms of strain by a second-order polynomial of the form

$$\xi = \alpha\epsilon^2 + \beta\epsilon + \gamma \tag{4.13}$$

where α, β and γ are constant for a given sensor and are obtained experimentally (at sensor strains $\epsilon > 0$, i.e. sensor never fully relaxed). Sensor constants for TILSS with varying degrees of degassing are presented in further sections.

4.2.2 Continuum robot proprioception

For multi-axis continuum robot proprioception, two stretch sensors mounted at orthogonal (or other non-opposing) positions on the circumference of the continuum segment can be used to measure the magnitude and x-y direction of bend. Figure 4.2 illustrates the vertebra configuration of a dual backbone segment that bends along x by θ_x and along y by θ_y, with two sensors mounted at a distance b from the bending origin and at angular offsets ϕ and $\phi + \frac{\pi}{2}$ from x.

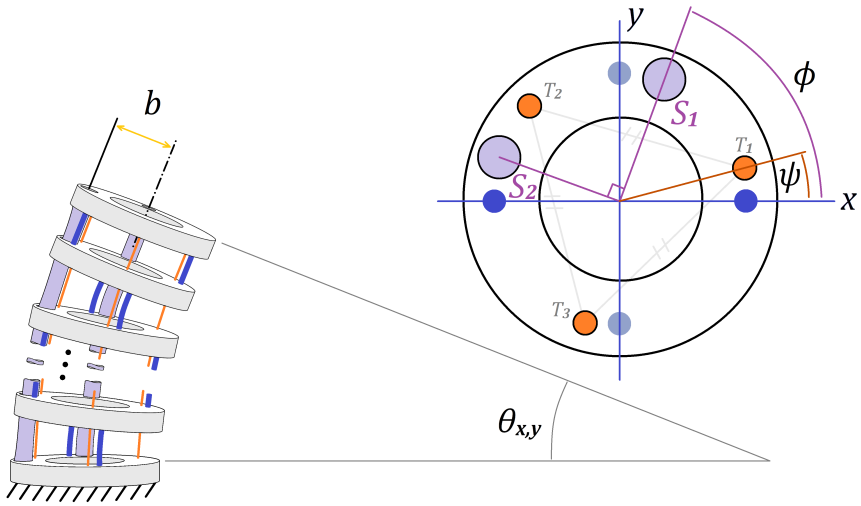


Figure 4.2: Schematic of the construction of a single continuum segment equipped with stretch sensors (S_1 and S_2) for bi-directional feedback and tendons (T_1, T_2 and T_3) for motion.

For this robot construction, the desired length L of each sensor can be calculated from the desired bend angles (θ_x and θ_y) using a constant curvature approximation:

$$L^{S_1} = L_a + b\left(\theta_x \cos\left(\phi\right) + \theta_y \sin\left(\phi\right)\right) \tag{4.14}$$

$$L^{S_2} = L_a + b\left(\theta_x \cos\left(\phi + \frac{\pi}{2}\right) + \theta_y \sin\left(\phi + \frac{\pi}{2}\right)\right) \tag{4.15}$$

where L_a is the rest (straight) length or neutral axis length of the robot segment with $L_a > L_0$.

Feedback control then uses the error in sensor lengths to calculate the desired corrective velocity along θ_x and θ_y and the required velocity component of each of the tendons $T_{1,2,3}$, based on their offset ψ from the x bending axis. The movement of each tendon can be defined by the sum of the contributions from $\theta_x \cos(\psi - \phi)$ and $\theta_y \sin(\psi - \phi)$ for each of $T_{1,2,3}$.

4.3 Sensor and manipulator construction methodology

As mentioned in previous chapters, resistive stretch sensors that use liquid conductors are constructed using an elastomer body. Authors such as [80,84] use casting silicone rubbers in additive manufactured moulds to create rectangular section sensors with an internal rectangular section liquid channel. Other authors such as [77] assemble the eutectic Gallium-Indium liquid metal sensors at temperatures below the melting point of the conductive material and embed them as solids before allowing them to melt. Serpentine robots present an opportunity to exploit cylindrical construction sensors, as vertebra often contain a number of holes parallel to the axis to guide tendons and services. This section covers the construction and characterisation of high-strain ionic liquid resistive stretch sensors with cylindrical construction. A summary of the equipment used in this chapter can be found in Appendix A.

4.3.1 Tubular stretch sensor material compatibility

Ionic liquids are salts that are liquid at low (and sometimes ambient) temperatures [79] and are primarily used as powerful solvents and catalysts for catalytic reactions in organic synthesis and electrochemistry [165]. These compounds are liquid at low

temperatures due to the weak interactions between large asymmetric organic cations and smaller organic or inorganic anions [166]. Ionic liquids present a number of advantages for their application in soft sensors, including low vapour pressure (low volatility), nonflammability, large temperature range in liquid phase and a wide temperature window with stable electrochemical properties [166].

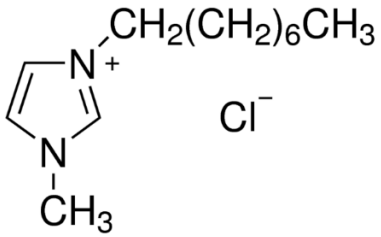
Particularly useful to their application in robotics is the liquid phase temperature range of ionic liquids (ILs). Typical operating temperature for in-situ repair of industrial assets is 15° to 25° but can be as low as 0° and as high as 40°. Many ionic liquids transition to glass at temperatures of 90° to 100° (which is low in relation to other solvents used in catalysis) and would not be suitable as resistive stretch sensors. ILs have a tendency to crystallize rapidly at the glass transition temperature which could easily result in catastrophic damage to sensors. For this reason, only ILs with melting point lower than $-10°C$ can be used within sensors.

Despite their advantages, ionic liquids present a challenge for robotics applications as they require long-term compatibility with the encapsulating and electrode materials. It is therefore essential that an IL is found which is chemically compatible with elastomers such as silicone rubber and which has a liquid temperature range that is suitable for in-situ maintenance of industrial assets.

Two candidate ILs were identified from literature for their temperature range:

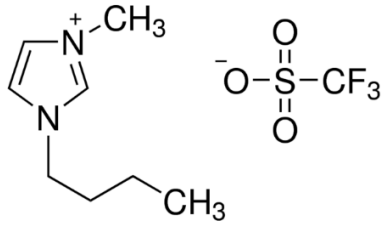
- 1-Methyl-3-octylimidazolium chloride (1-M-3O C)

  $C_{12}H_{23}ClN_2$ (Sigma Aldrich)



- 1-Butyl-3-methylimidazolium trifluoromethanesulfonate (1-B-3M T

  $C_9H_{15}F_3N_2O_3S$ (Sigma Aldrich)



Two tests were carried out to assess the chemical compatibility of both liquids with electrode and elastomer materials. A static corrosion test verified the long-term stability of the compounds when in contact. A galvanic corrosion test verified the long-term stability of the compounds when used as immersed electrodes. No such test has been described in previous published research. The elastomer selected is medical grade silicone tubing with grey colour. The electrode materials selected are high purity gold (20 carat, $Au83-17Zn$) and tin-copper solder ($Sn99-1Cu$, to electrically connect electrodes to sensor cables). Copper electrodes were not used due to their known reactivity with salts and ionic liquids.

The static corrosion trials consisted of immersing the candidate sensor component in ILs for 200 hours. The results of the static corrosion trials are shown in Table 4.1. 1-B-3M T was found to have no effect on any of the sensor components after long-term static exposure. 1-M-3O C was observed to transition to a more viscous gel when in contact with silicone rubber, however the resistivity of the IL was unchanged by this effect. Gelling of the liquid is likely to result in hysteresis due to the viscoelastic behaviour of the material. 1-M-3O C was also found to cause mild surface deterioration on the tin solder - an effect that is attributed to the chloride reacting with the small amount of alloyed copper. Gold electrodes were not affected by either IL.

The galvanic corrosion trials consisted of immersing the candidate sensor components, assembled as electrode pairs, in ILs for 120 hours while subjecting the two electrodes to an electric potential difference of $12V$. The results of the galvanic corrosion trials are shown in Table 4.2. 1-B-3M T was found to corrode both $Sn99-1Cu$ and $Au83-17Zn$ at the anode. In the case of $Sn99-1Cu$ the corrosion was catastrophic. 1-B-3M T was also found to significantly deteriorate (weaken and embrittle) the silicone rubber covering both anode and cathode regardless of electrode material - an effect that is attributed

Table 4.1: Long-duration static corrosion tests for $Sn99-1Cu$, $Au83-17Zn$ and silicone rubber in 1-M-3O C ($C_{12}H_{23}ClN_2$) and 1-B-3M T ($C_9H_{15}F_3N_2O_3S$).

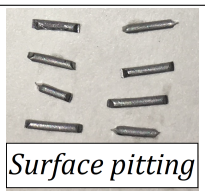
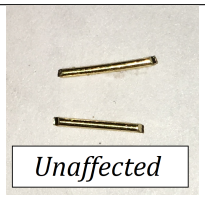
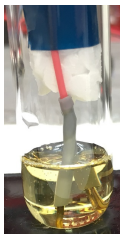
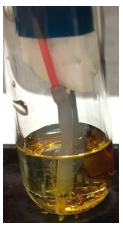
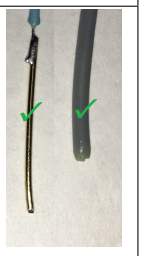
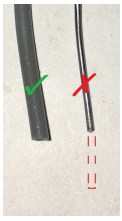
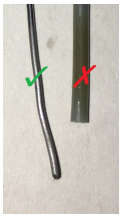
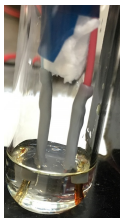
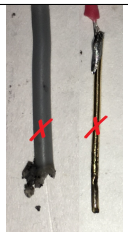
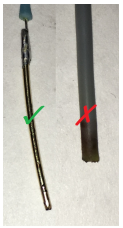
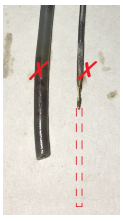
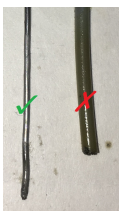
Ionic liquid	Electrode material	Electrode result	Silicone result
1-M-3O C	$Au83-17Zn$		
1-M-3O C	$Sn99-1Cu$		
1-B-3M T	$Au83-17Zn$		
1-B-3M T	$Sn99-1Cu$		

Table 4.2: Long-duration galvanic corrosion tests for $Sn99 - 1Cu$, $Au83 - 17Zn$ and silicone rubber in 1-M-3O C ($C_{12}H_{23}ClN_2$) and 1-B-3M T ($C_9H_{15}F_3N_2O_3S$) at $12V$.

Ionic liquid	Electrode material	30 seconds	3 hours	120 hours	Anode result	Cathode result
1-M-3O C	$Au83 - 17Zn$					
1-M-3O C	$Sn99 - 1Cu$					
1-B-3M T	$Au83 - 17Zn$					
1-B-3M T	$Sn99 - 1Cu$					

to the by-products of electrolytic decomposition or galvanic corrosion. 1-M-3O C had a similar effect on solder (although far less aggressively), with some of the deterioration also visible in the silicone exposed to the reaction by-products. In the case of 1-M-3O C with gold electrodes, however, no appreciable corrosion or deterioration was found in any of the sensor components.

Following these observations, a sensor was designed consisting of a silicone rubber conduit (of internal diameter $0.7mm$ and wall thickness $0.5mm$) filled with 1-Methyl-3-octylimidazolium chloride and terminated with two 20 carat gold electrodes with external electrical connections.

4.3.2 Manufacture and assembly of tubular ionic liquid stretch sensors (TILSS)

After a study of material compatibility and galvanic corrosion effects of ionic liquids (1-methyl-3-octylimidazolium chloride, 1-butyl-3-methylimidazolium trifluoromethanesulfonate) and electrode metals (Sn and Au), miniaturised tubular ionic liquid stretch sensors were constructed with the most suitable combination as follows:

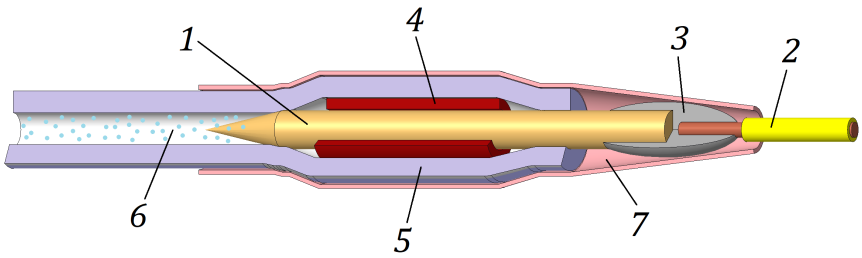


Figure 4.3: Construction of tubular ionic liquid stretch sensor electrode assemblies consisting of gold electrode (1), sensor wire (2), electrical joint (3), PVC sleeving (4), silicone tubing (5), ionic liquid (6) and heat shrink tubing (7).

1. *Electrode preparation*

   Approximately $10mm$ of $0.8mm$ diameter 20 carat gold wire was sharpened to a fine coaxial point (1 in Figure 4.3) and cleaned carefully with isopropyl alcohol. An electric wire (2) - AWG 30 or similar - was soldered to the blunt end of the gold wire using appropriate consumer electronics grade tin solder (3). Approximately

4.0mm of 1.2mm diameter polyvinyl chloride cable sleeving (4) was secured to the electrode near the tip (leaving approximately 2mm exposed including the tip) using cyanoacrylate adhesive. This process was repeated for the second electrode.

2. *Sensor body preparation*

   A length of medical grade silicone rubber tubing (5) was stretched (to soften and temporarily deform the viscoelastic material prior to filling) and cut to a length equal to 85% of the required sensor rest length (for a pre-stretch in use of 15% to 20%).

3. *Ionic liquid degassing*

   Approximately 0.5ml of 1-Methyl-3-octylimidazolium chloride (6) was vacuum degassed using a plugged syringe by using the piston to pull a vacuum inside the chamber and allowing air bubbles to merge and disappear. At least ten degassing cycles were performed.

4. *Sensor filling*

   The sensor was filled from one end with 1-Methyl-3-octylimidazolium chloride (6) using a syringe with a 22 gauge blunt tip needle until some liquid was visible on the open end. Leaving the needle inserted and immobile, excess liquid was cleaned from the sensor open end taking care not to contaminate the outside of the silicone tube but leaving the liquid flush with the opening of the silicone tube.

5. *First electrode attachment*

   One of the electrodes was inserted into the silicone tube, displacing liquid until the PVC sleeve was fully inside the silicone tube and until the silicone tube came into contact with the gold electrode past the PVC sleeve to serve as a secondary sealing surface. Approximately 13mm of 3mm diameter 4:1 or greater shrink ratio heat-shrink tubing (7) was applied over the length of the electrode and to overlap with the start of the electric cable. A drop of cyanoacrylate adhesive was applied to the edge of the heat-shrink tubing over the silicone tube to allow capillary action to suck adhesive into the interface. Heat was applied to the heat-shrink tubing at no

more than $120°C$ using a heat gun or hot iron to apply even pressure on the silicone tube and seal the liquid in the cavity.

6. *Sensor end preparation*

   Taking great care, the syringe was used to inject enough liquid to displace the volume of the needle while the needle was pulled out of the sensor and removed. It is at this point that the sensor would be threaded through any holes too narrow to fit the electrodes. The sensor was slowly crimped in the middle using tweezers or needle-nose pliers with width no greater than $2mm$ to force a drop of liquid out of the silicone tube, taking care not to damage the silicone. Excess liquid was cleaned from the sensor open end taking care not to contaminate the outside of the silicone tube but leaving the liquid flush with the opening of the silicone tubing.

7. *Second electrode attachment*

   The second electrode was inserted into the silicone tube at the same time as the pressure was released from the tweezers or needle-nose pliers, displacing liquid until the PVC sleeve was fully inside the silicone tube and until the silicone tube came into contact with the gold electrode past the PVC sleeve to serve as a secondary sealing surface. Approximately $13mm$ of $3mm$ diameter 4:1 or greater shrink ratio heat-shrink tubing (7) was applied over the length of the electrode and to overlap with the start of the electric cable. A drop of cyanoacrylate adhesive was applied to the edge of the heat-shrink tubing over the silicone tube to allow capillary action to suck adhesive into the interface. Heat was applied to the heat-shrink tubing at no more than $120°C$ using a heat gun or hot iron to apply even pressure on the silicone tube and seal the liquid in the cavity.

Two variations of the construction described above were implemented on the four DoF continuum arm design. These served to minimise the protrusion of the sensors beyond the vertebral disk, allowing for the continuum joints immediately adjacent to the electrode vertebra to achieve full mobility. The two variations are described later in this chapter.

Three sensors were constructed and vacuum degassed to varying degrees. Table 4.3

shows experimentally obtained values of α, β and γ for sensors with varying initial average bubble diameters and dissolved air concentrations, verifying claims made in Section 4.2.1. The sensor constants were calculated using second order polynomial regression of ξ with data from 54 strain cycles.

Table 4.3: Characterisation table for tubular stretch sensors.

Degassing cycles	Bubbles per mm^2	Mean dia. (μm)	Median dia. (μm)	α	β	γ	R^2
0	6.3	51.1	16.3	-2.40	-0.25	0.68	0.9991
2	2.9	21.0	9.9	-1.80	-0.36	0.82	0.9987
10	2.1	10.5	6.1	-1.20	-0.20	0.96	0.9929

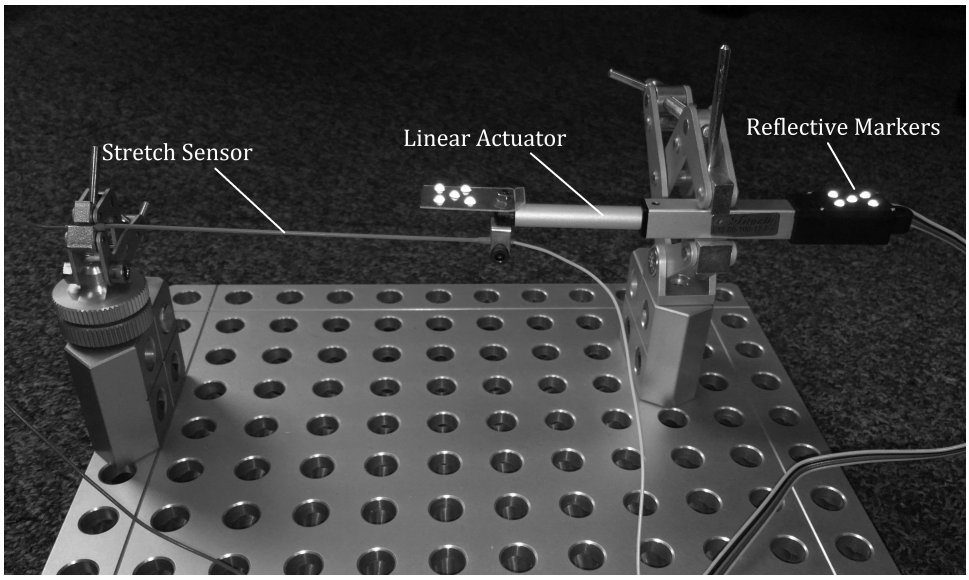


Figure 4.4: Setup for motion of a linear actuator and characterisation of a tubular ionic liquid stretch sensor. Reflective markers are used for tracking by the Vicon motion capture system.

The sensors were mounted on a test rig (Figure 4.4) consisting of two clamps on a fixture; one attached in a static position and another attached to the moving end of a *L12-50-100-12-P* DC geared linear actuator (Actuonix Motion Devices) with potentiometric position feedback. The linear actuator stretched the sensor from $115mm$ ($100 + 15\%$) to $165mm$. An *EMP373* portable computer (ACME) equipped with a *PCI-6229* IO board (16 bit, 250kS/s) and a *BNC-2110* BNC breakout board (National Instruments) sent pulse width modulated signals to an H-bridge connected to the DC motor windings and received

the analogue input from the feedback potentiometer. A *289/FVF* USB multimeter (Fluke) was used to measure and record the resistance of the sensor. An optical motion capture system (Vicon Motion Systems Ltd) was used to track the 3D motion of retro-reflective passive markers positioned on a surface attached to the mobile and static parts of the linear actuator. The system consists of four high-resolution Vantage 16 cameras.

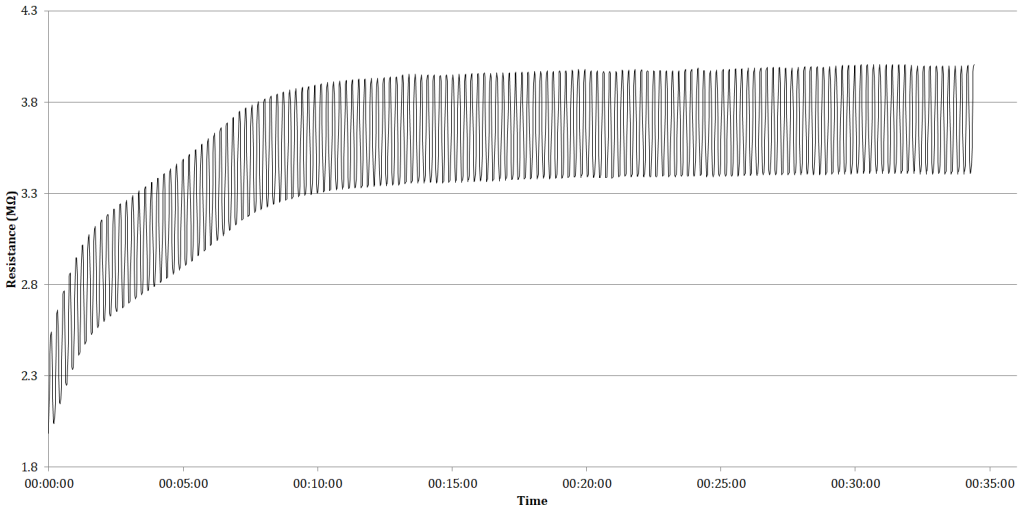


Figure 4.5: Plot of sensor 1 resistance over time during cyclical loading and unloading, showing the 10 to 12 minute warm-up time necessary for stable operation.

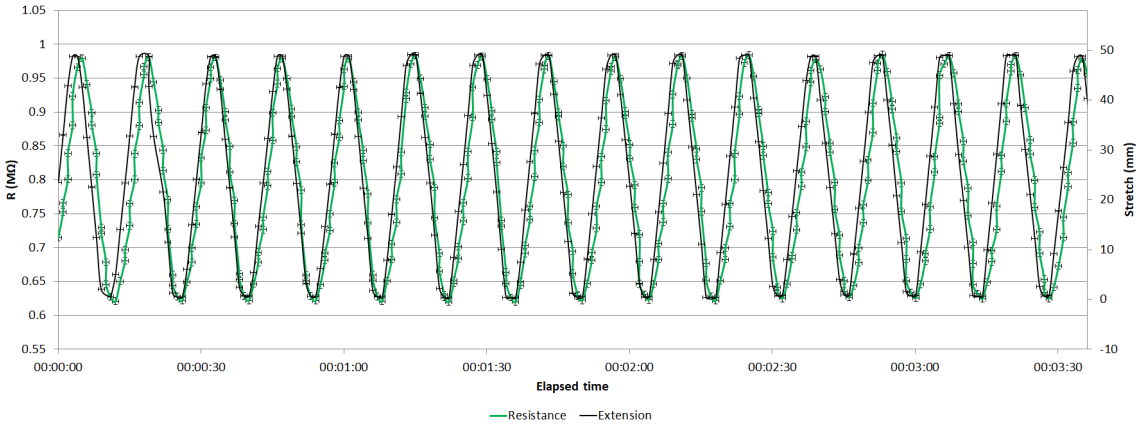


Figure 4.6: Raw stretch and resistance data from Sensor 2 during characterisation test.

It was soon observed that resistance increases significantly, independently of elongation, in the minutes following application of current by the multimeter before settling to a steady value. This warm-up time (measured to be 10 to 12 minutes) is attributed to a relaxation effect as described by Schmitt et al in their paper titled *Relaxation and electrophoretic effects in polyelectrolyte-plus-salt solutions* [167], where

the potential difference across the sensor (which in this case is high due to the constant current applied by the multimeter to a highly resistive - $M\Omega$s - sensor) creates a field that forces the long anion molecules into alignment with the smaller cations. This effect is analogous to having a large array of miniature rechargeable cells in series: as the molecules are pulled into alignment, the voltage and internal resistance of the 'cells' increase. 1.8 to 2.4V can be measured across disconnected stretch sensors after their warm-up period due to this relaxation and "charging" effect. Figure 4.5 shows the cyclical straining and unloading of a 1-M-3O C resistive sensor for 4000 seconds; the warming up period is clearly visible. The steady state capacitance of all sensors was measured to be zero, ruling out capacitive charging as a cause of the settling time.

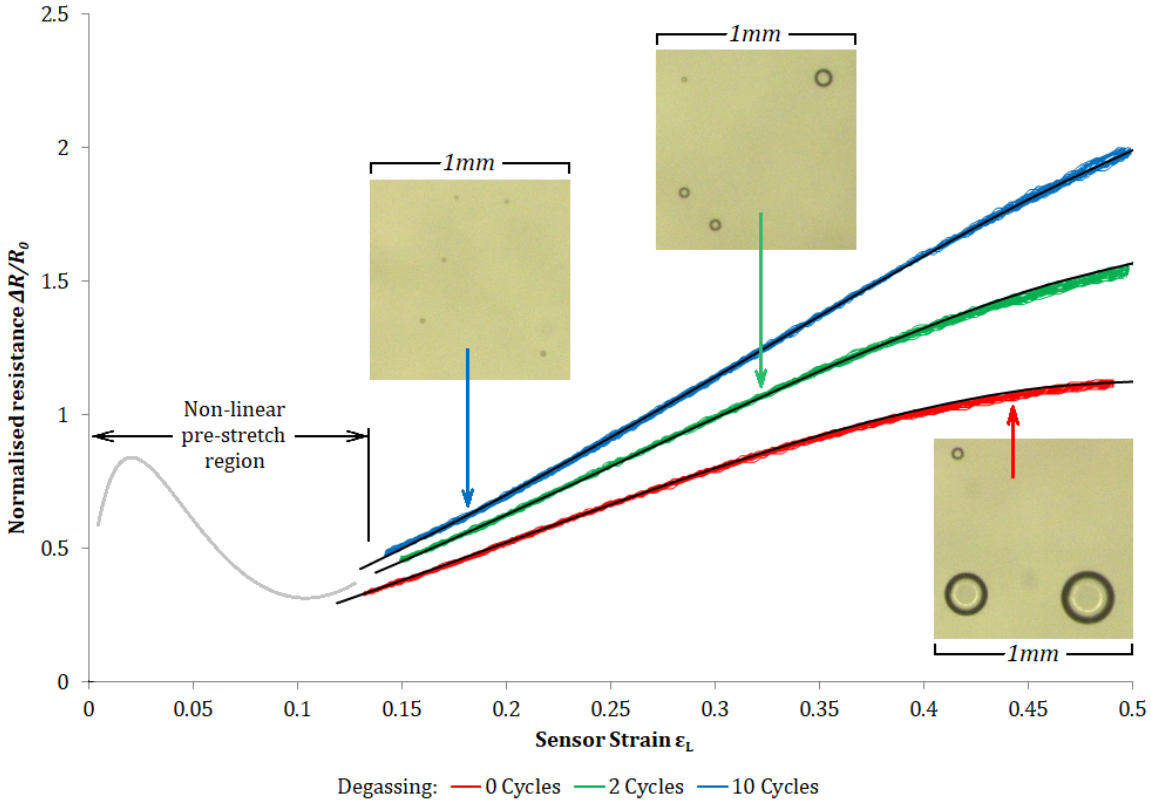


Figure 4.7: Plot of normalised resistance of three tubular ionic liquid stretch sensors with varying dissolved air content at strains from $\epsilon \approx 0.15$ to $\epsilon \approx 0.48$. Black lines show model using second order polynomial regression of ξ.

Initial tests of the stretch sensors consisted of stretching and relaxing the sensors after their warm-up period using the linear actuator. The position of the actuator and the resistance across the stretch sensor were recorded at a rate of $50Hz$. The actuator was moved to follow a triangular wave of amplitude $50mm$ at a rate of $9mm/s$ for ten

minutes (54 cycles). Figure 4.6 shows an example of the raw data from part of one of the sensor characterisation tests. The variable lag is attributed to the inconsistent acquisition rate of the multimeter used to collect the resistance data.

Results presented in Figure 4.7 indicate that the presence and size of air bubbles in solution do indeed influence the deformation ratio, with the effect of amplifying the quadratic terms of ξ. Table 4.3 shows the sensor characterisation constants α, β and γ for each of the three sensors tested. The second-order polynomial of best fit is shown for each sensor as a black line in Figure 4.7. The results also show a high level of repeatability and low hysteresis, predicting adequate controller feedback.

4.3.3 Construction and characterisation of 1-axis continuum manipulator

Chapter 3 presented a slender robot that includes conventional and continuum stages. However, given the small size and the difficulty in making changes to the boreblending flexible segments, two longer continuum robots were developed for the purpose of demonstrating the application of a novel stretch sensor – both were designed, built, assembled and commissioned by the present author. The first of these rigs was designed as a single-segment, single direction of flex, continuum robot equipped with a curvature-sensing ionic liquid resistive stretch sensor.

The dual-backbone serpentine section rig (Figure 4.8) consists of 10 resin vertebrae of diameter $13mm$ (1). Each vertebra tapers away from the bending plane toward two tendon through-holes (2) and four sensor through-holes (3). At the bending plane are four blind backbone holes (4) for the two pairs of super-elastic Nitinol backbone wires (5). A central passage (6) allows for routing of sensor cables from the distal (furthest from the base) electrodes.

Two $0.45mm$ diameter, 7-core braided stainless steel tendons (7 in Figure 4.8) are fixed to the final vertebra on the distal end and attached to two *LCM-201* (Omega Engineering) load cells (8). The load cells are attached to tendons that are fixed to spools (9). Two *5350366* stepper motors (10) (RS Pro) move the continuum segment.

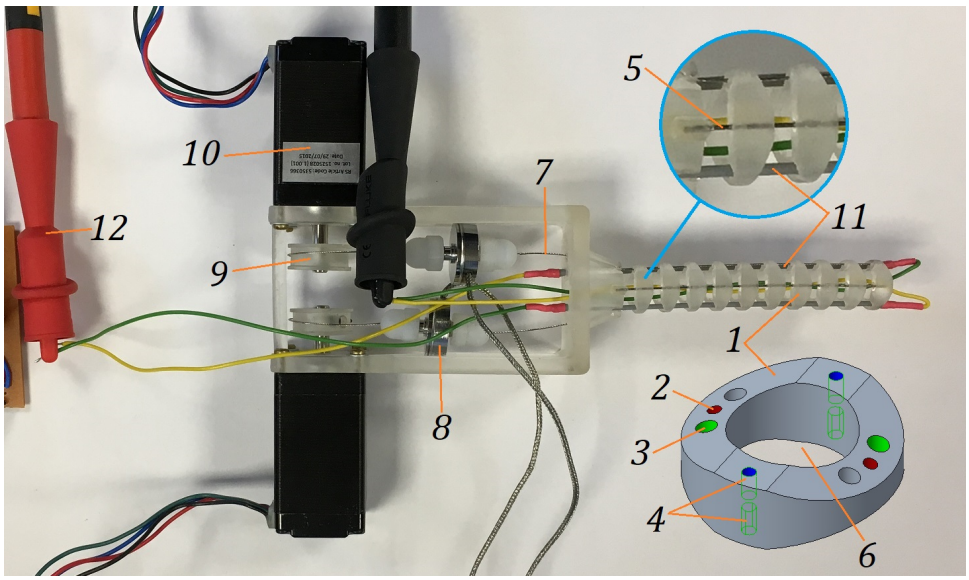


Figure 4.8: Single-segment, single-bend-direction, tendon-driven continuum robot with ionic liquid resistive stretch sensor for position feedback. Robot consists of vertebral discs (1) with tendon holes (2), sensor holes (3) and backbone holes (4). Vertebrae are linked together using super-elastic Nitinol rods (5). A central passage (6) can be used to deliver services to the robot end. Twisted stainless steel tendons (7) are attached to tension load cells (8) and driven by pulleys (9) on the shafts of stepper motors (10). Tubular ionic liquid stretch sensors (11) are used as proprioceptive feedback and are connected to a data acquisition device (12).

The sensors are vacuum degassed and homogenised 1-M-3O C tubular resistive stretch sensors (11). Only one sensor was used at any one time. Sensors were inserted through holes in each of the vertebrae after attachment of the first electrode and prior to attachment of the second electrode as described in previous sections. Sensor guide holes in the vertebrae (3) were exactly the same size as the relaxed sensor, resulting in a secure grip at the point where the sensor bulges around the electrode assembly (Figure 4.3). The sensors were assembled with a pre-loading exceeding the maximum possible stretch or compression to ensure complete range of measurement. Electrode wires connect to the data acquisition device via crocodile clips (12).

Movement of the actuators was calculated using

$$l_{in} = a - \sqrt{\left(\frac{2a^2}{\theta^2} - \frac{4ab}{\theta} + b^2\right)(1 - \cos(\theta))} \tag{4.16}$$

for calculation of the correction on the pulling side and

$$l_{out} = a - \sqrt{\left(\frac{2a^2}{\theta^2} + \frac{4ab}{\theta} + b^2\right)(1 - \cos(\theta))} \tag{4.17}$$

for calculation of the correction on the releasing side.

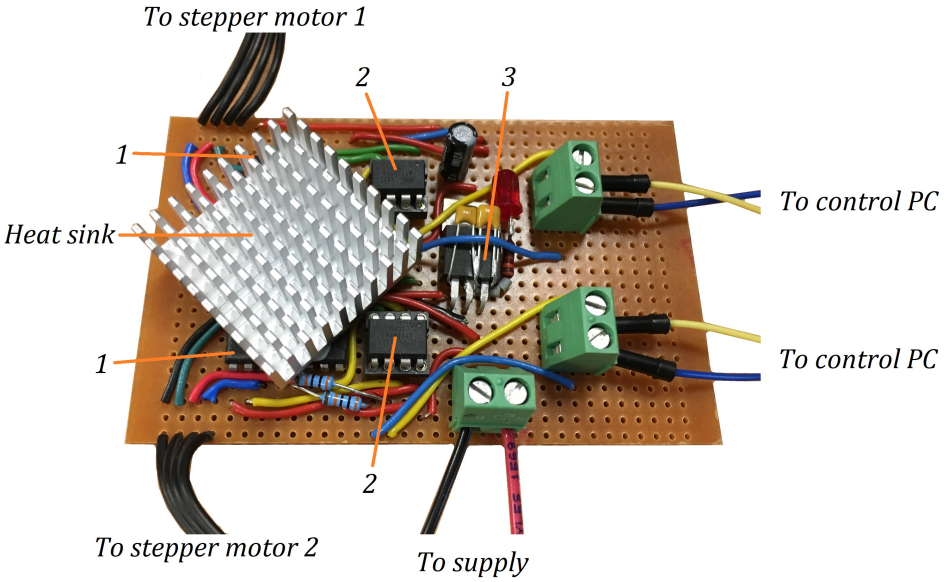


Figure 4.9: Single-segment continuum robot driving electronics including motor driver (1), micro-controllers (2) and voltage regulator (3).

The stepper motors shown in Figure 4.8 are driven by two *L293D* (STMicroelectronics) dual H-bridge motor drivers (1 in Figure 4.9). Each motor driver is commanded by an *ATTiny85* (ATMEL corp.) micro-controller (2) programmed to receive step and direction commands and convert them into quadrature signals for half-stepping the motor windings. An *LM7805* linear voltage regulator (3) supplies the micro-controllers with 5V DC.

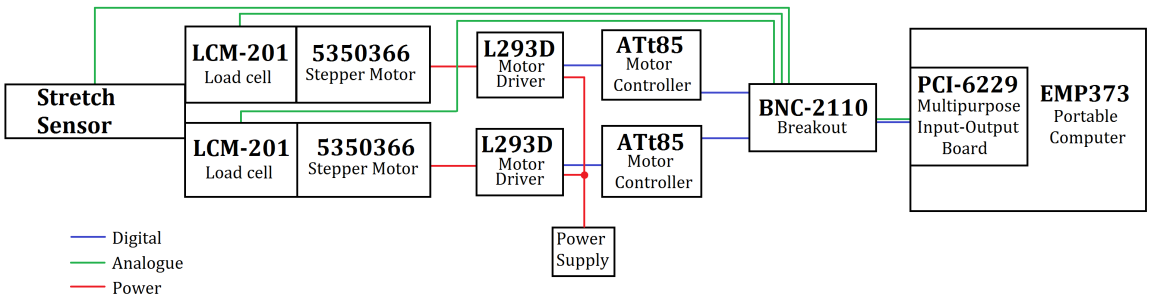


Figure 4.10: Single-segment continuum control schematic showing mechanical interfaces and electrical connections.

The *ATTiny85* micro-controllers are commanded using a *EMP373* rugged portable computer (ACME corporation) equipped with a *PCI-6229* (National Instruments) input output board and a *BNC-2110* (National Instruments) breakout board. Figure 4.10 shows the connection schematic for the single-segment continuum robot experimental rig.

The sensor was connected and left to rest for 15 minutes until resistance settled to a stable state to begin the calibration process. The continuum segment was commanded to follow a sinusoidal wave with amplitude $\pi/3$ and period 5 seconds. The position and orientation of the tip of the robot was recorded using an optical motion capture system (Vicon Motion Systems Ltd) consisting of four high-resolution *Vantage 16* cameras, with five retro-reflector markers mounted on a flat surface attached to the tip of the continuum segment. The resistance of the sensors was recorded using the built-in ADC of the *PCI-6229* board on the control PC. Figure 4.11 shows part of the recorded data used for calibration of the single segment feedback sensor.

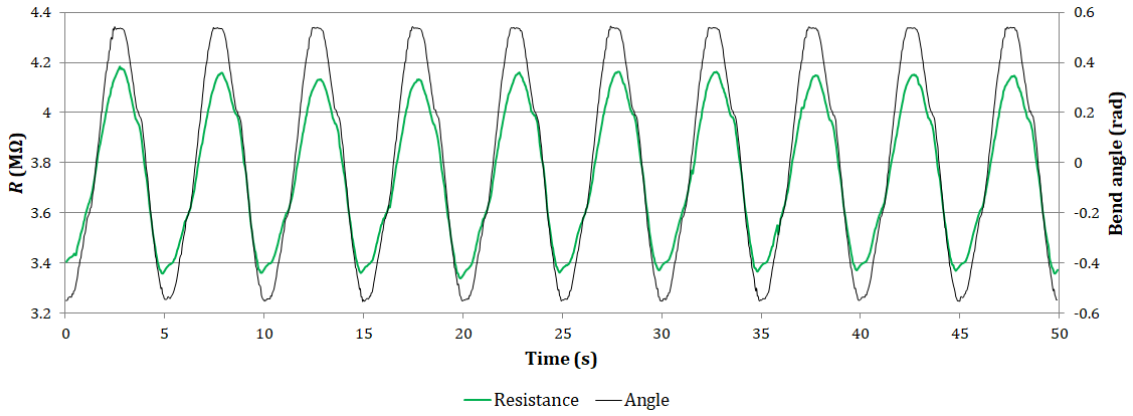


Figure 4.11: Raw bend angle and resistance data from one-segment continuum arm sensor characterisation tests.

The angle measurements presented in Figure 4.11 show regular disturbances to the smooth sinusoidal motion around one third of the way through a given sweep. This is attributed to tendon friction leading to slip-stick behaviour between the steel cable and resin vertebra. At around 0.2 radians the elastic force of the backbone overcomes the static friction force of one or more vertebra leading to irregular motion. This highlights the weakness of open loop continuum section control mentioned above, as the actuators were following verifiably sinusoidal trajectories.

Sensor strain, calculated using Equation 4.1, was compared to normalised resistance as shown in Figure 4.12. The sensor has poor signal-to-noise ratio compared to the results from the linear actuated single sensors due to the order of magnitude difference in sensor deformation across experiments. This also has the effect of magnifying the amplitude of hysteresis to approximately 3.0° of bend. The hysteresis is attributed to the viscoelasticity of the material, as the effect is reduced at lower speeds and almost eliminated in static measurements. This highlights a potential limitation of the tubular ionic liquid stretch sensors for applications that require high frequency movements. Despite this, a clear trend can be established and a characterisation curve fit to the data using second order polynomial regression.

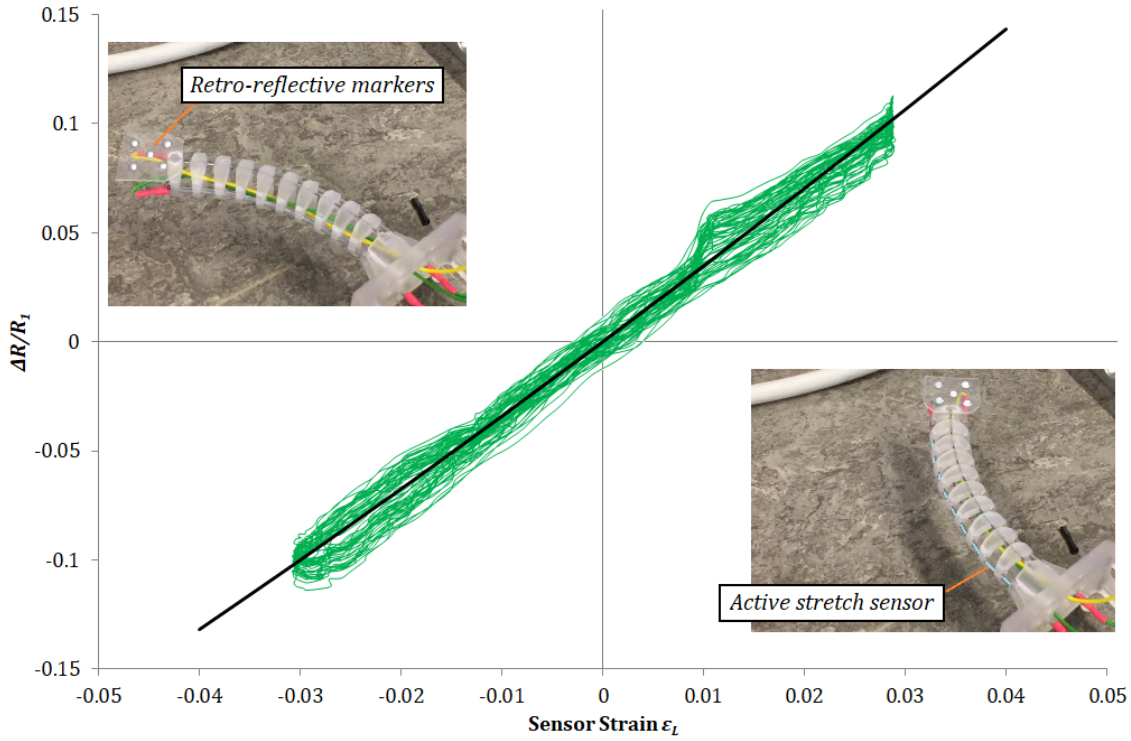


Figure 4.12: Plot of normalised resistance of single continuum segment ionic liquid stretch sensor for characterisation. Sub figures show the continuum segment at left and right limits of bend for the characterisation experiment (but not at mechanical bend limits). Resistance data shows hysteresis caused by the viscoelasticity of the sensor material.

The redundant sensor mounted on the continuum segment was tested in the same way to verify the procedure. Table 4.4 shows the sensor constants obtained from the characterisation tests.

Table 4.4: Characterisation table for tubular stretch sensors mounted on single-segment continuum robot.

Sensor	α	β	γ	R^2
CS1	-1.55	-0.29	1.22	0.9893
CS2	-1.43	-0.32	1.26	0.9817

4.3.4 Construction of 4-axis continuum manipulator

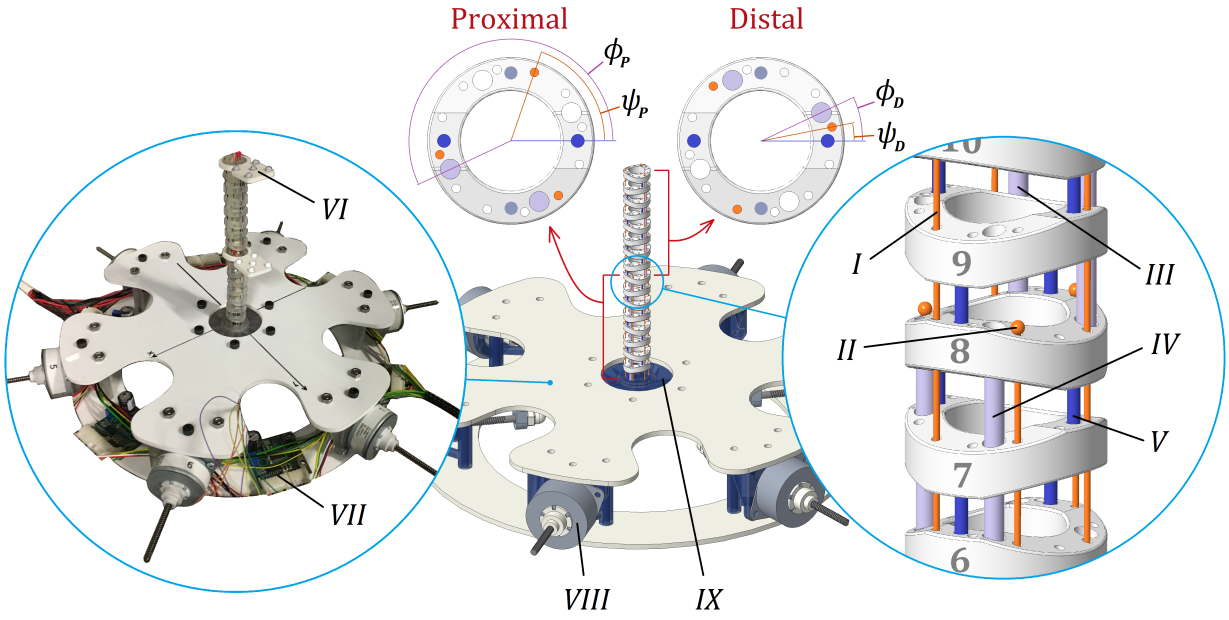


Figure 4.13: Two-segment, 4-axis, tendon-driven continuum robot with tubular ionic liquid stretch sensor proprioception. Details show distal segment (furthest from the base and actuators) tendons (I), proximal segment (closest to the base and actuators) tendons (II), distal segment sensors (III), proximal segment sensors (IV), flexible backbone (V), retroreflective tracking markers (VI), motor drivers (VII), linear actuators ($VIII$) and continuum robot base component (IX).

The second continuum robot constructed for experimentation with the tubular ionic liquid stretch sensors is a vertically mounted four-axis manipulator. The low cost, two-segment, dual backbone serpentine manipulator (Figure 4.13) consists of 16 resin (Clear V2.0, FormLabs, USA) vertebrae of diameter $13mm$ and thickness $5.0mm$, with the lower eight vertebrae forming the first (proximal) segment and the upper eight forming the second (distal) segment. Alternating bend directions at each vertebra give each manipulator segment two directions of flex. Each vertebra has a top and bottom

bending plane and corresponding tapers to allow a wider range of motion. One set of three $0.45mm$ diameter, 7-core braided stainless steel tendons (I) terminates after the sixteenth vertebra and drives the distal segment of the manipulator, while a second set of three tendons (II) terminates at the eighth vertebra and drives the proximal segment. For this construction, the tendon offset angles are $\psi_P = 75°$ and $\psi_D = 15°$ (for proximal and distal segments respectively).

One pair of orthogonal through holes in each vertebra houses the distal tubular ionic liquid stretch sensor (TILSS) (III) while a second pair of orthogonal through holes houses the proximal TILSS (IV). The proximal sensors run from the 0^{th} vertebra (the manipulator base plate IX) to the 8^{th} vertebra, the distal sensors run from the 8^{th} vertebra to the 16^{th} vertebra. Dual super-elastic Nitinol backbone rods (V) alternate bend direction after each vertebra, with a flexible length of $3.125mm$ each, giving each segment a length of $65mm$ and a total manipulator length of $130mm$. A central passage allows for routing of sensor cables from the distal electrodes and power supply for end effectors. For this construction, the sensor offset angles are $\phi_P = 205°$ and $\phi_D = 25°$.

Tendons are driven by six *100N-ELA* (RS Pro, UK) linear actuators ($VIII$) with *LP3575S* unipolar stepper motor drivers (VII). Six pulleys redirect the tendons by 90° from the linear actuators to the vertebrae holes. The stepper motor drivers are connected to the digital output ports of a *BNC-2110* breakout board (National Instruments, USA) and *PCI-6229* IO board and the robot is controlled from a *EMP373* portable computer (ACME Portable, USA) at a frequency of $250Hz$.

Retro-reflective passive markers were positioned on surfaces attached to the eighth and sixteenth vertebrae (VI) and an optical motion capture system (Vicon Motion Systems Ltd) was used to measure the position and orientation of the continuum segment ends.

The sensors are vacuum degassed tubular resistive stretch sensors which were pre-stretched to allow measurement in both bend directions (i.e. the sensor is under tension through the entire continuum segment stroke). U and S shaped electrodes were fitted to the centre and end vertebrae with bends on the gold wire immediately after the silicone tubing to allow full range of motion for adjacent vertebrae. The sensor cables were

connected to four isolated voltage dividers and subsequently to the analogue input ports of the *BNC-2110* breakout board (National Instruments, USA) and *PCI-6229* IO board (16 bit, 250kS/s).

The four sensors were connected and left to rest for 15 minutes until their resistance settled to a stable state to begin the calibration process. Each continuum segment was commanded to follow a sinusoidal wave with amplitude $\pi/3$ and period 5 seconds for 50 consecutive cycles in the x and y directions independently for a total of four calibration movements. The position and orientation of the tip of the robot was recorded using an optical motion capture system (Vicon Motion Systems Ltd) consisting of four high-resolution *Vantage 16* cameras. Sensor resistance was recorded using the built-in ADC of the *PCI-6229* board on the control PC.

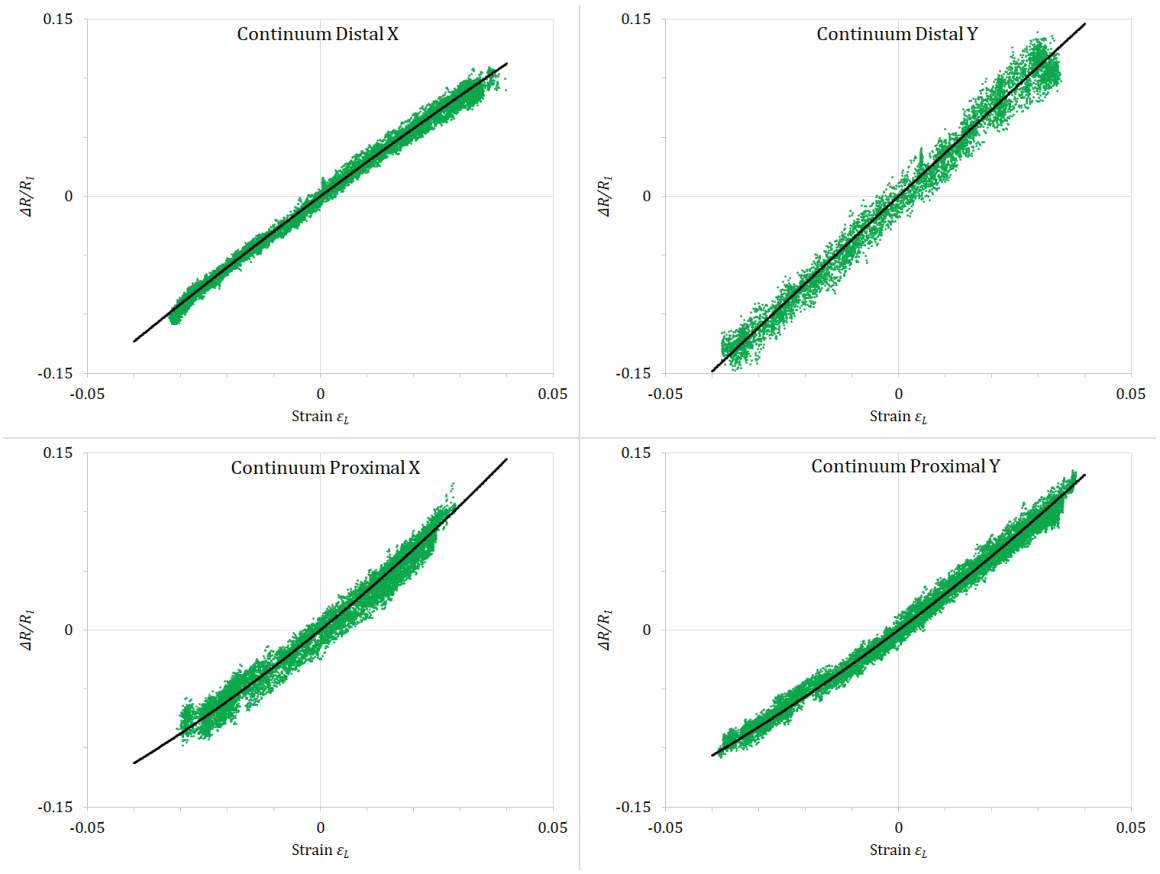


Figure 4.14: Plot of normalised resistance versus strain of two segment (proximal and distal), two bend direction (X and Y) continuum robot tubular ionic liquid stretch sensors for characterisation. Subtle differences in the sensors behaviour arising from the manufacture and assembly process can be seen as differences in sensor constants and electrical resistance. Hysteresis is present due to the viscoelasticity of the sensor material.

Sensor strain, calculated using the relation $L = L_0 + b\theta$, was calibrated against normalised resistance for each of the four TILSS as shown in Figure 4.14. Characterisation curves were fit to the data using second order polynomial regression. Table 4.5 shows the manipulator sensor constants, obtained using second order polynomial regression of ξ with data from 50 strain cycles (bends from $\epsilon = 0.15$ to $\epsilon = 0.25$).

Table 4.5: Sensor constants for dual-segment, multi directional continuum manipulator.

Sensor	α	β	γ	R^2
Proximal 1	-1.55	-3.24	1.10	0.978
Proximal 2	-1.53	-3.11	1.35	0.9822
Distal 1	-1.45	-2.50	0.98	0.9913
Distal 2	-1.63	-2.84	0.98	0.9615

The marked difference between the value of β for proximal and distal sensors was attributed to the difference in length and pre-stretch caused by a thick robot base component (XI in Figure 4.13), although the exact reason for the causation is outside the scope of this work.

It was observed that sensor resistance increases independently of elongation in the minutes following application of current before settling to a steady value. This warm-up time (measured to be 10 to 12 minutes regardless of sensor length or degree of degassing) was attributed to a relaxation effect as described in [167], where the potential difference across the sensor creates a field that forces the long anion molecules into alignment with the smaller cations.

The temperature sensitivity of Tubular Ionic Liquid Stretch Sensors was observed to be close to the thermal expansion coefficient of silicone rubber (590 to $790\mu\epsilon/\ ^\circ C$ [168]) when converted to $\Omega/\ ^\circ C$. While it will likely be desirable to use a third redundant sensor to compensate for temperature changes in the conditions of use of a continuum robot in real applications, this was not implemented in this work. Trials were carried out in spaces with ambient temperature control and initial resistance was calibrated before every

experiment.

4.4 Closed loop control of slender and compliant robots

The majority of tendon and fluid-driven continuum robots rely on open loop control where, based on knowledge of a model of the system, the actuators are commanded to move to a position that is expected to result in the desired end effector position. Despite the fact that actuators may be controlled accurately and with closed loop controllers, it is risky to assume that the continuum robot will behave exactly as predicted by a model. While continuum robot shape sensing has been achieved and described in existing literature (such as using electromagnetic position and attitude sensors, cameras and optical motion capture systems) and has been used for direct closed loop control, no solutions have been identified that achieve intrinsic (i.e built-in and without peripheral sensors) closed loop capabilities with a high degree of repeatability.

Having demonstrated the high signal-to-noise ratio and suitability of a tubular ionic liquid resistive stretch sensor for shape measurement, and having established a methodology for obtaining the calibration constants of such a sensor, it follows to implement it on an actuated system as a means of position feedback.

In this section, a closed loop control scheme is implemented first on a linear actuator with IL sensor position feedback, then on a single segment, single direction continuum robot with IL sensor position feedback, and finally on a multi-DoF, multi IL sensor, multi-actuator continuum manipulator.

4.4.1 Closed loop controller design

A single input single output position control loop uses sensor feedback to compare the measured state of an actuated device (such as a linear actuator or a tendon-driven continuum segment) to the desired state. The difference between desired and measured states is the present error, which serves as input for a controller that calculates the

required motion commands to reduce the error in a suitably fast, smooth and safe fashion. Figure 4.15 outlines the basic closed loop position control architecture for a resistive stretch sensor.

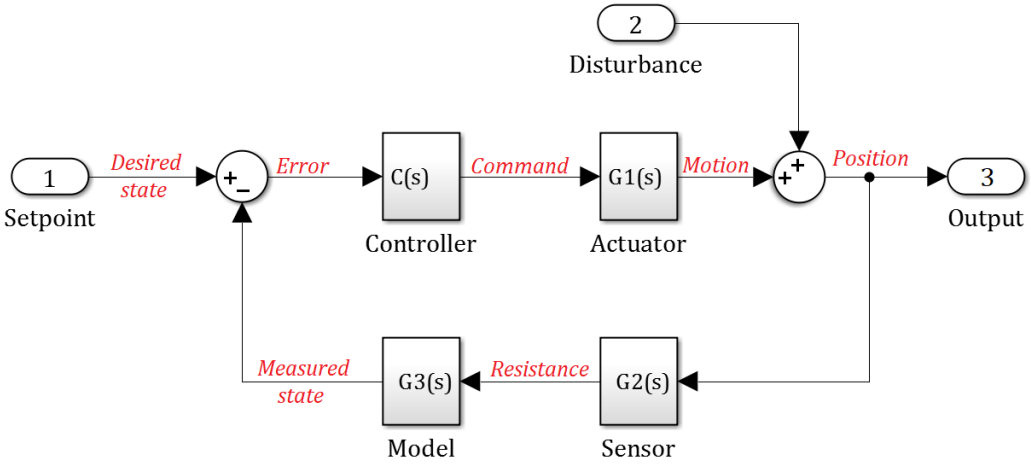


Figure 4.15: Closed loop control architecture for a single input, single output system. Desired position is compared to measured position (negative feedback) and error is used to influence the commands sent to the robot actuators.

There exists a wide variety of controllers to apply at $C(s)$, each designed to suit a particular type of system and some of which have been discussed in previous chapters. This chapter will explore the use of Proportional Integral Derivative or PID controllers, as they are well suited for single input single output systems and are inherently versatile [141]. The proportional term of a PID controller produces a command that is proportional to the value of error. The magnification or attenuation of the output is determined by a proportional gain K_P. The integral term of a PID controller produces a command that is proportional to the cumulative error of the system, with the effect of gradually removing steady state error. The speed with which the output grows based on persistent errors is determined by an integral gain K_I. The derivative term of a PID controller produces a command that is proportional to the rate of change of error, with the effect of damping the response of the system. The extent to which the output is altered by the speed of reaction is determined by a derivative gain K_D. Hence, the controller transfer function is given by:

$$C(s) = K_P + \frac{K_I}{s} + K_D s \tag{4.18}$$

The proportional, integral and derivative gains can be tuned using software provided an accurate model of the behaviour of the actuator and sensor are known (transfer functions $G1(s)$, $G2(s)$ and $G3(s)$ in Figure 4.15). In practice, even if $G2(s)$ and by extension $G3(s)$ can be derived from the characterisation equations described in Section 4.2, tuning is conventionally carried out by trial and error following guidelines such as those described in [141].

Sensor number 3 (which underwent the most vacuum degassing and homogenisation) was mounted on the linear actuator stretch rig (Figure 4.4) to implement and tune a PID closed loop controller. The control output was the PWM duty cycle which was used to drive the H bridges and DC motor. The actuator built-in potentiometer feedback was disconnected. The control gains were tuned to achieve a desirable response to a manual disturbance in stretch. Once tuned, the controller accuracy was verified using an optical motion capture system (Vicon Motion Systems Ltd) consisting of four high-resolution *Vantage 16* cameras. The desired position was defined as a square wave (yellow in Figure 4.16) of amplitude $35mm$ and period 14s. The frequency of the control loop was $100Hz$. 40 cycles were recorded and are shown in Figure 4.16. The grey line denotes one standard deviation from the mean (black line) in millimetres.

The constant slope of the rise and fall response is caused by saturation of the actuator speed. The effect of the reaction force from the elastic stretch sensor can be seen clearly in the response to step inputs (Figure 4.16), as there is overshoot in the release direction and undershoot in the loading direction. Despite this, the integral gain is enough to reduce the steady state error to near zero before the start of the following cycle. Integral wind-up was not observed with the conservative gains used in this test. The increase in variance during the load and release ramps is attributed largely to misalignment between successive cycles at the analysis stage.

While there may well be opportunity for improvement of the control tuning, the work presented here demonstrates the successful implementation of an ionic liquid resistive

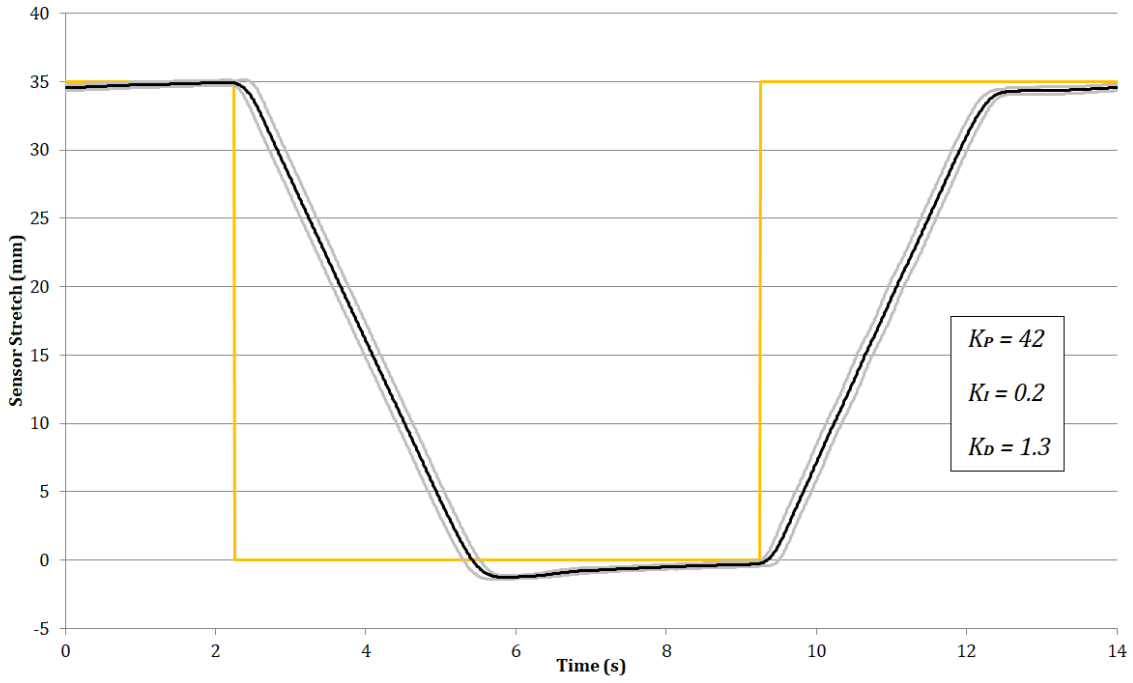


Figure 4.16: Closed loop response to square wave setpoint input for linear actuator with ionic liquid resistive stretch sensor feedback. Constant slope regions show saturation of actuator velocity. Overshoot during contraction is caused by the elastic force of the sensor assisting the actuator. Undershoot during extension is caused by the elastic force of the sensor opposing the actuator.

stretch sensor for position control of a simple actuator. The following sections go further to demonstrate the applicability of this technology to complex continuum robots with no other form of position feedback.

4.4.2 Control of continuum segments

A proportional, integral, derivative (PID) control scheme was applied to the single-segment continuum robot shown in Figure 4.8 and described in Section 4.3.3 with sensor number 1 as feedback (selected for its lower coefficient of determination R^2). The control scheme was modified to output a pulse frequency as opposed to a pulse width modulation duty cycle but was otherwise unchanged. With the faster stepper motors, it was possible to tune the PID constants to achieve accurate tracking and sharp step responses. The test desired position cyclical input was set to a number of step changes followed by a sinusoid (yellow in Figure 4.17) and the control frequency was set to $250Hz$. The black line is an example acquisition. The grey lines denote a range of

plus-minus one standard deviation from the mean of the 40 consecutive acquisitions taken during the experiment, in radians.

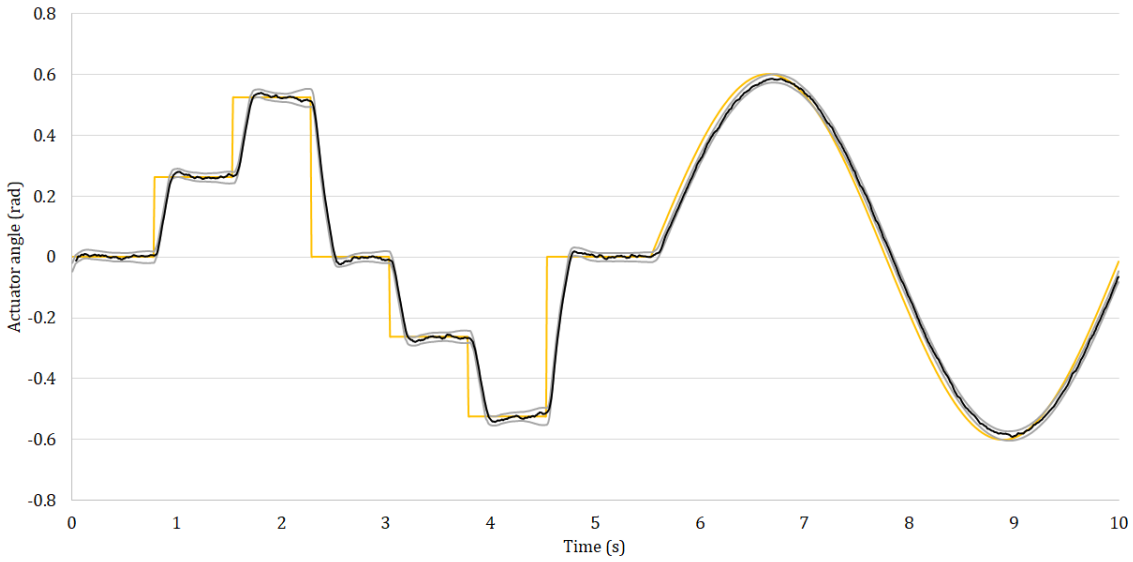


Figure 4.17: Closed loop response (black) to step and sinusoidal input (yellow) for single segment, single direction, serpentine continuum robot with tubular ionic liquid stretch sensor feedback. Grey lines mark standard deviation for 40 acquisitions.

Figure 4.17 shows that the controller achieved a tight response to step disturbances and a quick settling time. Accurate tracking of smooth motion was also demonstrated with sinusoidal movement. The maximum angular error of 1.7° corresponds to a position error of $1.47mm$, or 1.5% of the continuum length, demonstrating a marked improvement over the open loop method presented in Chapter 3 at 8.5%. The work presented in this section demonstrates the successful implementation of a tubular ionic liquid stretch sensor for position control of a single degree of freedom, slender and compliant actuator.

As was previously suggested (Figure 4.2), this methodology can be scaled to multi-direction continuum segments by the addition of an orthogonal tubular ionic liquid stretch sensor. Series concatenation of TILSS-enabled continuum segments can subsequently expand the capabilities of complex and even redundant slender and compliant robots.

Simultaneous control of the four axes was applied to the four-axis continuum manipulator shown in Figure 4.13 and described in Section 4.3.4. The control scheme was implemented by adding the velocity contributions from the four control loops (linked to the sensors) to each of the six linear actuators. Initial repeatability tests

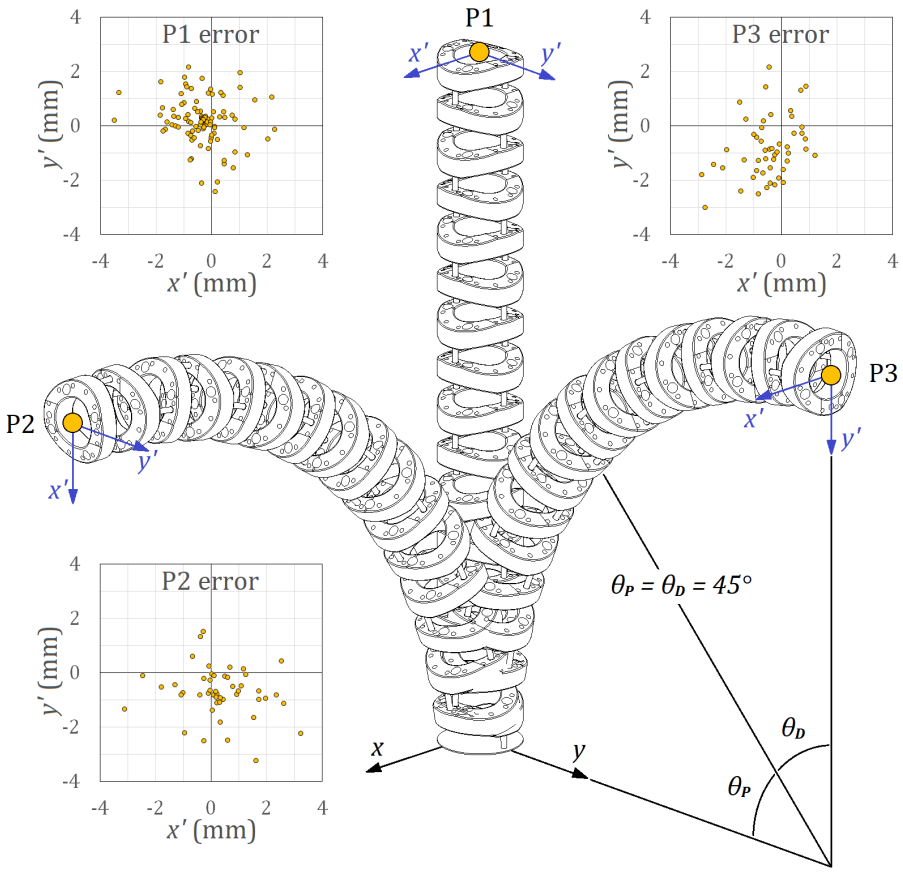


Figure 4.18: Experimental setup and results of point-to-point closed loop position control trials using ionic liquid stretch sensors as proprioceptive feedback, with three target position inputs for two-segment, dual bend direction continuum manipulator. Plots show distal vertebra position error for each of 50 cycles through three positions P1, P2 and P3 (with 100 points in vertical position P1 due to movement order).

consisted of synchronous movements of distal and proximal segments from straight to $\theta = 90°$ along x (with $\theta_{Dx} = \theta_{Px} = 45°$) and to $\theta = 90°$ along y (with $\theta_{Dy} = \theta_{Py} = 45°$) in the order P1 - P2 - P1 - P3 as shown in Figure 4.18. A standard deviation of 1.0% of total continuum length (TCL) was observed, with a maximum error of 2.7% TCL. Figure 4.18 shows the experimental setup for the initial trials and normal-view scatter plots of the resulting end vertebra centre position error following 50 cycles through the three target points.

A more complex target trajectory in task space involving simultaneous tracking with all sensors (in this case a $100mm$ diameter circle with $\theta_{Dx} = -\theta_{Px}$ and $\theta_{Dy} = -\theta_{Py}$ maintained throughout, at a rate of $5.24mm/s$) was converted into four sensor trajectories using constant curvature kinematics as described in [16, 20] and Chapter 3. Figure 4.19

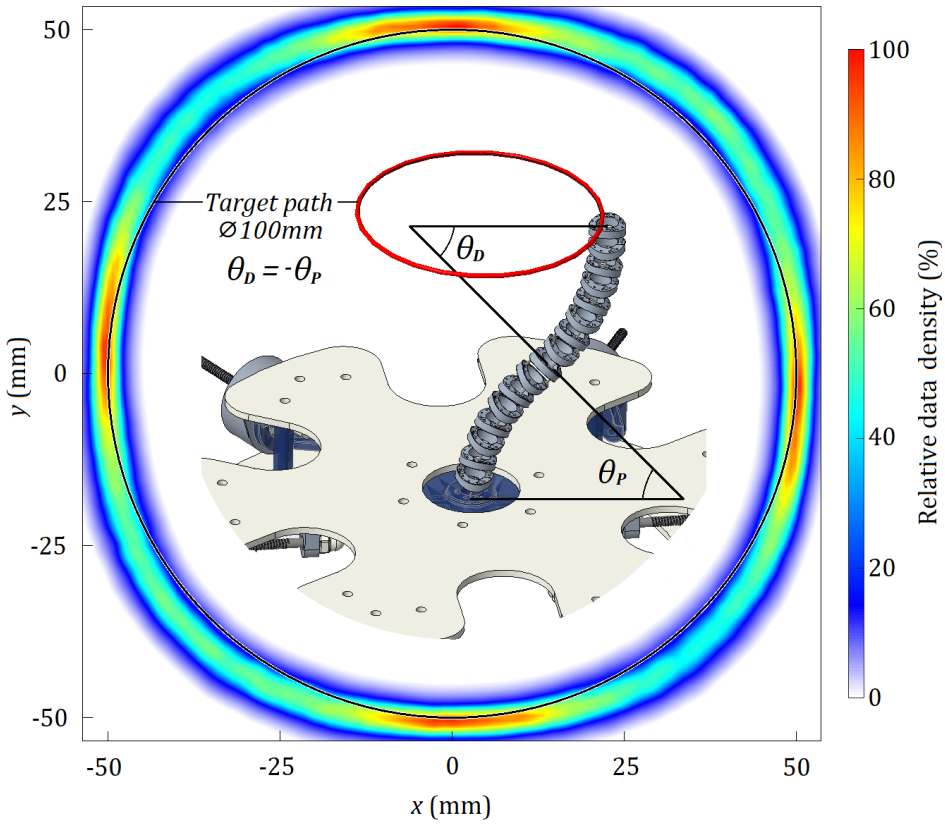


Figure 4.19: Results of closed loop position control using ionic liquid stretch sensors as proprioceptive feedback, with circular trajectory input for two-segment, dual bend direction continuum manipulator. Plot shows relative density of distal vertebra x-y position data points (for each mm^2 in the plot area) for 40 consecutive revolutions. End effector speed was commanded at $5.24mm/s$ or 1 revolution per minute.

presents the density of x-y position data after 40 revolutions - values were obtained by counting the number of position data points captured in a given square millimetre on the x-y plane, and were plotted relative to the maximum density (best performance) which occurs near the bending axes. Errors in z (not shown), which were observed to be small, form a conical spread consistent with the position of the continuum robot fulcrum.

The maximum error observed during closed loop control trials was 4.9% of Total Continuum Length. Deviation maxima occur at the intersection of the x and y bending axes and can be partly attributed to overestimation of the required input at axis intersections (by 0.067° per degree of bend) resulting from the constant curvature model. Modifying the forward kinematics described in Chapter 3 from a single constant curvature continuum bend per segment to eight short continuum bends (flexible backbones of length $\mathfrak{b}$) in alternating directions and eight straight sections (vertebrae of

length $\mathfrak{v}$) per segment (as shown in the Denavit-Hartenberg parameters on Table 4.6) results in an overestimation of 5.4% at the intersections of the two backbones. Controlling for this systematic error leaves 2.3% TCL variance attributable to feedback control.

Table 4.6: Corrected Denavit-Hartenberg convention parameters for dual-backbone, two-segment continuum robot.

Joint	$\boldsymbol{\theta}$	$\boldsymbol{\alpha}$ (°)	$\boldsymbol{d}$	$\boldsymbol{r}$
1	$\frac{\theta_{Px}}{2}$	0	0	$\sqrt{\frac{2\mathfrak{b}^2(1-\cos(\theta_{Px}))}{\theta_{Px}^2}}$
2	$\frac{\theta_{Px}}{2}$	90	0	$\mathfrak{v}$
3	$\frac{\theta_{Py}}{2}$	0	0	$\sqrt{\frac{2\mathfrak{b}^2\left(1-\cos\left(\theta_{Py}\right)\right)}{\theta_{Py}^2}}$
2	$\frac{\theta_{Py}}{2}$	90	0	$\mathfrak{v}$
⋮	⋮	⋮	⋮	⋮
15	$\frac{\theta_{Py}}{2}$	0	0	$\sqrt{\frac{2\mathfrak{b}^2\left(1-\cos\left(\theta_{Py}\right)\right)}{\theta_{Py}^2}}$
16	$\frac{\theta_{Py}}{2}$	90	0	$\mathfrak{v}$
17	$\frac{\theta_{Dx}}{2}$	0	0	$\sqrt{\frac{2\mathfrak{b}^2(1-\cos(\theta_{Dx}))}{\theta_{Dx}^2}}$
18	$\frac{\theta_{Dx}}{2}$	90	0	$\mathfrak{v}$
⋮	⋮	⋮	⋮	⋮
31	$\frac{\theta_{Dy}}{2}$	0	0	$\sqrt{\frac{2\mathfrak{b}^2\left(1-\cos\left(\theta_{Dy}\right)\right)}{\theta_{Dy}^2}}$
32	$\frac{\theta_{Dy}}{2}$	90	0	$\mathfrak{v}$ + End Effector

Figure 4.20 shows four passes from the circular trajectory described above commanded with closed loop control using Tubular Ionic Liquid Stretch Sensors feedback (solid line) and four passes with open loop control (dotted line), i.e. with the actuators following the required steps according to the calculated kinematics. The comparison suggests an improvement in accuracy of 64.7%, with a RMS error (calculated using the shortest distance between each measured point and the target trajectory) of 4.9% TCL in the open loop control case and 1.7% TCL in the closed loop control case. The observations also present an improvement in repeatability of 73.0%, with a standard deviation (of position error data) of 4.9% TCL in the open loop control case compared to 1.3% TCL when using TILSS as proprioceptive feedback. The open

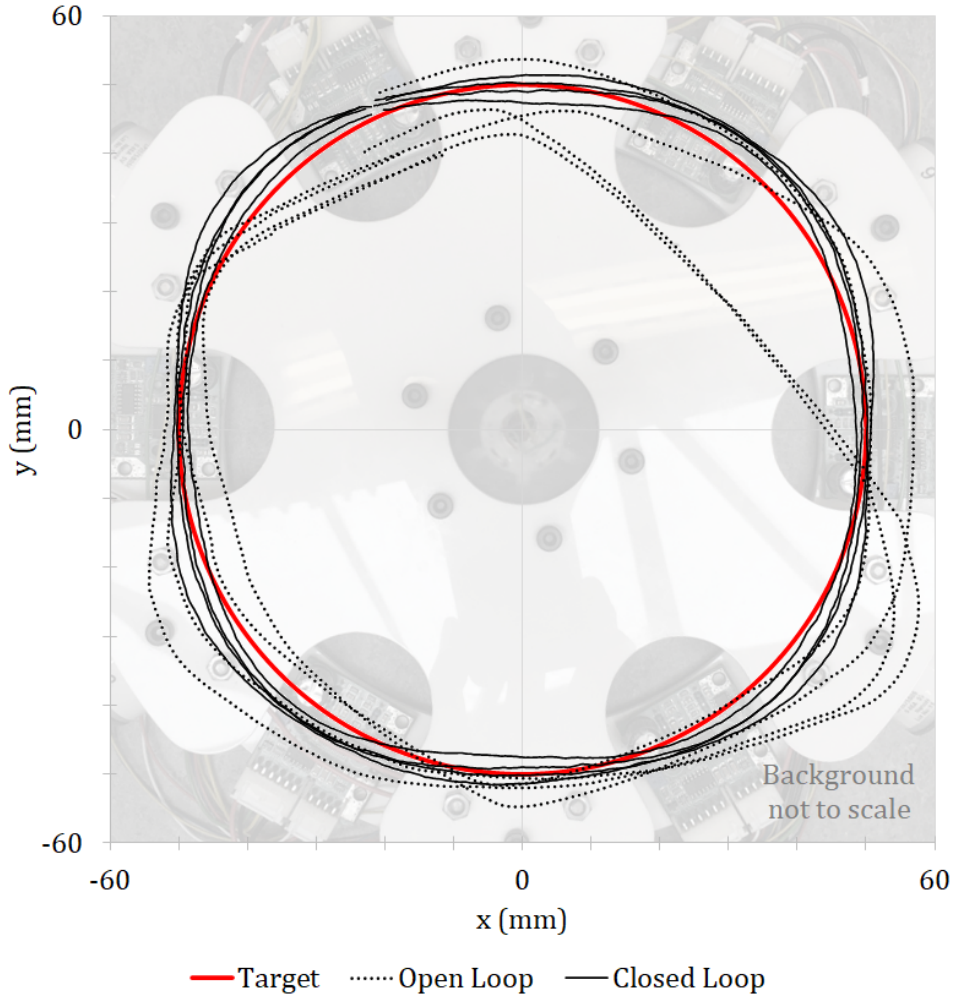


Figure 4.20: Comparison of open loop (dotted line) and closed loop control (solid line) accuracy for a two-segment, dual bend direction continuum manipulator following a 100mm diameter circular trajectory (red line). End effector speed was commanded at 5.24mm/s or 1 revolution per minute.

loop control results show a maximum error of 12.4% TCL and large jumps between start and end positions (greater than 10% TCL). The influence of the direction of tension of each tendon and actuator, visible as six distinct vertices in the open loop control data, is almost completely attenuated in the closed loop case. Likewise, the catastrophic effect of a small drop in tension in one of the proximal segment tendons (two of the passes with open loop control, Figure 4.20 top right) can be overcome by using feedback control with integral gain.

The results show a promising step towards low-cost, scalable position feedback for slender and compliant continuum robots.

4.5 Conclusions and future work

This chapter presents a novel methodology and application for a little-known type of resistive stretch sensor. The construction, characterisation and calibration of a tubular ionic liquid (conductive salt that is liquid at room temperature) hyper-elastic strain sensor are described and the sensor is applied as feedback for closed loop position control of a linear actuator, a simple continuum demonstrator and a complex continuum manipulator. The results show significant improvement in position accuracy over open loop control strategies such as those discussed in Chapter 3.

Tubular ionic liquid stretch sensors were constructed by filling thin pre-treated silicone rubber tubes with 1-methyl-3-octylimidazolium chloride - an ionic liquid that was found to be statically and electrically compatible with the sensor and conductor materials - and closed with gold electrodes at each end. Each sensor was characterised by subjecting it to stretch cycles and recording its electrical properties and exact elongation. The behaviour was described mathematically and approximated with a second order polynomial curve. Unique sensor constants were identified from each calibration and used to create the feedback transfer functions for control.

The results show that it is possible to use TILSS as feedback for position control of continuum robots, with laboratory demonstrations achieving errors as low as 1.5% of the total manipulator length. This work shows that it is possible to implement a low-cost, scalable position sensor for closed loop control of complex continuum actuators.

Further research on this area may endeavour to further miniaturise the tubular sensors and investigate the limits of small resistive sensors. While it is likely that signal-to-noise ratio will increase with lower diameter sensors, alternative options for resistance measurement such as high-frequency alternating current resistivity measuring hardware may be used to improve the performance of TILSS and their controllers.

Future work may also include the application of redundant sensors for temperature compensation, a consideration that becomes particularly important for longer robots with more degrees of freedom. The nature of resistive sensors often means that they are susceptible to temperature changes - indeed they are often used for temperature

measurement. A redundant sensor positioned somewhere on the circumference (or even central passage) of a continuum robot equipped with curvature-measuring sensors may be used to compensate for temperature and provide temperature readings for each continuum segment.

Finally, it may be possible to combine the closed loop control scheme described in this chapter with a method for reaction force control to accurately perform in-situ machining tasks such as those described in Chapter 3. This simultaneous control scheme is discussed in Chapter 6.

Chapter 5

New methods of force control for slender and compliant robots for in-situ machining

Detecting, measuring and controlling the forces between cutting tools and machined components is essential in circumstances where direct position control (e.g. depth of cut, feed speed and tool position) is inaccurate and/or impossible. This is particularly important when employing slender and compliant robots such as continuum robots, as even low contact forces can result in large deflections and small position errors can result in widely varying reaction forces. Figure 5.1 shows an example continuum manipulator with grinding end effector, where deflection from contact with a workpiece (estimated rest position shown as red outline), compounded with uncertainties in deflection due to weight and internal friction forces, results in uncontrolled machining force.

The challenging application of slender and compliant robots for machining presents a requirement for direct force measurement from the end effector. This chapter explores the use of airborne sound signals that result from the machining process to control the cutting force in closed loop for generating accurate machined features when performing in-situ robotic repair of complex installations. While the application of such a controller is intended for slender and compliant devices such as continuum robots, this chapter will

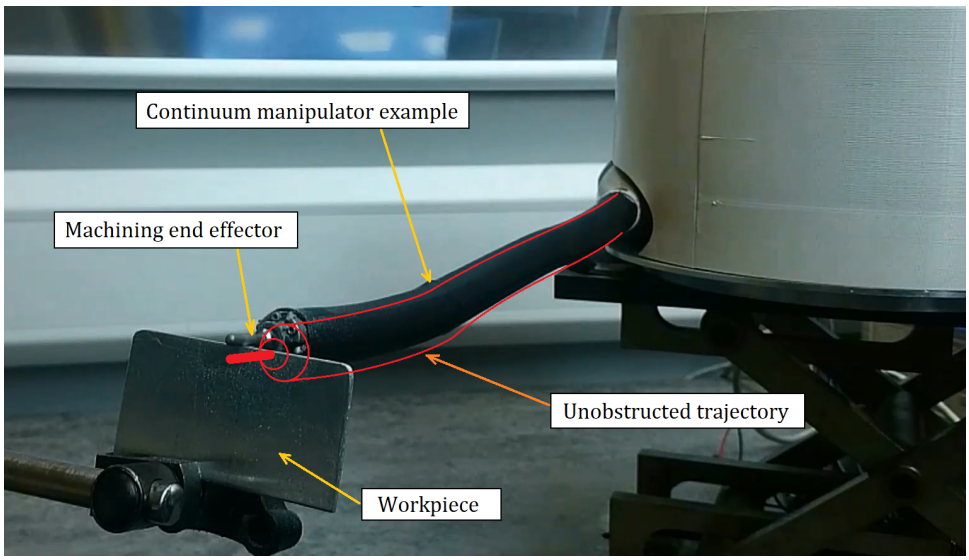


Figure 5.1: An example continuum manipulator equipped with a machining end effector for in-situ repair of high-value equipment (developed by [16]). Robot is deflected by contact during grinding operation on an aluminium sample. Red outline indicates the estimated position of the continuum robot without obstruction from the aluminium beam.

employ conventional jointed manipulators (Figure 5.2) as a way to isolate the uncertainty that arises from flexible stages, such as non-linear friction losses and curvatures, and create a robust force control methodology.

Sound signals generated during indentation at various cutting forces are analysed and used to calibrate a remotely mounted microphone sensor and signal processing control system. The power spectral density of the audible sound is used to estimate tool cutting force and the sound intensity used in turn to estimate the resulting process energy. The described controller uses intensity of sound to mitigate the effects of resonance with workpiece natural frequencies while controlling the spindle velocity of the tool based on the dominant audible frequency. The performance of the controller is validated using a representative test rig and demonstrated using a robotic arm to machine thin Ni-Cr-Co alloy cantilever beams with a miniature air-driven grinding tool.

5.1 Background

Conventionally, whenever possible, in-situ repair work on industrial installations such as gas turbine engines has been performed manually by use of specialist tooling with

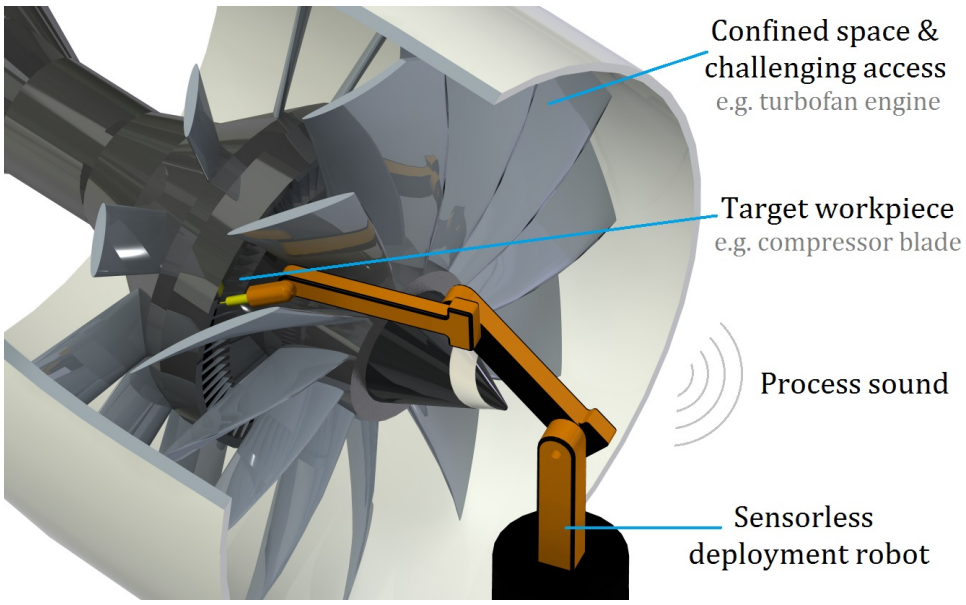


Figure 5.2: An example of in-situ repair of high-value equipment using robots with limited sensing capabilities to access difficult-to-reach components.

cutting, grinding and polishing end effectors to name a few. Due to this operational complexity there is growing interest in automating these repair interventions by using robotic instruments. As mentioned in previous chapters, chellenges in accessibility result in maintenance instruments that are long and slender [16, 45] which in turn limit the possibility to embed sensing systems (e.g. force or tactile) to support accurate reach of the target workspace. Thus, to ensure quality of the in-situ interventions, the probes must be equipped with miniaturised sensing systems, or assisted by remote sensors placed some distance away and using propagated signals (e.g. acoustic emission, light, sound) to optimise and control the in-situ intervention.

This work explores the use of high-speed, low-torque, air-driven grinding tools for material removal in confined spaces. The nature of the tool results in low contact forces and low material removal rates. For closed-loop force control to be achieved, the feedback method must be sensitive enough for this application.

As seen in the literature reviewed in Section 2.4.3, a number of approaches have previously been used to monitor machining properties using propagated signals. While airborne sound signals are more susceptible to distortion and noise, sensors that can be placed some distance away from the machining operation are more suitable for the in-situ

repair application. The objective of this work is to identify a method for closed loop force control that is applicable to sensorless robots and useful for repair of difficult-to-access industrial assets.

In this context, a robotic tool equipped with a method for online process monitoring using sound signals derived from the machining operation can be highly efficient for closed loop control of different operations (e.g. grinding, milling) in inaccessible and especially in blind workspaces. With such facilities in place, automated in-situ repair applications could be performed with precision and reliability.

5.2 Characterisation of sound features for force control

The predominant audible sound features that arise from a machining operation such as grinding can be predicted based on an understanding of the core phenomena. A method is described here to obtain and analyse the sound features and demonstrate that the sound emissions of a given system can be used for closed loop force control of a robot for in-situ grinding within remote spaces and without the need for additional sensing.

5.2.1 Description of audible sound emissions during grinding

The airborne sound generated during grinding using miniature air-driven tools is expected to come primarily from the following sources:

1. The sounds caused by periodic impacts between the abrasive elements or grits of the tool and the workpiece. The frequency of these contacts is dictated by the size and spatial distribution of the abrasive grains, the diameter, and the speed of rotation of the tool S. Common grinding tools operate at over 20sm/s (surface metres per second) [169] and have small ($<$ 1mm) grains that are randomly distributed resulting in ultrasonic white noise. Wear of the grinding burr influences the distribution of grits and affects this sound feature.

2. The sounds associated with the rotating turbine of the air-driven spindle and grinding tool. Cyclical events related to whole rotations of the tool such air passing turbine blades and oscillations of the grinding tool contribute to sound with a frequency that matches the speed of rotation. This can be verified using non-contact instruments such as laser tachometers.

3. The natural frequencies of the workpiece. The mechanical action of the grinding tool could excite the workpiece at its natural frequencies and it is possible to predict the resulting sound emissions using finite element analysis. This information can be supported with measurements acquired through impact testing and laser vibrometry equipments. Higher cutting forces result in more energy being transferred to the workpiece in the form of vibration.

4. The noise generated by the exhaust air from the air-driven spindle. The sound produced by the venting air is determined by the diameter and pressure drop across the exhaust holes. The range of noise frequencies produced by this exhaust air depends on the speed of rotation of the turbine [170].

5. The noise arising from echoes and interference with the surroundings. Complex industrial installations (such as gas turbine engines) present geometries that can reflect and distort sound, and thus could affect the power and direction of the signals. However, due to the high geometrical variety of workspaces where the robotic system for in-situ grinding can operate, interference effects are only be discussed in relation to the observations during closed loop testing.

It is documented [171] that air-driven high-speed spindles (such as those used in this work) have near-linear torque-speed relations. When employed with grinding tools, an increase in the forces associated with chip formation, ploughing of material, and friction between tool and workpiece [172] leads to a decrease in spindle velocity. Although the tangential and radial forces (F_T and F_R in Figure 5.3) also depend on factors such as workpiece material, feed speed v_f, depth of cut h, grit size and type of abrasive grains [169], the behaviour of a particular air spindle, tool and workpiece combination can be

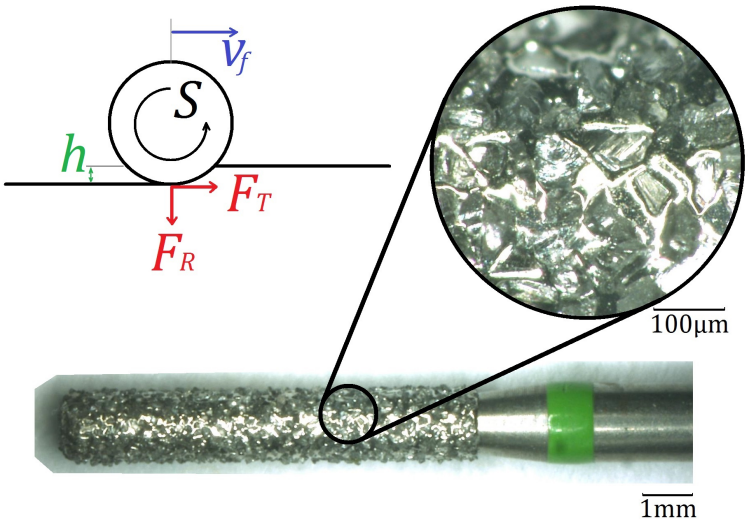


Figure 5.3: Representation of a small grinding tool driven by a miniature air-driven spindle and the forces, velocities and displacements of the tool relative to workpiece surface.

obtained experimentally. Hence, by identifying, tracking and controlling the sound frequency associated with spindle rotation speed (item two on the list above), it is possible to control grinding force in closed loop.

A theoretical torque/speed line can be obtained from the stalling torque τ_s and the idle spindle velocity S_{idle} of the turbine tool using Equation 5.1.

$$\tau = \tau_s - \frac{\tau_s * S}{S_{idle}} \tag{5.1}$$

The ratio of tangential force to radial force, $\mu = F_T/F_R$, changes depending on the level of engagement of the abrasive tool with the workpiece material. An increase in engagement coefficient leads to an increase of the tangential force observed for a given radial force, shown in Figure 5.4 as a change in F_R/S. This engagement coefficient can change as a result of increasing feed speed v_f at a given radial force F_R. Furthermore, tool wear and the resulting reduction in grit efficacy can also change the engagement coefficient, although quantifying this change is outside the scope of this work.

Given that the spindle speed can be measured by analysing the dominant sound frequencies (those associated with cyclical events), knowledge of the real torque-speed line can be used to indirectly estimate the radial force relative to a reference value and hence to enable closed loop force control of the grinding process.

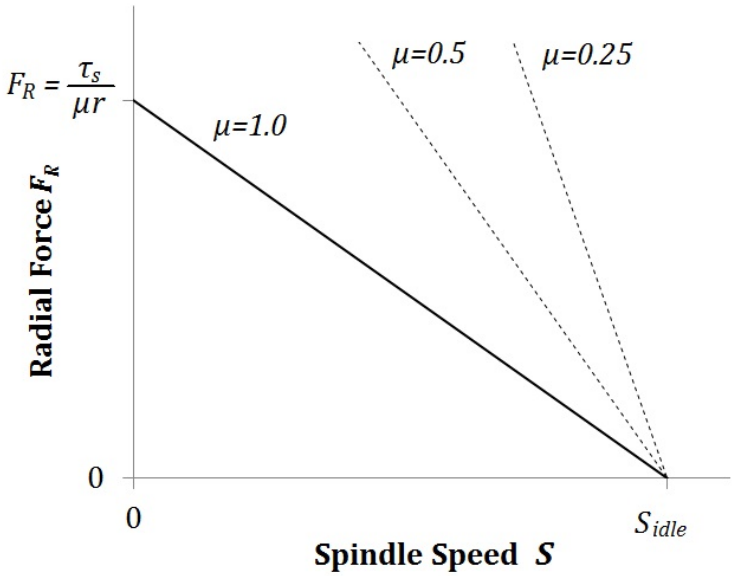


Figure 5.4: Theoretical dependence radial force v. spindle speed for an air turbine tool of radius r with engagement coefficient μ.

5.2.2 Acquisition of calibration data

Before implementing this approach on a robotic system for automatic grinding, a calibration test rig consisting of a grinding tool mounted on a pivoting arm with variable offset mass (Figure 5.5) was designed to obtain the sound signals associated with different levels of radial force F_R. The offset mass ranges from $0g$ to $135g$ with $45g$ increments, giving a range of radial contact forces of $0N$ to $1.32N$. The mass is isolated from the vibrations of the machining process by a spring-damper consisting of a wire rope isolator and a tension spring. An adjustable counterweight (mounted on a threaded rod on the opposite side of the fulcrum to the variable offset mass) is used to level the tool for a radial force close to 0 N when unloaded. When the air spindle is operating, the offset mass of the weights forces the grinding tool into the workpice with a force equal to the weights added, creating an indentation. In addition to the radial cutting force, the position of the contact along the length of the workpiece can also be adjusted and was randomised during the tests to nullify any effect of location of contact on the results. A summary of the equipment used in this chapter can be found in Appendix A.

A miniature air-driven spindle (*Presto Aqua Lux* NSK-Nakanishi) with a maximum idle (unloaded) speed of $350kRPM$ ($S = 5833Hz$) and a stalling torque of $\tau_s = 1.22mNm$

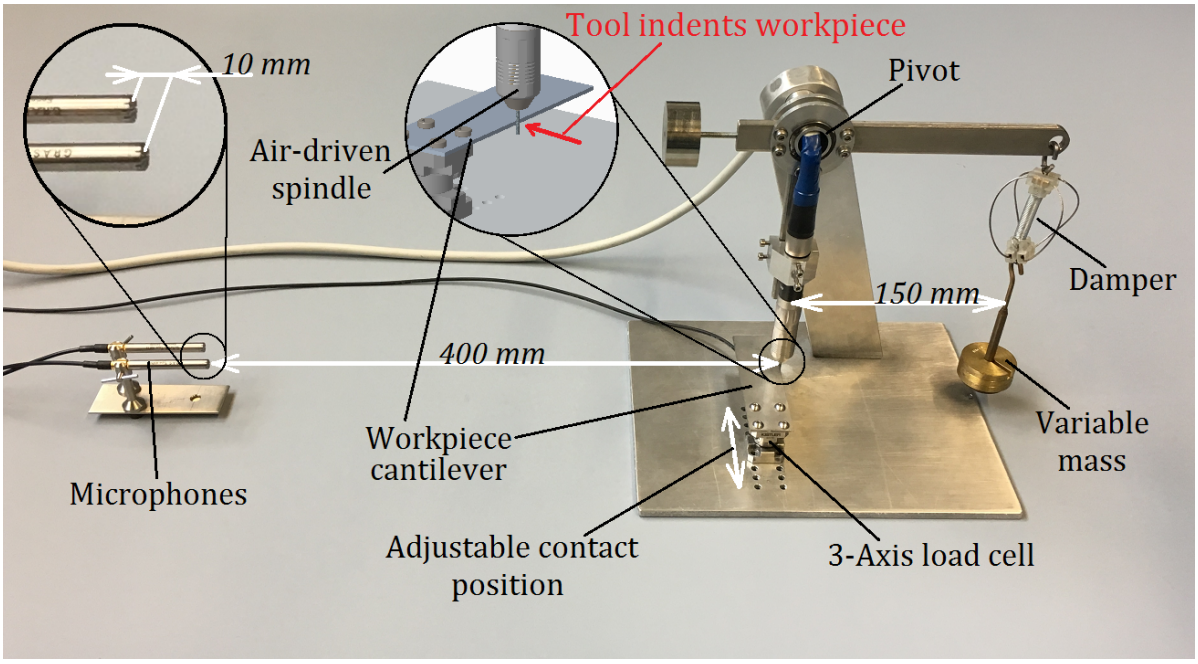


Figure 5.5: Test rig for monitoring audible sound signals during grinding at different radial force intervals. Variable offset mass was used to control the radial force. Two microphones were used to capture the sound and pressure gradient in the direction of propagation from the tool. A 3-axis load cell captured the calibration force data.

[171] was used to grind workpieces ($100mm$ x $30mm$ x $1.6mm$) made of Nickel-Chromium-Cobalt alloy. The workpiece was attached from one end as a cantilever such that the natural frequencies of the beam could be calculated and verified with ease. A new 1.6mm diameter $118\mu m$ grit electroplated diamond grinding tool (Edenta AG) was fitted to the spindle for each of the tests to nullify any effect of tool wear on the results.

A modal response analysis of the cantilever beams (modelled in conjunction with the dynamometer and constrained rigidly by the four attachment screws) was carried out using PTC Creo Simulate software and the results were experimentally validated using a tap testing apparatus (with the cantilever secured rigidly with four attachment screws to a steel block held tightly in a clamp), the results of which can be seen in Figure 5.6. FEA and tap test natural frequencies matched to within 7.5%.

The workpieces were mounted on a 3-axis dynamometer (*9317B* Kistler) with a sensitivity of 25.71 pC/N in X an 25.48 pC/N in Y to measure the cutting forces F_R and F_T respectively during calibration grinding tests. The force sensor consists of three orthogonal piezo elements that yield an electric charge which is proportional to the

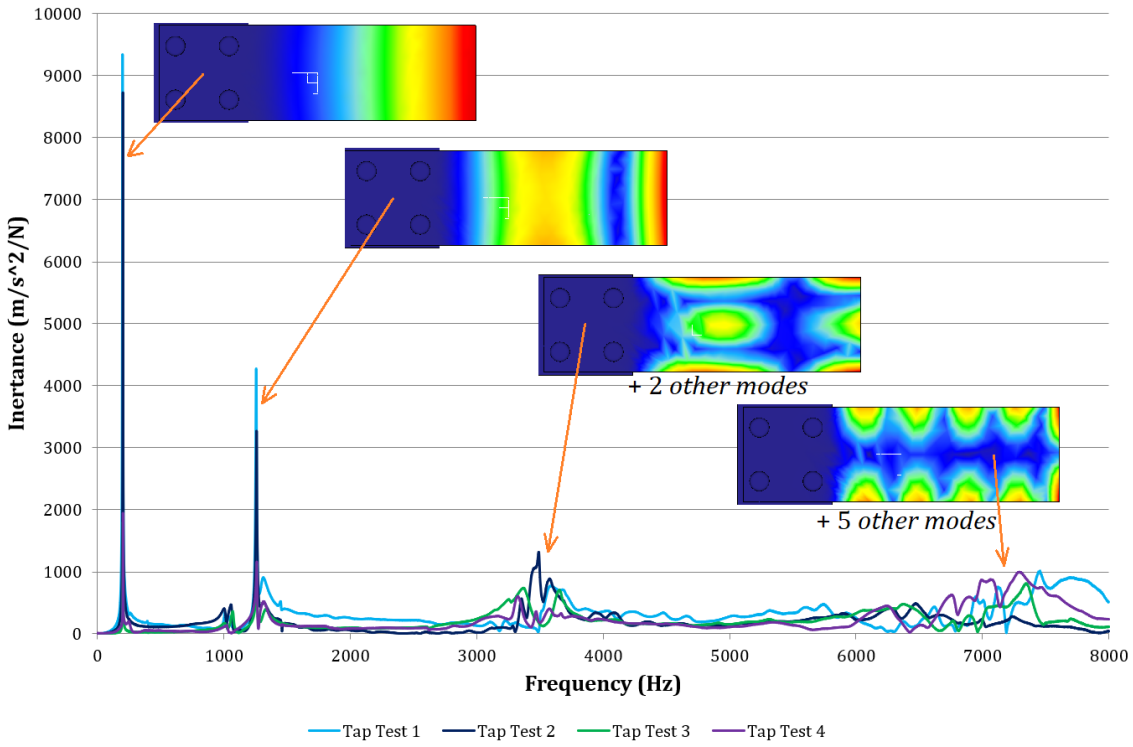


Figure 5.6: Tap test frequency response of cantilever beams and corresponding modes of vibration as simulated in Creo Simulate software. Vertical axis shows the ratio of workpiece acceleration to hammer force input (inertance or accelerance).

force. The three axes are not configured to measure torsion, but the high rigidity and high maximum moments ($5Nm$ about z axis) allow the sensor to accurately measure forces acting on the cantilever beam some distance from the sensor axis. The dynamometer was used with its low-range settings ($\pm$60N in X and Y). A Kistler multichannel charge amplifier (Type 5017), with an effective resolution for this sensor of 0.39mN, was used throughout this work. The maximum drift for the charge amplifier is 0.03pC/s, or 0.0012N/s and a time constant of $10,000$s was used. Preliminary trials with this setup showed a background noise standard deviation of 1.95mN and an average signal-to-noise ratio during grinding of 32.2 dB.

Two *40PH CPP* free-field array microphones with *12AL CPP* pre-amplifiers (G.R.A.S. Sound & Vibration), with operating frequency range between 10Hz and 20kHz (frequencies above and below these values are outside the frequency response of the microphone and will not interfere with measurements or be detectable), were positioned 400 mm from the spindle. This distance was chosen to limit free-field

spherical propagation loss and remain realistic for an in-situ repair operation. Two microphones were used with a 10 mm gap between them to obtain the pressure gradient between two points for the intensity calculation. Sound signals were acquired for 0.1 seconds at 50kHz using an *EMP373* portable computer (ACME) equipped with a *PCI-6229* IO board (16 bit, 250kS/s) and a *BNC-2110* BNC breakout board (National Instruments).

Tests were repeated eighteen times for every level of radial force in a random order as shown in Table 5.1.

Table 5.1: Description of calibration experiment trials.

Factor	No. of Levels	Description of Levels
Radial cutting force	4	$\approx 0N$ $0.4N$ $0.8N$ $1.2N$
Position of contact	3	Three points along the workpiece $30mm$ apart
Repetitions	6	

For every trial, the air spindle was started away from the workpiece to allow it to reach idle speed and placed to rest against the workpiece with no transverse movement. Sample signals were collected two seconds after the tool contact with the workpiece to ensure that any vibration of the offset mass had been attenuated by the damper. With the charge amplifier settings used, there was no noticeable drift or loss of force signal fidelity.

5.2.3 Acoustic sensor calibration

After collecting sound samples from multiple grinding indentations, the following methodology was followed to extract useful sound features for force control.

Dominant audible frequency

The power spectral density (PSD) of the sound in V^2/Hz was calculated to detect the frequencies associated with the sources described in Section 5.2.1. It was observed that, generally, the audible frequency with the highest magnitude is associated with the rotation of the spindle (as seen in the example shown in Figure 5.7). Other peaks are associated with the resonant frequencies of the workpiece and the sound of exhaust air. To capture those frequencies related to spindle rotation (for closed loop control), a Butterworth highpass filter was implemented in software to remove frequencies lower than 500Hz, as they can be ignored as background noise. Force was acquired from the dynamometer in the F_R direction to be correlated to the sound monitored spindle speed.

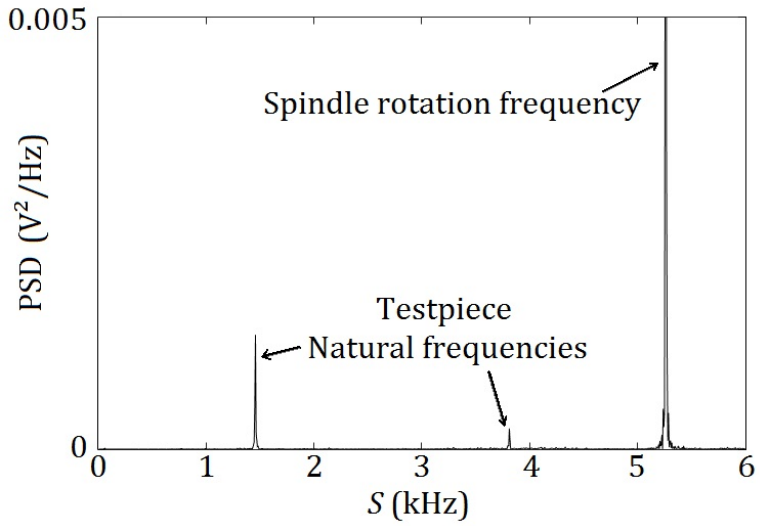


Figure 5.7: Power spectral density plot at audible frequency S for a typical sample with electroplated diamond grinding tool.

The plot of radial force against spindle speed (Figure 5.8) shows that the slowing of the tool rotation at increased radial force can be measured using sound features (PSD peaks). The increased variance (horizontal error bars show one standard deviation) at high radial forces can be attributed to the sound arising from the natural frequencies of the vibrating workpiece overpowering the sound of the rotating spindle, making it difficult to track the spindle speed.

The change in engagement coefficient from $\mu = 0.25$ to $\mu = 0.9$ observed in Figure 5.8 is attributed to a substantial rise in tangential force due to an increase in depth of cut

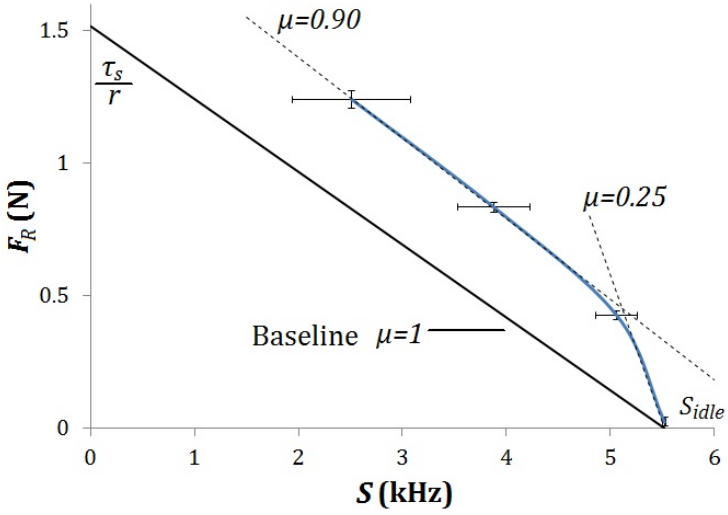


Figure 5.8: Measured radial force F_R vs. spindle speed S (dominant audible frequency). Dotted lines show engagement coefficient μ during sliding friction ($\mu = 0.25$) and after the tool's abrasive grains engage the workpiece ($\mu = 0.90$).

and in energy transferred to the workpiece during ploughing [169]. The measurements are also consistent with the observations made by [172].

It is expected that tool wear will influence the engagement coefficient during operation. The rate at which this happens is explored in the closed loop control section. While tool wear does have an effect on the relation between audible features and contact force, the machining task under investigation is small (approximately 10% to 20% of the tool life) and the contact is light enough (usually less than 50% of stall forces) that electroplated diamond burrs do not experience any significant abrasive wear. The effect of wear may become important and require compensation for operations requiring more prolonged or aggressive grinding; however, when addressing in-situ repairs of industrial assets priority will often be given to replacing inexpensive tools for optimal performance.

Sound intensity

Sound intensity is associated to the energy carried by acoustic waves as they cross an area of interest and it can be calculated by measuring the pressure gradient between two points along direction x perpendicular to this area [173]. Hence, the sound intensity between

points a and b along x can be expressed as:

$$I = 10 \log_{10} \left(\frac{\frac{P_a + P_b}{2\rho \Delta x} \int (P_a - P_b)\, dt}{I_0} \right) \tag{5.2}$$

where Δx is the distance between points a and b, P_a and P_b are the pressure levels at a and b respectively and ρ is the air density. The conventional reference intensity value of $I_0 = 1pW/m^2$ is used in this study for intensity calculations [173]. The distance between the two microphones Δx was set to 10mm, as it must be smaller than the shortest wavelength expected (approx. 17mm). Points a and b point in the direction of the workpiece as shown in Figure 5.5.

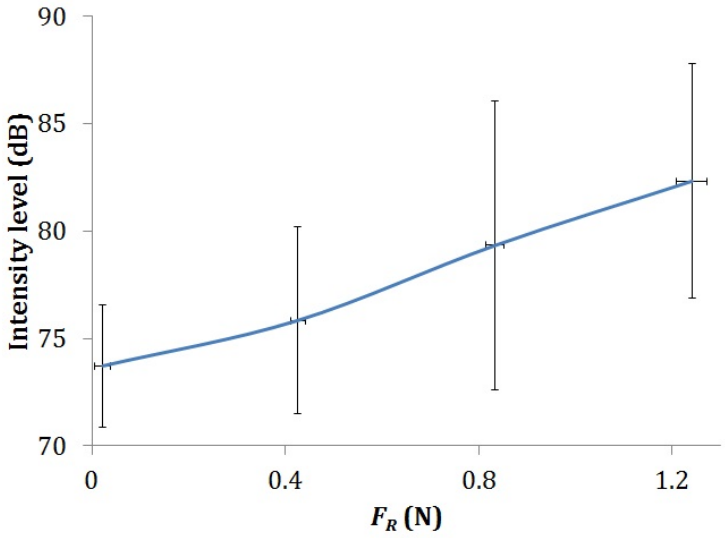


Figure 5.9: Sound intensity level I vs. measured radial force F_R. Sound intensity increases with force, variance between tests is high.

The overall sound intensity level was found to increase with radial force at a rate of approx. 6.5dB/N, as shown in Figure 5.9 where each marker represents eighteen data points. This rise in sound intensity can be attributed to an increase in energy transferred to vibration of the workpiece, vibration of the tool and to exhaust air at higher pressures. Although the baseline intensity varied between trials it was observed that, when the grinding tool decelerated enough to match a workpiece natural frequency, the measured sound intensity increased by 5 to 10dB. This can be seen to some extent in the variance of the measurements shown in Figure 5.9, particularly at 0.82N where the tool approached

a resonant frequency of 3.65kHz. Hence, despite being too variable for closed loop force control, intensity measurement can be used to identify and quantify workpiece resonance.

Other sound features

Other sound features were tested for correlation with machining forces, albeit with less success than those mentioned in previous subsections. Sound intensity level at workpiece natural frequencies and direct measurement of signal amplitude were investigated as options for machining force feedback.

It has been mentioned that a rise in sound intensity can be attributed to an increase in energy transferred to vibration of the workpiece. It was therefore expected that sound signals filtered around beam natural frequencies and analysed for pressure gradient and intensity may show stronger correlation to machining force than overall airborne power. This theory was tested at four natural frequencies (identified using FEA and verified using tap tests as shown in Figure 5.6).

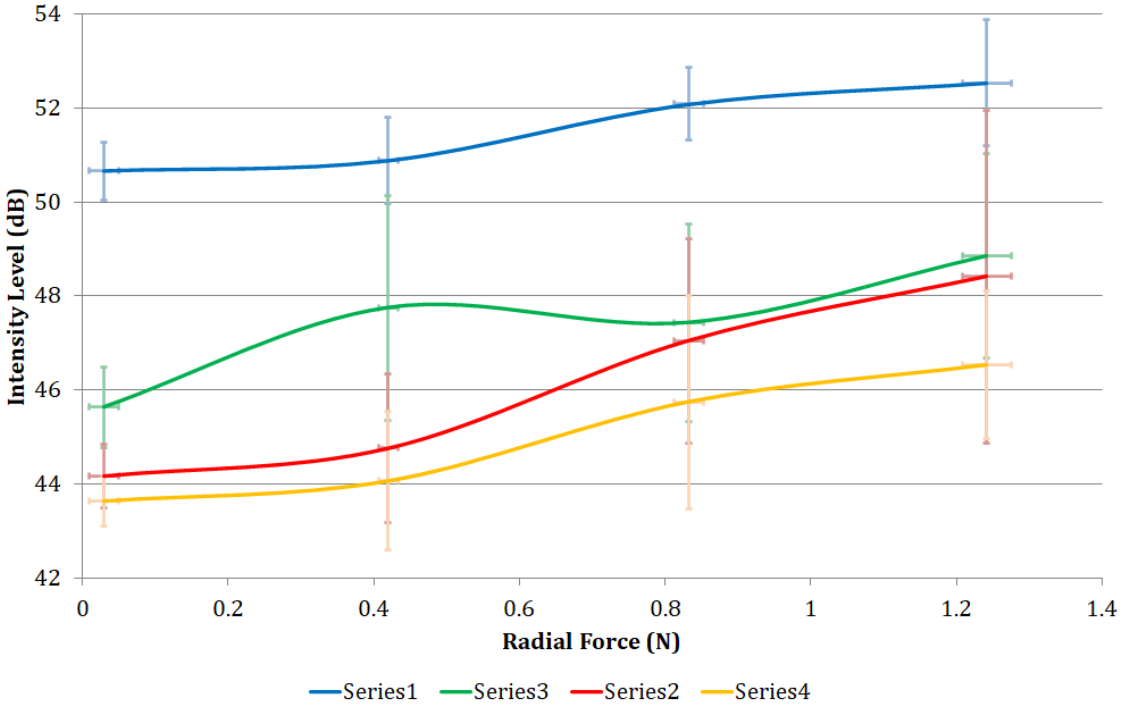


Figure 5.10: Sound intensity level vs. measured radial force for discrete frequencies. Correlation is weaker at low forces.

A $300Hz$ wide bandpass filter centred around each of the four selected natural frequencies ($200Hz$, $1360Hz$, $3550Hz$ and $7450Hz$) was applied to the sound samples of

each trial. The resulting signal pairs were then used to calculate intensity level using Equation 5.2. The resulting trends (shown in Figure 5.10) suggest that, while there is clear correlation between contact force and intensity at some frequencies, variability in energy transfer (probably due to resonance) results in different points of inflection and peaks for each natural mode of vibration. The effect is that none of the individual signals provides adequate signal-to-noise ratio for the entire range of forces.

A similar test was carried out using raw signal amplitude instead of intensity, with the advantage of requiring only one microphone. The root mean square of the normalised signal was calculated using the expression

$$V_{RMS} = \sqrt{\frac{\sum_{i=1}^{n} (V_i - V_{mean})^2}{n}} \tag{5.3}$$

where n is the number of discrete voltage values in one sample (in this case 50000) and V_{mean} is the average voltage for the duration of the sample.

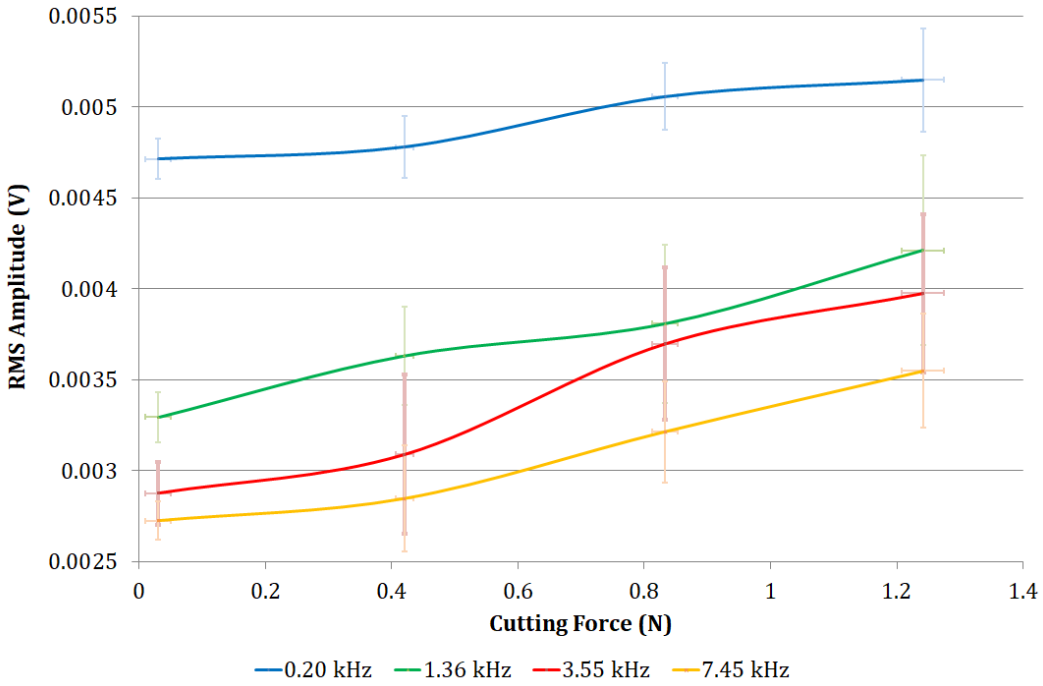


Figure 5.11: Sound signal RMS voltage vs. measured radial force for discrete frequencies.

The resulting trends (shown in Figure 5.11) are similar to the intensity values, although with marginal improvement in signal-to-noise ratio. The improvement is attributed to lower susceptibility to filter damping. The damping effect of filters on

sound signals is magnified by the use of dual-microphone pressure gradients in the intensity calculation. The use of single microphone methods also leaves the method susceptible to environmental noise coming from any direction.

Another disadvantage of using energy (from sound intensity or RMS voltage) at specific workpiece natural frequencies as a force signal is the added calibration requirements. Reliance on such signals would mean a requirement to identify the natural frequency of every workpiece before a repair. While it may be possible to calculate these using finite element analysis for known components, unknown features or damaged features would require physical testing. When operating in confined spaces it is unlikely to be possible to carry out the necessary frequency response tests.

It is clear that the most suitable signals are dominant frequency (from power spectral density) and overall energy from intensity of sound. The dominant sound frequency can therefore be used to predict radial force, while the sound intensity can be used to detect when workpiece natural frequency vibrations may overpower the sound of the spindle rotating. Together, these sound features can be used as robust feedback for a novel closed loop force controller as discussed in the following section.

5.3 Closed loop force control using sound features

Early trials using only the dominant frequency (spindle speed) as a controller input resulted in inevitable loss of control at moderate forces due to more energetic workpiece vibration frequencies overpowering the spindle velocity. The outcome varied randomly between driving the spindle into the workpiece (causing a stall) or retracting the spindle fully away from the workpiece. Subsequent improvements led to the control strategy outlined in this section.

To use sound features for closed loop force control, the controller must be calibrated using ambient noise and the sound of the spindle running at idle (unloaded) speed. The controller can then be tuned to achieve the desired behaviour.

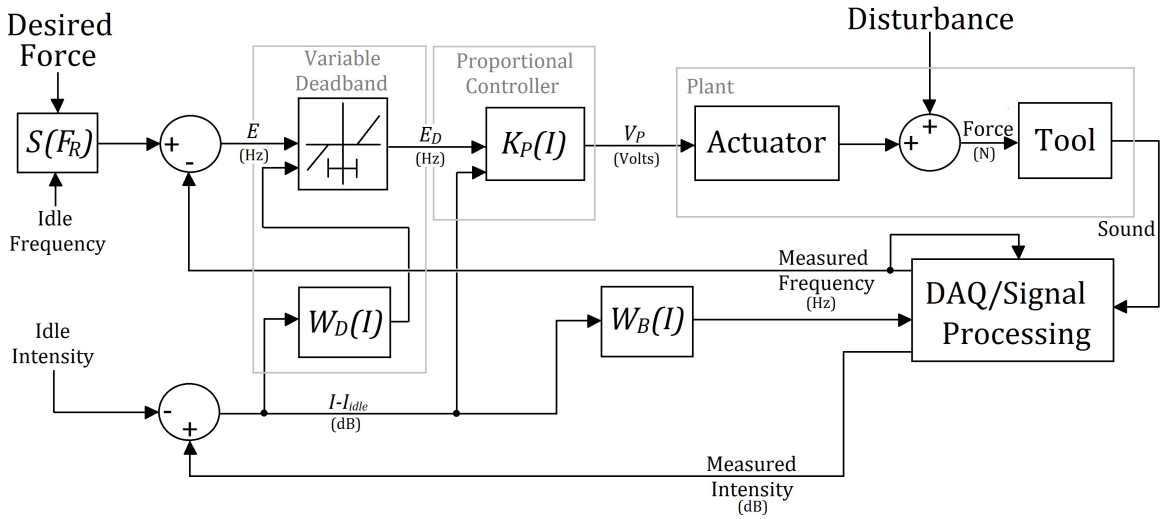


Figure 5.12: Proposed closed loop control of radial grinding force with single actuator using audible sound features as feedback. $W_D(I)$, $K_P(I)$ and $W_B(I)$ determine the effect of intensity on deadband width, proportional gain and bandpass filter width respectively.

5.3.1 Controller calibration methodology

To calibrate the controller a measurement of sound with the spindle running unloaded was taken to identify the dominant frequency (idle spindle speed) from the power spectral density. This idle spindle speed is used as a reference value for the case $F_R = 0$N. The data was then analysed to obtain the idle sound intensity using Equation 5.2. The idle intensity gives an indication of the total energy coming from the grinding process as well as the distance between the microphones and the source. Small variations in this distance during operation do not affect the performance of the controller after calibration, as the intensity is expected to fluctuate naturally. However, if the distance between the workpiece and the microphones is expected to change significantly during operation (such as when machining a large feature), the propagation intensity losses associated with distance must be taken into account. In the work undertaken here, the small variations in machining distance during operation do not change intensity enough to affect the controller.

A bandpass filter centred around the highest peak of the PSD of the signal is then implemented. The value of frequency at the centre of the filter varies on each iteration of the controller, such that when applied to subsequent measurements, the filter tracks the frequency associated with spindle speed S as it slows down or speeds up, provided that the changes are gradual enough to remain within the filter bandwidth.

5.3.2 Closed loop controller design

The proposed control architecture is a proportional controller with variable deadband width and variable gain (Figure 5.12). The controller inputs are the target force and the calibration constants for idle spindle speed and idle sound intensity. The difference between the desired spindle speed (the setpoint) and the measured S is multiplied by a proportional gain to obtain a value to drive the plant actuator (e.g. an analogue voltage signal). The actuator affects the radial force between the air-driven tool and the workpiece, changing the sound of the grinding process. The data acquisition and control equipment captures and processes the signals from the microphones to obtain values of frequency and intensity for the following control loop. The microphones' response frequency is 20 kHz (with a drop of $10dB$ by 25kHz), and sound is sampled at 50 kHz. Due to the length of the captured signal on each iteration ($0.1s$ to allow enough data for PSD and filters robustness), the effective frequency of the control loop is 10Hz. Hence, the response of the force controller to perturbations is attenuated at frequencies higher than approximately 5 Hz.

Target Frequency

It was assumed that the engagement coefficients during light contact ($\mu_1 = 0.25$) and grinding ($\mu_2 = 0.9$) remain constant (negligible tool wear and feed speed) regardless of the idle velocity of the tool. In circumstances where tool wear is significant μ_2 can be defined as a variable that changes with time, ground distance and material removed according to further calibration experiments. The gradual transition between the two slopes occurs at radial force F_{eng} and can be approximated using a smooth interpolation function of the form

$$f_{int} = \frac{1 + \tanh\left(k\left(F_R - F_{eng}\right)\right)}{2} \tag{5.4}$$

where $k \in \mathbb{R}$ and determines how gradual or abrupt the transition is.

Interpolating the two engagement coefficient lines gives an equation of best fit (5.5) that can be used to identify the target spindle speed S based on a desired radial force F_R, and to be used as a setpoint during closed loop control (Figure 5.12).

$$S = S_{idle}\left(\left(1 - \frac{r}{\tau_s}F_R\mu_1\right) + \frac{1+\tanh\left(k\left(F_R - F_{eng}\right)\right)}{2}\left(\frac{r}{\tau_s}\left(F_R\left(\mu_1 - \mu_2\right) + F_{eng}\left(\mu_2 - \mu 1\right)\right)\right)\right) \tag{5.5}$$

A value of 4 was chosen for k to achieve the smooth transition seen in Figure 5.8.

Variable Deadband

A deadband with variable width is introduced to make the controller capable of ignoring variations in frequency resulting from small disturbances in force during machining without excessively lowering the proportional gain. Here, an increase in sound intensity indicates that the workpiece is vibrating with more energy at its natural frequencies. If the spindle velocity approaches an overpowered natural frequency, the controller will mistake the natural frequency for a change in tool speed and take undesired corrective action. The effect of this natural frequency can be minimised by making the width of the deadband W_D a function of sound intensity I and idle intensity I_{idle}. Therefore, the input error to the proportional controller (see Figure 5.12) can be expressed as:

$$E_D = \begin{cases} E + \frac{W_D(I)}{2} & \text{for } E < -\frac{W_D(I)}{2} \\ 0 & \text{for } -\frac{W_D(I)}{2} \leq E \leq \frac{W_D(I)}{2} \\ E - \frac{W_D(I)}{2} & \text{for } \frac{W_D(I)}{2} < E \end{cases} \tag{5.6}$$

where E is the difference between the setpoint frequency and the measured frequency; E_D is the error used for proportional control. The deadband width $W_D(I)$ has upper and lower saturation limits σ_{HD} and σ_{LD} respectively and is given by:

$$W_D(I) = \text{sat}\left[(I - I_{idle}) * K_D\right]_{\sigma_{LD}}^{\sigma_{HD}} \tag{5.7}$$

where $\text{sat}[x]_L^H = \max(L, \min(H, x))$. The values of deadband gain K_D and other constants are shown in Table 5.2.

Table 5.2: Control constants used in closed loop controller tests.

K_D	35	K_P	0.14	K_B	45
σ_{HD}	150	σ_{HP}	0.6	σ_{HB}	250
σ_{LD}	75	σ_{LP}	0.1	σ_{LB}	100

Proportional Controller

Similar to the deadband, the proportional gain constant K_P is tuned to lower the proportional gain of the controller when the intensity of sound exceeds a given threshold above idle intensity, preventing large inputs by the actuator when faced with resonant interference. Hence, the effective control signal or voltage from the proportional controller V_P is given by:

$$V_P = E_D * \text{sat}\left[(\sigma_{HP} + \sigma_{LP}) - (I - I_{idle}) * K_P\right]_{\sigma_{LP}}^{\sigma_{HP}} \tag{5.8}$$

where σ_{HP} and σ_{LP} are the upper and lower bounds of the proportional gain and sat[] is the saturation function. The ouputs of the controller are a direction signal and pulse width modulation signal to the actuator H-bridge. A proportional controller was chosen over a PI, PD or PID controller due to the relatively high latency caused by the acquisition of sound signals. The introduction of integral or derivative terms was not found to improve stability in this case (see future work). However, if the actuation used position control rather than velocity control, an integral term would be essential for force tracking.

Plant

The output voltage/signal from the control hardware drives an actuator (shown in Figure 5.13) that moves the tool towards or away from the workpiece, changing the radial force acting on the tool and hence the depth of cut. The plant is the physical system and can be described as a number of processes in series including backlash, actuator response time, robot kinematics, tool torque/speed characteristics and airborne signal time delays and losses (Figure 5.12).

Data Acquisition and Signal Processing

Every 0.1 seconds, the signal from the two microphones (sampled at 50kHz) is analysed to obtain the intensity of sound coming from the workpiece (Equation 5.2). A Butterworth bandpass filter centred around the dominant frequency calculated on the previous measurement S_{z-1} ignores any sound that is not related to the spindle rotation, and provided this speed has not changed dramatically since the previous measurement, the highest PSD of the filtered signal gives the dominant frequency of the current measurement S_z. Like the variable deadband and proportional controller, a bandwidth function, $W_B(I)$, controls the width of the bandpass filter used to isolate the spindle speed frequency from background noise. When the energy of the workpiece vibration rises due to resonance or changes in background noise, the bandwidth narrows to further isolate the signal from the noise. The bandwidth function, $W_B(I)$, can be defined as:

$$W_B = \text{sat}\left[(\sigma_{HB} + \sigma_{LB}) - (I - I_{idle}) * K_B\right]_{\sigma_{LB}}^{\sigma_{HB}} \tag{5.9}$$

where σ_{HB} and σ_{LB} are the upper and lower limits of the filter width, the values of which are shown in Table 5.2.

In summary, the microphones listen to the process and a bandpass filter isolates the frequency associated with the rotation of the spindle. On each control cycle, the bandpass filter moves to centre around the highest power frequency, effectively tracking the spindle speed. As the tool slows down and excites workpiece natural frequencies, sound intensity increases and the controller reacts by pre-emptively increasing the deadband, lowering the proportional gain and narrowing the bandwidth of the filter, reducing the risk of a natural frequency being mistaken for the spindle rotation. The spindle velocity is controlled in closed loop to achieve the desired radial force.

5.3.3 Experimental validation of the controller

The controller design described in Section 5.3.2 was implemented on *LabVIEW 2014* software at a rate of 10Hz using the control constants outlined in Table 5.2. The EMP373

portable computer equipped with a PCI-6229 IO board (described in previous sections) was used to gather data and send control signals to the actuators. The operation of the controller was verified using a test rig (Figure 5.13) and demonstrated using a robotic arm in an environment resembling a complex industrial enclosure.

Controller performance tests

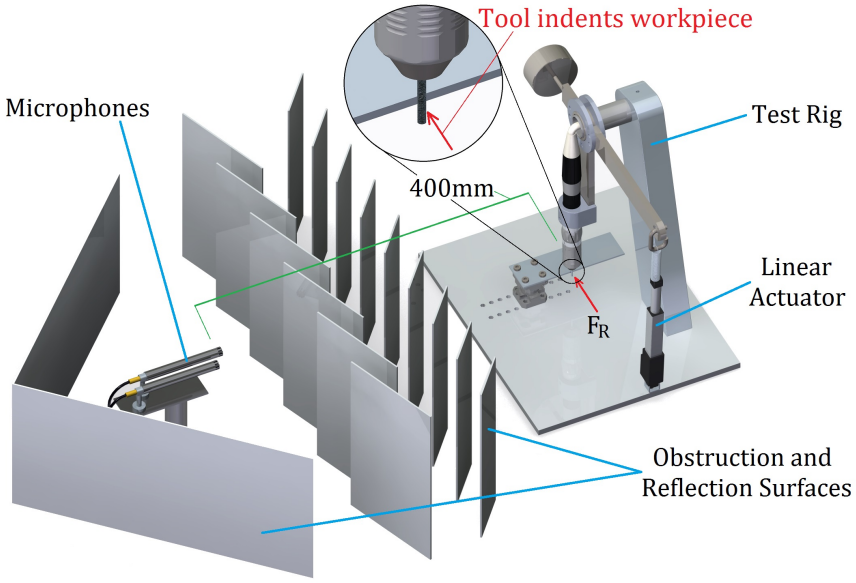


Figure 5.13: Test setup for controller validation. Microphones are separated from the source of the sound by a number of obstruction and reflection surfaces during some tests.

The performance of the controller was initially validated using the cantilever test rig to measure the radial force and material removal rate of the grinding tool with and without closed loop force control. For each trial the tool contacted the workpiece for 60 seconds, the contact forces were measured with the *9317B* dynamometer and the volume of removed material was calculated by measuring the size of the indentation using a *VHX-100* digital microscope (Keyence Corporation) as shown in Figure 5.14.

The trials at constant radial force were carried out using the offset mass test rig (Figure 5.5) at six radial force intervals from 0.22 to 1.32N (increments of 0.22N). The offset mass was then replaced with a *L12-50-100-12-P* DC geared linear actuator (Actuonix Motion Devices) for the tests with closed loop force control (Figure 5.13) at four radial force targets from 0.3 to 1.2N (increments of 0.3N). When the air spindle is operating, the linear actuator forces the grinding tool into the workpiece creating an

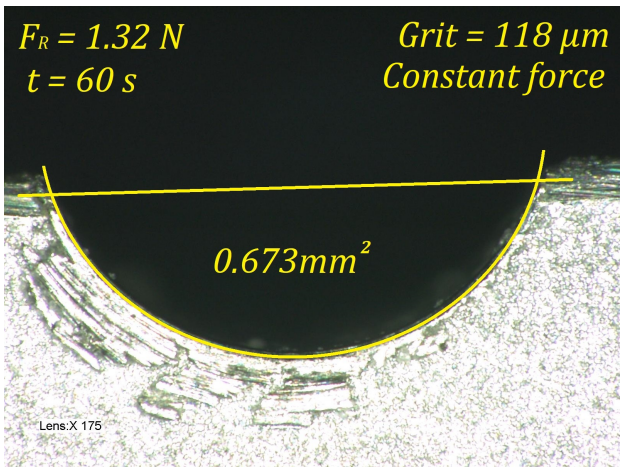


Figure 5.14: Material removal rate experiment sample for EPD tool at constant radial force force of 1.32N taken with Keyence VHX-100 digital microscope at 175X magnification.

indentation. The closed loop force control trials were conducted first with direct line of sight (no obstructions) between the microphone and the workpiece. Finally, the same experiments were completed with reflection and obstruction surfaces resembling the stator and rotor blades of an aeroengine shown in Figure 5.13, to determine whether such obstacles affect the controller. All tests were repeated nine times.

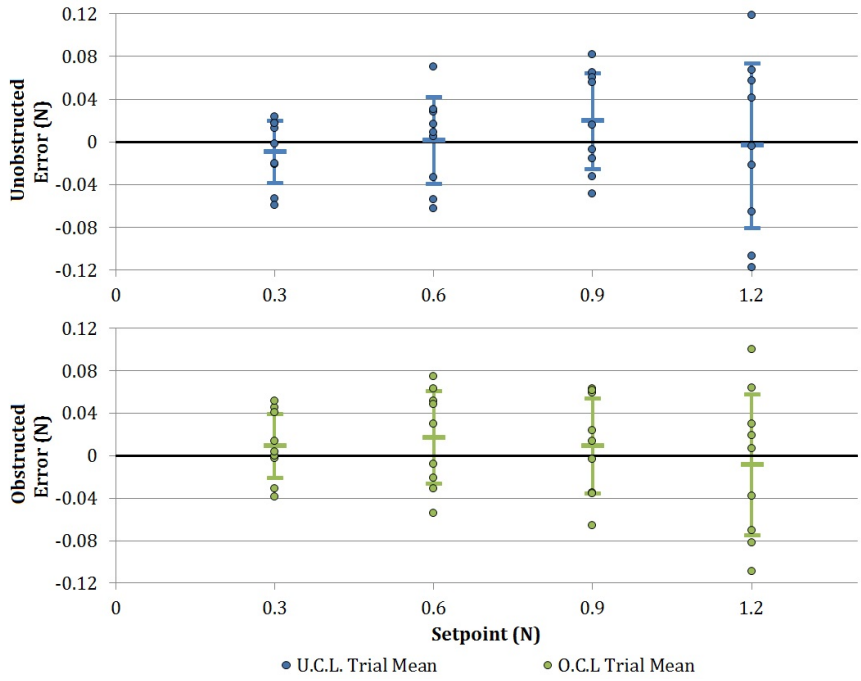


Figure 5.15: Closed loop radial force controller performance for 72 cutting trials, each lasting 60 seconds. Top sub-plot shows unobstructed closed loop (UCL) trials, bottom sub-plot shows obstructed closed loop (OCL) trials. Markers indicate mean force error for a given trial. Bars indicate standard deviation.

Table 5.3: Standard deviation values for obstructed and unobstructed closed loop control tests.

Setpoint (N)	Unobstructed st. dev.	Obstructed st. dev.
0.3	0.029	0.030
0.6	0.041	0.044
0.9	0.045	0.045
1.2	0.077	0.066

Figure 5.15 shows the radial force deviations observed during closed-loop control at each target force. Deviations were calculated by comparing the mean force during each trial to the desired force. Bars on the plot shows the standard deviation for each setpoint, also shown in Table 5.3. The results show that the controller achieves effective tracking, with the worst performance characterised by a precision (standard deviation) of $0.08N$ (unobstructed $1.2N$) and a trueness (average mean error) of $0.02N$ (unobstructed $0.9N$). Hence, the sensor is said to have an accuracy of $0.08N$.

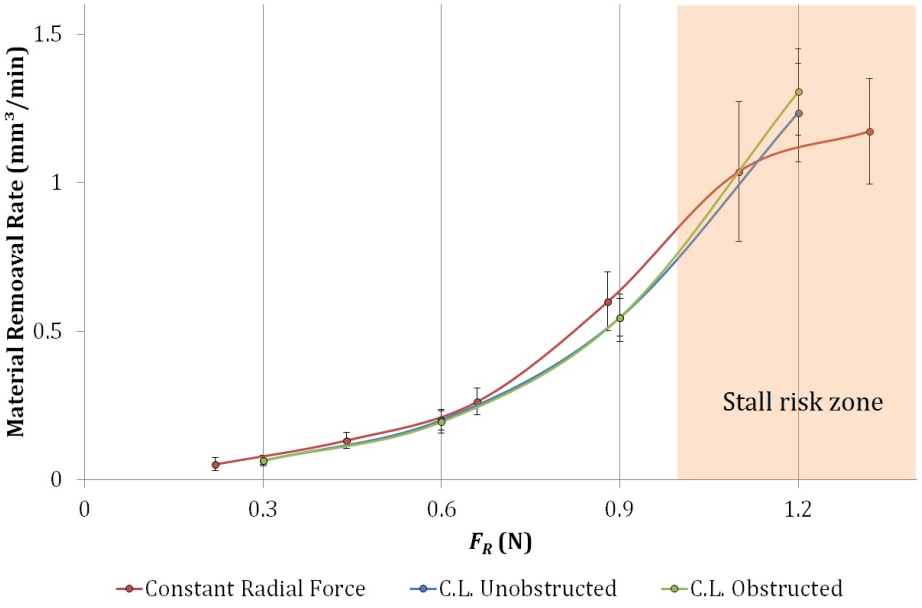


Figure 5.16: Material removal rates at known radial forces and using airborne sound features for closed loop radial force control. Tool was found to stall at forces greater than $1.0N$.

The material removal rates achieved by the acoustic closed loop force controller (Figure 5.16) also align closely with the rates measured at known radial forces. This demonstrates that the closed loop control of spindle velocity using sound features

provides an accurate way of controlling radial force during grinding. No substantial difference was observed between obstructed and unobstructed trials.

A stall risk zone of the air driven spindle was defined at radial forces greater than 1.0N. Contact force was found to oscillate significantly within the stall risk zone, often resulting in loss of power and void results. Despite this, the mean force of successful trials closely approaches the desired force, suggesting that regardless of the variance in frequency during calibration (attributed to oscillations in the offset mass setup), the calculated engagement coefficient closely describes the real system.

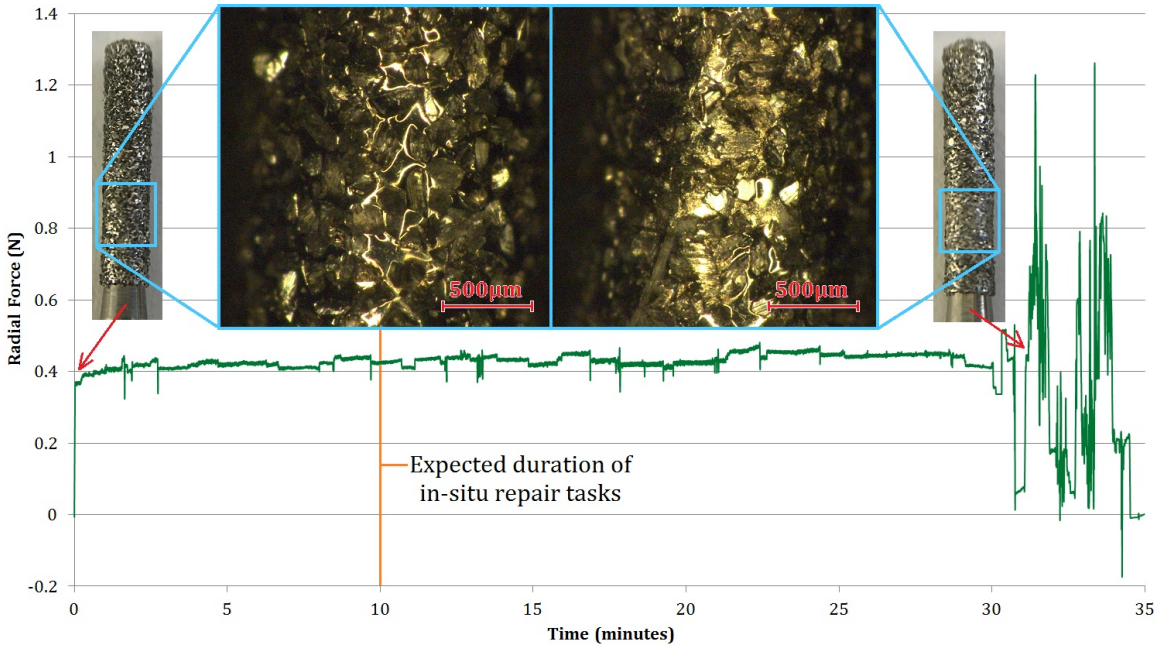


Figure 5.17: Tool wear experiment results show radial force tracking works effectively until control is lost at excessive wear levels. Inset figures show worn abrasive grains in area of contact.

To evaluate the susceptibility of the proposed controller to tool wear, the cantilever test rig (Figure 5.13) was used to indent a workpiece at constant force using acoustic feedback force control for a long period of time. The contact force was set to 0.4 N and the burr was left in contact with the workpiece until a change in behaviour was observed. Contact was concentrated to a 1.6mm portion of the tool to accelerate wear (ordinarily the entire length of the burr would be used). The results shown in Figure 5.17 indicate that force tracking remains effective far beyond the expected duration of in-situ tasks, with tool wear that far exceeds the threshold at which burrs would ordinarily be replaced.

After 30 minutes of continuous machining the controller was unable to track the frequency and started to overshoot widely, likely due to the reduced engagement coefficient.

Radial force was found to creep up (by approximately 10% over 30 minutes) during the long-duration trials (Figure 5.17) This rise in contact force can be attributed to a lower engagement coefficient resulting from worn abrasive grits. While quantifying the influence of wear on the engagement coefficient is outside the scope of this work, it is important to understand the limitations of the proposed controller for applications that require prolonged in-situ machining with worn tools.

Machining demonstration

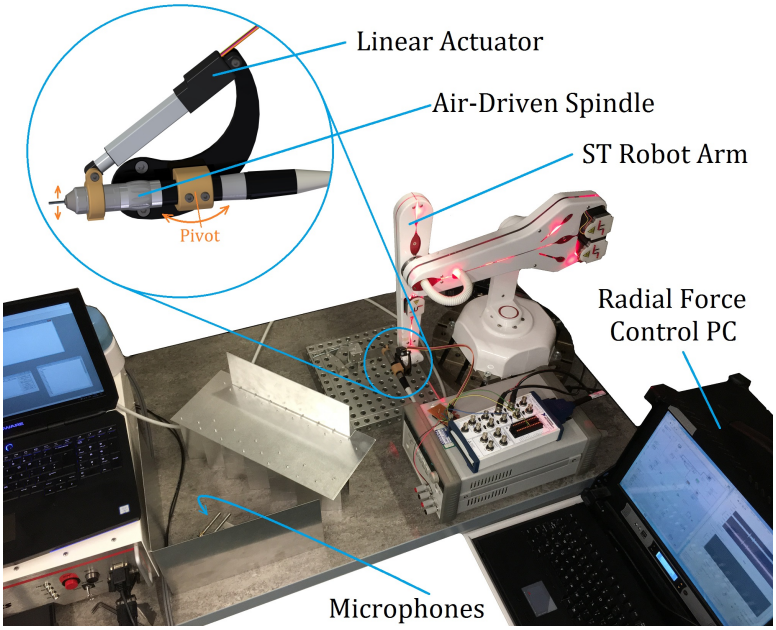


Figure 5.18: Demonstration setup for closed loop force control using sound features. 5-axis robot arm was used to control the feed speed u_f along a cantilever beam and a linear actuator was used to control the tool radial force F_R.

To validate the controller in a more realistic application, the grinding tool and *L12-50-100-12-P* DC geared linear actuator were attached to the end effector of a *R12-5* 5-degree-of-freedom robotic arm (ST Robotics; Figure 5.18). The robot arm was used to feed the tool back and forth, creating 90° cuts on the edge of three different workpieces ($100mmx30mmx1.6mm$) made from Nickel-Chromium-Cobalt alloy (Figure 5.19).

- A workpiece with a straight edge (Figure 5.19a)

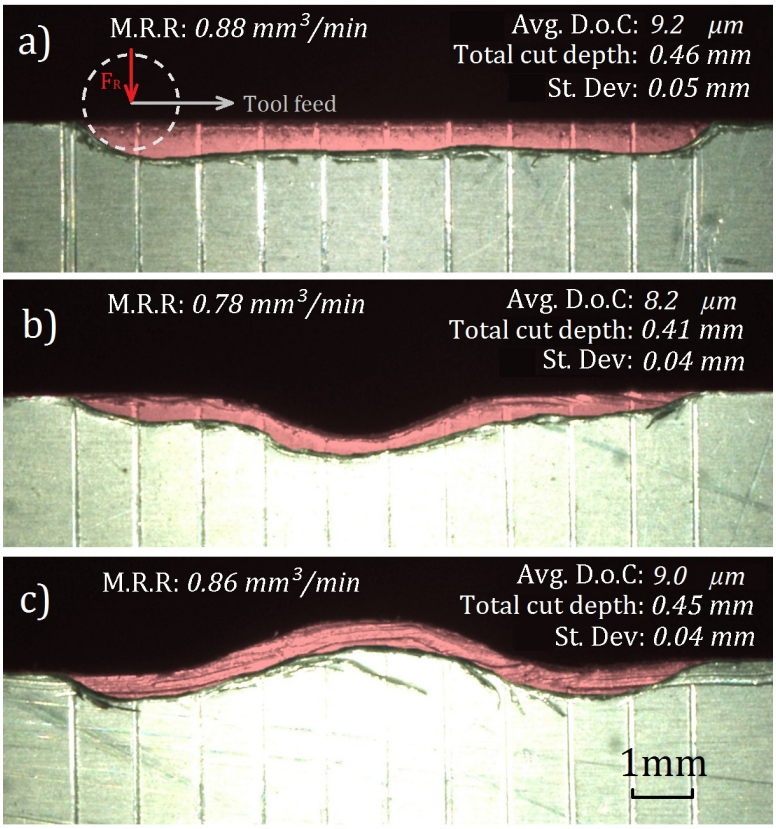


Figure 5.19: Demonstration results: A straight (a), concave (b) and convex (c) target workpiece geometry machined using a 5-DoF robot to feed the spindle and tool back and forth 50 times, and using audible sound features for closed loop force control. Red area shows removed material. Standard deviation of depth calculated from 10 samples taken at 1mm intervals.

- A workpiece with a concave indentation previously ground by hand (Figure 5.19b)
- A workpiece with a convex protrusion previously ground by hand (Figure 5.19c)

The irregular workpiece surfaces were used to test the ability of the sound force controller to adjust the radial motion axis (linear actuator in Figure 5.18) and follow an unknown path. It is important to note that the robot arm was not programmed to follow the different paths, but rather to maintain a constant radial force, hence a constant stock of removed material (depth of cut). Each of the tests consisted of fifty 10mm passes at a feed rate of $u_f = 1$mm/s along the workpiece with a target force of 0.9N, resulting in an expected material removal rate of approximately $0.5mm^3/min$. Total material removed during the test is indicated by the red colour in Figure 5.19.

The robotic arm successfully removed material along the three different unknown

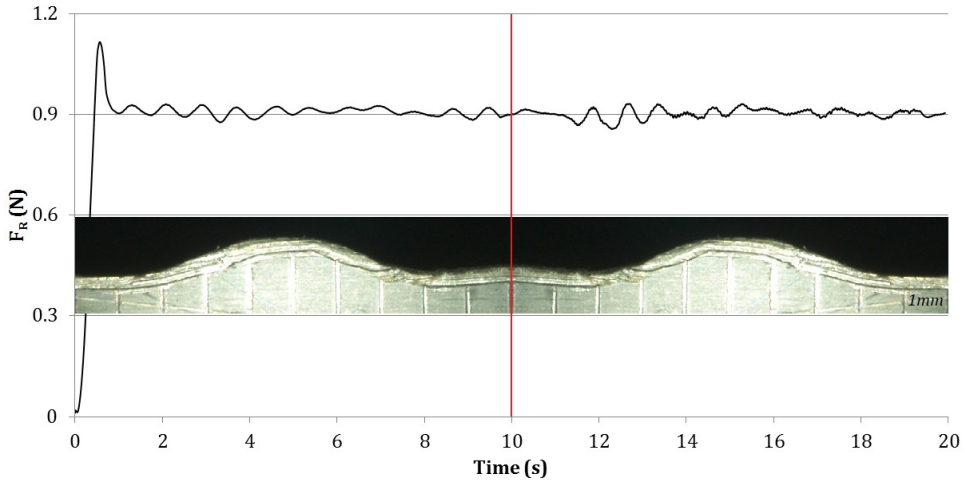


Figure 5.20: Radial force during first two passes of convex protrusion cut (going back and forth once, hence the mirror image).

surfaces using only the sound features to control radial force. An average material removal rate of $0.84mm^3/min$ was measured with a standard deviation in depth of cut of $50\mu m$ or less (Figure 5.19). The fact that the material removal rate measured exceeds the rate obtained with the test rig (Figure 5.16) can be attributed to the smaller contact area (and hence higher pressure) between tool and workpiece due to a non-zero feed speed. Figure 5.20 shows filtered (lowpass, $100Hz$) radial force data for the first two passes of the convex protrusion cut. The measurements show consistent force tracking (within $0.08N$), which was maintained throughout the majority of the trial.

The objective of this study is to demonstrate the application of a force controller using sound features with the intention that this methodology is applicable to other processes and, most importantly, applicable to slender and compliant robots. In particular we are referring here to an in-situ geometrical correction of a component in an industrial asset, where the micro-aspects of surface quality (e.g. roughness) are less important. It is possible that future work could design tools optimised for specific applications such that, given a material, spindle speed, tool type and machining force combination, machining quality and efficiency can be maximised (such as in the example of [174]).

5.4 Conclusions and future work

This work shows that it is possible to use sound features to inform a controller and operate a machining instrument with closed loop force control. An adaptive proportional controller was designed to use inputs from both dominant frequencies and sound intensity to achieve a steady spindle velocity and hence a near constant radial force. The controller also uses changes in the intensity of sound to vary control parameters such as proportional gain, deadband width and filter settings to mitigate the risk of workpiece resonant frequencies affecting the control.

The closed loop control method described was able to closely match the calibration radial forces and replicate the material removal rate achieved using a constant grinding force test rig. The force controller was used to machine approx 0.44mm deep features on thin cantilever beams with unknown edge profiles (concave, convex and straight) despite having no position control, thus demonstrating the ability to follow edges 'blind' using sound for force control. The susceptibility of the controller to small disturbances and variability in machining conditions means that the cuts produced had an uneven bottom with a standard deviation equal to 0.05mm in depth of cut along the machining path. In future the airborne sound force controller could be used as part of a hybrid position-force controller to achieve optimal material removal rate as well as dimensional accuracy of the machining operation. Tests of the effect of tool wear on controller performance indicate that the method works appropriately for the useful life of the burrs tested, despite losses in accuracy at high wear levels. In future work, the changes in performance could be further quantified and added to the controller for longer duration machining tasks.

The controller was demonstrated using a 5-axis robot arm with position encoders, but this method could be applied to operate non-conventional robots with limited position accuracy such as continuum and soft robots. Closed loop force control of such robots would allow for in-situ machining operations to be carried out in more inaccessible industrial components.

While the process described in this work is the high-speed grinding of metallic components, this methodology can be applied to other machining processes that

produce audible sound, such as drilling, milling, polishing, sandblasting, laser ablation, and abrasive water jetting provided that the sound can be associated with one or more machining parameters.

Future work: The versatility and performance of this controller could be improved by continuously processing the sound signals, such as by using a field programmable gate array (FPGA) for intensity and power spectral density calculations. This would allow the control loop to operate with lower latency and therefore at higher frequencies. This would in turn allow for more complex control structures such as PID to tune the response of the controller to perturbations in machining forces.

The controller could also be made more robust by introducing a cascade controller with an inner velocity control loop for the actuator, ensuring more predictable response and better control authority. Additionally, extra microphones could be used for noise cancellation to allow such a force control strategy to be used in noisy industrial settings.

Finally, it is possible to optimise the resulting surface characteristics for particular workpiece and tool combinations. This would achieve improved surface quality, material removal rate and tool life while employing air spindle speed-based force control. This will require modelling the behaviour of the tool at different stages of tool wear. Such work could result in quality consistent with the high standards associated with the aerospace and energy industries.

Chapter 6

Simultaneous position and force control of a slender and compliant in-situ machining robot

This thesis has introduced two novel methods of feedback control: a method for position control using tubular ionic liquid stretch sensor feedback and a method for force control using airborne sound features feedback. This chapter covers the implementation and demonstration of a simultaneous position-force control scheme using the novel sensors described in previous chapters. The objective of this chapter is to demonstrate the compatibility of the two methods and the ability to deliver a solution for accurate positioning for in-situ repair using low-cost sensors and existing hybrid control hierarchy structures.

6.1 Background

Simultaneous position and force control is essential for in-situ machining robots, as precise contact with their immediate environment is required during operation. Position control alone risks damage to the robot, cutting/abrasive tool, or workpiece by collision or over-exertion if a nearby object constrains its motion. Force control alone leaves the robot without a reference coordinate system and hence unable to achieve particularly

useful machining tasks. Precise interactions with nearby objects requires a combination of control strategies which, in the case of slender and compliant in-situ machining robots, are guided by Tubular Ionic Liquid Stretch Sensors (TILSS) and airborne acoustic emissions.

A popular method of simultaneous control is to create two parallel independent control loops, each with their own inputs and outputs. As mentioned in Chapter 2 problems often arise when the output of one loop becomes a disturbance in another loop, as this can result in difficult or even impossible tuning. In contact force control there are always process interactions that induce relations between the control loops. In compliant robots, movement of actuators changes the state of both variables, which introduces strong interactions between motion and force control.

Distinct parallel control loops can influence a single plant in a stable way by assigning predefined hierarchies to control structures in specific task directions. In [145], constrained and unconstrained direction (defined by the geometry of the environment) are controlled with force and position feedback respectively. This is similar to what was demonstrated in Chapter 5 Section 5.3.3, where the machining direction was controlled with the novel force controller and the feed translation was controlled separately by the robotic arm. However, unlike applications that require contact or following of static surfaces, machining requires position control in the depth direction, making this approach unsuitable without other loop-closing strategies or position limiters.

Another approach to simultaneous control is to evaluate the current end effector parameters and return a task specification that assigns the required weights and directions to the different control variables. This situation awareness allows robots programmed with hybrid position-force controllers [140, 143, 144] to transition from positioning to exerting forces. By removing conflicting control loops and the necessary hierarchy, the force control becomes more predictable and fine-adjustable. However, without a detailed model of the environment it is impossible to assign task specifications, making this method unsuitable for unpredictable environments.

Parallel control loops with strong determinative interactions can be rearranged to

form two nested loops due to the causality of force feedback as discussed in section 2.5.1. In practice an outer force loop with priority over the setpoint of an inner position loop results in stable interaction. Despite the stability, this method loses position accuracy by influencing the desired position directly from contact force.

It can be seen that despite previous advances towards practical simultaneous force and position control of continuum robots, the solutions are limited by assumptions of constant shape environment or well-defined model of the surroundings. Hence, a scheme is proposed to modify the nested loops control structure to account for the nature of in-situ machining tasks, as well as the specific sensors presented in this thesis.

6.2 In-situ machining simultaneous control scheme

A simultaneous control strategy for in-situ machining must be capable of producing accurate features following complex 3-dimensional trajectories and applying known contact forces during grinding. Crucially, the control method must be capable of adapting to the changing trajectory as material is removed. While conventional simultaneous control methods such as those mentioned in previous sections do not satisfy these requirements, it is possible to improve the nested loops control scheme to account for the variation in depth and achieve consistent machining of a true shape.

6.2.1 Simultaneous position and force control methodology

The proposed simultaneous control strategy combines elements from some of the previously discussed methods from literature into a novel arrangement. The scheme consists of an outer, constrained direction only, biased-output, proportional + integral, airborne sound machining force sensor (ASMFS) feedback, stiffness control loop with a threshold global interrupt and an inner, direction invariant, proportional + integral + derivative, tubular ionic liquid stretch sensor (TILSS) feedback, position control loop. Figure 6.1 shows the proposed strategy in schematic form. A summary of the equipment used in this chapter can be found in Appendix A.

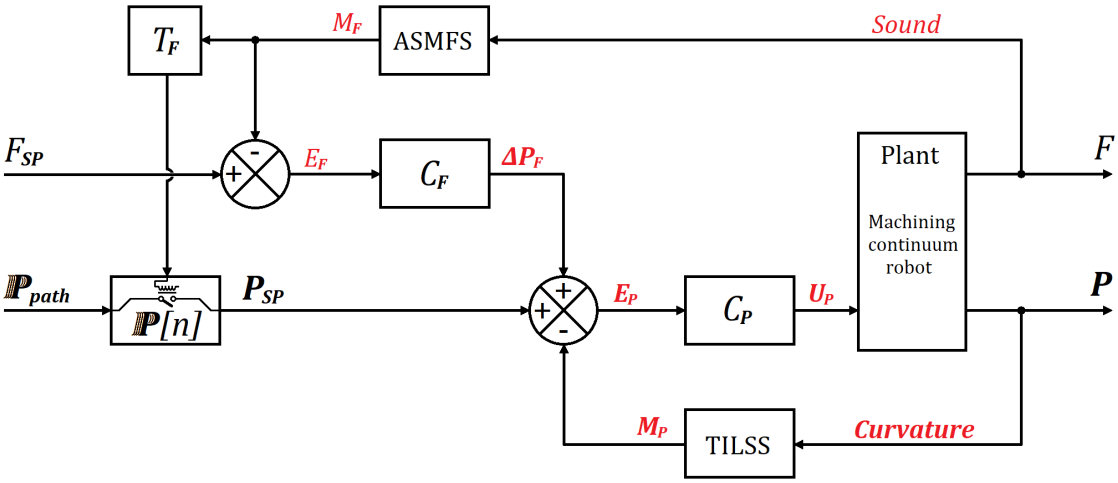


Figure 6.1: Simultaneous position and force control methodology schematic for airborne sound machining force sensor and tubular ionic liquid stretch sensor equipped continuum robot.

Force control

The force setpoint F_{SP} defines the target radial force for the machining operation. The Airborne Sound Machining Force Sensor described in Chapter 5 is used to measure the current machining force F based on the sound emissions from the grinding process. The difference between desired and actual machining force E_F is the input to the force controller C_F.

The force controller output is a position vector $\boldsymbol{\Delta P_F}$ to influence the position control loop, and consists of a one-directional, biased-output, PI, sound-based controller:

- **One-directional:** The controller output is a vector that is radial to the grinding tool and normal to the longest edge of the workpiece, i.e. towards or away from the workpiece. Similar to [145], a task space separation constrains the actions of the force controller to the relevant axis for machining.

- **Biased-output:** The controller output cannot be negative, as the position must never be commanded to exceed the desired position towards the workpiece, i.e. to remove more material than desired. Any proportional or integral contribution that would result in a negative output is ignored and saturated to zero.

- **Proportional + Integral:** The controller output is proportional to the machining force error and proportional to the cumulative machining force error. The integral term can act in both positive and negative directions provided the output does not drop below zero. As mentioned in Section 5.3.2, the integral term ensures tracking stability for a position-controlled actuator.

- **ASMFS:** Airborne sound machining force sensor. As discussed in Chapter 5, the controller uses sound frequency to estimate machining force and sound intensity to mitigate the negative effects of resonance with workpiece natural frequencies.

Hence, the proposed force controller transfer function is given by:

$$C_F(s) = \text{sat}\left[\frac{\boldsymbol{\zeta}}{\|\boldsymbol{\zeta}\|} + K_P + \frac{K_I}{s}\right]_0^{\infty} \tag{6.1}$$

where $\boldsymbol{\zeta}$ is the cross product of the end effector and workpiece edge vectors, such that positive is away from the workpiece. The integral term is also saturated to zero to prevent it from reaching large negative values while the tool is idle or at low forces.

The effect of this strategy is a "compression only" stiffness control behaviour where the output is spring compression or position setpoint correction.

Position control

The position setpoint $\boldsymbol{P_{SP}}$ defines the target position in Cartesian coordinates for each control cycle. The machining path consists of a sequence of target positions that are reachable by the continuum robot end effector and that define the outline of the finished machined cut. The output of the force controller $\boldsymbol{\Delta P_F}$ is used to correct the setpoint to achieve the desired force. The Tubular Ionic Liquid Stretch Sensors described in Chapter 4 are used to measure the current continuum robot segment positions $\boldsymbol{P}$ based on the curvature of the backbone elements. The difference between desired and actual position $\boldsymbol{E_P}$ is the input to the position controller C_P.

The position controller output is a series of frequency and direction commands $\boldsymbol{U_P}$ for the robot's linear stepper motors, and consists of a position invariant, PID, curvature-

based controller:

- **Position invariant:** The position controller behaves the same anywhere in the working envelope. Hence, the machining path can be positioned anywhere in the reach of the end effector with no loss in functionality of the simultaneous controller. The pseudo-inverse Jacobian method for inverse kinematics described in Chapter 3 was used to convert the Cartesian coordinates into distal and proximal X and Y angles.

- **Proportional + Integral + Derivative:** As described in Chapter 4, a PID controller can be tuned for each of the four sensors to achieve desirable position tracking to within 2.3% of total continuum length. The position controller should be overdamped to prevent any overshoot into the workpiece which could lead to instability with the force controller.

- **TILSS:** The position loop uses tubular ionic liquid stretch sensors to directly measure the continuum robot outer surfaces strain and calculate curvature and end effector position using forward kinematics as described in Chapter 3.

Hence, the proposed force controller transfer function is given by:

$$C_P(s) = K_P + \frac{K_I}{s} + K_D s \tag{6.2}$$

The effect of this inner position loop is accurate end effector positioning and a moderately dampened response to the stiffness controller during machining. A single execution of the machining path results in unobstructed movement until the tool contacts the workpiece while attempting to reach the finished machined cut position, which engages the force controller. The feed speed (along the unconstrained direction) continues to be determined by the execution of the position path.

Force threshold

It is likely that for most machining tasks, more than one machining path execution is required to remove enough material to reach the machining path, i.e. reduce the stiffness

control position vector $\boldsymbol{\Delta P_F}$ to zero for the entirety of the movement. The number of passes required to complete the cut depends on the size of the cut and the force setpoint F_{SP}. Therefore, a force threshold T_F was introduced to monitor the force output and determine whether the current pass was successful in following the design path.

The output from the force controller must be zero for the duration of the machining pass to signify that no deflection was necessary to achieve the finished machined shape. Furthermore, due to the compliant nature of in-situ continuum manipulators, small cuts (or final passes of larger cuts) are likely to result in low machining forces that may not reach the force setpoint F_{SP}. Allowing machining to continue at forces below F_{SP} ensures accurate removal up to the specified machining path. This is analogous to spring cuts in conventional milling and turning, where workpiece and tool elasticity provide the cutting force and continue removing material without a commanded change in depth of cut. Therefore, the threshold function T_F commands the position controller to continue cycling through the machining path until a specified limit force F_{th} is not met for the duration of a machining pass.

Hence, for a machining path of length m discrete position setpoints numbered n, the force threshold logic is given by:

$$\frac{\sum_{i=n-m}^{n} M_F(i)}{m} \geq F_{th} \tag{6.3}$$

where the output is either true (continue machining) or false (operation complete).

6.2.2 Control method implementation

The proposed simultaneous position and force controller was implemented using an *EMP373* portable computer (ACME) equipped with a *PCI-6229* IO board (National Instruments) and two *BNC-2110* BNC breakout boards (National Instruments) for sensor input and actuator command output (Figure 6.2). The test rig developed in Chapter 4, Section 4.3.4 was fitted with a miniature air-driven spindle (as described in Chapter 3) incorporated into the last vertebra of the distal section. A friction grip,

1.8mm diameter cylindrical electroplated diamond grinding burr (118μm grit) was attached to the spindle. The continuum arm was covered with polyamide braiding to increase its torsional rigidity at high bend angles.

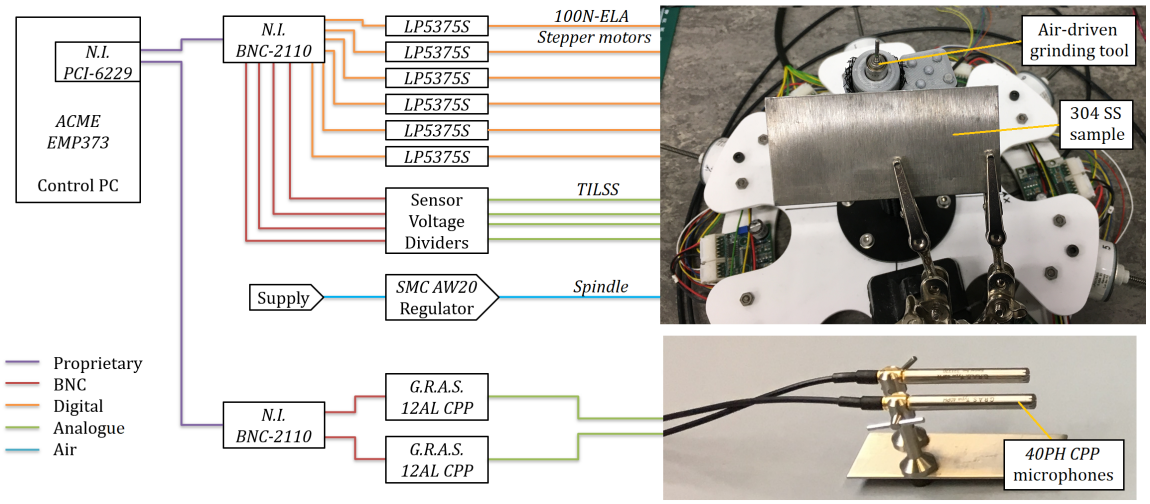


Figure 6.2: Hardware schematic and initial setup for simultaneous position and force control implementation.

Two *40PH CPP* free-field array microphones with *12AL CPP* pre-amplifiers (G.R.A.S. Sound & Vibration) were positioned approximately 400mm from the continuum arm axis to capture the machining sound. The microphones were spaced 10mm from each other as described in Chapter 5 to measure pressure gradient for intensity calculation.

The above control scheme was implemented using *LabVIEW 2014* (National Instruments) with the position control loop running at 60Hz and the force control loop running at 20Hz (due to the limitations of the microphone data capture and processing). Force effects were assumed to remain constant for every three cycles of position control, which was not found to affect tracking significantly. Sound was sampled at 50kHz.

Samples consisted of five 304 stainless steel rectangular plates 85mm x 40mm x 710μm and three wooden mixing sticks of thickness 1.6mm (tested to verify the application of the controller to soft, anisotropic materials). The samples were mounted approximately 20mm from the straight position of the continuum manipulator (Figure 6.2), with the top edge of the workpiece aligned with the manipulator x axis. The workpiece edge was

positioned lower than the grinding burr to necessitate bend of the proximal continuum segment and ensure full range of motion, as well as to utilise a larger proportion of the electroplated diamond tool surface on each machining pass. A side-view schematic of the experiment setup is shown in Figure 6.3. To account for variations in plate width and final position after mounting, each cut was preceded by a manual calibration movement to define the position of the workpiece edge axis.

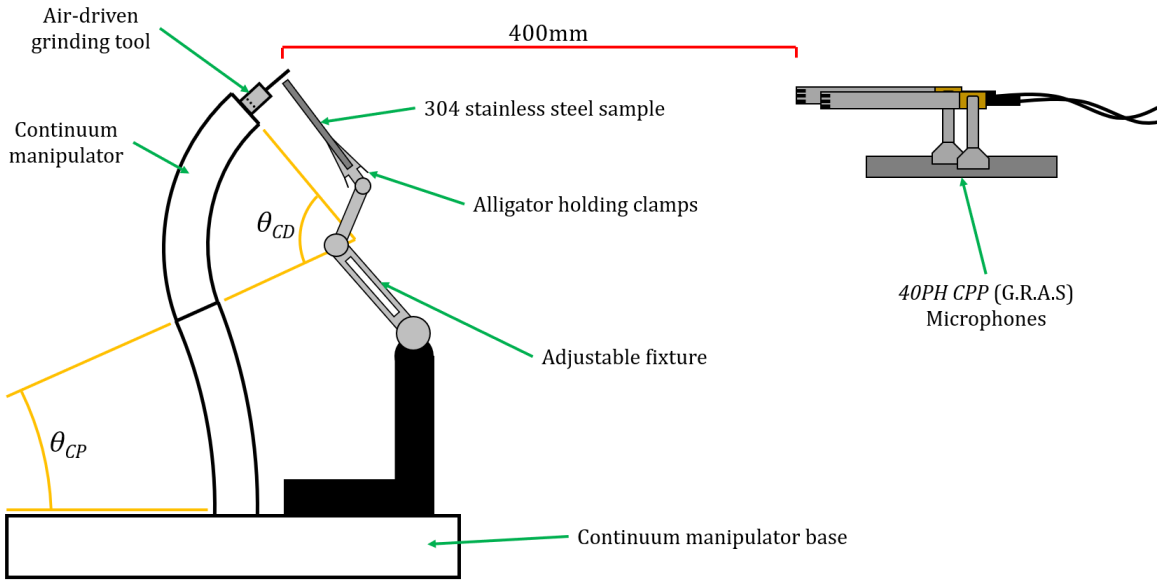


Figure 6.3: Simultaneous position and force control setup schematic (side view). An adjustable fixture holds the sample at an angle close to the machining end effector of the continuum manipulator. Two microphones measure sound and pressure gradient in the direction of propagation from the tool.

The force behaviour of the miniature air-driven spindle was calibrated at known contact forces using a *9317B* 3-axis dynamometer (Kistler). Calibration trials consisted of a number of manual cuts on a beam mounted on the sensor with periodic acquisition of microphone data at various forces. The cantilever arm was removed from the test rig described in Section 5.2.2 and shown in Figure 5.5 and the continuum manipulator end effector was brought into contact with the workpiece and force sensor. Stall torque was assumed to follow the turbine radius relation observed by [171] for a value of $\tau_s = 1.15mNm$. The calibration data is shown in Figure 6.4.

The idle speed for the miniature air spindle was observed to be lower than that of the test rig used in Chapter 5, but the behaviour or the tool during grinding was almost

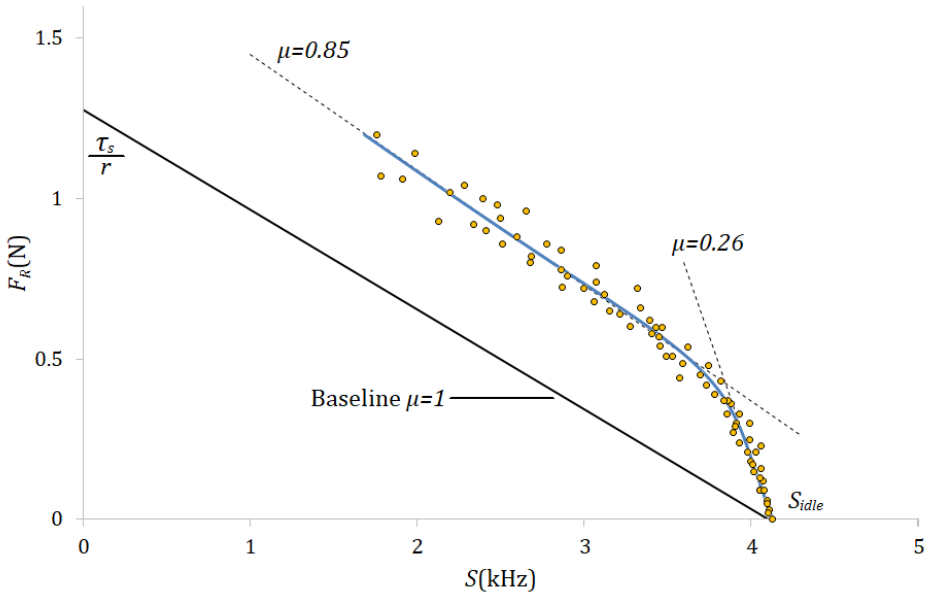


Figure 6.4: Measured radial force F_R vs. spindle speed S (dominant audible frequency) for miniature air spindle calibration. Dotted lines show engagement coefficient μ during sliding friction and after abrasive grain engagement.

unchanged, with a similar F_{eng}, μ_1 and μ_2. A limit force of $F_{th} = 0.1N$ was used for this tool, with a target force of $F_{SP} = 0.6N$ during closed loop control.

The modified kinematics described in Table 4.6, Section 4.4.2 were implemented in the code to achieve accurate control in the entire work envelope at the expense of cycle speed. The PID control constants for each sensor were tuned for the lower cycle time and overdampened requirement. Once the position loop was tuned to the desired response, the force loop PI control constants were tuned to achieve the desired stiffness and stable tracking.

The target trajectory was defined as a sinusoidal curve with dimensions $18mm$ x $3mm$ as described by the equation

$$y = 1.5 \cos\left(\frac{2\pi}{18}x\right) - 1.5 \tag{6.4}$$

where x are millimetres along the beam edge and y are cut depth. The path consisted of 2160 points equispaced along x (120 points per millimetre) and their coordinates were transformed to the manipulator coordinate system. With the position control loop execution rate of $60Hz$, the target feed speed v_f along x was $0.5mm/s$. The machining

trajectory ends with a $6mm/s$ straight-line traverse back to the start of the curve for a total pass duration of 39 seconds.

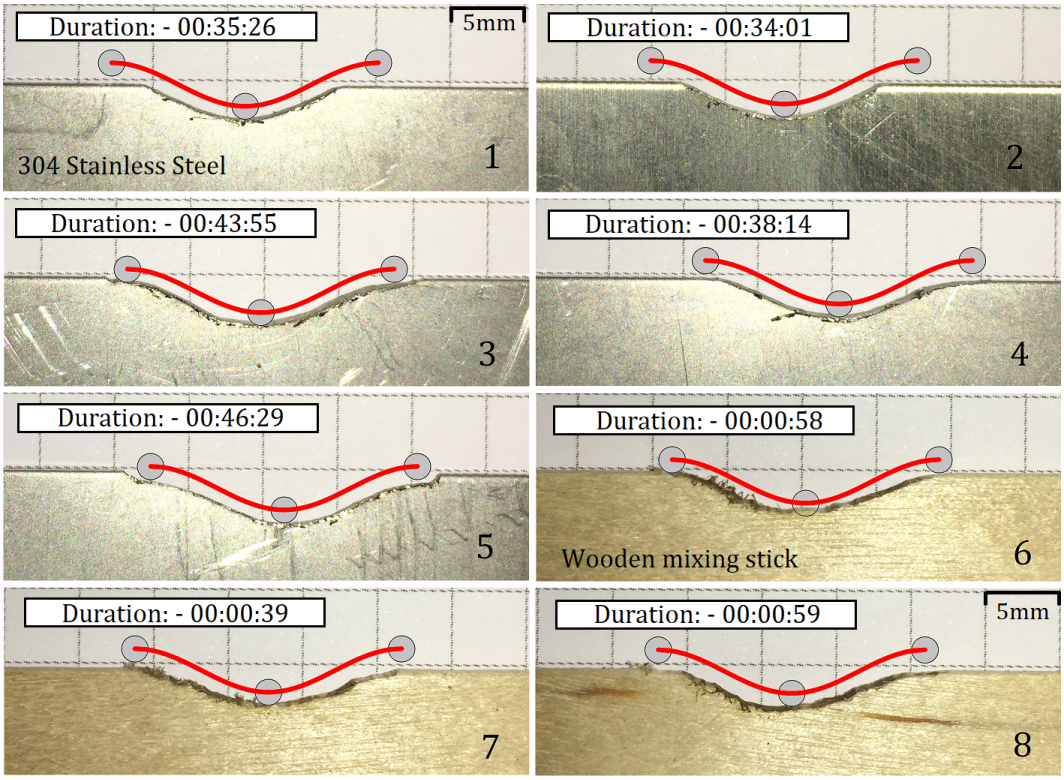


Figure 6.5: Simultaneous position and force control implementation results, with duration for each trial (hours:minutes:seconds). Red line shows desired trajectory. Samples 1-5 are 304 stainless steel; samples 6-8 are thin wood (mixing sticks).

Figure 6.5 presents the results of the eight samples machined during implementation trials. It can be seen that the proposed simultaneous control strategy is generally successful in following the desired shape while maintaining an adequate cutting force for grinding. Differences in depth are largely attributed to errors during the manual calibration movements to define edge axis position. When the manipulator is calibrated at the edge of the workpiece, stretch sensor readings define that datum; errors in this datum result in cut shapes that are lifted from (e.g. samples 1 and 2 in Figure 6.5) or sunken into the workpiece (e.g. sample 5 in Figure 6.5). Although the trials were carried out near the origin and along one axis (an area observed to behave predictably as seen in Chapter 4, Figure 4.19) an error of 1.5% to 2.3% of manipulator length is still expected and fully explains the cut position discrepancy.

For all of the stainless steel samples, the resulting cut was observed to be wider than

the target dimensions by approximately 8% to 10%. This is particularly clear in samples 3 and 5, where the surface has been machined beyond the bounds of the target lines. This is attributed to position errors arising from TILSS inaccuracies and averaged over multiple consecutive passes.

Machined feature depth was observed to be accurate in the metal samples where it can be measured relative to the starting depth (such as trials 3 and 5 in Figure 6.5), measured to be $2.88mm$ and $2.96mm$ respectively. This is attributed to the large number of passes eventually averaging out errors in position control until a pass is completed below the threshold force F_{th}. Likewise, machined feature shape was observed to be accurate despite the distortion in length, with smooth curvatures on all metal samples, likely also due to the averaging effect of the large number of passes required.

In contrast, the soft material samples clearly highlight position control errors, whether in depth (such as sample number 6), shape (such as sample number 7) or width. With only one or two passes before F_{th} was met, there were not enough passes to correct the errors present from TILSS noise.

Material removal rate for metal samples was measured to be $0.42mm^3/min$ on average (taking into account real material removed), which is 5.6 times faster than the $0.075mm^3/min$ achieved with the same tool operating with constant depth passes in Chapter 3. This highlights the importance of force control during grinding, as it can accelerate material removal by optimising the interaction between abrasive tool and workpiece. If the material removal rate can be preserved for thinner samples, the boreblending procedure demonstrated in Chapter 3 could be completed in under ten minutes using the method presented.

6.3 Machining demonstration using simultaneous position and force control

Following successful implementation of the simultaneous position and force control scheme, two demonstration experiments were devised to highlight the capabilities of the

system in the context of in-situ repair of industrial assets. The first test demonstrates the use of the simultaneous controller to remove a defect from a damaged edge of unknown topology while achieving an accurate shape cut. The second test demonstrates the use of the proposed scheme on a dented blade from the high pressure compressor (HPC) of a Rolls-Royce *Trent XWB* turbofan engine.

One application of in-situ grinding instruments is to remove stress-concentrating damage from highly loaded components to extend their lifespan beyond scheduled engine overhauls, hence preventing unscheduled engine removals. One such repair is the boreblending procedure described in Chapter 3, where compressor blades affected by foreign object damage (FOD) are smoothed using grinding burrs. FOD of compressor blades is often from impact on leading or trailing edges, resulting in bends or kinks.

The dual-segment, dual-direction continuum manipulator was set up for simultaneous position and force control on a simulated boreblending repair. One of the 304 stainless steel plates was cut and bent (changing the edge profile without removing material) using manual tools to simulate FOD. The damaged edge can be seen in Figure 6.6a. The plate edge was then aligned with the manipulator x axis as described in Section 6.2.2, a manual calibration movement was used to locate the edge and a machining path identical to those shown in Figure 6.5 was executed.

Figure 6.6b shows the machining progress approximately 8 minutes into the repair. While protrusions are still present at this stage, the uniform cutting force at uniform feed speed can be observed to result in gradual smoothing of irregular features. Figure 6.6c shows the machining progress after approximately 24 minutes and it is clear at this point that the irregular surface has been significantly smoothed. Beyond this point, the repair proceeds much like an unaffected sample with irregularities eliminated by the large number of grinding passes.

Like the unknown-topology cuts described in Section 5.3.3 (Figure 5.19), the results from this experiment demonstrate the robustness of the proposed simultaneous controller, with a shape and cut duration consistent with the observations on undamaged samples. The manipulator was able to remove material at a consistent rate regardless of the changes

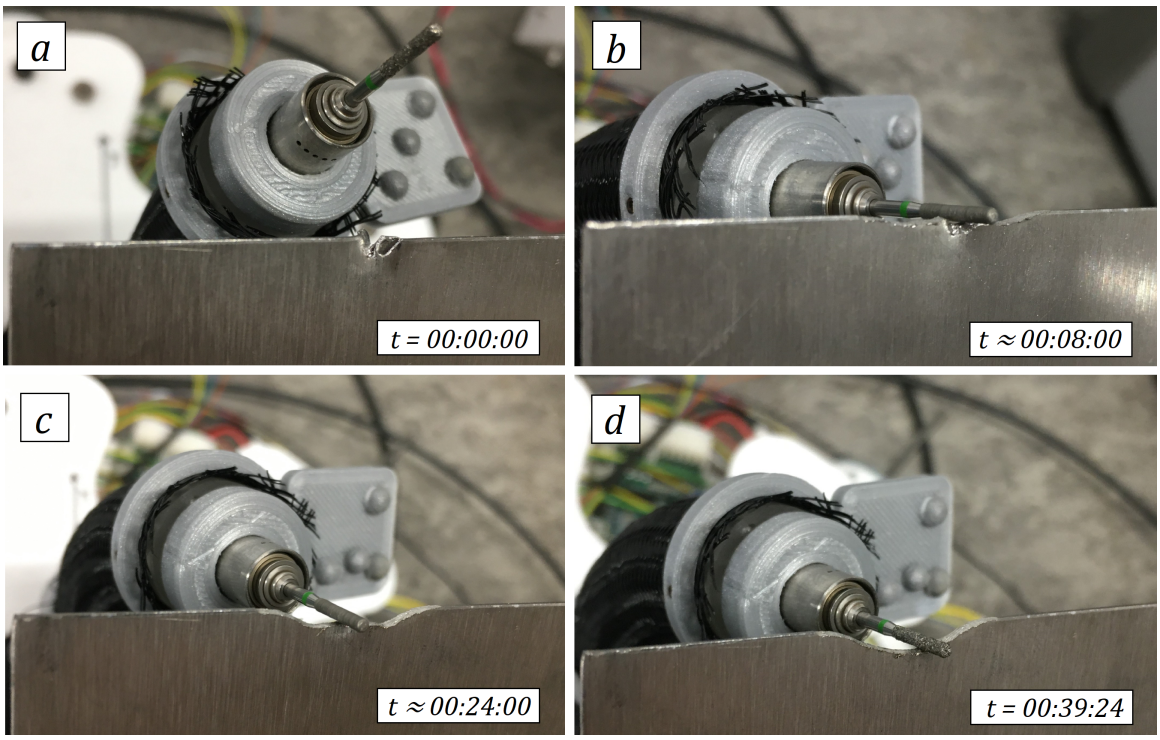


Figure 6.6: Simultaneous position and force control demonstration on damaged 304 stainless steel component with unknown topology. Frames show progress at various times (hours:minutes:seconds).

in contact direction and contact area. A plot of machining force for the duration of the machining trial is presented in Figure 6.7, where F_R points are coloured at 1 second intervals in their approximate positions relative to the sample. Force data is based on output from the airborne sound machining force sensor, as a load cell was not fitted in this setup.

The plot in Figure 6.7 shows that the bulk of the material is removed at the target force of $0.6N$, however a substantial fraction is removed with spring cuts below the target force, where the position controller is tracking the desired path. Deflections of the compliant body of the robot (and hence small stretch sensor errors) cause real end effector position errors that result in low contact forces and discrepancies in final cut shape.

Force tracking during bulk removal (red in Figure 6.7) was measured to be $6.02N$ with a standard deviation of $0.09N$.

A side effect of the robot compliance and resulting spring cuts is a longer duration of repair. While most of the material is removed with high forces in the first 24 minutes (Figure 6.6c), the final stages of the repair include most of the low-force passes resulting

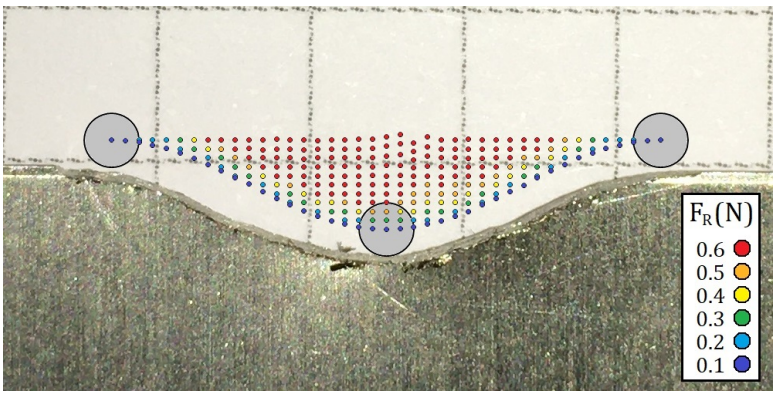


Figure 6.7: Radial force F_R and approximate position for select points during controller demonstration on damaged component with unknown topology. Force data is based on airborne sound machining force sensor output.

in lower material removal rate and disproportionately long duration (Figure 6.6d). This could be addressed by allowing the force loop to command limited negative values of $\boldsymbol{\Delta P_F}$, tuned to the stiffness of the mechanical system, while raising the force threshold F_{th} to an appropriately high value. However, this approach would require accurate task space mapping (such as in [143]) to prevent runaway force dominance. The increased susceptibility to position feedback errors would also result in undesirable overshoot and possible oscillation and loss of control.

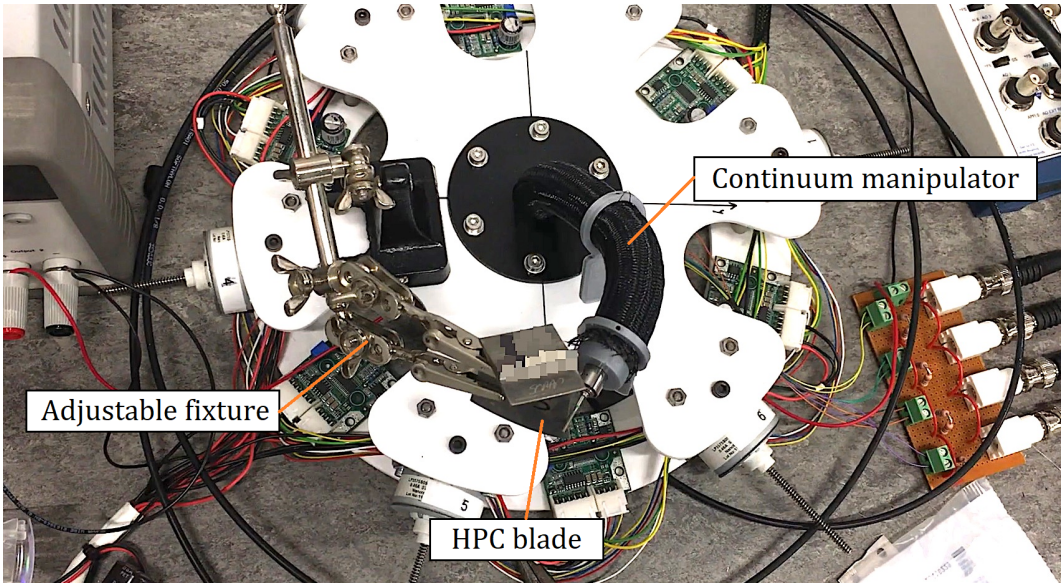


Figure 6.8: Experimental setup for simultaneous position and force control of a continuum manipulator. End effector is a high-speed air-driven grinding tool, workpiece is an aeroengine high-pressure compressor blade secured using an adjustable fixture. Further trials aligned blade edge with manipulator x axis.

The proposed simultaneous position and force controller was demonstrated on a moderately dented HPC blade from a Rolls-Royce *Trent XWB* turbofan engine (Figure 6.8). The blade (Figure 6.9a) is made of a high-temperature nickel superalloy similar to INCONEL® alloy 718. Despite the material being similar to that used during tests in Chapter 5, the geometry of the blade (and therefore its natural frequencies) is significantly different from that of the cantilever beams used throughout this work. However, the force control strategy is designed to be insensitive to changes in workpiece geometry and resonance, as the intensity gains are not dependent on tool speed.

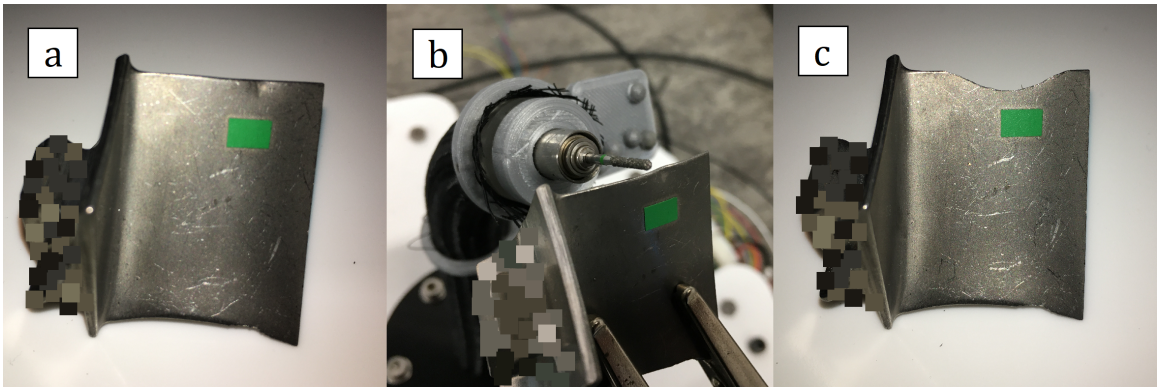


Figure 6.9: Simultaneous position and force control demonstration on lightly dented high pressure compressor blade from Rolls-Royce *Trent XWB* turbofan engine. Frames show before (a) and after (c) images of the compressor blade as well as setup during edge calibration.

The HPC blade was mounted approximately $20mm$ from the straight position of the continuum manipulator (Figure 6.9b), with the dominant direction of the curved trailing edge of the workpiece aligned with the manipulator x axis. The blade edge was positioned lower than the grinding burr to necessitate bending of the proximal continuum segment and ensure full range of motion, as well as to utilise a larger proportion of the electroplated diamond tool surface on each machining pass. A manual calibration movement was used to locate the edge (specifically the position on the curved edge where the sinusoidal cut starts) and a machining path identical to those shown in Figure 6.5 was executed.

Figure 6.9c shows the completed blend after 44 minutes and 40 seconds of machining. The finished profile closely resembles the results of all previous cuts on metallic samples. Material removal rate was measured to be $0.38mm^3/min$, which is over five times faster than the $0.075mm^3/min$ achieved with the same tool operating

with over-cautious constant depth passes in Chapter 3. This demonstrates the effectiveness of using airborne sound features as machining force feedback in combination with tubular ionic liquid stretch sensors for closed loop position and force control of complex continuum manipulators that are slender and compliant.

6.4 Conclusions and further improvements

The work presented in this chapter demonstrates the effectiveness and compatibility of the position and force controllers described in Chapters 4 and 5. Where previous chapters described the implementation of a position controller that uses tubular ionic liquid stretch sensors as feedback and of a force controller that uses airborne sound features from machining as feedback in isolation, this work shows the two schemes working simultaneously to achieve consistent machining of accurate features.

A simultaneous position and force control methodology was introduced consisting of an outer, constrained direction only, biased-output, proportional + integral, airborne sound machining force sensor feedback, stiffness control loop with a threshold global interrupt and an inner, direction invariant, proportional + integral + derivative, tubular ionic liquid stretch sensor feedback, position control loop. The scheme uses machining sound to calculate the cutting force and modify the position setpoint, thereby changing the contact forces and the path of the manipulator end effector. The process is repeated until the path can be completed without modification from the force controller and until the contact forces fall below a threshold value meaning that the tool is only lightly in contact with the work and the desired shape has been achieved.

The proposed simultaneous position and force controller was tested using the dual-segment, dual-bend-direction continuum robot manipulator described in Chapter 4, equipped with 4 tubular ionic liquid stretch sensors and the air-driven spindle grinding tool described in Chapter 3. The microphones and signal processing hardware and software described in Chapter 5 were positioned near the operation to measure grinding contact force. A sinusoidal cutting path was defined and the manipulator was calibrated to cut metallic and wooden components mounted within its working volume. The

results show consistent finished cut dimensions and consistent material removal rate, demonstrating accurate position and force control of a machining instrument.

The position accuracy was observed to be less than 2% of the continuum manipulator length, a result which is consistent with the findings of Chapter 4. Force accuracy during tracking was observed to be $0.09N$, or 1.5% of the target force, a result which is also consistent with the findings of Chapter 5. Thus it is possible to assume that the novel simultaneous position and force control strategy presented is fully compatible with the novel position and force feedback methods presented in this thesis.

Finally, the simultaneous position and force controller was demonstrated on more realistic simulated samples for in-situ repair consisting of a damaged plate with irregular topology and a dented compressor blade from a production turbofan engine. The success of these trials highlights the robustness and versatility of the proposed control methodology.

Further improvements in machining speed and quality could be made by introducing multiple thresholds, where the bulk of the material is removed with aggressive settings and the final passes are executed with lower feed speeds and forces. In addition to this, the path definition could be modified in real time to allow parts of the machining sequence to be removed once forces fall below a value, to ensure that only the areas of the blend that require high forces continue to be machined with the aggressive settings. These and other such changes could be explored in depth to optimise the performance of the proposed simultaneous position and force controller.

Future work may also include further exploration of parallel loops schemes such as those described in [145] for their application in machining, as it may simplify the creation of additional task definitions. The definition of additional task spaces (such as areas where force control acts only in a specific direction or with specific settings) would make the controller more specialised to a specific application, but would unlock multiple options for performance enhancement. These changes could be used to exclude parts of the environment or important components or to assign different material and/or geometry properties to various features of interest.

Chapter 7

Thesis conclusions and further work

This chapter discusses the outcomes and achievements of this thesis, with emphasis on how these advances address prior research gaps and limitations in the state of the art. The thesis concludes with a view towards the future, presenting a summary of possible areas of further research in the field of position and force control of slender and compliant robots for in-situ machining.

7.1 Discussion of challenges and project objectives

As stated in the introductory chapter, the goal of this work was to identify novel solutions for sensing, modelling, actuating and controlling slender and compliant robots to enhance the accuracy of positioning and the repeatability of operations when applying forces to the environment, such as during machining. The further criterion of identifying solutions that are practical for in-situ repair also applies.

Maintenance operations such as inspection, measurement and machining on industrial assets often requires access to internal components through small openings. Equipment such as power generating turbomachinery, nuclear reactors and aeroengines rely on tight seals and precise fits, resulting in designs with as few openings as possible. Robots for in-situ interventions therefore require small diameters, slender designs and often compliant structures. This work has presented advances towards precisely controllable slender and compliant robots for use in these challenging environments.

Following a detailed literature search, a number of past approaches for slender and compliant robots were identified, along with position and force control methods suited for a variety of applications.

- Slender and compliant robots with dexterous end effectors have been described widely for their application in minimally invasive surgery, human-safe manipulation and in-situ repair of complex machines. While some of these examples use fluid pressure and soft muscles for movement, serpentine tendon-driven robots with flexible backbones appeared to offer a suitable design for in-situ machining tasks, due to their ability to deliver services though a central passage and their high stiffness. *Hence, this work aimed to explore the miniaturisation of a serpentine dual-backbone architecture for in-situ machining and improve the state of the art in position and force control*

- The popularity of slender and compliant robots - due to their advantages in medicine and engineering - has resulted in a wide body of literature exploring ways to accurately control their position. This includes extrinsic methods such as electromagnetic trackers and cameras, as well as intrinsic methods that include built-in optoelectronic bend sensors, optical fibre strain sensors and curvature stretch sensors; however, the limitations of in-situ repair of complex industrial assets makes extrinsic methods impractical. *Hence, this work aimed to explore novel methods for closed loop position control of continuum robots using intrinsic, miniaturisable sensors.*

- While the intersection of continuum robots and machining force control had not been explored in depth by previous authors, a wide range of literature describes methods for contact force in tendon-driven robots (such as for tissue examination in medical applications), methods for detecting and monitoring contact forces during machining (such as with wrist-mounted load cells) and methods for remote sensing of force signals. *Hence, this work aimed to explore miniaturisable methods of force sensing applicable to slender and compliant robots for in-situ machining.*

- Simultaneous position and force control is frequently required for manipulation tasks and has been thoroughly investigated in literature. While the vast majority of prior work has been on robots with conventional joints, a number of authors have applied parallel and hybrid control schemes to continuum robots with some success. However, the application has almost exclusively been diagnosis of and interaction with soft tissue in medical fields, where the forces do not result in changes and responses such as those observed during machining. *Hence, this work aimed to build on existing methods for simultaneous position and force control using novel forms of feedback for a slender and compliant machining robot.*

Prior literature presented a number of interesting concepts for detailed research, which this thesis sought to bring to light. The following points summarise unique concepts for in-situ machining robot architecture, position control of slender continuum robots, force control of compliant machining robots and simultaneous position and force control of specialised slender and compliant machining instruments.

- In the search for a suitable construction methodology of a slender robot for in-situ machining, the dual-flexible-backbone architecture of tendon-driven continuum robots (such as the one presented in [8] was identified for the scalability of the design and the ability to deliver services through a hollow central passage. The addition of feed and twist degrees of freedom (such as those described in [32]) was observed to allow for a more versatile design. *Hence, a novel hybrid mechanical architecture incorporating conventional (rotary and prismatic) joints as well as dual-backbone flexible continuum joints was explored in this thesis as a case study for in-situ repair of aeroengine compressor stages using a machining tool.*

- The search for miniaturisable intrinsic position sensors for slender and compliant robots (such as dual-flexible-backbone continuum robots) uncovered a methodology frequently used in soft robots, consisting of elastic channels filled with or consisting of electrically conductive materials. Such sensors could be configured to behave as skin strain gauges on continuum segments, mounted some

distance from the bending planes. Resistive stretch pads that use conductive liquids (such as those described by [84]) were used to accurately measure hand and neck movements. Drawing inspiration from these advances, *this thesis explored the use of resistive stretch sensors to provide position feedback for slender and compliant, metal-construction robots (such as dual-flexible-backbone continuum robots), and demonstrated their suitability for closed loop shape control.*

- The review of literature on force feedback methods made it quickly apparent that new approaches were necessary for machining with miniature, slender and compliant robots. The search for suitable sensors revealed machining parameter monitoring research that made use of propagated signals such as acoustic emissions and airborne sound (such as described by [138] during disk cut-off grinding of concrete), although never used for closed loop control. However, the concept was theorised to be suitably scalable, and *this thesis endeavoured to apply a remote, airborne sound-based force sensor for closed loop control of machining forces for in-situ applications with slender and compliant robots.*

- The search for suitable methods for simultaneous force and position control of slender and compliant robots for machining in challenging environments with unknown topology resulted in a condensed selection of task-space and actuation-space-based approaches. As approaches that rely on accurate knowledge of the environment were ruled out, more versatile concepts were assessed for their applicability using the unique sensors of previous sections; *this thesis built on the concept of nested loops controllers, with unique novel features for the specific application under investigation.*

The ability to perform accurate movements and apply accurate forces with machining end effectors inside complex machinery and unknown environments has the potential to reveal new possibilities of in-situ repair tasks too challenging for previous technologies, and may even bring about new methods for component manufacture and assembly.

7.2 Academic findings and engineering validations

This work introduces novel approaches to position and force control of slender and compliant robots, such as the novel hybrid-architecture dual-flexible-backbone continuum robot also described. Advances in position feedback, force feedback and closed loop control methodologies, as well as simultaneous control schemes to bring them into synchrony have been described and documented. The following subsections summarise the main achievements of this thesis.

7.2.1 Novel combined architecture slender and compliant robot for remote controlled in-situ boreblending

Chapter 3 of this thesis presented a case study of the development of a slender and compliant robot for in-situ machining.

A novel hybrid mechanical architecture was introduced following a detailed study of the degree of freedom of manual tools for abrasive removal of foreign object damage on aeroengine compressor blades, a procedure known as boreblending, and following a thorough analysis of the working volume within specific stages of the high-pressure compressor of a Rolls-Royce *Trent XWB* aeroengine (the scenario selected for this case study). The hybrid design (led by Dr Adam Nagy-Sochacki and assisted by the present author) combined linear, rotary and tendon-driven continuum stages in a self-contained, nested carriages layout. The continuum segments formed the tip of the slender section and provided three independent degrees of actuation by flexion of Nitinol dual backbones (following a compliant joint buckling study carried out by the present author). The end effector consisted of a high-speed air-driven spindle with a receptacle to accept friction grip grinding burrs. A miniature stereo camera mounted near the tip was used to capture measurements of the workpiece for analysis and to define the shape of the repair.

The forward and inverse kinematics of this hybrid design were derived using the Denavit-Hartenberg convention and the Jacobian pseudo-inverse method (an iterative

approach to solve complex kinematics). The approach was validated experimentally using an optical motion capture system and found to have a tip positioning accuracy of 8.5% of the total continuum length (a measure used to compare different approaches within this work).

A remote operation workflow (led by Dr Bilal Nasser and assisted by the present author) was created to allow a skilled operator to control, define and oversee the repair from a distant high-level controller. A self-sufficient, latency-invariant low-level controller received instructions and calculated the actuator space movements to carry out the machining paths. This low-level controller used sensors to identify unexpected problems and respond appropriately before alerting the operator. A custom communication protocol was implemented to combine reliable data and media transfer.

The system performance was tested by machining a number of similar cuts on compressor blades, with a shape RMS error of $64\mu m$. The robot was successfully demonstrated on a Rolls-Royce *Trent XWB* aeroengine.

The test study presented in Chapter 3 served not only to successfully address and demonstrate an industrial need, but also to identify and highlight shortcomings in conventional open loop approaches to position and force control. These shortcomings included:

1. A lack of position feedback, leading to reliance on inaccurate assumptions about the behaviour of non-linear elements of the design, such as friction losses and super-elastic flexion of materials like Nitinol.

2. A lack of force feedback, leading to unreliable performance in the event of unexpected surface features, and unnecessarily time-consuming fixed depth of cut passes.

3. A lack of synchronised position and force control, leading to sub-optimal material removal and excessive task durations.

The rest of this thesis made progress towards addressing these issues with a view to strengthen future designs.

7.2.2 Novel methodology for position feedback using tubular ionic liquid stretch sensors

Chapter 4 presented advances in position control of slender and compliant robots.

A novel methodology for construction and calibration of tubular ionic liquid stretch sensor was developed, and the resulting sensors were used as feedback for position control of continuum stages. Tubular ionic liquid stretch sensors were constructed by filling pre-treated silicone rubber tubes with an imidazolium salt that is liquid at room temperature, and closed with gold electrodes at each end. A material compatibility study determined that 1-methyl-3-octylimidazolium chloride was a suitable ionic liquid with sufficient conductivity and stability, and with low reactivity with other component materials. The tubes could be fitted through holes in the component vertebral disks of continuum segments for shape measurement.

Sensors were calibrated by subjecting them to stretch cycles while recording their electrical characteristics and mechanical strain. The behaviour was described mathematically using new derivations of viscoelastic deformation and approximated with a second order polynomial curve (taking account of unique calibration sensor constants for each tubular sensor).

A PID closed loop control scheme was implemented using voltage drop across the sensor to inform the duty cycle for control of a linear actuator and a simple planar continuum stage. The resulting position tracking achieved errors as low as 1.5% of the total continuum length, suggesting a marked improvement over the open-loop case study of Chapter 3

Four tubular ionic liquid stretch sensors were then installed as feedback on a complex, two-segment, two-bend-direction continuum manipulator to demonstrate the scalability of the methodology to more sophisticated robot architectures. The results showed precise tracking of trajectories (to within 2.3% of the total continuum length) and promising robustness regardless of incorrect tensioning or erroneous starting configuration.

The work presented in Chapter 4 of this thesis demonstrated the implementation of a low-cost, scalable position sensor for closed loop control of complex continuum

manipulators.

7.2.3 Novel methodology for force feedback using airborne sound machining force sensor

Chapter 5 presented advances in force control of slender and compliant robots for in-situ machining.

A novel methodology was described to use audible sound features to inform a controller and operate a machining robot with closed loop force control. The sensor consists of two microphones and a signal processing system configured to identify the dominant frequency of sound (associated with the speed of rotation of an air-driven spindle and burr) and the intensity of sound (based on directional pressure gradients).

The airborne sound machining force sensor was calibrated by extracting sound features during grinding at known constant contact forces (achieved using a cantilever weight rig). Signals were analysed and calibration relations were assigned based on the mechanics of tool-workpiece interactions. The airborne sound frequency was observed to relate to contact force by virtue of the torque-speed characteristics of the spindle, while the intensity of sound was found to relate to transmitted energy in the form of workpiece vibration and therefore used to identify resonance.

A manipulator was used to perform simple machining tasks with constant force, using the airborne sound machining force sensor as feedback. The closed loop control scheme used a proportional only velocity controller to track contact force with dominant frequency, and a variable gain, variable deadband and variable moving bandpass filter width driven by the calculated sound intensity.

The force control strategy was demonstrated using a five-axis robot arm with a sixth tool axis to machine constant force and constant depth features on cantilever beams with unknown topology. This demonstrated the controller's ability to follow edges using force control and to achieve tight tracking despite disturbances.

The work presented in this chapter demonstrated the implementation of a widely scalable, low cost force sensor for closed loop control of machining manipulators; an

approach very much applicable to slender and compliant robots such as dual-flexible-backbone continuum robots.

7.2.4 Novel simultaneous position and force control scheme for slender and compliant machining robots

Chapter 6 presented advances in the simultaneous position and force control of slender and compliant robots for in-situ machining, and demonstrated the compatibility of the position and force controllers described in Chapters 4 and 5.

A simultaneous position and force control scheme was described, consisting of a, constrained, biased, PI force control outer loop (using airborne sound machining force sensor feedback) with a nested PID position control inner loop (using tubular ionic liquid stretch sensor feedback). Additionally, a global threshold interrupt was implemented to terminate machining at the desired shape. The force control output was limited to act in the direction perpendicular to the long edge of the workpiece and perpendicular to the tool rotation axis, resulting in a robust controller capable of reacting to unknown topologies such as those found in compressor blades with foreign object damage.

The simultaneous position and force controller was tested using a dual-segment, two-bend-direction continuum manipulator equipped with an air-driven spindle and grinding burr. Four tubular ionic liquid stretch sensors were used to measure position, while two microphones placed some distance away were used to measure machining contact force. A cutting path was defined and the manipulator executed the cut with constant maximum force on a number of samples, with a shape accuracy of 2.0% of total continuum length and a force accuracy of 1.5% of target force.

The nested control loops methodology was demonstrated on a dented high pressure compressor blade from a Rolls-Royce Trent XWB aeroengine. The blade was successfully machined with a stress relieving feature similar to those performed during boreblending.

Successful trials demonstrated the robustness and versatility of the simultaneous control method described in this chapter, as well as the effectiveness and compatibility of the position and force controllers described in this thesis.

7.3 Future work

The proposed systems and methodologies have been validated against mathematical models and physical demonstrations presented in this thesis. However, further research in the areas covered in this section could bring substantial improvements to subsequent robotic systems.

7.3.1 Enhancing position control of slender and compliant robots for in-situ machining

Further work with tubular ionic liquid stretch sensors may seek to further miniaturise their construction and identify the limits of scalability of the construction presented in Chapter 4. This may require exploring alternative conductors as well as alternative options for measurement of resistance or resistivity.

Future work may also look to include redundant sensors in each segment to provide temperature compensation. This addition would not only allow the manipulator to operate in realistic industrial environments without prior calibration, but may also be used to provide useful information about the environment and even create a temperature map of the surroundings during in-situ tasks.

Additional research could be made into the possibility of retro-fitting stretch sensors on sensorless continuum robots by 3D printing complex sleeves with internal sensor channels. This could allow for a number of existing in-situ repair technologies to be controlled with improved accuracy and reliability.

7.3.2 Enhancing force control of compliant robots for in-situ machining

Further work with airborne sound machining force sensors may seek to improve the versatility and performance of the controller by processing the sound signals continuously rather than at discrete intervals of multiple thousands of pressure acquisitions. This could be achieved using field programmable gate arrays or other

appropriate hardware for real-time calculation of frequency domain features and sound intensity. This would eliminate the need to acquire and process batches of $0.1s$ of data at a time and allow for orders of magnitude of improvement in sample speeds and therefore vastly expand the options available for control scheme definitions, such as the inclusion of more sophisticated tuned control structures to enhance the response to perturbations.

The controller could also be made more robust by introducing a nested loops or cascade controller approach to regulate actuator velocity. While the present controller outputs a voltage or pulse frequency that is theoretically linked to velocity, a cascade controller could be used to have that output be the input of a separate inner control loop that regulates the velocity with its own feedback and tuning (such as acceleration and jerk settings). This would result in more predictable motion and therefore better control authority.

Adding extra environmental microphones could also allow for more robust operation in noisy industrial environments where more than one air-driven spindle may be present.

Additional research could be made into the possibility of optimising the resulting surface characteristics for particular workpiece and tool combinations, where improved surface quality and material removal rate can be tuned for any given tool and at any state of tool wear.

7.3.3 Enhancing simultaneous position and force control of slender and compliant robots for in-situ machining

Further work on simultaneous position and force control using tubular ionic liquid stretch sensors and airborne sound machining force sensors as feedback could be made by introducing a multi-threshold partial completion strategy, with different feed speed and contact force settings for bulk removal and final polish.

In addition to this, the machining path could be changed once part of the path has reached one of the thresholds. By skipping or speeding over sections of the machining path that have already reached the net depth, it would be possible to improve the performance

and reduce the time taken further.

Future work may also include further exploration of alternative simultaneous control loop architectures such as parallel loops or hybrid controllers, where applicable to particular in-situ repair tasks. Such changes may make it possible to modify and add task definitions, such as no-go areas and variable component materials.

7.3.4 The future of specialised slender and compliant robotic systems for in-situ machining

In light of the technological and scientific advances described in this thesis, future slender and compliant robots for in-situ machining could be designed taking account of the improved capabilities afforded by novel sensors and control strategies.

- Continuum robot vertebrae may be designed with additional holes in the proximal stages for tubular stretch sensors, as well as redundant holes for temperature-sensing redundant sensors.

- Continuum sections of slender robots may be designed with longer reach and dexterity in light of the improved positioning accuracy, as well as with added degrees of freedom in light of the miniature size sensors.

- Slender and compliant manipulators may be separated from their actuation packs by long distance cable conduits regardless of the possibility of undesirable tendon stretch, in light of the new inclusion of position feedback.

- Slender and compliant robots may be designed with redundant tubular ionic liquid stretch sensors for temperature compensation and measurement, and employed for tasks requiring temperature measurement or mapping in extreme environments such as industrial assets, medical interventions, search and rescue and marine inspection in light of the temperature sensing capabilities of such sensors.

- Compliant, long reach robots with machining end effectors may be designed for tasks that require higher levels of contact force confidence, as well as improved consistency

of material removal in light of the new inclusion of force feedback.

- End effectors may be designed with any form of material removal or processing tool that produces repeatable airborne sound signals, in light of the new methodology for calibration of remote sensors.

- Robotic solutions may be attempted for tasks that require dexterity and accuracy of machined shapes in difficult to reach places, in light of the new methods of simultaneous position and force control for machining using slender and compliant devices.

7.4 Closing remarks

From horse-drawn ploughs to steam locomotives to continuum robots for in-situ machining, humans have always sought to create tools that make life easier and improve living conditions. The twenty-first century has seen great leaps in the field of robotics and greatly advanced the variety and function of tools at mankind's disposal. The advances in position and force control described in this body of work build on the collective experience of engineers and scientists past and present, and will, hopefully, serve to expand this library of ingenuity and creativity and provide new additions to the toolbox of future researchers.

References

[1] Robert C. Allen. *The British industrial revolution in global perspective*. New approaches to economic and social history. Cambridge University Press, Cambridge; New York, 2009.

[2] Klaus Schwab. *The fourth industrial revolution*. Crown Business, New York, first U.S. edition. edition, 2016.

[3] International Federation of Robotics. Service robots global sales value reaches 12.9 billion usd. `https://ifr.org/news/service-robots-global-sales-value-reaches-12.9-billion-usd`, September 2019.

[4] Alexander Zelinsky. *Field and service robotics*. Springer, Berlin ; New York, 1998.

[5] D. Axinte and I. Walker. Robots for in situ interventions. *IEEE Robotics & Automation Magazine*, 26(1):8, 2019.

[6] P. Qi, C. Qiu, H. B. Liu, J. S. Dai, L. D. Seneviratne, and K. Althoefer. A novel continuum manipulator design using serially connected double-layer planar springs. *IEEE-ASME Transactions on Mechatronics*, 21(3):1281–1292, 2016.

[7] N. Simaan, R. Taylor, and P. Flint. A dexterous system for laryngeal surgery. *2004 IEEE International Conference on Robotics and Automation, Vols 1- 5, Proceedings*, pages 351–357, 2004.

[8] X. Dong, M. Raffles, S. Cobos-Guzman, D. Axinte, and J. Kell. A novel continuum robot using twin-pivot compliant joints: Design, modeling, and validation. *Journal of Mechanisms and Robotics-Transactions of the ASME*, 8(2), 2016.

[9] S. Song, Z. Li, M. Q. H. Meng, H. Y. Yu, and H. L. Ren. Real-time shape estimation for wire-driven flexible robots with multiple bending sections based on quadratic bezier curves. *IEEE Sensors Journal*, 15(11):6326–6334, 2015.

[10] T. Mahl, A. Hildebrandt, and O. Sawodny. A variable curvature continuum kinematics for kinematic control of the bionic handling assistant. *IEEE Transactions on Robotics*, 30(4):935–949, 2014.

[11] K. Xu and N. Simaan. An investigation of the intrinsic force sensing capabilities of continuum robots. *IEEE Transactions on Robotics*, 24(3):576–587, 2008.

[12] K. Groom, L. Wang, N. Simaan, and J. Netterville. Robot-assisted transnasal laryngoplasty in cadaveric models: Quantifying forces and identifying challenges. *Laryngoscope*, 125(5):1166–1168, 2015.

[13] C. He, S. X. Wang, H. Q. Sang, J. H. Li, and L. N. Zhang. Force sensing of multiple-dof cable-driven instruments for minimally invasive robotic surgery. *International Journal of Medical Robotics and Computer Assisted Surgery*, 10(3):314–324, 2014.

[14] R. Buckingham and A. Graham. Nuclear snake-arm robots. *Industrial Robot-an International Journal*, 39(1):6–11, 2012.

[15] S. Cobos-Guzman, D. Palmer, and D. Axinte. Kinematic model to control the end-effector of a continuum robot for multi-axis processing. *Robotica*, 35(1):224–240, 2017.

[16] X. Dong, D. Axinte, D. Palmer, S. Cobos, M. Raffles, A. Rabani, and J. Kell. Development of a slender continuum robotic system for on-wing inspection/repair of gas turbine engines. *Robotics and Computer-Integrated Manufacturing*, 44:218–229, 2017.

[17] M. W. Hannan and I. D. Walker. Kinematics and the implementation of an elephant's trunk manipulator and other continuum style robots. *Journal of Robotic Systems*, 20(2):45–63, 2003.

[18] M. W. Hannan and I. D. Walker. Novel kinematics for continuum robots. *Advances in Robot Kinematics*, pages 227–238, 2000.

[19] M. W. Hannan and I. D. Walker. The 'elephant trunk' manipulator, design and implementation. *2001 IEEE/ASME International Conference on Advanced Intelligent Mechatronics Proceedings, Vols I and Ii*, pages 14–19, 2001.

[20] I. D. Walker, H. Choset, and G. S. Chirikjian. Snake-like and continuum robots. *Springer Handbook of Robotics*, pages 481–498, 2016.

[21] A. Degani, H. Choset, A. Wolf, and M. A. Zenati. Highly articulated robotic probe for minimally invasive surgery. *2006 IEEE International Conference on Robotics and Automation (ICRA), Vols 1-10*, pages 4167–+, 2006.

[22] Y. Kim, S. S. Cheng, and J. P. Desai. Towards the development of a spring-based continuum robot for neurosurgery. *Medical Imaging 2015: Image-Guided Procedures, Robotic Interventions, and Modeling*, 9415, 2015.

[23] J. N. Ding, R. E. Goldman, K. Xu, P. K. Allen, D. L. Fowler, and N. Simaan. Design and coordination kinematics of an insertable robotic effectors platform for single-port access surgery. *IEEE-ASME Transactions on Mechatronics*, 18(5):1612–1624, 2013.

[24] M. Calisti, M. Giorelli, G. Levy, B. Mazzolai, B. Hochner, C. Laschi, and P. Dario. An octopus-bioinspired solution to movement and manipulation for soft robots. *Bioinspiration & Biomimetics*, 6(3), 2011.

[25] F. Renda, M. Giorelli, M. Calisti, M. Cianchetti, and C. Laschi. Dynamic model of a multibending soft robot arm driven by cables. *IEEE Transactions on Robotics*, 30(5):1109–1122, 2014.

[26] C. Meng, W. D. Xu, H. Y. Li, H. A. Zhang, and D. Xu. A new design of cellular soft continuum manipulator based on beehive-inspired modular structure. *International Journal of Advanced Robotic Systems*, 14(3), 2017.

[27] R. J. Kang, D. T. Branson, T. J. Zheng, E. Guglielmino, and D. G. Caldwell. Design, modeling and control of a pneumatically actuated manipulator inspired by biological continuum structures. *Bioinspiration & Biomimetics*, 8(3), 2013.

[28] R. J. Murphy, M. D. M. Kutzer, S. M. Segreti, B. C. Lucas, and M. Armand. Design and kinematic characterization of a surgical manipulator with a focus on treating osteolysis. *Robotica*, 32(6):835–850, 2014.

[29] C. Bergeles, A. H. Gosline, N. V. Vasilyev, P. J. Codd, P. J. del Nido, and P. E. Dupont. Concentric tube robot design and optimization based on task and anatomical constraints. *IEEE Transactions on Robotics*, 31(1):67–84, 2015.

[30] P. Sears and P. E. Dupont. Inverse kinematics of concentric tube steerable needles. *Proceedings of the 2007 IEEE International Conference on Robotics and Automation, Vols 1-10*, pages 1887–1999, 2007.

[31] J. P. Swensen, M. D. Lin, A. M. Okamura, and N. J. Cowan. Torsional dynamics of steerable needles: Modeling and fluoroscopic guidance. *IEEE Transactions on Biomedical Engineering*, 61(11):2707–2717, 2014.

[32] D. C. Rucker, R. J. Webster, G. S. Chirikjian, and N. J. Cowan. Equilibrium conformations of concentric-tube continuum robots. *International Journal of Robotics Research*, 29(10):1263–1280, 2010.

[33] P. E. Dupont, J. Lock, and B. Itkowitz. Real-time position control of concentric tube robots. *2010 IEEE International Conference on Robotics and Automation (ICRA)*, pages 562–568, 2010.

[34] P. E. Dupont, J. Lock, B. Itkowitz, and E. Butler. Design and control of concentric-tube robots. *IEEE Transactions on Robotics*, 26(2):209–225, 2010.

[35] J. Jeon, B. J. Yi, K. Shin, and W. Kim. Kinematic modelling and configuration estimation for elastic wire using minimum sensors. *Proceedings of the Institution of Mechanical Engineers Part C-Journal of Mechanical Engineering Science*, 229(12):2195–2206, 2015.

[36] S. Hasanzadeh and F. Janabi-Sharifi. An efficient static analysis of continuum robots. *Journal of Mechanisms and Robotics-Transactions of the ASME*, 6(3), 2014.

[37] J. Ha and P. E. Dupont. Designing stable concentric tube robots using piecewise straight tubes. *IEEE Robotics and Automation Letters*, 2(1):298–304, 2017.

[38] S. Song, Z. Li, H. Y. Yu, and H. L. Ren. Electromagnetic positioning for tip tracking and shape sensing of flexible robots. *IEEE Sensors Journal*, 15(8):4565–4575, 2015.

[39] C. C. Zhang, Y. Lu, S. Song, and M. Q. H. Meng. Shape tracking and navigation for continuum surgical robot based on magnetic tracking. *2017 IEEE International Conference on Information and Automation (IEEE ICIA 2017)*, pages 1143–1149, 2017.

[40] M. M. Dalvand, S. Nahavandi, and R. D. Howe. Fast vision-based catheter 3d reconstruction. *Physics in Medicine and Biology*, 61(14):5128–5148, 2016.

[41] I. S. Godage, G. A. Medrano-Cerda, D. T. Branson, E. Guglielmino, and D. G. Caldwell. Modal kinematics for multisection continuum arms. *Bioinspiration & Biomimetics*, 10(3), 2015.

[42] B. A. Jones and I. D. Walker. Practical kinematics for real-time implementation of continuum robots. *IEEE Transactions on Robotics*, 22(6):1087–1099, 2006.

[43] B. A. Jones and I. D. Walker. Kinematics for multisection continuum robots. *IEEE Transactions on Robotics*, 22(1):43–55, 2006.

[44] Y. Shapiro, G. Kosa, and A. Wolf. Shape tracking of planar hyper-flexible beams via embedded PVDF deflection sensors. *IEEE-ASME Transactions on Mechatronics*, 19(4):1260–1267, 2014.

[45] X. Dong, M. Raffles, S. C. Guzman, D. Axinte, and J. Kell. Design and analysis of a family of snake arm robots connected by compliant joints. *Mechanism and Machine Theory*, 77:73–91, 2014.

[46] R. R. J. Maier, W. N. MacPherson, J. S. Barton, M. Carne, M. Swan, J. N. Sharma, S. K. Futter, D. A. Knox, B. J. S. Jones, and S. McCulloch. Embedded fiber optic sensors within additive layer manufactured components. *IEEE Sensors Journal*, 13(3), 2013.

[47] J. Kang, J. Zeng, X. H. Guo, X. J. Gong, T. W. Li, J. S. Yu, and K. He. Impact and vibration monitoring method of composite flexible structures based on FBG sensor network. *2017 International Conference on Optical Instruments and Technology Advanced Optical Sensors and Applications*, 10618, 2017.

[48] A. Lamberti, G. Chiesura, G. Luyckx, J. Degrieck, M. Kaufmann, and S. Vanlanduit. Dynamic strain measurements on automotive and aeronautic composite components by means of embedded fiber Bragg grating sensors. *Sensors*, 15(10):27174–27200, 2015.

[49] A. Rajabzadeh, R. C. Hendriks, R. Heusdens, and R. M. Groves. Classification of composite damage from FBG load monitoring signals. *Sensors and Smart Structures Technologies for Civil, Mechanical, and Aerospace Systems 2017*, 10168, 2017.

[50] M. Yeager, A. Whittaker, M. Todd, H. Kim, C. Key, and W. Gregory. Impact detection and characterization in composite laminates with embedded fiber Bragg gratings. *Structural Health Monitoring - from Sensing to Diagnosis and Prognosis*, 188:156–162, 2017.

[51] T. L. T. Lun, K. Wang, J. D. L. Ho, K. H. Lee, K. Y. Sze, and K. W. Kwok. Real-time surface shape sensing for soft and flexible structures using fiber Bragg gratings. *IEEE Robotics and Automation Letters*, 4(2):1454–1461, 2019.

[52] K. Oman, B. Van Hoe, K. Aly, K. Peters, G. Van Steenberge, N. Stan, and S. Schultz. Instrumentation of integrally stiffened composite panel with fiber Bragg

grating sensors for vibration measurements. *Smart Materials and Structures*, 24(8), 2015.

[53] F. Khan, A. Denasi, D. Barrera, J. Madrigal, S. Sales, and S. Misra. Multi-core optical fibers with Bragg gratings as shape sensor for flexible medical instruments. *IEEE Sensors Journal*, 19(14):5878–5884, 2019.

[54] Y. L. He, L. Q. Zhu, G. K. Sun, M. X. Yu, and M. L. Dong. Design, measurement and shape reconstruction of soft surgical actuator based on fiber Bragg gratings. *Applied Sciences-Basel*, 8(10), 2018.

[55] H. Liu, A. Farvardin, R. Grupp, R. J. Murphy, R. H. Taylor, I. Iordachita, and M. Armand. Shape tracking of a dexterous continuum manipulator utilizing two large deflection shape sensors. *IEEE Sensors Journal*, 15(10):5494–5503, 2015.

[56] R. J. Roesthuis and S. Misra. Steering of multisegment continuum manipulators using rigid-link modeling and FBG-based shape sensing. *IEEE Transactions on Robotics*, 32(2):372–382, 2016.

[57] J. Sheng, N. J. Deacon, J. P. Desai, and IEEE. A large-deflection FBG bending sensor for sma bending modules for steerable surgical robots. In *International Conference on Robotics and Automation (ICRA)*, IEEE International Conference on Robotics and Automation ICRA, pages 900–906, 2019.

[58] D. Y. Feng, W. J. Zhou, X. G. Qiao, and J. Albert. Compact optical fiber 3d shape sensor based on a pair of orthogonal tilted fiber Bragg gratings. *Scientific Reports*, 5, 2015.

[59] J. Wang, K. Y. Tao, W. S. Zhu, J. F. Jiang, and T. G. Liu. A FBG-oct catheter to reconstruct vascular shape in intravascular optical coherence tomography. *IEEE Photonics Technology Letters*, 31(9):701–704, 2019.

[60] K. Mandal, F. Parent, S. Martel, R. Kashyap, and S. Kadoury. Vessel-based registration of an optical shape sensing catheter for mr navigation. *International Journal of Computer Assisted Radiology and Surgery*, 11(6):1025–1034, 2016.

[61] R. J. Roesthuis, M. Kemp, J. J. van den Dobbelsteen, and S. Misra. Three-dimensional needle shape reconstruction using an array of fiber Bragg grating sensors. *IEEE-ASME Transactions on Mechatronics*, 19(4):1115–1126, 2014.

[62] X. H. Yi, J. W. Qian, Y. N. Zhang, Z. Zhang, and L. Y. Shen. 3-d shape display of intelligent colonoscope based on FBG sensor array and binocular vision. *2007 IEEE/ICME International Conference on Complex Medical Engineering, Vols 1-4*, pages 14–19, 2007.

[63] N. Rahman, N. J. Deaton, J. Sheng, S. S. Cheng, and J. P. Desai. Modular FBG bending sensor for continuum neurosurgical robot. *IEEE Robotics and Automation Letters*, 4(2):1424–1430, 2019.

[64] M. Cianchetti, F. Renda, A. Licofonte, and C. Laschi. Sensorization of continuum soft robots for reconstructing their spatial configuration. *2012 4th IEEE Ras & Embs International Conference on Biomedical Robotics and Biomechatronics (Biorob)*, pages 634–639, 2012.

[65] P. Polygerinos, N. Correll, S. A. Morin, B. Mosadegh, C. D. Onal, K. Petersen, M. Cianchetti, M. T. Tolley, and R. F. Shepherd. Soft robotics: Review of fluid-driven intrinsically soft devices; manufacturing, sensing, control, and applications in human-robot interaction. *Advanced Engineering Materials*, 19(12), 2017.

[66] S. Barrau, P. Demont, A. Peigney, C. Laurent, and C. Lacabanne. Dc and ac conductivity of carbon nanotubes-polyepoxy composites. *Macromolecules*, 36(14):5187–5194, 2003.

[67] N. S. Lu, C. Lu, S. X. Yang, and J. Rogers. Highly sensitive skin-mountable strain gauges based entirely on elastomers. *Advanced Functional Materials*, 22(19):4044–4050, 2012.

[68] M. Amjadi, Y. J. Yoon, and I. Park. Ultra-stretchable and skin-mountable strain sensors using carbon nanotubes-ecoflex nanocomposites. *Nanotechnology*, 26(37), 2015.

[69] C. S. Boland, U. Khan, C. Backes, A. O'Neill, J. McCauley, S. Duane, R. Shanker, Y. Liu, I. Jurewicz, A. B. Dalton, and J. N. Coleman. Sensitive, high-strain, high-rate bodily motion sensors based on graphene-rubber composites. *ACS Nano*, 8(9):8819–8830, 2014.

[70] Y. R. Jeong, H. Park, S. W. Jin, S. Y. Hong, S. S. Lee, and J. S. Ha. Highly stretchable and sensitive strain sensors using fragmentized graphene foam. *Advanced Functional Materials*, 25(27):4228–4236, 2015.

[71] L. Flandin, A. Hiltner, and E. Baer. Interrelationships between electrical and mechanical properties of a carbon black-filled ethylene-octene elastomer. *Polymer*, 42(2):827–838, 2001.

[72] P. K. Pramanik, D. Khastgir, S. K. De, and T. N. Saha. Pressure-sensitive electrically conductive nitrile rubber composites filled with particulate carbon-black and short carbon-fiber. *Journal of Materials Science*, 25(9):3848–3853, 1990.

[73] M. Amjadi, A. Pichitpajongkit, S. Lee, S. Ryu, and I. Park. Highly stretchable and sensitive strain sensor based on silver nanowire-elastomer nanocomposite. *ACS Nano*, 8(5):5154–5163, 2014.

[74] X. Xiao, L. Y. Yuan, J. W. Zhong, T. P. Ding, Y. Liu, Z. X. Cai, Y. G. Rong, H. W. Han, J. Zhou, and Z. L. Wang. High-strain sensors based on zno nanowire/polystyrene hybridized flexible films. *Advanced Materials*, 23(45):5440–5452, 2011.

[75] S. S. Yao and Y. Zhu. Wearable multifunctional sensors using printed stretchable conductors made of silver nanowires. *Nanoscale*, 6(4):2345–2352, 2014.

[76] S. Rosset and H. R. Shea. Flexible and stretchable electrodes for dielectric elastomer actuators. *Applied Physics a-Materials Science & Processing*, 110(2):281–307, 2013.

[77] V. Wall and O. Brock. Multi-task sensorization of soft actuators using prior knowledge. *2019 International Conference on Robotics and Automation (ICRA)*, pages 9416–9421, 2019.

[78] Y. L. Park, B. R. Chen, and R. J. Wood. Design and fabrication of soft artificial skin using embedded microchannels and liquid conductors. *IEEE Sensors Journal*, 12(8):2711–2718, 2012.

[79] D. Y. Choi, M. H. Kim, Y. S. Oh, S. H. Jung, J. H. Jung, H. J. Sung, H. W. Lee, and H. M. Lee. Highly stretchable, hysteresis-free ionic liquid -based strain sensor for precise human motion monitoring. *ACS Applied Materials & Interfaces*, 9(2):1770–1780, 2017.

[80] Y. Wang, S. Gong, S. J. Wang, G. P. Simon, and W. L. Cheng. Volume-invariant ionic liquid microbands as highly durable wearable biomedical sensors. *Materials Horizons*, 3(3):208–213, 2016.

[81] S. H. Zhang, F. X. Wang, J. J. Li, H. D. Peng, J. H. Yan, and G. B. Pan. Wearable wide-range strain sensors based on ionic liquids and monitoring of human activities. *Sensors*, 17(11), 2017.

[82] L. Hines, K. Petersen, and M. Sitti. Inflated soft actuators with reversible stable deformations. *Advanced Materials*, 28(19):3690–3696, 2016.

[83] J. T. Muth, D. M. Vogt, R. L. Truby, Y. Menguc, D. B. Kolesky, R. J. Wood, and J. A. Lewis. Embedded 3d printing of strain sensors within highly stretchable elastomers. *Advanced Materials*, 26(36):6307–6312, 2014.

[84] K. Noda, K. Matsumoto, and I. Shimoyama. Stretchable force sensor array using conductive liquid. *26th IEEE International Conference on Micro Electro Mechanical Systems (MEMS 2013)*, pages 681–684, 2013.

[85] S. Russo, T. Ranzani, H. B. Liu, S. Nefti-Meziani, K. Althoefer, and A. Menciassi. Soft and stretchable sensor using biocompatible electrodes and liquid for medical applications. *Soft Robotics*, 2(4):146–154, 2015.

[86] L. Cai, L. Song, P. S. Luan, Q. Zhang, N. Zhang, Q. Q. Gao, D. Zhao, X. Zhang, M. Tu, F. Yang, W. B. Zhou, Q. X. Fan, J. Luo, W. Y. Zhou, P. M. Ajayan, and

S. S. Xie. Super-stretchable, transparent carbon nanotube-based capacitive strain sensors for human motion detection. *Scientific Reports*, 3, 2013.

[87] D. J. Cohen, D. Mitra, K. Peterson, and M. M. Maharbiz. A highly elastic, capacitive strain gauge based on percolating nanotube networks. *Nano Letters*, 12(4):1821–1825, 2012.

[88] U. H. Shin, D. W. Jeong, S. M. Park, S. H. Kim, H. W. Lee, and J. M. Kim. Highly stretchable conductors and piezocapacitive strain gauges based on simple contact-transfer patterning of carbon nanotube forests. *Carbon*, 80:396–404, 2014.

[89] S. Ozel, N. A. Keskin, D. Khea, and C. D. Onal. A precise embedded curvature sensor module for soft-bodied robots. *Sensors and Actuators A-Physical*, 236:349–356, 2015.

[90] W. J. Tao, E. H. Skorina, F. C. Chen, J. Mclnnis, M. Luo, and C. D. Onal. Bioinspired design and fabrication principles of reliable fluidic soft actuation modules. *2015 IEEE International Conference on Robotics and Biomimetics (RoBio)*, pages 2169–2174, 2015.

[91] M. Luo, Y. X. Pan, E. H. Skorina, W. J. Tao, F. C. Chen, S. Ozel, and C. D. Onal. Slithering towards autonomy: a self-contained soft robotic snake platform with integrated curvature sensing. *Bioinspiration & Biomimetics*, 10(5), 2015.

[92] S. Ozel, E. H. Skorina, M. Luo, W. J. Tao, F. C. Chen, Y. X. Pan, and C. D. Onal. A composite soft bending actuation module with integrated curvature sensing. *2016 IEEE International Conference on Robotics and Automation (ICRA)*, pages 4963–4968, 2016.

[93] H. C. Zhao, R. K. Huang, and R. F. Shepherd. Curvature control of soft orthotics via low cost solid-state optics. *2016 IEEE International Conference on Robotics and Automation (ICRA)*, pages 4008–4013, 2016.

[94] H. C. Zhao, J. Jalving, R. K. Huang, R. Knepper, A. Ruina, and R. Shepherd. A helping hand soft orthosis with integrated optical strain sensors and emg control. *IEEE Robotics & Automation Magazine*, 23(3):55–64, 2016.

[95] H. C. Zhao, K. O'Brien, S. Li, and R. F. Shepherd. Optoelectronically innervated soft prosthetic hand via stretchable optical waveguides. *Science Robotics*, 1(1), 2016.

[96] S. Hamill, J. Whitehead, P. Ferenz, R. F. Shepherd, H. Kress-Gazit, and IEEE. Resilient task planning and execution for reactive soft robots. In *International Conference on Robotics and Automation (ICRA)*, IEEE International Conference on Robotics and Automation ICRA, pages 5148–5154, 2019.

[97] T. C. Searle, K. Althoefer, L. Seneviratne, H. B. Liu, and IEEE. An optical curvature sensor for flexible manipulators. *2013 IEEE International Conference on Robotics and Automation*, pages 4415–4420, 2013.

[98] S. Chiaverini, B. Siciliano, and L. Villani. A survey of robot interaction control schemes with experimental comparison. *IEEE-ASME Transactions on Mechatronics*, 4(3):273–285, 1999.

[99] H. C. Cho, J. K. Min, and J. B. Song. Hybrid position and force control of a robot arm equipped with joint torque sensors. *2013 10th International Conference on Ubiquitous Robots and Ambient Intelligence (URAI)*, pages 577–579, 2013.

[100] A. Wahrburg, J. Bos, K. D. Listmann, F. Dai, B. Matthias, and H. Ding. Motor-current-based estimation of cartesian contact forces and torques for robotic manipulators and its application to force control. *IEEE Transactions on Automation Science and Engineering*, 15(2):879–886, 2018.

[101] C. D. Tong, M. Q. Wang, B. G. Zhao, Z. S. Ping, and P. Zheng. A novel sensorless control strategy for brushless direct current motor based on the estimation of line back electro-motive force. *Energies*, 10(9), 2017.

[102] S. Kim and J. Bae. Force-mode control of rotary series elastic actuators in a lower extremity exoskeleton using model-inverse time delay control. *IEEE-ASME Transactions on Mechatronics*, 22(3):1392–1400, 2017.

[103] A. Calanca and P. Fiorini. Impedance control of series elastic actuators based on well-defined force dynamics. *Robotics and Autonomous Systems*, 96:81–92, 2017.

[104] K. Kong, J. Bae, and M. Tomizuka. Control of rotary series elastic actuator for ideal force-mode actuation in human-robot interaction applications. *IEEE-ASME Transactions on Mechatronics*, 14(1):105–118, 2009.

[105] S. Oh and K. Kong. High-precision robust force control of a series elastic actuator. *IEEE-ASME Transactions on Mechatronics*, 22(1):71–80, 2017.

[106] K. Kosuge, H. Takeuchi, and K. Furuta. Motion control of a robot arm using joint torque sensors. *IEEE Transactions on Robotics and Automation*, 6(2):258–263, 1990.

[107] T. Gold, A. Volz, and K. Graichen. External torque estimation for an industrial robot arm using joint torsion and motor current measurements. *IFAC Papers online*, 52(15):352–357, 2019.

[108] N. M. Ceriani, A. M. Zanchettin, P. Rocco, A. Stolt, and A. Robertsson. Reactive task adaptation based on hierarchical constraints classification for safe industrial robots. *IEEE-ASME Transactions on Mechatronics*, 20(6):2935–2949, 2015.

[109] A. Wahrburg, E. Morara, G. Cesari, B. Matthias, and H. Ding. Cartesian contact force estimation for robotic manipulators using Kalman filters and the generalized momentum. In *IEEE International Conference on Automation Science and Engineering (CASE)*, IEEE International Conference on Automation Science and Engineering, pages 1230–1235, 2015.

[110] M. Van Damme, P. Beyl, B. Vanderborght, V. Grosu, R. Van Ham, I. Vanderniepen, A. Matthys, D. Lefeber, and IEEE. Estimating robot end-effector force from noisy

actuator torque measurements. In *IEEE International Conference on Robotics and Automation (ICRA)*, IEEE International Conference on Robotics and Automation ICRA, pages 1108–1113, 2011.

[111] R. M. Inigo and R. M. Kossey. Closed-loop control of a manipulator arm using a wrist force sensor. *IEEE Transactions on Industrial Electronics*, 34(3):371–378, 1987.

[112] G. Palli, L. Moriello, U. Scarcia, and C. Melchiorri. An underwater robotic gripper with embedded force/torque wrist sensors. *IFAC Papers online*, 50(1):11209–11214, 2017.

[113] Z. J. Wang, W. Y. Liu, B. Y. Cui, J. He, Z. X. Li, and Y. S. Zhao. Research on robot surface tracking motion based on force control of six-axis wrist force sensor. *Advances in Mechanical Engineering*, 7(1), 2015.

[114] L. Jamone, L. Natale, G. Metta, and G. Sandini. Highly sensitive soft tactile sensors for an anthropomorphic robotic hand. *IEEE Sensors Journal*, 15(8):4226–4233, 2015.

[115] Z. Kappassov, J. A. Corrales, and V. Perdereau. Tactile sensing in dexterous robot hands - review. *Robotics and Autonomous Systems*, 74:195–220, 2015.

[116] T. Hoshi, H. Shinoda, and IEEE. Robot skin based on touch-area-sensitive tactile element. *IEEE International Conference on Robotics and Automation (ICRA)*, pages 3463–+, 2006.

[117] T. P. Tomo, M. Regoli, A. Schmitz, L. Natale, H. Kristanto, S. Somlor, L. Jamone, G. Metta, and S. Sugano. A new silicone structure for uskin-a soft, distributed, digital 3-axis skin sensor and its integration on the humanoid robot icub. *IEEE Robotics and Automation Letters*, 3(3):2584–2591, 2018.

[118] T. P. Tomo, S. Somlor, A. Schmitz, L. Jamone, W. J. Huang, H. Kristanto, and S. Sugano. Design and characterization of a three-axis hall effect-based soft skin sensor. *Sensors*, 16(4):11, 2016.

[119] Y. Noh, J. Bimbo, S. Sareh, H. Wurdemann, J. Fras, D. S. Chathuranga, H. Liu, J. Housden, K. Althoefer, and K. Rhode. Multi-axis force/torque sensor based on simply-supported beam and optoelectronics. *Sensors*, 16(11):22, 2016.

[120] P. Polygerinos, P. Puangmali, T. Schaeffter, R. Razavi, L. D. Seneviratne, K. Althoefer, and IEEE. Novel miniature mri-compatible fiber-optic force sensor for cardiac catheterization procedures. *2010 IEEE International Conference on Robotics and Automation*, pages 2598–2603, 2010.

[121] P. Polygerinos, A. Ataollahi, T. Schaeffter, R. Razavi, L. D. Seneviratne, and K. Althoefer. Mri-compatible intensity-modulated force sensor for cardiac catheterization procedures. *IEEE Transactions on Biomedical Engineering*, 58(3):721–726, 2011.

[122] R. E. Goldman, A. Bajo, and N. Simaan. Compliant motion control for multisegment continuum robots with actuation force sensing. *IEEE Transactions on Robotics*, 30(4):890–902, 2014.

[123] A. Bajo and N. Simaan. Kinematics-based detection and localization of contacts along multisegment continuum robots. *IEEE Transactions on Robotics*, 28(2):291–302, 2012.

[124] A. Bajo and N. Simaan. Hybrid motion/force control of multi-backbone continuum robots. *International Journal of Robotics Research*, 35(4):422–434, 2016.

[125] C. Liu, G. F. Wang, X. D. Qin, and L. Zhang. The online monitoring of surface quality based on time-frequency spectrum analysis of acoustic emission. *Functional Manufacturing and Mechanical Dynamics Ii*, 141:564–568, 2012.

[126] T. W. Liao, F. M. Tang, J. Qu, and P. J. Blau. Grinding wheel condition monitoring with boosted minimum distance classifiers. *Mechanical Systems and Signal Processing*, 22(1):217–232, 2008.

[127] I. Buj-Corral, J. Alvarez-Florez, and A. Dominguez-Fernandez. Acoustic emission analysis for the detection of appropriate cutting operations in honing processes. *Mechanical Systems and Signal Processing*, 99:873–885, 2018.

[128] A. Rabani, I. Marinescu, and D. Axinte. Acoustic emission energy transfer rate: A method for monitoring abrasive waterjet milling. *International Journal of Machine Tools & Manufacture*, 61:80–89, 2012.

[129] Z. J. Lv, Q. Xiang, and J. Z. Pang. An artificial immune algorithm based intelligent monitoring system in grinding process. *Manufacturing Process Technology, Pts 1-5*, 189-193:2759–2763, 2011.

[130] T. Blum and I. Inasaki. A study on acoustic-emission from the orthogonal cutting process. *Journal of Engineering for Industry-Transactions of the ASME*, 112(3):203–211, 1990.

[131] W. Konig, Y. Altintas, and F. Memis. Direct adaptive-control of plunge grinding process using acoustic-emission (AE) sensor. *International Journal of Machine Tools & Manufacture*, 35(10):1445–1457, 1995.

[132] R. H. Sturges. Monitoring milling processes through ae and tool part geometry. *Journal of Engineering for Industry-Transactions of the ASME*, 114(1):8–14, 1992.

[133] Y. G. Zeng and E. Forssberg. Application of vibration signal measurement for monitoring grinding parameters. *Mechanical Systems and Signal Processing*, 8(6):703–713, 1994.

[134] E. M. Rubio and R. Teti. Cutting parameters analysis for the development of a milling process monitoring system based on audible energy sound. *Journal of Intelligent Manufacturing*, 20(1):43–54, 2009.

[135] P. Iskra and C. Tanaka. A comparison of selected acoustic signal analysis techniques to evaluate wood surface roughness produced during routing. *Wood Science and Technology*, 40(3):247–259, 2006.

[136] T. Thaler, P. Potocnik, I. Bric, and E. Govekar. Chatter detection in band sawing based on discriminant analysis of sound features. *Applied Acoustics*, 77:114–121, 2014.

[137] G. Zoller, V. Wall, and O. Brock. Acoustic sensing for soft pneumatic actuators. *25th IEEE/RSJ International Conference on Intelligent Robots and Systems (IROS)*, pages 6986–6991, 2018.

[138] L. Robben, S. Rahman, J. C. Buhl, B. Denkena, and B. Konopatzki. Airborne sound emission as a process monitoring tool in the cut-off grinding of concrete. *Applied Acoustics*, 71(1):52–60, 2010.

[139] M. A. Khan, K. Basit, S. Z. Khan, K. A. Khan, and A. G. Starr. Experimental assessment of multiple contact wear using airborne noise under dry and lubricated conditions. *Proceedings of the Institution of Mechanical Engineers Part J-Journal of Engineering Tribology*, 231(12):1503–1516, 2017.

[140] M. H. Raibert and J. J. Craig. Hybrid position-force control of manipulators. *Journal of Dynamic Systems Measurement and Control-Transactions of the ASME*, 103(2):126–133, 1981.

[141] Dale E. Seborg, Thomas F. Edgar, and Duncan A. Mellichamp. *Process dynamics and control*. Wiley, Hoboken, 2nd edition, 2004.

[142] R. Volpe and P. Khosla. A theoretical and experimental investigation of explicit force control strategies for manipulators. *IEEE Transactions on Automatic Control*, 38(11):1634–1650, 1993.

[143] O. Khatib. A unified approach for motion and force control of robot manipulators - the operational space formulation. *IEEE Journal of Robotics and Automation*, 3(1):43–53, 1987.

[144] T. Yoshikawa. Dynamic hybrid position force control of robot manipulators - description of hand constraints and calculation of joint driving force. *IEEE Journal of Robotics and Automation*, 3(5):386–392, 1987.

[145] S. Chiaverini and L. Sciavicco. The parallel approach to force position control of robotic manipulators. *IEEE Transactions on Robotics and Automation*, 9(4):361–373, 1993.

[146] M. Mahvash and P. E. Dupont. Stiffness control of surgical continuum manipulators. *IEEE Transactions on Robotics*, 27(2):334–345, 2011.

[147] M. C. Yip and D. B. Camarillo. Model-less hybrid position/force control: A minimalist approach for continuum manipulators in unknown, constrained environments. *IEEE Robotics and Automation Letters*, 1(2):844–851, 2016.

[148] E. Boudreault, B. Hazel, J. Cote, and S. Godin. In situ post-weld heat treatment on martensitic stainless steel turbine runners using a robotic induction heating process to control temperature distribution. *27th IAHR Symposium on Hydraulic Machinery and Systems (IAHR 2014), Pts 1-7*, 22, 2014.

[149] B. Hazel, J. Cote, Y. Laroche, and P. Mongenot. A portable, multiprocess, track-based robot for in situ work on hydropower equipment. *Journal of Field Robotics*, 29(1):69–101, 2012.

[150] Intuitive Surgical. About da vinci systems. `https://www.davincisurgery.com/da-vinci-systems/about-da-vinci-systems`, April 2020.

[151] W. J. Lang. The art of borescope photography. *Materials Evaluation*, 45(12):1361–1369, 1987.

[152] R. J. Valkenburg and A. M. McIvor. Accurate 3d measurement using a structured light system. *Image and Vision Computing*, 16(2):99–110, 1998.

[153] H. Kieu, T. Y. Pan, Z. Y. Wang, M. Le, H. Nguyen, and M. Vo. Accurate 3d shape measurement of multiple separate objects with stereo vision. *Measurement Science and Technology*, 25(3), 2014.

[154] Richard Wolf GmbH. Aerospace applications. `https://www.richard-wolf.com/en/solutions/aerospace-applications/`, April 2020.

[155] N. Lobontiu and J. S. N. Paine. Design of circular cross-section corner-filleted flexure hinges for three-dimensional compliant mechanisms. *Journal of Mechanical Design*, 124(3):479–484, 2002.

[156] C. A. Klein and C. H. Huang. Review of pseudoinverse control for use with kinematically redundant manipulators. *IEEE Transactions on Systems Man and Cybernetics*, 13(2):245–250, 1983.

[157] Librestream. Enabling remote video inspections. `https://librestream.com/solutions/remote-video-inspections/`, April 2020.

[158] B. Briscoe, A. Brunstrom, A. Petlund, D. Hayes, D. Ros, I. J. Tsang, S. Gjessing, G. Fairhurst, C. Griwodz, and M. Welzl. Reducing internet latency: A survey of techniques and their merits. *IEEE Communications Surveys and Tutorials*, 18(3):2149–2196, 2016.

[159] R. Noordally, X. Nicolay, P. Anelli, R. Lorion, and P. U. Tournoux. Analysis of internet latency : the reunion island case. *Asian Internet Engineering Conference (AIntEC 2016)*, pages 49–56, 2016.

[160] H. B. Wang, M. Totaro, and L. Beccai. Toward perceptive soft robots: Progress and challenges. *Advanced Science*, 5(9):17, 2018.

[161] M. Rolf and J. J. Steil. Efficient exploratory learning of inverse kinematics on a bionic elephant trunk. *IEEE Transactions on Neural Networks and Learning Systems*, 25(6):1147–1160, 2014.

[162] M. E. Giannaccini, C. Q. Xiang, A. Atyabi, T. Theodoridis, S. Nefti-Meziani, and S. Davis. Novel design of a soft lightweight pneumatic continuum robot arm with decoupled variable stiffness and positioning. *Soft Robotics*, 5(1):54–70, 2018.

[163] Angel A. J. Torriero and Muhammad J. A. Shiddiky. *Electrochemical properties and applications of ionic liquids*. Nova Science Publishers, Hauppauge, N.Y., 2010.

[164] R. Pal. New models for the complex shear modulus of nondilute emulsions of two immiscible viscoelastic liquids. *Colloid and Polymer Science*, 280(7):616–623, 2002.

[165] Z. S. Qureshi, K. M. Deshmukh, and B. M. Bhanage. Applications of ionic liquids in organic synthesis and catalysis. *Clean Technologies and Environmental Policy*, 16(8):1487–1513, 2014.

[166] M. H. G. Prechtl and P. S. Campbell. Metal oxide and bimetallic nanoparticles in ionic liquids: synthesis and application in multiphase catalysis. *Nanotechnology Reviews*, 2(5):577–595, 2013.

[167] A. Schmitt, J. P. Meullenet, and R. Varoqui. Relaxation and electrophoretic effects in polyelectrolyte solutions .2. polyelectrolyte-plus-salt solutions. *Biopolymers*, 17(5):1249–1255, 1978.

[168] Albright Technologies. Part design. `https://albrightsilicone.com/part-design/`, April 2020.

[169] Ioan D. Marinescu. *Handbook of machining with grinding wheels*. CRC Press, Taylor & Francis Group, CRC Press is an imprint of the Taylor & Francis Group, Boca Raton, second edition. edition, 2016.

[170] Bill Gunston. *The development of jet and turbine aero engines*. Patrick Stephens, Sparkford, Somerset, 2nd edition, 1997.

[171] J. E. Dyson and B. W. Darvell. Torque, power and efficiency characterization of dental air turbine handpieces. *Journal of Dentistry*, 27(8):573–586, 1999.

[172] U. S. P. Durgumahanti, V. Singh, and P. V. Rao. A new model for grinding force prediction and analysis. *International Journal of Machine Tools & Manufacture*, 50(3):231–240, 2010.

[173] Finn Jacobsen and Peter Moller Juhl. *Fundamentals of general linear acoustics*. John Wiley & Sons Inc., Chichester, West Sussex, United Kingdom, 2013.

[174] A. V. Gopal and P. V. Rao. The optimisation of the grinding of silicon carbide with diamond wheels using genetic algorithms. *International Journal of Advanced Manufacturing Technology*, 22(7-8):475–480, 2003.

Appendix A

Equipment index

Chapter 3 hardware

Description	Model	Manufacturer	Quantity
Servo actuator	FHA-8C-50	Harmonic Drive	1
Linear actuator	L-220.50SG	Physik Instrumente	1
Linear actuator	L-220.20SG	Physik Instrumente	6
Load cell	LCM201	Omega Engineering	6
Stereo borescope	Mentor Visual iQ 4mm	Waygate Technologies	1
Engine turning actuator	Turning Tool Controller	Olympus	1
Linear actuator controller	C843	Physik Instrumente	2
Servo drive	Gold DC Whistle	ELMO Motion Control	1
Microprocessor	Arduino Pro Mini 328	ATMEL corp.	1
USB to serial device	USB-Serial	FTDI	1
Force data capture system	iNET-400	Omega Engineering	1
Pneumatic pressure regulator	AW20	SMC	1
Pneumatic solenoid valve	VX2	SMC	1
USB frame grabber	HDMI-USB	Magewell	1
Local network router	AC750	TP-Link	1
Video gauge	N/A	IMETRUM	1
Motion capture camera	Vantage 16	VICON	4
Site camera	Onsight 2500R	Librestream	1
Control PC (low level)	EMP373	ACME Portable	1
Control PC (high level)	Seahawk 100	ACME Portable	1
Turbofan engine	Trent XWB	Rolls-Royce	1

Chapter 4 hardware

Description	Model	Manufacturer	Quantity
DC linear actuator	50-100-12-P	Actuonix Motion Devices	1
Control PC	EMP373	ACME Portable	1
Input/output board	PCI-6229	National Instruments	1
BNC breakout	BNC-2110	National Instruments	1
Load cell	LCM201	Omega Engineering	2
Stepper motor	5350366	RS Pro	2
Microprocessor	ATtiny85	ATMEL corp.	2
Motor driver	L293D	STMicroelectronics	2
Voltage regulator	LM7805	STMicroeletronics	1
Motion capture camera	Vantage 16	VICON	4
Linear actuator	100N-ELA	RS Pro	6
Stepper motor driver	LP3575S	RS Pro	6

Chapter 5 hardware

Description	Model	Manufacturer	Quantity
Air-driven spindle	Presto Aqua Lux	NSK-Nakanishi	1
Pneumatic pressure regulator	AW20	SMC	1
3-axis load cell	9317B	Kistler	1
Array microphone	40PH CPP	G.R.A.S.	2
Pre-amplifier	12AL CPP	G.R.A.S.	2
Control PC	EMP373	ACME Portable	1
Input/output board	PCI-6229	National Instruments	1
BNC breakout	BNC-2110	National Instruments	1
Digital microscope	VHX-100	Keyence Corporation	1
DC linear actuator	50-100-12-P	Actuonix Motion Devices	1
Robot arm	R12-5	ST Robotics	1

Chapter 6 hardware

Description	Model	Manufacturer	Quantity
Control PC	EMP373	ACME Portable	1
Input/output board	PCI-6229	National Instruments	1
BNC breakout	BNC-2110	National Instruments	1
Linear actuator	100N-ELA	RS Pro	6
Stepper motor driver	LP3575S	RS Pro	6
Pneumatic pressure regulator	AW20	SMC	1
Array microphone	40PH CPP	G.R.A.S.	2
Pre-amplifier	12AL CPP	G.R.A.S.	2
3-axis load cell	9317B	Kistler	1
Motion capture camera	Vantage 16	VICON	4
Digital microscope	VHX-100	Keyence Corporation	1